Politecnico di Milano
Department of Mechanical Engineering
Doctoral Programme In Mechanical Engineering

UNCERTAINTY EVALUATION AND PERFORMANCE VERIFICATION OF A 3D GEOMETRIC FOCUS-VARIATION MEASUREMENT

Doctoral Dissertation of:
Wahyudin Permana SYAM

Supervisors:
Prof. Giovanni MORONI

Tutor:
Prof. Stefano BERETTA

The Chair of the Doctoral Program:
Prof. Bianca Maria COLOSIMO

2014 - XXVII Cycle

Abstract

Quality is an important aspect of a product. High quality product ensures the functionality of assembled products and the interchangeability among products from different manufacturers. To verify product quality, tolerance verification (geometrical measurement) by means of coordinate measuring systems has to be carried out. Advancement of manufacturing technology enables a significant reduce of critical dimensions, together with an increase of geometric complexity. This creates challenges in coordinate metrology: tolerances become tighter. Optical-based metrology instruments are a potential option to verify these tolerances. But of course also in this case traceability is a fundamental aspect to ensure reliable measurement results.

This thesis addresses the problem of traceability of a focus-variation microscope as 3D coordinate measuring system. First, the traceability of the instrument will be discussed considering its performance. Proposals for reference artifacts and procedures to conduct performance verification according to the ISO10360-8 and ISO10360-3 standards are presented. These proposals consider both 3-axis and 4-axis configurations of the instrument.

Second, an approach is presented for task-specific uncertainty evaluation by simulation, coherent with the ISO15530-4 standard. The proposed simulation approach is based on spatial statistic model considering the correlation among captured points. To support the simulation and consider all significant error sources, characterization studies to investigate the influencing factors of measurement by focus-variation microscopy are presented, too. Finally, industrial case studies are carried out to validate the simulator developed. The validation conforms to the ISO15530-4 standard.

As a byproduct of this study, algorithms to associate ideal substitute geometries to sampling points will be discussed. An improvement of non-

linear least square fitting is presented, based on the optimization of the initial solution through chaos method.

Keywords: uncertainty evaluation, performance verification, 3D measurement, fitting geometry, optical metrology

To my father,
Syam Wasugai,
my mother,
Rimbawati Gunung Suryapradja
and my sister
Wilsya Intania Syam

Acknowledgements

It is my dream to have an opportunity to conduct and finish a PhD abroad. In the beginning, it seems impossible for a person coming from Gebe, a tiny island on the east of Indonesia. But, we never know what will happen in the future. What we can do is try all the best of what we can do as well as pray to God. There is a saying of "*Do the best and god will do the rest*". I kind of believe in this saying. Of course, I can not finish this study only by my self, there are a lot of people around me that make this thesis possible. For this reason, I would like to thank them for their support, especially my father, mother and sister who always support my decision and pray for me.

I would like to specially thank Prof. Giovanni Moroni who has given me opportunity for doing PhD in Department of Mechanical Engineering, Politecnico di Milano. Not only this opportunity he has given me, but also guidances and suggestions to complete my thesis. Also to Dr. Stefano Petró, I would like to thank him for his guidance and technical discussion throughout my PhD period. In addition, Dr. Stefano Petró is the one who taught me about tactile CMM machine that we have in our lab. Prof. Giovanni Moroni and Dr. Stefano Petró are very patient to have guided a "hard-headed" student like me. All of the knowledge I obtained from them are very valuable and will be useful throughout my life.

I am grateful to Dr. Marco Cavallaro who has been helping me during my first PhD period to solve problems not directly related to it and also for his accompany during my PhD period. Ramiz Assaf has helped me a lot in finding a place to stay in Saronno, a small beautiful city in Italy. Thanks to Alessia Beretta who helps me many times to solve problem in my early stage, such as purchasing a train card, changing my correct surname in the system, etc. Also to Francesco Arleo and his family, a very kind friend who

shared office with me in my first year. I spent every Christmas day in his house with his family. I am really honored to receive this invitation. Luca Pagani is also a very kind person who has helped me in many ways. His family have invited me to their house in the second day of Christmas. The hospitality from Francesco's and Luca's family are really really appreciated by me. I will not forget the help from Nicla Frigerio, my office mate, who also has helped me to solve many problems. I remember when I was disturbing her very much to find a new house in Saronno and to talk to the agenzia. Some friends in Saronno contributes to my enjoyable stay in the city, they are Osama, Diya, and Emad. Special thanks to Abu Ayyash who has been my house mate during my PhD period.

Other special thanks are to friends who are always with me for the coffee and lunch break, they are Dariush Ebrahimi, Andrea Ratti, Anteneh Yemane and Laura Silipo. Thanks to Dariush Ebrahimi who has been a good discussion partner. Thanks to Andrea Ratti who always reminds me about something dangerous. Andrea is also my best partner to play "Golden Axe I and II". Thanks to Anteneh and Laura, a new friend in department, who have been patiently answering my questions, even though they are not an important one. These friends make an enjoyable stay in department and also to reduce my stress.

Francesco Cacciatore and Pasquale Aquilino are the two technicians in the lab who have contributed a lot to my thesis results. Without them, I can not obtained results for my thesis. Their technical suggestion in the lab are very appreciated by me. Last but not least, I would like to thank Silvia and Anna who always busy to solve our problem related to PhD procedure. And finally, to all persons who have contributed to the success of my thesis which I can not mention them one by one.

Saronno, 16 November 2014

Wahyudin P. Syam

Contents

List of Figures

LIST OF FIGURES

List of Tables

Chapter 1

Introduction

1.1 Performance verification and uncertainty of measurement in coordinate metrology

In modern manufacturing, quality is a main concern of the manufacturing organization [Loch et al. [2003]]. Technology advancement in manufacturing enables to scale down critical dimension with the increase of part geometric complexity [Hansen et al. [2006]]. This situation poses new challenges in quality control of a product. High quality product guarantees part interchangeability among manufacturers. To guarantee the quality of a product, tolerance verification has to be carried out in accordance with the design specifications to decide whether the product/part conforms to the specifications or not. The tolerance verification process should be carried out by means of coordinate metrology. In coordinate metrology, traceability is the main issue in order to obtained a reliable measurement result. VIM [BIPM et al. [2008]] defines traceability as:

"property of a measurement result whereby the result can be related to a reference through a documented unbroken chain of calibrations, each contributing to the measurement uncertainty "

There are three fundamental issues related to traceability issue in coordinate metrology, which are calibration of metrology instrument properties for error compensation, performance evaluation of metrology instrument and uncertainty of measurement (fig. 1.1). VIM [BIPM et al. [2008]]. For all the three fundamental issues in traceability,

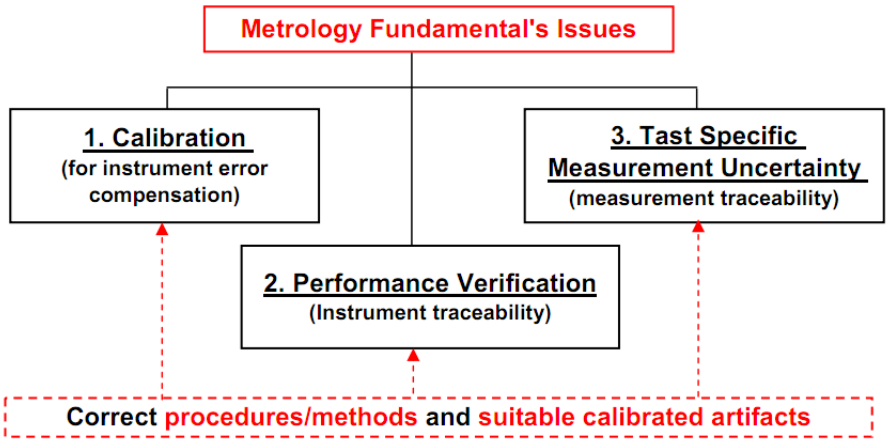

Figure 1.1: Metrology fundamental of calibration and traceability.

standardized procedures and calibrated artifacts are needed to address these issues. The calibrated artifact is used to create an unbroken-chain link to the international standard of length. Calibration is defined according to VIM [BIPM et al. [2008]] as:

"operation that, under specified conditions, in a first step, establishes a relation between the quantity values with measurement uncertainties provided by measurement standards and corresponding indications with associated measurement uncertainties and, in a second step, uses this information to establish a relation for obtaining a measurement result from an indication "

In the calibration process, the systematic error of the coordinate metrology instrument is quantified and then compensated to increase the instrument's accuracy regardless of the imperfection of the components geometry. Error compensation can be applied both by hardware and software/numerical adjustment. In software compensation, error models (cinematic, dynamic, and thermal error) of the machine are derived and fitted by the calibration data. Afterward, the volumetric error of the instrument can be mapped and then compensated for each position in the working volume [Schwencke et al. [2008]],[Ibaraki and Knapp [2012]],[Leach [2009]],[Leach [2011]].

In general, the calibration step should be carried out by the manufacturer to be able to supply an accurate machine to the customer. Hence, there should be a procedure

to verify the stated accuracy of the instrument for both the manufacturer and especially for the customer. This procedure is called performance verification. Performance verification is a procedure to verify the maximum error which can be obtained by the instrument in the whole measuring volume (Maximum Permissible Error/MPE), both for length measurement error and probing error. These two parameters become the basis for the manufacturer to accept their manufactured instrument and for the user to consider purchasing an instrument and to re-verify the purchased instrument coming from the manufacturer. This procedure is standardized in ISO 10360 series for various types of instruments, including both contact and non-contact instrument.

After performance verification, the last fundamental issue in metrology is measurement uncertainty. In every measurement result, it is not complete only to present the measurement result without the stated uncertainty of the measurement. Hence, to make the measurement results reliable and comparable, the measurement uncertainty has to be quantified such that confidence interval of the results can be stated and can be compared when the measurements are carried out by different instruments and in different conditions. In real situations, it happens that on the user side they will conduct inspection of the incoming parts received from the supplier to verify that the parts supplied by the vendor are according to their specification. A fundamental concept of measurement uncertainty is it is task specific [Wilhelm et al. [2001]],[ISO/TS15530-1 [2013]]. Task specific means that every different type of measurement, such as those for different shapes, materials, positions, and measurement strategies, etc, will have their own unique measurement uncertainty. Estimation of measurement uncertainty should be precise in the sense that it is not under-estimated or over-estimated. Under/over-estimation of measurement uncertainty will result in unwanted consequences to the total production cost [Moroni et al. [2011]].

The importance of measurement uncertainty can be found both in the pre-production and post-production phase. Illustrations of the importance of measurement uncertainty for both pre-production and post-production phase are shown in fig. 1.2. In pre-production, high measurement uncertainty will significantly reduce process capability [Kunzmann et al. [2005]]. Fig. 1.2a explains the influence of uncertainty in preproduction phase. Before a mass production is carried out, it is required to conduct a process capability test, in which a series of short run is carried out and tolerances are

verified. Standard deviation calculated from this measurement series is used to calculate the process capability (C_p). Subsequently, measurement uncertainty will greatly affect the process capability. High measurement uncertainty will under-estimate the process capability. On the other hand of post-production, an invalid decision of product acceptance-rejection (conformance) test in post-production is proportional to the increase of uncertainty [ISO14253-1 [1998]]. There are three main zones defined in ISO14253-1 related to conformance/non-conformance test as shown in fig. 1.2b, which are conformance zone, non-conformance zone, and uncertainty range (U range). They definition according to ISO 14253-1 are:

Conformance zone: *"Specification zone reduced by the expanded uncertainty of measurement, U"*

Non Conformance zone: *"Zone(s) outside the specification zone extended by the expanded uncertainty of measurement, U"*

uncertainty range: *"Range(s) close to the specification limit(s) where neither conformance nor non-conformance can be proved taking into account the uncertainty of measurement. The uncertainty range(s) is(are) located around the specification limit (one-sided specification) or specication limits (two-sided specification) and has the width of 2 U"*

where specification zone is defined as "Specified values of the characteristic giving upper and/or lower bounds of the permissible value". The decision made should be based on these zone, which are (with reference to fig. 1.2b):

1. *Conformance Zone*: If the measurement result of a part is inside this zone, then the part is accepted.
2. *Non Conformance Zone*: If the measurement result of a part is inside this zone, then the part is rejected.
3. *Uncertainty range (U range)*: If the measurement result of a part is inside this zone, then one can not state whether the part is accepted or rejected.

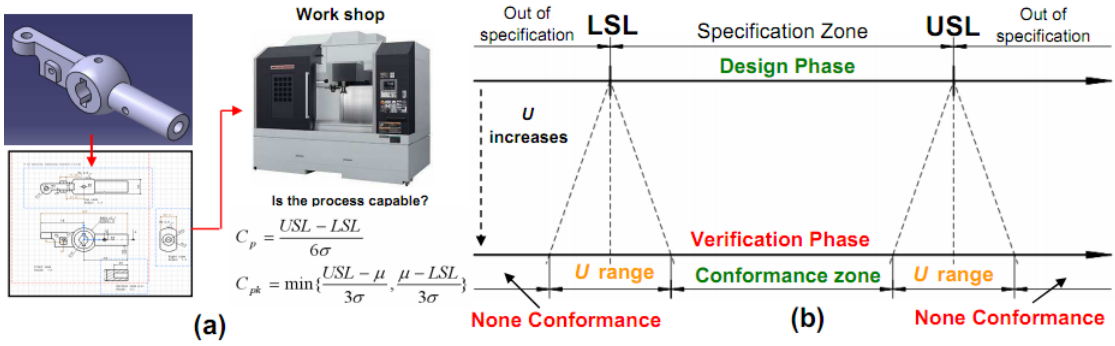

Figure 1.2: Effect of uncertainty (a) in pre-production phase and (b) in post-production phase.

Based on this standard, high measurement uncertainty will reduce the conformance zone (fig. 1.2b). Moreover, it increases cost of manufacturing process in order to make the process still within a tight conformance zone.

A manufactured part is going to the micro-scale level, in term of dimensions and structure, driven by the need of micro-scale applications [Masuzawa [2000]], [Alting et al. [2003]]. Furthermore, the advance of information and communication technology (ICT) and supply chain system have endorsed a global manufacturing system where an assembled product is constituted by many sub-parts from different suppliers all around the world [Huang et al. [2013]]. As a consequence, a measurement will be carried out in different places, by different operators, and using different instruments. Thus, quantification of measurement uncertainty to guarantee measurement traceability is very important.

At the micro-scale level, there are two types of measurement: micro-geometric measurement and surface texture measurement (fig. 1.3). Micro-scale level can be both micro-size and micro-feature in a large size object. Both of the measurement types are important. Micro-geometric measurement is usually a measurement related to dimensional characteristic (length, radius, diameter, thickness, etc) and geometrical characteristic (flatness, cylindricity, roundness, location, etc). While for surface measurement, this deals with characterization of a parameter of the texture of a surface, such as the roughness, waviness, bearing area, etc.

The measurement of micro-geometric features and surface textures, together with their relation with the functionality of the part is becoming the focus by considering

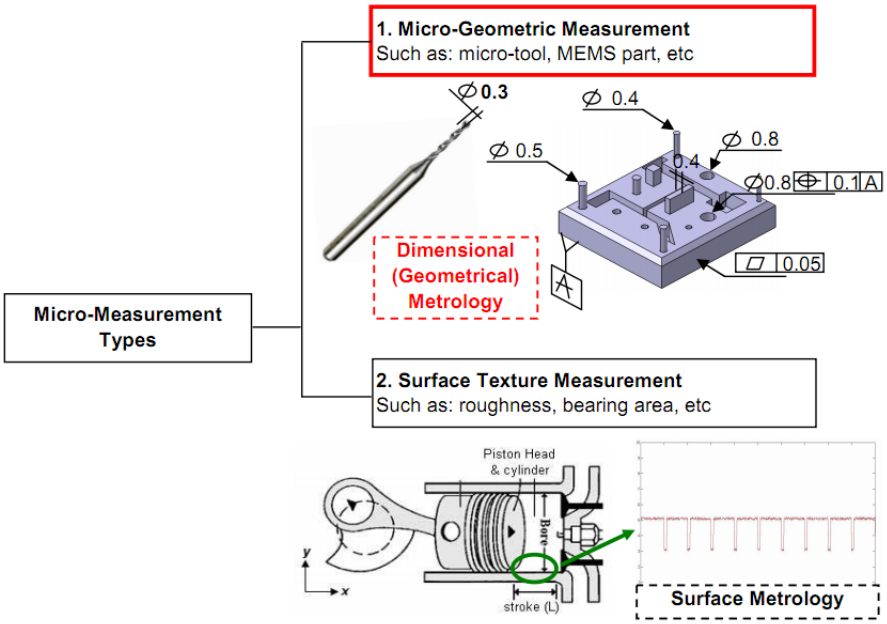

Figure 1.3: Type of micro-measurement.

its important role in micro manufacturing [Jiang and Whitehouse [2012]], [Whitehouse [2011]]. For example, quality control of micro-geometric feature, such as MEMS for lab-on-chip product, guarantees the assembly of this product. Other important roles of micro-geometric feature are in biotechnology and medicine, micro drug delivery to deliver the medicine directly to the target inside the body is very important to increase the effectiveness of the curing processes, micro-biological sensors are needed for analysis of biological process, replication technique at the micro-scale which is micro-injection molding need micro-fluidics devices and dealing with micro-channel, micro-tool measurement, micro-mold, etc. Also for surface texture measurement, it guarantees the performance of a combustion engine because the surface texture of the cylinder block has to be designed such that it contains a bearing area to reserve the oil as well as a contact area to support the piston such that the engine operates as expected. Another examples are engineered surface texture to produce a hydrophobic glass for car window such that a dirt can not attach to the window glass and surface-texture micro dimple to increase bonding strength between two surfaces. In this thesis, we focus on micro-geometric measurement.

Going to micro-geometric measurement, there are two main methods for such mea-

surement, which are contact and non-contact methods. The contact method is already practiced since the beginning of measurement and then scaled down in the micro-scale. In the contact method, the measurement process is already well understood and a rigorous model of the measurement is available for meso-scale level. In fact, contact instrument is also undergoing development for micro-scale geometric measurement. Some commercial contact-based instrument for micro geometric measurement are currently available such as ZEISS F25 and TrinNano CMM. In fact, the limitation of these contact instrument is that the diameter of the stylus tip, e.g. smallest diameter for F25 stylus tip is 100 μm. This situation limits the accessibility of a micro feature. In addition for contact method, there are some parts that risk being damaged as the parts size decreases and micro-feature accessibility issues. Moreover, measurement speed is also becoming a major drawback of this method. On the other hand, non-contact methods give more flexibility and higher speed for micro-scale measurements which are important for in-line part inspection. For non-contact method, it is divided into two sub-groups, which are *optical* and *non-optical* method. Example of non-optical method are atomic force microscopy (AFM), ultrasound microscopy (UM), and computed-tomography (CT-scan).

AFM measured a surface structure without physically touching the surface, instead by sensing the force generated between the instrument's tip and the atom of the surface. The limitation of this instrument is that the tip diameter is around 30 μm. Due to this reason, accessibility issues is still faced and and measurement speed is very slow. Moreover, vertical range of the instrument is around 20 μm and $150 \times 150 \mu m$ scanning area. This small measuring range significantly reduces instrument's flexibility to measure various size of micro-part.

UM uses an ultrasonic transducer to send ultrasonic wave to the sample and subsequently, analyze the behavior of the wave whether they are transmitted, reflected or deflected [Hellier and Shakinozsky [2012]]. Resolution of the scanning is proportional to frequency of the wave. Non-contact UM, which is one of several type of UM, is more promising since there is no direct contact between the surface and UM sensor. This type is called Electromagnetic Acoustic Transducer Ultrasound Microscopy (EATUM) and is shown in fig. 1.4. EATUM is very suitable UM method for micro-geometry measurement. The main advantage of this instrument is it can measure internal part of the sample which solves the accessibility problem that the lens-based instruments

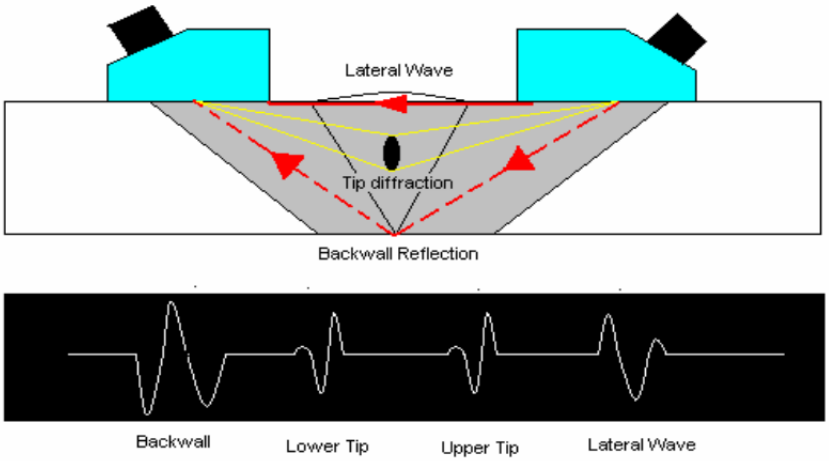

Figure 1.4: Electromagnetic Acoustic Transducer Ultrasound Microscopy (EATUM) [Hellier and Shakinozsky [2012]].

have. Attention should be considered that a complete knowledge of the behavior of ultrasonic wave in interacting with a material should be required; otherwise measurement accuracy will significantly decrease.

CT-scan working principle starts from an X-ray source. This X-ray will propagate through the work piece material. The electromagnetic energy of the X-ray is attenuated due to material absorption and scattering. This attenuation depends on the length of travel into the absorbing material, material composition and material density. The attenuated X-ray, which pass through the material, is detected in the X-ray detector panel. The detected X-ray will form a 2D gray image. Thanks to Radon transformation, 3D voxel model of the work piece can be reconstructed from the detected X-ray on the panel detector [Kruth et al. [2011]]. There are two common types of CT-scan: Cone beam and Fan beam (fig. 1.5). Main advantages of CT-scan, as ultrasound microscopy, are ability to measure internal part as well as the surface of a sample and ability to measure different types of material. A significant limitation currently occur in CT-scan is poor metrological performance. Its resolution is much lower compared to most of other non-contact method. In fact, the measurement result is affected by the thickness homogeneity of the sample. Moreover, high data storage to process the data and reconstruct the 3D voxel model is required.

In this thesis, non-contact *optical* instrument type is used. Unfortunately, for non-contact (both optical and non-optical methods), the interaction between the measured

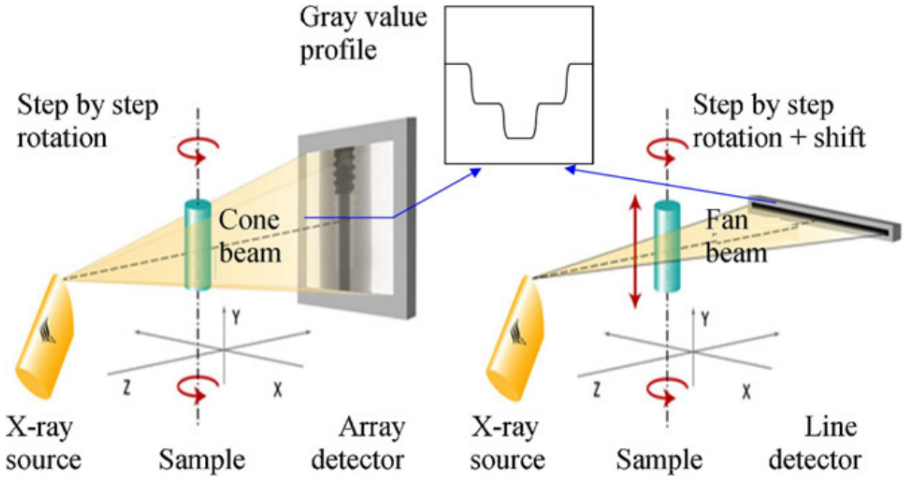

Figure 1.5: CT-System (left) Cone beam CT and (right) Fan beam CT [Kruth et al. [2011]].

artifact and the instrument is not very well understood compared to that of the contact method [Schwenke et al. [2002]], [Hocken et al. [2005]], [Hansen et al. [2006]]. Hence, the uncertainty of micro-scale measurement by optical measurement is still considerably higher than the contact method [Tosello et al. [2009]], [Tosello et al. [2010]], [Carmignato and Savio [2011]]. Fig. 1.6 illustrates the flow and complexity of non-contact measurement for estimation of measurement uncertainty. In this figure, an example of micro-geometric measurement by an optical instrument is shown. A manufactured micro feature is measured with a certain measurement plan (parameters and procedure). Dimensional and geometrical data are derived such that tolerance verification can be carried out. In this stage, the results have to be compared with the nominal value. As being explained in ISO14253-1 that to decide a part conform or not conform to the specification, uncertainty of the measurement results should be quantified. An invalid decision can cause a subsequent problems. For example, if a defected part is accepted, in the next assembly process, the components can not be assembled altogether which cause another source of cost, such as production delay, etc. Other condition is that, if a good part is rejected, it has to be re-worked or scrapped. This will become a significant lost if the part is a high cost one. To quantified the uncertainty, the main requirement is that the error sources of the measurement coming from the instrument, measurement plane, environment, and other factors have to be understood and also

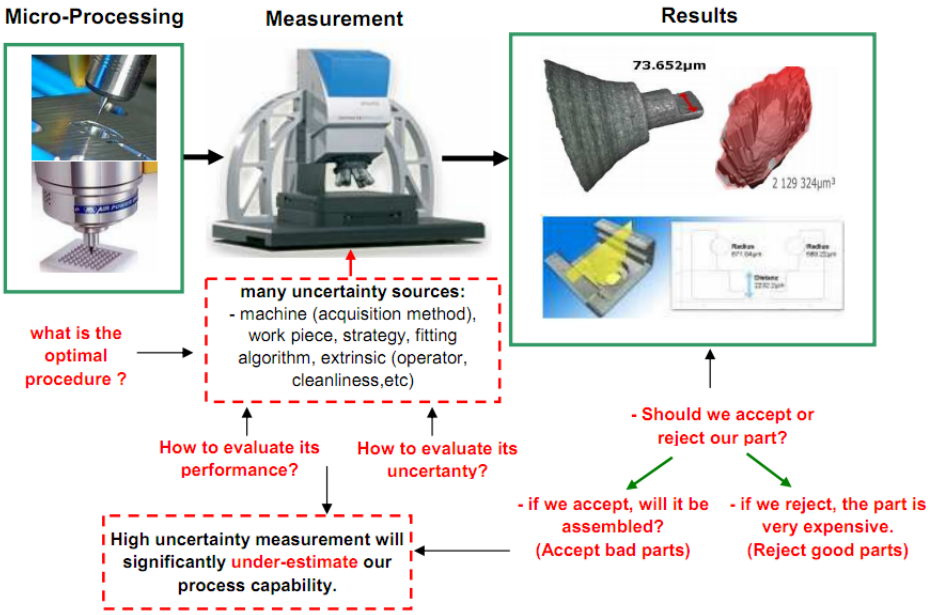

Figure 1.6: Optical micro measurement and the role of measurement uncertainty.

quantified.

1.2 Optical micro metrology

Originally, non-contact micro optical metrology comes from surface metrology instruments. Indeed, the basic working principles of optical micro-metrology are described in ISO25178-6 series. In addition, a relatively new application of X-ray tomography in 3D measurement will be briefly described. Non-contact instruments provide advantages over the contact one, such as flexibility and speed. The instruments are able to capture part surface data without a risk to damage the surface. In relatively short time, many points can be captured in one measurement cycle. Beside these advantages, the instruments have some limitations especially those equipped with microscope objective lens [Leach and Haitjema [2010]]. Firstly, largest slope of a surface which can be measured depends on the numerical aperture (NA) of the lens. NA can be formulated as:

$$NA = n\ sin\alpha \tag{1.1}$$

where n is the refractive index of medium between the lens and the part surface and α is acceptance angle of the aperture. Secondly, minimum resolution of the instrument

is limited by the wavelength of light used. Resolution is defined as minimum distance between two distinguishable lateral features. Resolution of a perfect optical system following Rayleigh criterion is given by:

$$r = 0.61\frac{\lambda}{NA} \tag{1.2}$$

where λ is the wavelength of the light. And finally, measurement result should be interpreted carefully and it is more difficult compared to the contact one due to the complex interaction between electromagnetic wave (light) and the part surface.

Basically, non-contact instruments are divided into two classes: instruments which measure real part surface and those that measure only the statistical surface parameter such as scatter light method (area-integrating method) [Leach and Haitjema [2010]]. The later class is not considered in this study. There are various method used by non-contact instrument to measure the real part surface. These methods are listed in [ISO25178-6 [2010]]. Moreover, most of the methods are explained in more detail in [Leach [2011]].

1.2.1 Confocal Microscopy

In confocal microscope, a light source illuminates a pinhole object to the workpiece through the objective lens to create a point illumination. The light is reflected back to the objective lens and then deflected by a semi-transparent mirror to second pinhole, placed in front of photo detector and acts as spatial filter. The instruments will scan vertically within a certain given range. A point which is in focus position will have higher intensity value on the detector. Hence, the height (Z)-position of the point is determined by fitting the intensity data to get the position in which the intensity is the highest. This type of instrument has vertical and lateral resolution in the range of 2-150 nm and 150-5000 nm, respectively.

1. Confocal Microscope

Construction of confocal microscope is depicted in fig. 1.7a. A monochromatic light source, which is a laser source, is used in this configuration. The discrimination pinhole, located in front of the detector, rejects the light which is out of focus (thicker than the depth of focus of the objective lens). At each instance, only single point on the workpiece is illuminated. As such, a beam scanning procedure of the light should be carried

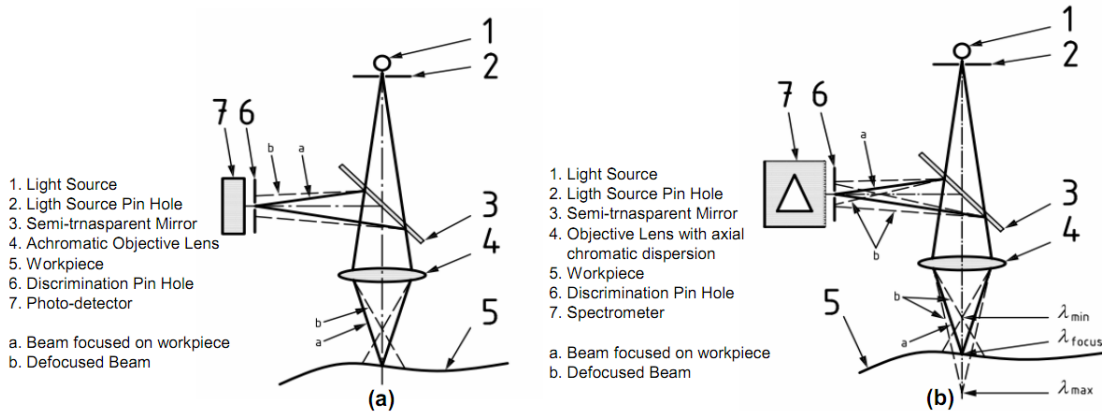

Figure 1.7: Schematic view of (a) Confocal microscope, (b) Chromatic Confocal Microscope [ISO25178-602 [2010]].

out to illuminate all the field of view (FOV) of the surface (area scanning) [ISO25178-602 [2010]]. There are three types of available beam scanning: Confocal Laser Scanning method by using multiple mirrors to scan the beam, Spinning-disk (Nipkow Disk) by using a series of moving pinhole on a disc, and Programmable Array Microscope (PAM) by using electronically controlled spatial light modulator (SLM) which produces a set of moving pinhole. The advantages of this method are possibility of using high NA lens such that a high slope angle of surface can be measured (up to 70^0), very high lateral resolution, and independent of the surface color. Meanwhile, the drawback of this system are longer measuring time due to light beam scanning procedure and some difficulties in illuminating part of the surface due to the need of coaxial illumination.

2. Chromatic Confocal Microscope

Advantages of non-monochromatic light to evaluate the z coordinate of a point are utilized by chromatic confocal microscope [ISO25178-602 [2010]]. The only difference with the confocal one is the use of chromatic objective lens. Different focus distance will be obtained by different wavelengths and only the focus one will pass the discrimination hole. In this instrument, the detector used is replaced by spectrograph, a device which analyzes the chromatic property of the light and identifies the maximum intensity wavelength (fig. 1.7b). The advantage is that there is no vertical scanning needed to identify the z of a point. The z-range is limited by the difference between the focal distance of the shortest optical wavelength and the longest one. This method

is relatively faster than the classic confocal one since there is no vertical scanning. In fact, its drawbacks are limited vertical range, lower lateral resolution, and surface color influence. For the resolution, this instrument has around 0.01-10 nm for the vertical resolution, which is the highest among other methods. Meanwhile, for lateral resolution, the range is 400-600 nm.

1.2.2 Interferometry

Micro-geometric and surface topography measurement by interferometric technique involve an analysis of interference fringe between incident light from the work piece surface and reference light to the reference mirror. There are two common types of this instrument: Phase-shifting Interferometry and Coherence Scanning Interferometry.

1. Phase-Shifting Interferometry (PSI)

In this instrument type [ISO25178-603 [2011]], beam splitter directs two beams, a beam of light to the reference flat, and smooth, mirror and a beam to the part surface. These two beams reflect back to the splitter and form a fringe in an image sensor. This fringe is a superimposed signal from the two beams and has a series of dark and white band. Hence, a difference of optical path is created and the shift (fringe) variations are measured. A piezoelectric actuator is used to translate the reference mirror to create the difference optical path. Schematic view of PSI is depicted in fig. 1.8. Calculation of relative surface height Z_{ij} at point ij-th is formulated as:

$$Z_{ij} = \frac{\lambda \phi_{ij}}{4\pi} \tag{1.3}$$

where λ is the wavelength of the light and ϕ_{ij} is the fringe variation at ij-th location. Laser is commonly used for the illumination. PSI is able to have 1 nm repeatability for height measurement [Leach [2011]]. Limited Z-range and small working distance (distance between the lens and object to b observed) are some drawbacks of this system.

2. Coherence Scanning Interferometry (CSI)

CSI is also known as white-light interferometry, which uses white light as its illumination instead of monochromatic one, such as laser source (fig. 1.9). Relative Z_{ij} position is obtained by using localization of interference fringe during the vertical scanning. As

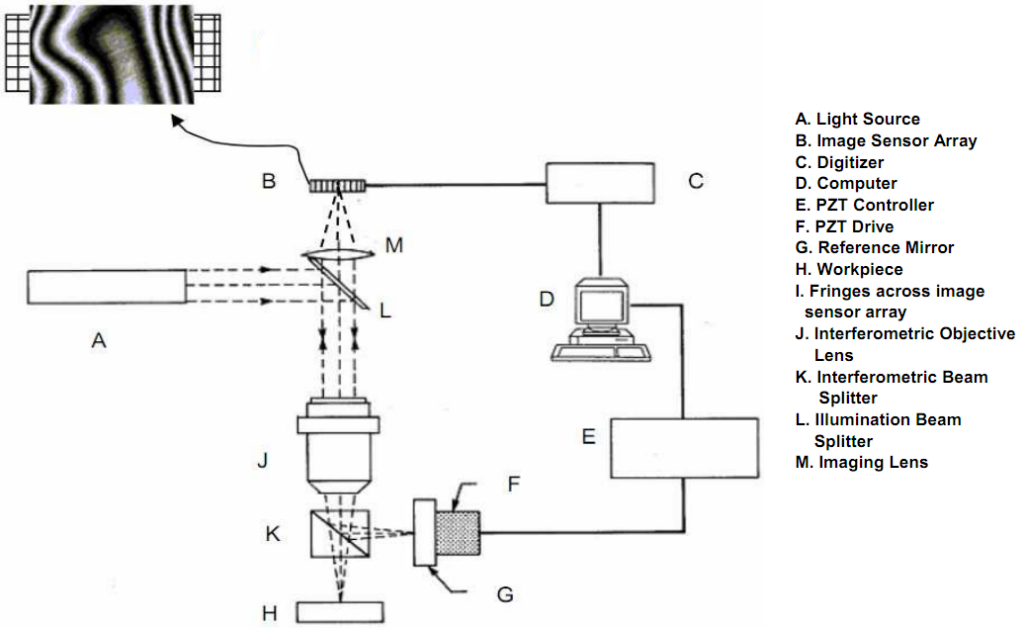

Figure 1.8: Phase-shifting Interferometry [ISO25178-603 [2011]].

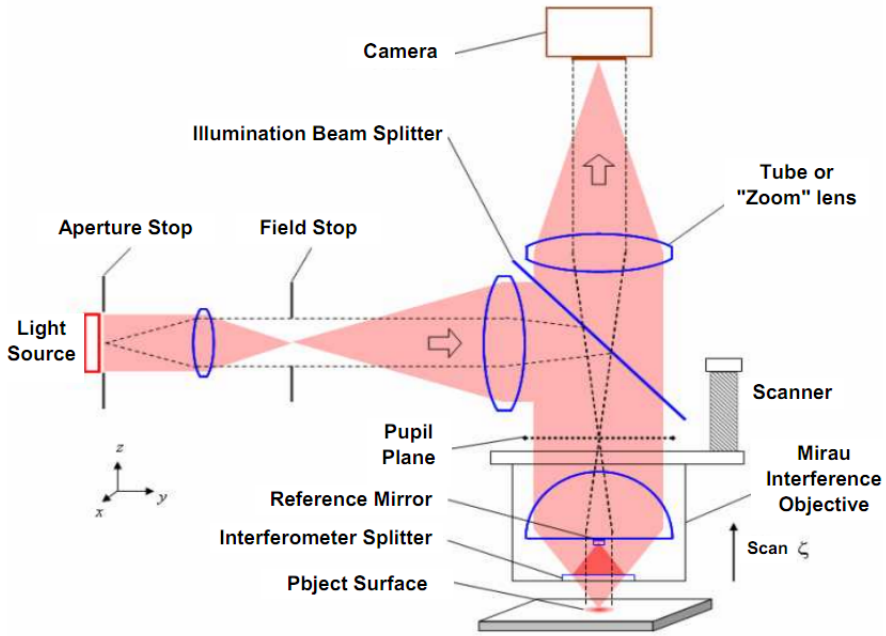

Figure 1.9: Coherence Scanning Interferometry [ISO25178-604 [2011]].].

such, the localization can be determined from the highest-contrast fringe at each pixel within the field of view. This system is very similar to microscope with coaxial illumination with additional beam splitter to create the interference signal. Fringe intensity on Michelson interferometry is demonstrated as:

$$|E|^2 = 2E_0^2\left(1 + cos\left(\frac{2\pi}{\lambda}\Delta x\right)\right) \tag{1.4}$$

where E_0 is the amplitude interference beam electric field, λ is the wavelength of monochromatic light, and Δx is the length difference between the incident and reference beams. Strong point of this system is its very high vertical resolution. In addition, it can produce a complete 3D area surface data by a single vertical scan using a Charge-Coupled Device (CCD) image sensor. In contrary, its lens has small NA which make it not able to measure high slope surface angle (maximum limit is around 15^0). Finally, problems will occur if the surface is too much diffused since the incident light is not reflected back.

1.2.3 Point Auto-Focus Instrument (PAF)

Working principle of PAF is automatically focusing a point of laser beam with a very small diameter (commonly 1 μm) to part surface [ISO25178-605 [2011]]. Area measurement is obtained by moving the XY-stage through the FOV area since it is working for a point measurement for each scanning cycle. Fig. 1.10 illustrates the instrument part and working principle. The position of the reflected laser beam from the part surface in the image sensor changes when the lens directs the beam on the surface in different vertical location. The lens displacement to get the laser on focus position at each surface is equal to the surface height. The advantages of PAF are independent of surface color and transparency such that it is very useful in lens geometry and surface measurement and high measurement accuracy [Leach [2011]]. Besides, the limitation which can be observed in this instrument are small vertical range, limited lateral resolution constrained by the objective optical resolution, and limited vertical resolution due to auto-focus repeatability and vertical linear axis resolution.

1.2.4 Digital Holography Microscopy (DHM)

DHM is an area measuring method from a single image taken in few microsecond, resulting around 20 frame per second (FPS) in live mode [Leach [2011]]. Basic working

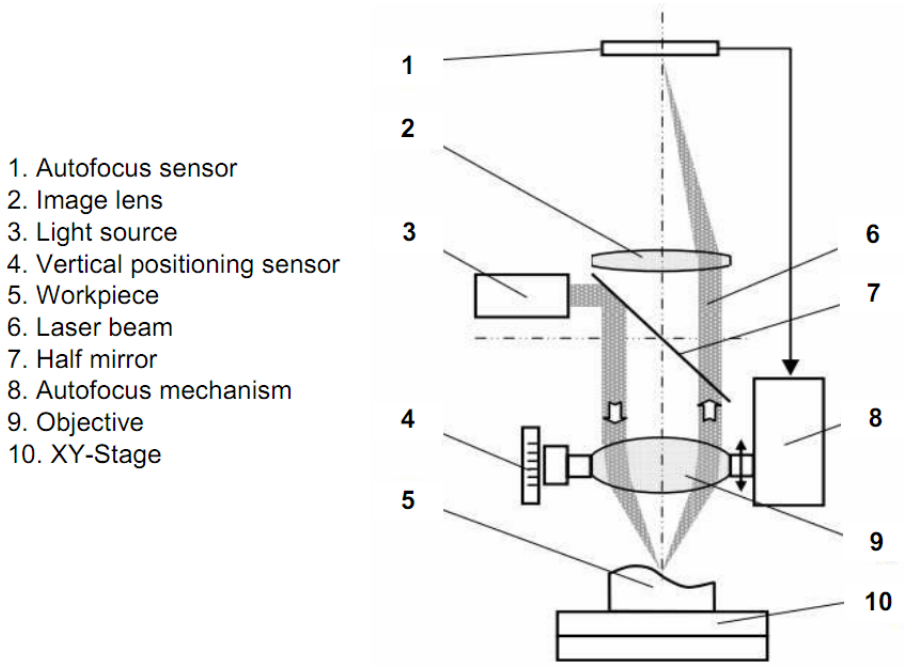

Figure 1.10: Point autofocus probe [ISO25178-605 [2011]].

principle of DHM is by analyzing the hologram on the image sensor (1.11). This hologram is resulted from interference of two waves. The first wave is the one reflected back from the part surface (O) and the reference one (R). The obtained hologram can be expressed as:

$$I_H = R^2 + O^2 + R * O + RO* \tag{1.5}$$

where * is denoting the complex conjugate, R is reference wave and O is objective wave. Subsequent filtering and reconstruction process from the obtained hologram have to be carried out to get the final surface data [Leach [2011]]. Vertical resolution of this instrument solely depends on the wavelength of the light, which can be easily certified and stabilized compared to mechanical displacement. A very high vertical resolution of 0.1 nm can be obtained by DHM since there is no mechanical scan and insensitive to vibration with 0.001 nm of repeatability. Since, DHM working from an image acquisition, it can provide high speed measurement. In addition, transparent sample can be measured with DHM. On the other hand, limitations of DHM are parasitic interference

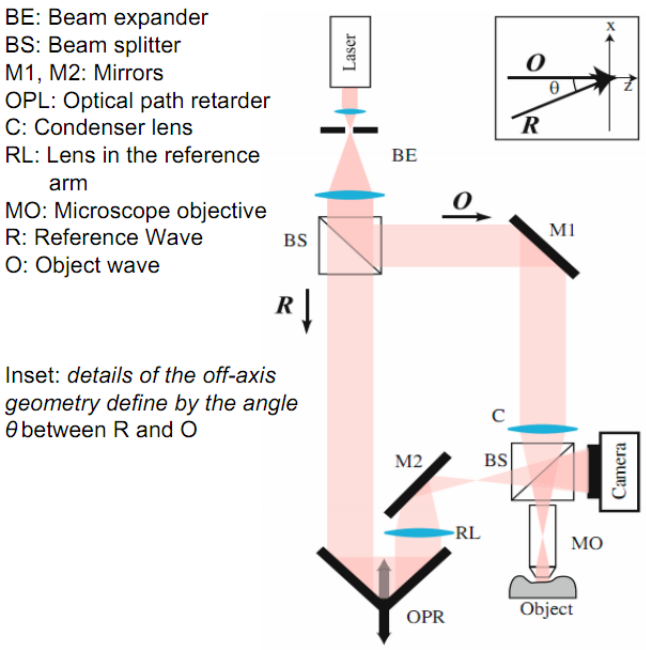

Figure 1.11: Digital Holography Microscope [Leach [2011]].

and statistical noise resulted by its off-axis geometry, limitation of vertical range which is limited by the wavelength of the light, sample limitation for light scattering and very thin surface.

1.3 Focus-Variation Microscopy (FVM)

In this study, FVM instrument is used. The main reason is this instrument has considerably large working volume of 100x100x100 mm. In addition, with 5X lens, a large working distance of the objective lens and the work piece surface can be obtained. This specification give the instrument capability to be used as micro CMM for micro 3D geometric measurement. Moreover, with the 4-axis rotation unit, the instrument can solve many undercut problems of the workpiece surface, which is a great advantage for geometrical measurement. This instrument is currently being drafted in ISO standard [ISO/DIS25178-606 [2013]]. FVM scans vertically a surface to locate the z-position in which the highest focus variation value is obtained within a FOV area [Leach [2011]]. Each scan process captures the image of the workpiece surface by sensing the incoming radiance of the surface to the charge-couple device (CCD) image sensor. It was

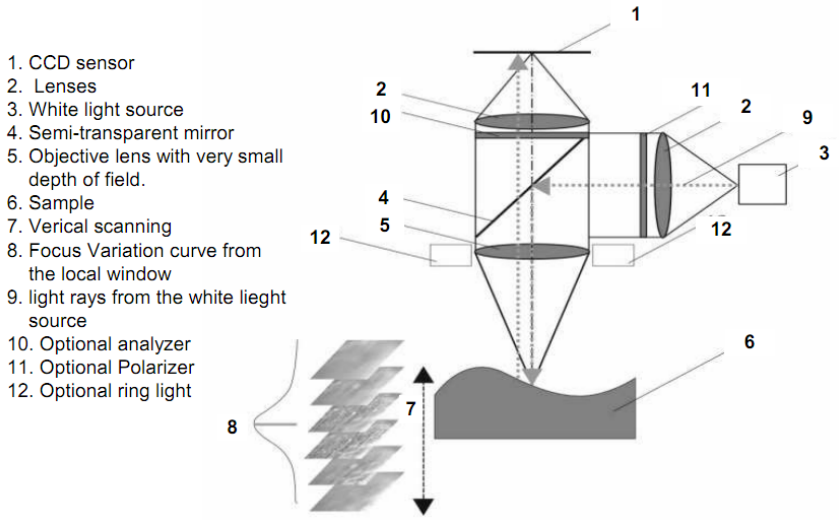

Figure 1.12: Focus Variation Instrument [Leach [2011]].

originally proposed by Nayar and Nakagawa [Nayar and Nakagawa [2011]] and further developed into a commercial high resolution optical 3D micro metrology [Danzl et al. [2010]]. Fig. 1.12 depicts the working principle of FVM. When the surface (on each point position within the FOV area) is in focus, the point image will be sharp and its difference compared to its neighborhood will be high, as such the variation of the focus will be higher compared to the value which is not in focus position (de-focus). This situation is illustrated in fig. 1.13a. The FOV area size depends on the objective lens used. It is inversely proportional to the magnification level of the lens. The higher the magnification lens used, the lower the FOV area will be. There are three types of illumination which can be used to capture the surface: standard coaxial light, ring light, and polarized light for highly reflective surface. Technical specification of this instrument related to its objective lens is shown in table 1.1. The FVM instruments provides three types of illumination: axial-light, ring-light, and polarized light. Polarized light is used to measure very high reflective surfaces. Furthermore, there are four types of basic user defined parameters: exposure time (brightness), contrast, vertical resolution, and lateral resolution. These parameters are the primary parameters which have to be defined by the user. The focus measure (FM) on each z-position $F_z(x, y)$ is formulated as:

$$F_Z(x, y) \quad = \quad FM(reg_w(I_Z(x, y))) \tag{1.6}$$

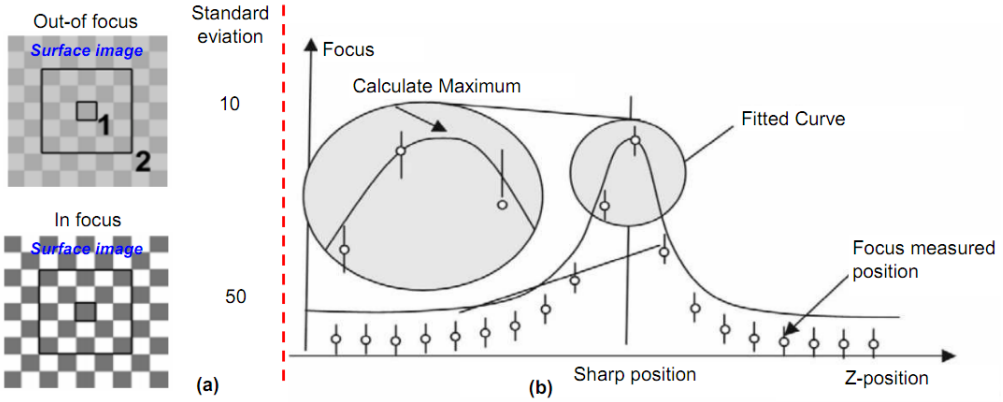

Figure 1.13: Determination of focus variation value and its Z-location [Leach [2011]].

Specification	5X	10X	20X	50X	100X
Minimum lateral sampling distance [μm]	1.76	0.88	0.44	0.18	0.09
Maximum vertical resolution [nm]	410	100	50	20	10
Working distance (WD) [mm]	23.5	17.5	13	10.1	3.5
Filed of View (FOV) X x Y [mm x mm]	2.858 × 2.175	1.429 ×1.088	0.715 × 0.544	0.286 × 0.218	0.109 × 0.15

Table 1.1: Details specifications related to the objective lens. Working distance is defined as Distance between workpiece surface and objective lens

where $reg_w(I_Z(x,y))$ is the local region of the image $I_Z(x,y)$ at position Z and centered at (x,y) coordinate. The most common calculation for FM is:

$$FM = \frac{1}{n^2} \sum_{reg_W(Iz,x,y)} \left(GV_i - \bar{G}V\right)^2 \tag{1.7}$$

where GV_i is the grey value of the $i-th$ pixel and $\bar{G}V$ is the average grey value of $reg_w(I_Z(x,y))$. After $F_Z(x,y)$ is obtained for each (x,y) and z-level of the vertical scanning, a function will be fitted to determine the z-location where the focus variation value (FM) is the highest (fig. 1.13b). There are several methods of fitting this function: maximum value method, polynomial fitting, and point spread function (PSF) curve fitting [Leach [2011]].

The maximum value method is the easiest method and the fastest one. Instead, this method has tge least accurate fitting result. this method is formulated as:

$$depth \;\; Z = arg(max\ F_Z), \quad for\ z_1 \leq z \leq z_n \tag{1.8}$$

The second alternative method for the fitting task is by using polynomial fitting. The method uses least square technique. The fitting result will be more accurate will some trade of in the computation speed. the polynomial function to be fitted and the fitting criterion are:

$$p(z) = az^2 + bz + c \tag{1.9}$$
$$\arg\min_{a,b,c} \sum_{z_1 \leq z \leq z_n} (F_z - [az^2 + bz + c])^2$$

The solution of eq. 1.9 can be nominally solved by deriving function $p(z)$ as $p'(z) = 2az + b = 0$. Hence, the maximum z can be calculated as:

$$z_{maximum} = -\frac{b}{2a} \tag{1.10}$$

The third alternative is fitting by PSF of the optical system. This method gives the highest accurate fitting result to obtained $z_{maximum}$, but the computation speed will be the slowest since the fitting procedure is computationally extensive.

In general, optical instrument is prone to outliers, which are points numerically very far (significantly larger) compared to the other points. Due to this reason, the a post processing has to be carried to remove the outliers in order to get a good measurement result. Example of outliers removal is depicted in fig. 1.14.

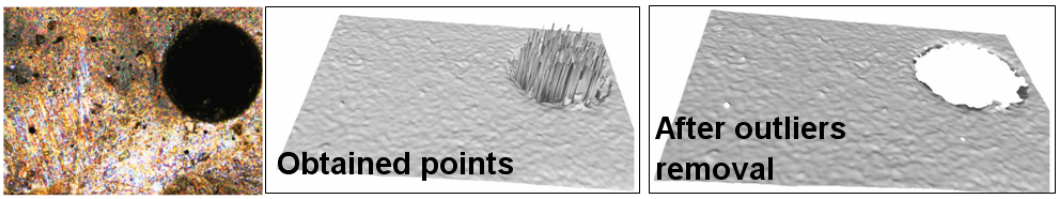

Figure 1.14: Outlier removal after points acquisition [Leach [2011]].

Advantages of FVM method are its capability in measuring the highest slope angle of a surface compared to other techniques, relatively higher speed measurement, ability to capture the surface true texture and color, possibility to utilize many types of illumination systems (including combination of them) to be able to measure various type of surfaces. For the limitation, this instrument needs minimum surface roughness, required for focus variation calculation, of 10 nm to guarantee that the variation of a point compared to its surrounding can be calculated. In addition to a very smooth surface, this instrument can not measure transparent sample such as optical lens.

1.4 Research questions

This research focuses on micro-geometric measurement focus variation microscopy (FVM) instrument. There are three researches questions that arise from this field, which are:

1. *What is performance verification in FVM instrument?*
2. *What are the error sources which influence measurement uncertainty in FVM instrument?*
3. *How is it possible to estimate "task-specific" uncertainty in FVM instrument?*

1.5 Thesis aims and structure

This thesis will address the three research questions mentioned above. Firstly, problems in performance verification of optical instrument are described. The ISO 10360 standards series exist as a guidance for performance verification of non-contact (or combination of contact and non-contact) measurements [ISO10360-7 [2011]], [ISO10360-8 [2013]], [ISO10360-9 [2011]], [ISO10360-11 [2011]]. Indeed, there are no detailed procedures and artifacts for this verification. In this thesis, a procedure and its artifact

for performance verification of optical instrument are proposed for FVM instrument. Secondly, error sources which contributes to measurement uncertainty are studied. Finally, A proposal for the estimation of "task-specific" by simulation method will be presented. To validate the proposed uncertainty estimation method, real case studies are presented for both dimensional (size) and geometrical (form) measurements.

Therefore, the thesis is structured as follows:

1. Chapter 2: Performance verification for optical metrology in general and specifically for FVM are introduced. State of the art study related to this aspect has been carried out. Proposal for artifact and procedure for performance verification for both 3-axis and 4-axis configuration are presented and discussed.

2. Chapter 3: A simulation-based approach is proposed to estimate task-specific uncertainty considering significant error sources involved in measurement by means of FVM. These error sources related to the instrument are proposed and studied based on the theory of image formation. From this study, FVM (optical) instrument has a lot more error sources which influence the measurement result and its uncertainty. Filtering procedures are discussed to handle the outliers found in the obtained points from FVM measurement. Finally, validation of the proposed simulation approach is presented.

3. Chapter 4: Related to uncertainty evaluation, case studies are proposed and presented. The case studies consist of size (dimensional) and form measurement. A comparison among results from several filtering procedure are also discussed.

4. Chapter 5: A general conclusion which summarizes all stated problems and the proposed solution is presented. After the general conclusion, a future outlook from the current results is given.

5. Appendix A: Related to this study, fitting and automatic measuring algorithm are very important. The state of the art of these algorithms are presented. An improvement for the least-square fitting of non-linear geometry is proposed and discussed. Moreover, this fitting is used for the least-square fitting in the whole thesis.

Chapter 2

Performance verification of focus-variation measuring system

2.1 State of the art

Performance verification of coordinate metrology instruments (both contact and non-contact) is an important activity to assure the traceability of the instrument to the international standard of length [BIPM et al. [2008]]. Both manufacturers and users of the instrument need the performance verification for their instrument acceptance and re-verification. Detail procedure and reference (calibrated) artifact are needed. ISO 10360-series provides the general principle and error parameters to be quantified and verified.

Performance verification for conventional contact instrument such as coordinate measuring machine (CMM) is already well-known and well-diffused into both instrument manufacturer and user and is standardized in ISO10360 part 1-5. In addition, common reference artifacts for the procedure are available, such as gage block and ball-bar. On the other hand, despite the various and emerging method for non-contact instruments, detail procedure as well as the reference artifact to support the procedure and create the traceability path is still lacking. For micro-geometric and surface texture measurement, most of the methods are based on optical distance sensing as can be found in [ISO25178-6 [2010]]. In [ISO10360-8 [2013]], the standard deals with this type of instrument. ISO10360 series standard also provide guidance for performance verification of other non-contact instrument. For measurement method by image probing,

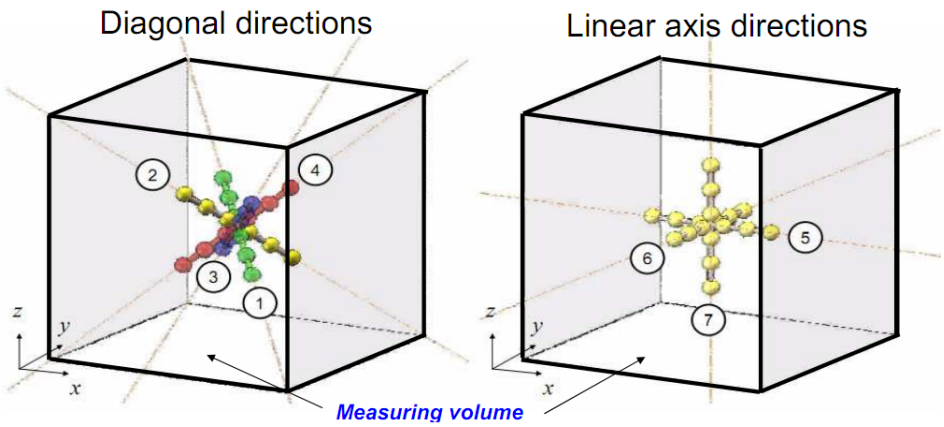

Figure 2.1: Measurement direction for volumetric length measurement error [ISO10360-8 [2013]].

based on 2D image measurement, it is standardized in [ISO10360-7 [2011]]. The main drawback of this instrument is that it can not produce 3D surface data; hence many measurements can not be carried out by this instrument, such as for profile/surface texture and depth of a feature measurement and of course 3D geometric measurement. Finally, for micro measurement by CT-scan, and may also includes ultrasonic microscopy since they share similar capability which is measuring internal part, the performance verification guide can be found in [ISO10360-11 [2011]].

FVM instrument is grouped as optical distance probing in which a 3D point cloud is obtained and the measurement procedure is carried out from the obtained point cloud. As such, ISO10360-8 is followed. In ISO10360-8, maximum permissible errors have to be verified. These errors include length measurement error as the main performance characteristic, probing form error, probing size error (for unilateral probing, such as in non-contact method) and flatness error (only for non-contact instrument). This standard do not include rotation axis error, as such for rotation axis performance verification, only ISO10360-3 is available as a guide.

Length measurement error describes the maximum error which can be obtained inside the whole measuring volume. As such, the procedure always required measurements along four diagonal of the measurement volume and along the three x-, y-, and z- axis (fig. 2.1). The four diagonals directions are compulsory. For each of these directions, there should be five different length measurements. At least 66% of the measuring length in the specified direction should be covered for the length error measurement

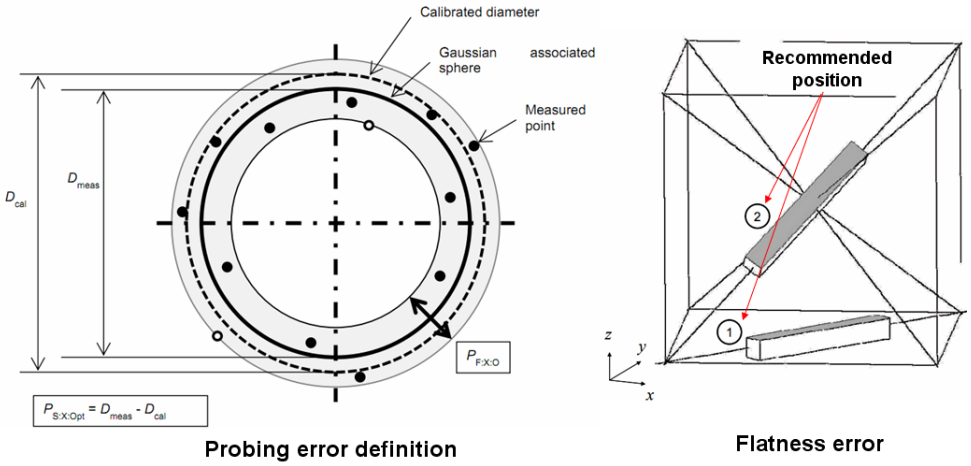

Figure 2.2: probing error definition and flatness error evaluation [ISO10360-8 [2013]]

verification. In addition, since most of non-contact instruments captured a sphere in unilateral direction, additional probing size error is introduced. Length measurement error describes global error of the measuring system. The length measurement error is defined as:

$$E_{Uni:X:ODS} = L_{Uni.meas} - L_{Uni.cal} \qquad for\ unidirectional\ measurement \tag{2.1}$$
$$E_{Bi:X:ODS} = L_{Bi.meas} - L_{Bi.cal} \qquad for\ bidirectional\ measurement$$

where $L_{Uni.meas}$ and $L_{Bi.meas}$ are the measured distance/length by means of unidirectional and bidirectional measurement, respectively. Bidirectional measurement means that the measurement are taken from two different direction, for example measurement a sphere by means of tactile instrument in which the tactile approaching the sphere from two different directions for two diametrically opposite points. Meanwhile, unidirectional means that the measurement is taken from one direction only as can be found in optical instruments. $L_{Uni.cal}$ and $L_{Bi.cal}$ are the calibrated value of the distance/length for both unidirectional and bidirectional. symbol X is to define the type of instrument (in this case "Tr") and from which the distance measurement is derived, for example from the measurement of a sphere. ODS indicates that the measurement is associated with least-squared fitting.

The two other errors which have to be evaluated are probing error and flatness measurement error. These two other requirement is shown in fig. 2.2. For the probing

error, it is divided into two groups by which it is derived. They are probing error by representative points and probing error by point cloud. Specially for probing error by point cloud, it is not obligatory to be performed if a CMM is equipped with sensor measuring individual discrete points. Main difference of the two types of probing errors are for the one derived by representative points, the fitting procedure is applied to selected 25 points taken from the obtained point clouds uniformly and equally spaced. Meanwhile for the one by point cloud, the fitting procedure is applied to the whole obtained point cloud and commonly the value will be larger than the other type of probing error. The detail of the probing error parameters are explained as follow.

The probing error by representative points consist of two type of error, which are probing size error ($P_{Size:X:ODS}$) and probing form error ($P_{Form:X:ODS}$). Probing errors (form and size) represent an error of sensing a single point of the part surface and also, it represents a local error. Probing form error is obtained by calculating the form error of a sphere fitted by Gaussian fitting procedure meanwhile probing size error is obtained from radius deviation of the fitted sphere. Subsequently, with reference to fig. 2.2left, $P_{Size:X:ODS}$ is defined as:

$$P_{Size:X:ODS} = D_{meas} - D_{cal} \tag{2.2}$$

where S refers to size, X is type of sensor behavior which is Tr in this case. Tr means that the sensor is moved by CMS. According to ISO10360-8, optical instrument has three types of sensor configuration, which are translatory, articulating and stationary (fig. 2.3). D_{meas} and D_{cal} are measured and calibrated diameter, respectively. $P_{Size:X:Opt}$ is obtained by fitting a sphere with least-square fitting method from selected 25 points. Mean while, $P_{Form:X:Opt}$ is defined as:

$$P_{Form:X:ODS} = max|d_{outer} - d_{inner}| \tag{2.3}$$

where d_{outer} and d_{inner} are the distance of the farthest points in which all of other points lie in between.

The second type of probing error is the error calculated from obtained point cloud. There are two types of probing error go this type, which are probing dispersion value $P_{Form.Sph.D95\%:X:ODS}$ and probing size error all $P_{Form.Sph.All:X:ODS}$. The probing dispersion value is determined by a spherical shell which contained 95% of the points. It

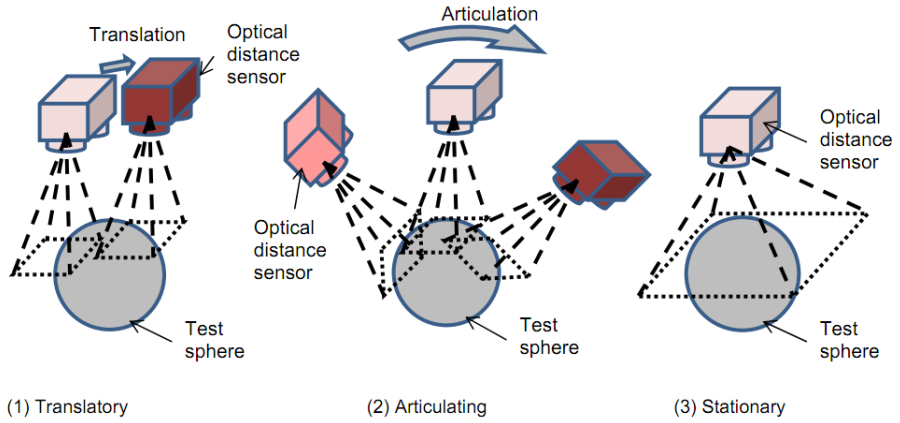

Figure 2.3: Type of sensor type [ISO10360-8 [2013]]

is calculated as:

$$P_{Form.Sph.D95\%:X:ODS} = max|d_{outer} - d_{inner}|_{95\%\ points} \tag{2.4}$$

Meanwhile, the probing error size all is calculated as:

$$P_{Form.Sph.All:X:ODS} = D_{meas} - D_{cal} \quad from\ all\ points \tag{2.5}$$

The other requirement of this standard is flat measurement error. This evaluation is important with relation to surface texture measurement and is related to noise of the vertical axis. The standard required a calibrated flat standard artifact to be measured in two positions (fig. 2.2right). The flatness error measurement is defined as:

$$E_{Form:X:ODS} = max|d_{outer} - d_{inner}| \tag{2.6}$$

where X refers to identical meaning as previously stated for length measurement and probing error In conclusion, ISO10360-8 required three type of performance verification, which are: length measurement error, probing (size and form) error and flat measurement error.

2.1.1 Procedure and artifact: Existing implementation

Performance verification of a 3D geometric measuring system requires both procedure and calibrated artifact. Reference or calibrated artifacts are very important for the traceability chain of the instrument to the international standard of length (definition of meter). A calibrated artifact should be a simple one to ease manufacturing

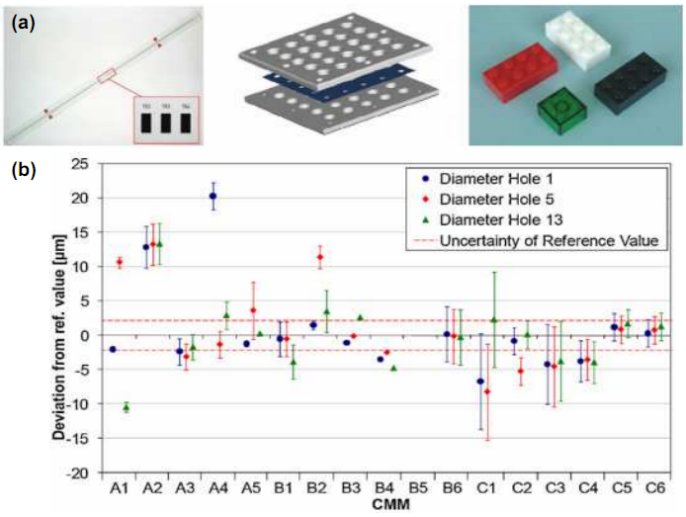

Figure 2.4: (a) Artifacts used in comparison study (b) Results of the performance comparison conducted by Carmignato et el. [Carmignato et al. [2010]].

and calibration process, thus reducing the artifact cost. Beside, simple design will ease the verification procedure [Marinello et al. [2008]]. Also for procedure, it should be practical such that can be implemented in reasonable time. Many studies have been conducted regarding the procedure and artifact for performance evaluation of non-contact metrology instruments in macro-scale metrology. The studies consist of straight forward accuracy comparison by inter-laboratory or round robin test as well as procedure development. In [Carmignato et al. [2010]], they conducted comparison study of the performance of optical metrology instrument by sequence of industrial tests. The results show that difference accuracy performance of the measurement results was obtained which is defined as deviation from the reference value (fig. 2.4b). The comparison used three types of artifacts (fig. 2.4a).

Also for macro optical metrology, [Gestel et al. [2009]] proposed a calibrated flat measurement (fig. 2.5) for performance evaluation of laser scanner. This flat form is selected since the plane geometry to be fitted is a linear optimization problem and robust fitting procedure is already available. Their proposed procedure is to evaluate the deviation of flatness value from the reference value by varying the depth of scanning and scanning in and out of plane orientation. They found that, the accuracy is best when the scanning depth is near the object and systematic error of the deviation can be reduced by warming up the instrument.

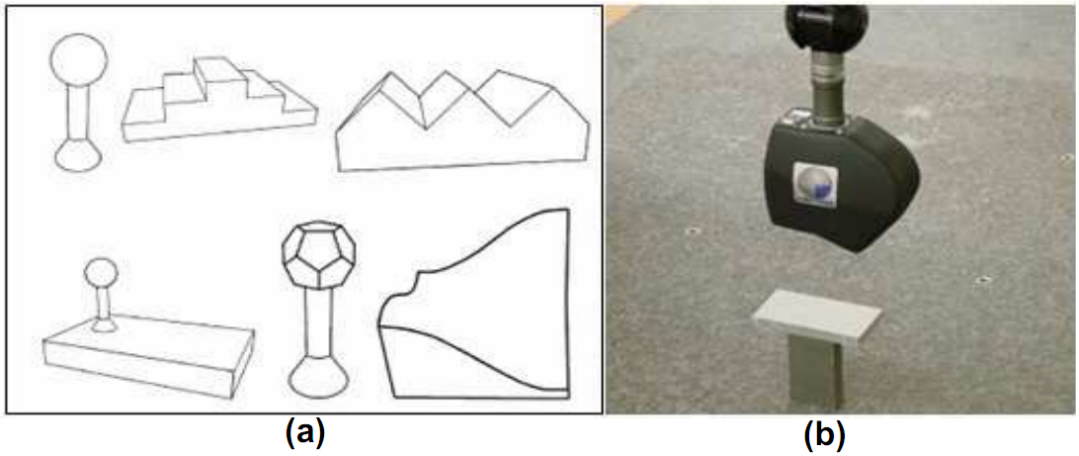

Figure 2.5: (a) options of artifacts, (b) selected flat surface artifact Gestel et al. [2009]].

A famous gage repeatability and reproducibility (GR&R) test can be used for fast analysis of the performance of instruments [Burdick et al. [2005]]. This technique uses Analysis of Variance (ANOVA) model considering random effect to assess a measuring instrument. The test basically measured and compared variance contributed by the instrument with respect to the total variability of the measurement contributed by other factor other than the instrument, such as operator, measurement day, etc. There are two important parts four GR&R study, they are repeatability and reproducibility. Here, repeatability is defined as variation calculated from the results of identical part measurements under identical condition (identical instrument, operator, etc). Meanwhile, reproducibility is defined as variation calculated from measurement results obtained from different conditions, such as: different operator, different measurement day, different parameter, etc on the same part. From the comparison of these repeatability and reproducibility, one can consider whether an instrument is suitable to do the measurement or otherwise. This test has been well-established for metrology instrument analysis.

A proposal from Neuschaefer-Rube et al. [2013] suggested a hemisphere artifact. The artifact was made on a zerodour plate with size of 90 x 90 mm. Total of nine spheres were put on the plate with certain configuration. Radius of the spheres are 2.5 mm. Distance among center of the spheres are the material measure of the proposed artifact. The artifact was calibrated with tactile CMM with calibration uncertainty of 0.2 μm. The artifact can be used for optical transmission illumination instrument with

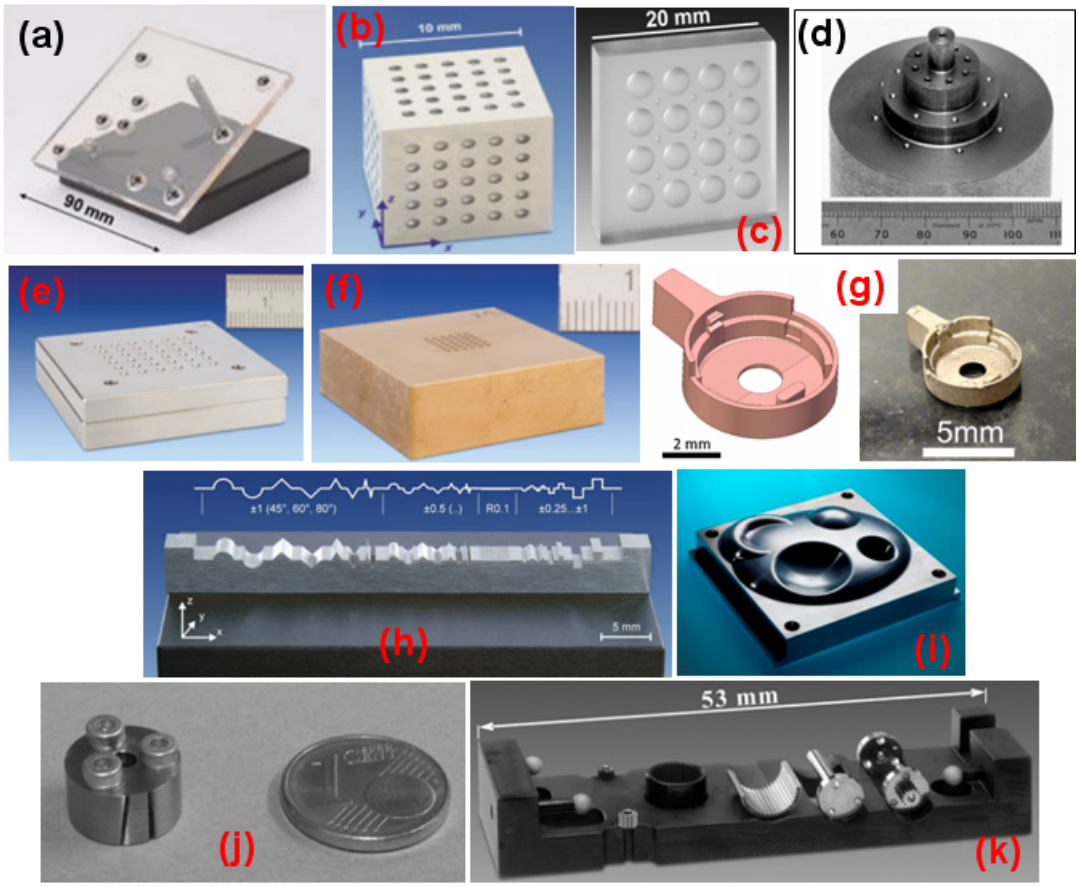

Figure 2.6: Existing artifact related to micro optical metrology.

subsequent image processing to be able to capture the sphere surface for distance measurement. This hemisphere artifact is illustrated in fig. 2.6a. *Physikalisch-Technische Bundesanstalt* (PTB) proposed a spherical calottes artifact for micro optical metrology performance evaluation [Neuschaefer-Rube et al. [2008]]. The artifact is shown in fig. 2.6b. Form of the artifact is a cube with 3x5x5 spherical calottes with radius of each sphere is 400 μm. The material of the artifact is titanium and was manufactured by means of sink and wire electrical discharge machining (EDM). The distance between sphere center is the material measure. Conventional CMM was used to calibrate the artifact with expanded calibration uncertainty of 1 μm. The idea of this artifact is there a single mismatch position of the calottes, allowing five different parallel length measurement distance as required by ISO10360-8. Similar to sphere cube calottes, PTB [Neuschaefer-Rube et al. [2008]] also developed a sphere plate calottes (fig. 2.6c).

The artifact is made of zerodour glass-ceramic manufactured by polishing and grinding processes. There are 4x4 array of 3 mm spherical calottes. CMM was used for the calibration with expanded calibration uncertainty of 1.5 μm.

A proposal for reference artifact (fig. 2.6d) to evaluate the performance of focus-variation based measuring machine has been proposed by [Hiersemenzel et al. [2013]]. The shape of the artifact is a multi-diameter cylinder having stainless steel made spheres on each face of the cylinder. The spheres are arranged such that they are aligned on face and body diagonals. The spheres have 1 mm of diameter. The measurements of the sphere center, in order to calculate spheres distances, were carried out with 50X lens. Ring light and polarizer were used for illumination. Resolutions set for the measurement are 2.93 μm and 0.68 μm, for lateral and vertical resolution, respectively. Distance among center of the spheres and sphere diameter are used to asses its length measurement error. One of measurement result with this artifact is a distance between sphere of 7.122 mm ($\sigma = 1\mu m$). For comparison, the result from CMM measurement is 7.112 mm ($\sigma = 0.06\mu m$). Their main goal is to fully implement ISO10360-8 for FVM instrument as well as to provide a way for fast interim check.

Two micro ball plates artifact were proposed by PTB [Neuschaefer-Rube et al. [2008]]. First is a micro ball plates with 6x6 array stainless steel spheres were proposed. The spheres have radius of 1 mm (fig. 2.6e). The nominal distance of the spheres is 4 mm. The second type is similar artifact with smaller stainless steel spheres with radius of 0.25 mm (fig. 2.6f). The nominal distance between spheres is 1.3 mm. Both the artifacts, the sphere has around Rz of 500 μm and were glued on canonical cavities on the plate. Special for the second artifact which has smaller spheres, a surface roughen process was applied with ultrasonic bath utilizing polishing agent.

Furthermore, a proposal of a metalized liquid crystal polymer (LCP) by electroless nickel as reference artifact of injection molded micro part measurement was reported by [Tosello et al. [2009]]. The artifacts are used for accuracy assessment optical non-contact instrument. In addition, they are also used for calculating the task-specific measurement uncertainty of injection-molded hearing aid component (fig. 2.6g). Efforts to asses the errors in measuring free-form have also been proposed. First effort is proposed by Savio for tactile CMM measurement [Savio and De Chiffre [2002]],[Savio et al. [2002]]. In their proposal, calibrated artifact for free-form measurement can be resembled from combinations of several simple artifacts and their location. The types

of artifacts and their location configurations can be chosen to resemble the free-form part as close as possible. In [Neuschaefer-Rube et al. [2013]] and [Neuschaefer-Rube et al. [2008]], an artifact with various type of form (micro contour reference standard) was developed in PTB (fig. 2.6h). The contour consist of cylinder segment, slope areas and steps with different size and dimension. The main goal is to proposed a traceable artifact for specific form measurement task with optical instrument. The idea is derived from artifact for tactile stylus instrument acceptance and re-verification testing. EDM was used to manufactured the artifact with generated surface roughness Rz=1.4 μm. This level of roughness is suited for optical instrument. National Physical Laboratory (NPL) proposed a calibrated artifact for free-form surface measurement performance verification (2.6i). This artifact is constituted by combination among basic features having both concave and convex spherical shapes. Moreover, as can be found in [Neuschaefer-Rube et al. [2008]], a micro hole standard artifact made by PTB was proposed for verification of tactile-optical instrument (fibre-gauge). It is shown in fig. 2.6j. The artifact embodied a calibrated micro-hole of (nominally) 0.125 mm of diameter and 2 mm in depth. Also for tactile-optical instrument, a micro-gear standard was proposed by PTB. It is consisted of micro-planetary gear with outer diameter of 6 mm 2.6j. A rough ball is also combined in side the artifact. This ball has 2 mm diameter which is used to define the coordinate. By this artifact, measurement results with different orientation can be obtained. Back-light illumination can be used to measure the artifact due to its cutouts design.

2.1.2 What is lacking?

Optical metrology instruments have recently obtained a wide diffusion in the market and application. Instead, a unified calibration procedure, and especially a unified calibration artifact for micro-geometric measurement, is still lacking [Acko et al. [2012]]. This lacking is illustrated in 2.7. ISO10360-8 defines instrument traceability by performing verification test. It only defines the general requirement and the parameter that have to be derived in the verification process, e.g. direction in performing the test (4-diagonals and 3-linear axis). Instead, detail procedure and artifact are not defined. There are already studies to propose a method or procedure to asses the accuracy of non-contact micro-measurement instrument. There are proposals for procedure and artifact for performance verification of instruments based on optical distance sensor.

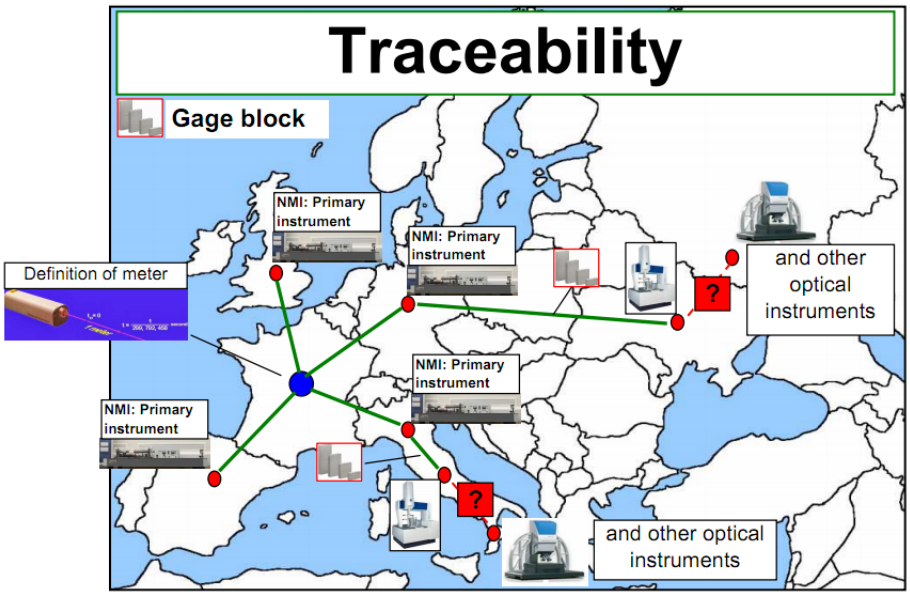

Figure 2.7: Traceability gap for optical instrument.

Unfortunately, the proposed studies (the artifact and procedure) for verification procedure are not completely following the standard guide ISO10360-8. For example, there is not yet available a verification procedure implements performance verification along diagonals and linear axis covering at least 66% length of measuring directions. Subsequently, from various types of the proposed artifacts, none of them fully comply with the ISO10360-8 standard. In addition, in order to increase the instrument capability to access the part surface, such as undercut surface, an additional rotational axis (4th-axis) is added by the manufacturer. The verification of this rotational axis is not currently addressed in ISO10360-8. By this, ISO10360-3 also has to be considered for the performance verification of the instrument. Hence, effort should be done to elaborate and develop proposal so that the ISO10360-8 standard as well as ISO10360-3 standard can be applied and used both by the manufacturer and user of the instruments.

2.2 Focus-Variation microscopy configurations

The focus-variation based optical instrument used has a maximum working volume of 100 x 100 x 100 mm with maximum working distance (with 5X lens) of 23.5 mm. In addition, with the 5X lens, the resulted FOV is about 2.8 x 2.1 mm. With this

technical specification, the instrument can be used as a CMM machine, thus, a micro optical CMM for geometry measurement. Micro optical CMM has advantages over micro tactile CMM, such as accessibility to part surface (without the risk to damage it) and ability to acquire many points within short time as well as more comprehensively covering of a surface measurement (related to geometrical tolerancing). Besides, in general, optical CMM is easier to use compared to the tactile one in term of measurement planning. In spite of the advantages, traceability is the main issue for optical CMM. In this section, new artifact and new procedure for performance verification of optical CMM are presented. The performance verification complies with IS10360-8 and ISO10360-3. They are divided into two types of instrument configurations: 3-axis configuration and 4 (3+1)-axis configuration. In different configuration, the artifact as well as the verification procedure will be different. In addition, total measuring volume will be reduced when 4-axis configuration is set. As such, performance verification should be separately addresses for both types of configuration. In this performance verification, objective nose piece of 5X magnification lens was used since it has the maximum working distance. As consequence, it will reduce the risk of collision between the objective nose piece and the part. In addition, it gives also maximum FOV so as to cover more measurement area with single image FOV measurement. In each type of performance verification, a reference calibrated artifact will be proposed since this artifact is a fundamental element to achieve instrument traceability. The role of the proposed artifacts in the traceability chain is presented in fig. 2.8. As can be seen in this figure, the proposed artifacts (along with the procedure) link the traceability of optical CMM to tactile CMM, which is traced to the definition of meter trough laser interferometry.

2.3 Measurement with 3-axis configuration

In this configuration, a maximum measuring volume capability of 100x100x100 mm can be obtained (fig. 2.9). The stage gives X-Y axis movement, and Z-axis movement is from the optical head. Maximum Permissible Error (MPE) of length measurement will be verified based on ISO10360-8 requirements [ISO10360-8 [2013]].

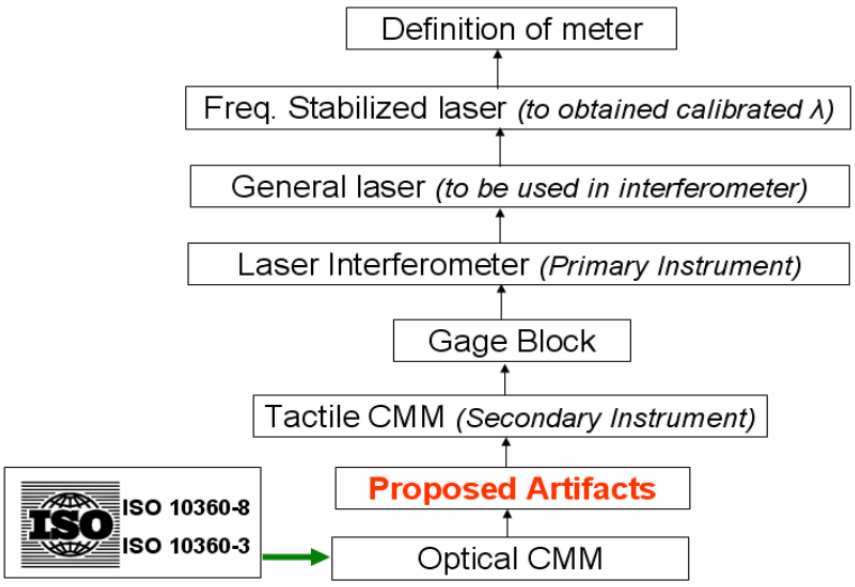

Figure 2.8: The role of the proposed artifacts in the traceability chain.

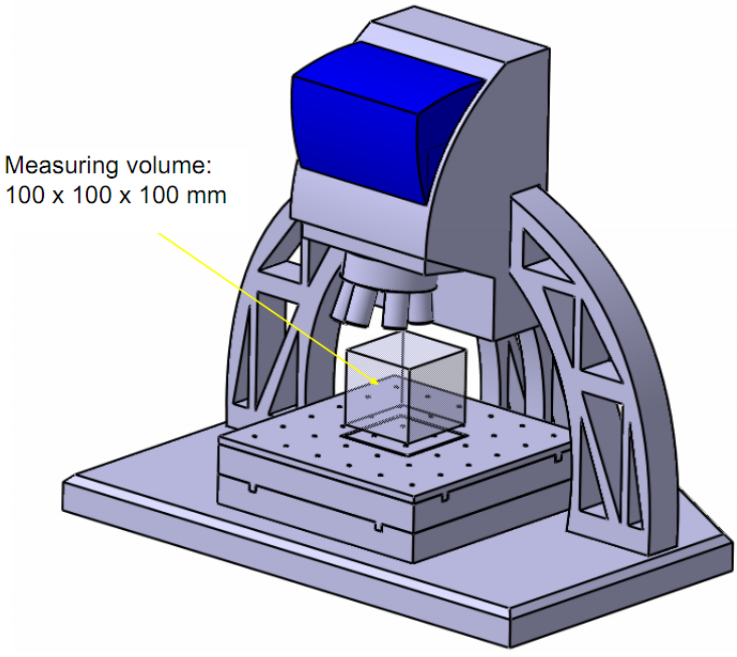

Figure 2.9: Focus-variation based instrument in 3-axis configuration.

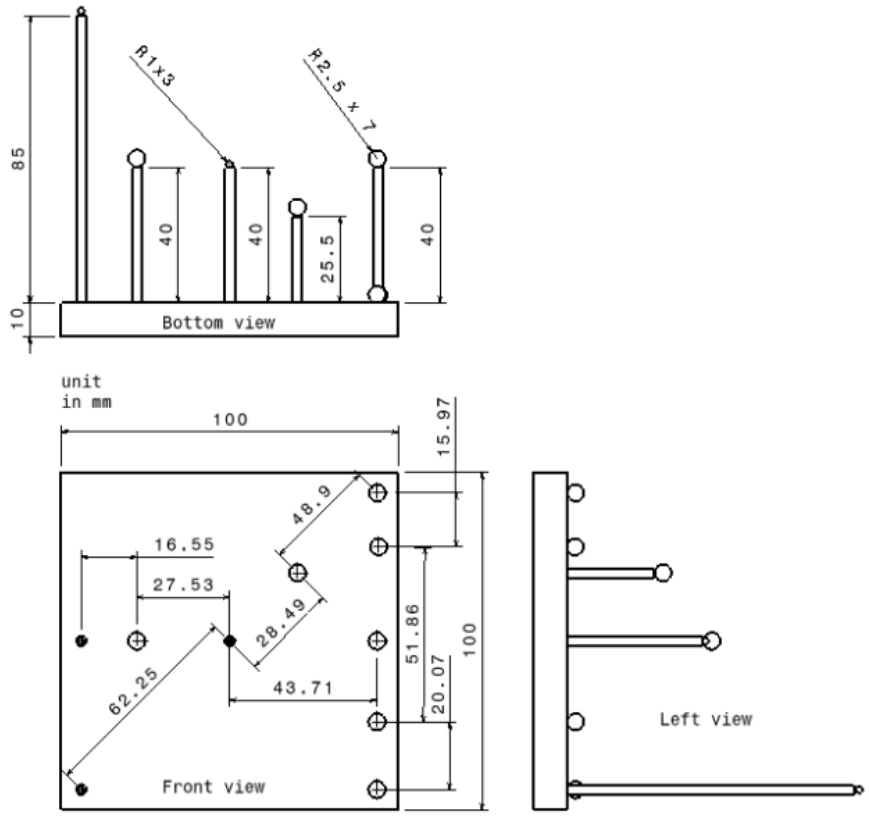

Figure 2.10: 2D Technical drawing of the proposed artifact for 3-axis configuration performance verification.

2.3.1 Proposed Artifact

In our proposed artifact, the whole volumetric error assessment is considered. The artifact consists of precision spheres made of steel. They are supported by rods of different length to set the height of the sphere inside the measuring volume. A square steel plate is used as base. Metal glue was used to paste the spheres on the rods. Glue was chosen to avoid mechanical deformation of the spheres by e.g. welding or screwing. Technical drawing of the proposed artifact for this type of performance verification is shown in fig. 2.10. Fig. 2.11 shows the side and top view of the artifact. The selected balls are grade G10 steel balls [ISO3290-1 [2008]], characterized by a roughness tolerance on Ra of 20 nm and form and diameter tolerance both equal to 250 nm. The highest G3 grade balls based on [ISO3290-1 [2008]] can not be used since it cannot be measured by a focus variation instrument. As explained in Leach [Leach [2011]], focus

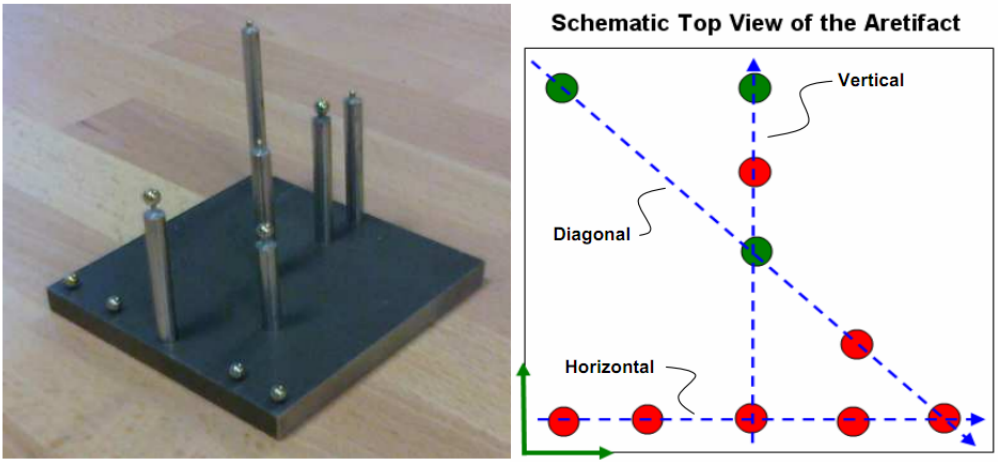

Figure 2.11: The proposed artifact for 3-axis configuration performance verification.

variation needs certain level of roughness such that the focus of a point relative to its neighbors can be differentiated (there is a contrast with respect to the neighborhood pixel). Otherwise, no point can be captured on the surface of the part. The minimum roughness required for point sampling is 10 nm.

The key idea of the artifact design is the selection of sphere diameter and location. Spheres were selected by two differing diameters: 2 mm and 5 mm shown in green and red respectively in 2.11. Spheres of 2 mm diameter have been selected such that they can be measured with only single image field by using a 5x magnification lens. 5 mm diameter balls are used so that image stitching will be needed to capture the surface of the sphere. Therefore, the performance verification considers the stitching procedure of the obtained surface to have a comprehensive evaluation by taking into account stitching error.

Finally, the balls reciprocal locations were designed in order to comply with the ISO 10360-8 standards series [ISO10360-8 [2013]] for performance verification. Four series of balls are present in the artifact, each one characterized by differing configuration: two in-line configurations at constant height (0 mm and 50 mm) and one diagonal configuration (2.11). By 90^0 rotating the artifact, all positions configuration for performance verification stated in ISO 10360-8 can be achieved. Based on this, the volumetric measurement error can be assessed. In each configuration, for both in-line and diagonal, there are four spheres which have different reciprocal distances. The distances among

the spheres in each configuration are different. By this five different length measurements can be carried out by defining a series of spheres couples with minimum number of spheres used. As consequence, the artifact is easier to manufacture and calibrate. In this study, only two configurations were used: in-line configuration with height of 50 mm and diagonal configuration (the horizontal configuration is additional) since with these two configurations, the main requirement of ISO10360-8 can be satisfied. This in-line configuration was rotated to evaluate the x- and y-axis distance measurement. Lengths among spheres in each configuration are then calibrated by mean of certified tactile CMM.

2.3.2 Calibration of artifact

The calibration was carried out to determine the reciprocal location of the spheres. The artifact calibration was carried out according to a multiple strategies measurement. This procedure does not require a reference artifact which can reduce the cost of calibration process. Instead, calibration uncertainty is determined by varying the orientation of the artifact while performing the calibration. The idea of this procedure is to carry multiple different strategies to measure the artifact such that volumetric error of the CMM can also be taken into account in the calibration uncertainty (more precise estimation). This is an alternative way for the calibration of unique artifacts. A tactile CMM with $E_{0,MPE} = 2 + \frac{L}{300}\mu m$ (where L is the measured length in mm) was used. The notation $E_{0,MPE}$ is defined in ISO standard [ISO10360-2 [2009]].

Four different orientations were selected. On each orientation, five measurement repetitions were carried out to be able to evaluate the repeatability contribution to the total calibration uncertainty. After the locations of the spheres are calibrated, the distance between two spheres can be calculated. The relative distances are derived from the measurement of the coordinates of the center of the spheres obtained by fitting the points measured on the spheres themselves. With this procedure, the obtained calibration uncertainties can be smaller than the instrument's $E_{0,MPE}$. The reasons are the random error in determining the sphere center is reduced by least-square (Gaussian) fitting of several hundreds of points. Second, the scale error is compensated by comparing the measured length with the measured reference gage block. Third, averaging effect from total 20 measurements is also reducing the random error. Table 2.1 shows

	Orientation (J=1)	**Orientation (J=2)**	**Orientation (J=3)**	**Orientation (J=4)**
Cycle (i=1)	y_{11}	y_{12}	y_{13}	y_{14}
Cycle (i=2)	y_{21}	y_{22}	y_{23}	y_{24}
Cycle (i=3)	y_{31}	y_{32}	y_{33}	y_{34}
Cycle (i=4)	y_{41}	y_{42}	y_{43}	y_{44}
Cycle (i=5)	y_{51}	y_{52}	y_{53}	y_{54}
Average (Y_j)	Y_1	Y_2	Y_3	Y_4
Standard Deviation (S_j)	S_1	S_2	S_3	S_4

Table 2.1: Data sheet for the calibration procedure.

table for measurement data in the calibration process. The table consists of four different orientations. In each orientation, replications are carried out five times. Average and standard deviation are calculated for each orientation.

There are two values calculated from the calibration process: calibrated length and calibration uncertainty. The calibrated length y_{corr} is defined as:

$$y_{corr} = y - E_L \tag{2.7}$$

where y is the average of all measurements carried out to the measured object and E_L is average distance measurement error. E_L is calculated by:

$$E_L = L\ E_{L_{prop}} \tag{2.8}$$

where L is the measured length and $E_{L_{prop}}$ is error proportional to the measured length L. To determine $E_{L_{prop}}$, measurement of reference length standard (in this case gage block) was carried out. The selected length of reference standard (gage block) is the one closest to the measured distance L. Hence, $E_{L_{prop}}$ is calculated by:

$$E_{L_{prop}} = \frac{1}{n}\sum_{i=1}^{n}\frac{L^i_{measstd} - L_{calstd}}{L_{calstd}} \tag{2.9}$$

where L_{calstd} is calibrated length of the selected gage block. $L^i_{measstd}$ is the i-th length measurement of the selected gage block and n is number of gage block measurement in different orientation of the CMM working volume.

After determining the calibrated length (distance), the calibration uncertainty is determined as follow:

$$U = k\sqrt{\frac{u_{rep}^2}{n_1} + \frac{u_{geo}^2}{n_2} + u_{corr}^2} \tag{2.10}$$

where k is uncertainty expanded factor with 95

Uncertainty related to repeatability of CMM measurement u_{rep} is calculated as:

$$u_{rep} = \sqrt{\frac{1}{n_2}\sum_{j=1}^{n_2} S_j^2} \tag{2.11}$$

where S_j is standard deviation of measurement in j-th each orientation and n_2 is number of orientation which is equal to 4. S_j is calculated as:

$$S_j = \sqrt{\frac{1}{n_1 - 1}_i \sum_{i=1}^{n_1}(y_{ij} - y_j)^2} \tag{2.12}$$

where y_{ij} is the i-th measurement in j-th orientation,y_j is the average of measurement in j-th orientation. Number of replications in each orientation is denoted as $n_1 = 5$. y_j is defined as:

$$y_j = \frac{1}{n_1}\sum_{i=1}^{n_1} y_{ij} \tag{2.13}$$

Subsequently, uncertainty contributor due to CMM and part geometric error u_{geo} is determined as:

$$u_{geo} = \frac{1}{\sqrt{n_2}}\sqrt{\frac{1}{n_2 - 1}\sum_{j=1}^{n_2}(y_j - y)^2} \tag{2.14}$$

where the average of the total measurement is calculated as:

$$y = \frac{1}{n_1 n_2}\sum_{j=1}^{n_2}\sum_{i=1}^{n_1} y_{ij} \tag{2.15}$$

Finally, length correction uncertainty is calculated as:

$$u_{corr} = \frac{L}{L_{calstd}}\sqrt{\left(\frac{U_{calstd}}{2}\right)^2 + \frac{u_{measstd}^2}{n_3}} \tag{2.16}$$

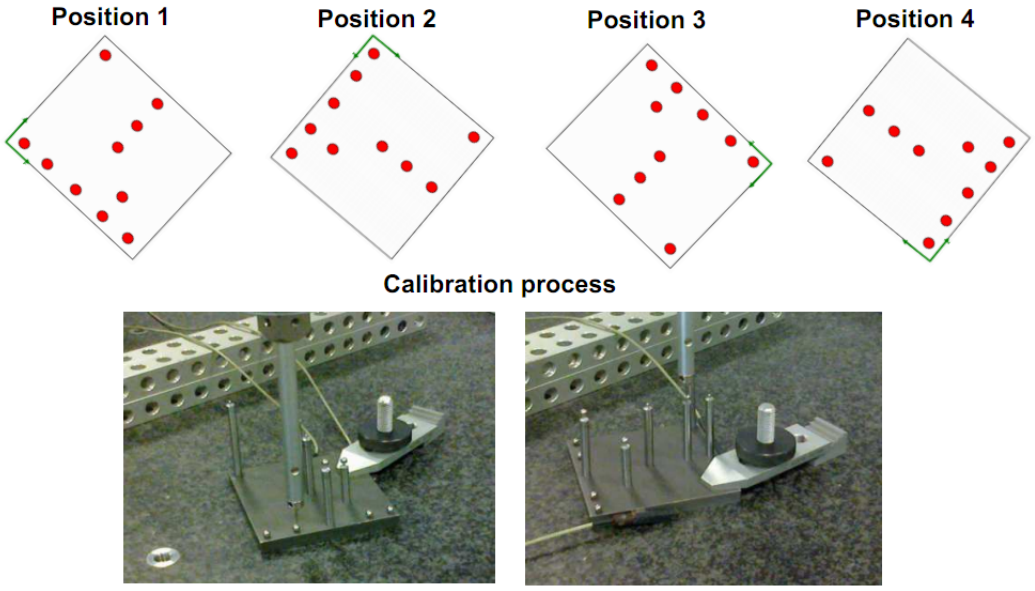

Figure 2.12: Artifact calibration: four different position orientations and the process.

where L is the nominal distance of the selected gage block. U_{calstd} is the expanded uncertainty of the calibrated length of the selected gage block from the calibration certificate. $u_{measstd}$ is the standard deviation of the selected gage block measurements and calculated as:

$$u_{measstd} = \sqrt{\frac{1}{n_3 - 1}\sum_{i=1}^{n_3}(L^i_{measstd} + L_{measstd})^2} \tag{2.17}$$

while $L_{measstd}$ is the average of selected gage block measurement $L^i_{measstd}$, and determined by ($n_3 = 3$):

$$L_{measstd} = \frac{1}{n_3}\sum_{i=1}^{n_3} L^i_{measstd} \tag{2.18}$$

Note that since it is only a single part, then the uncertainty originating from manufacturing process and uncertainty due to temperature difference in measuring other similar parts are not taken into account.

The artifact calibration process is shown in 2.12. The selection of the four different positions should be carefully addressed since in each position the locations of all spheres should be different. Thus, the configuration is skewed to comply with this requirement. The obtained calibration uncertainty is between 300 nm and 800 nm (depending on

Type	Lengths [mm]
Horizontal	15.5345(2), 20.4984(3), 52.09833(8), 72.5966(1), 88.1312(1)
Vertical	27.10321(2), 42.8299(2), 43.2367(2), 69.8460(2), 86.0548(2)
Diagonal	48.9354(2), 62.0765(2), 80.0656(2), 93.6609(2), 139.2402(3)

Table 2.2: List of length distances with their calibration uncertainty expressed according to GUM [100:2008 [2008]].

Workpiece	Exposure time	Contrast	Vertical resolution	Lateral resolution
Stopper	1.45 ms	0.81	0.4 μm	7.82 μm

Table 2.3: The measurement parameters used to measure the artifact's spheres in the performance verification test.

the considered length). Detail results of calibration of the lengths are depicted in table 2.2.

2.3.3 Performance verification: proposed procedure and results

The performance verification focuses on the evaluation of the instrument's moving stage comply with ISO10360-8. The measurement parameters used to measured the steel sphere for the performance verification test is detailed in table 2.3. This measurement parameters are also used for the performance verification of FVM instrument with 4-axis configuration since the artifacts use identical sphere type. Figure 2.13 shows the procedure of the verification process. In this figure, four compulsory volume diagonal directions and two X and Y axis directions are presented. These four diagonals measurements are obtained by rotating the artifact 90^0 clockwise. It is worth to note that, in diagonal 3 configuration, the last sphere on the bottom can not be measured since collision between the objective nose piece and the tallest sphere can not be avoided. The reason is, if the height of the tallest sphere is reduced, the minimum requirement of 66% of the volume height coverage can not be achieved as required by the ISO 10360-8. Due to the configuration of the optical CMM, verification in exactly Z-axis direction is impossible. As replacement, additional one direction which is an arbitrary diagonal direction was carried out to have seven directions measurement verification as required by the followed standard. Fig. 2.14 2.13 shows the alternative for the 7th position as

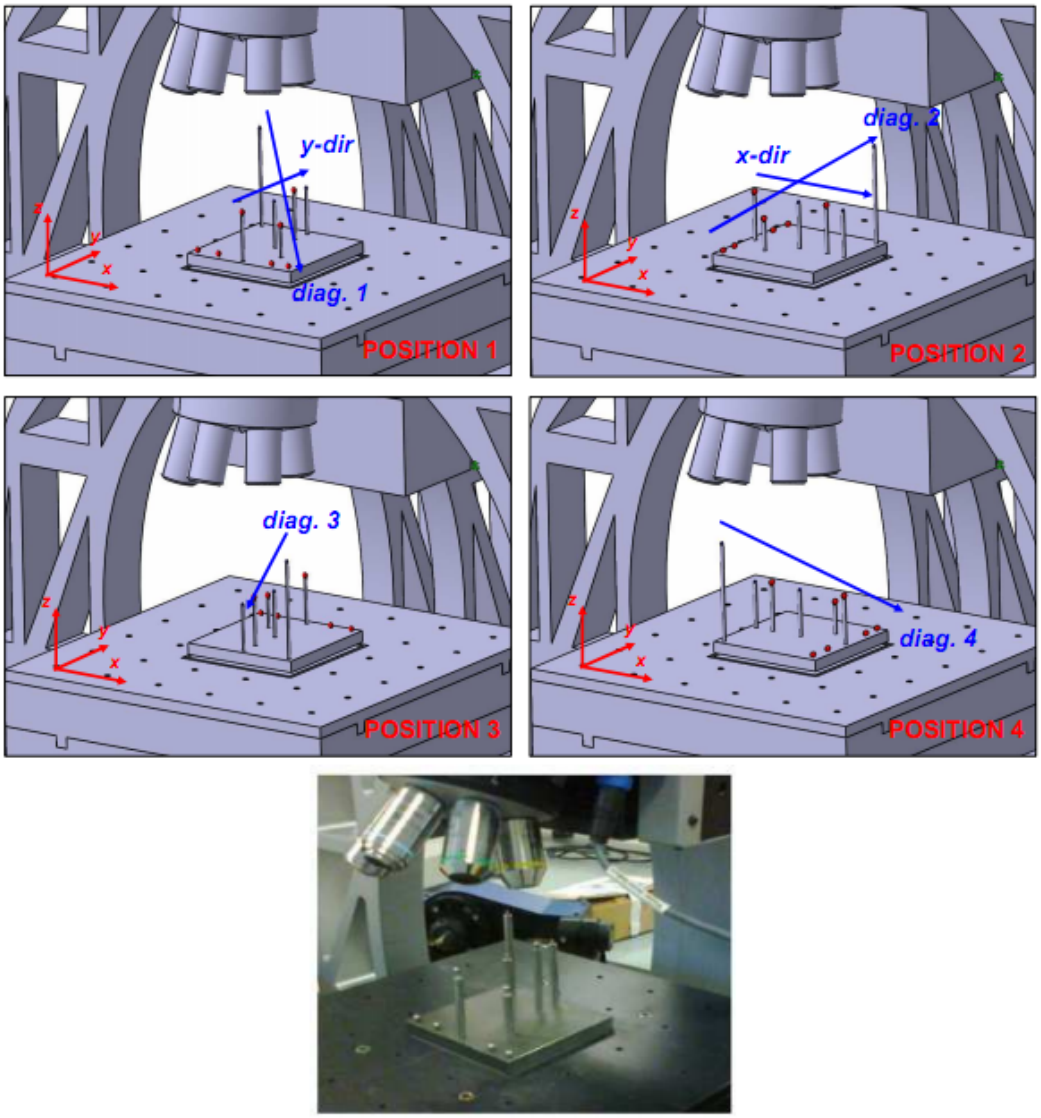

Figure 2.13: Performance verification procedure for 3-axis system configuration.

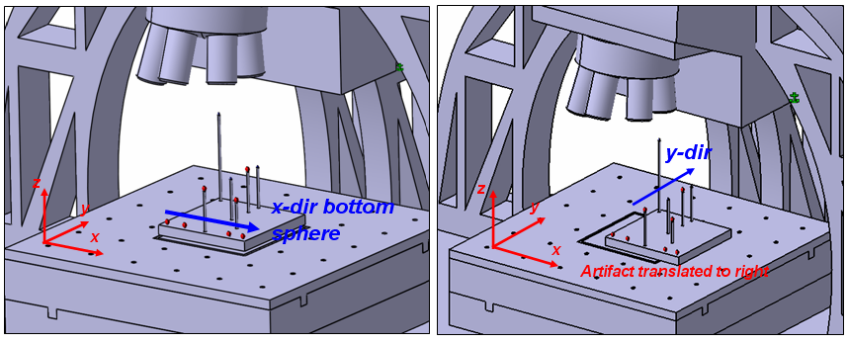

Figure 2.14: Alternative for the 7th position.

required by standard. In this figure, the measurement of the sphere on the bottom can be used as the 7th position. Other alternative is the y-direction measurement after translating the artifact to the right. The objective lens used for this performance evaluation has a 5x magnification such that the largest field of view (FOV) and working distance can be obtained. Vertical resolution of the z-stage was not maximized (default value) since it is a form measurement rather than a surface roughness measurement. By this, the acquisition time can be reduced. Since the length is the distance between two sphere centers, sphere measurements were carried out. The center of the sphere was obtained by averaging from three measurement of the sphere. To measure the 2 mm spheres, only single image measurement was utilized, thus there is no stitching process to capture the required sphere surface. On the contrary, stitching of four images was carried out to measure 5 mm diameter spheres. Therefore, the stitching process is taken into account in the evaluation of the center of the spheres. By considering stitching error, the verification results will have more comprehensive representation of the instrument's error.

The points of the spheres are supposed to be independent each other. Since there is no intersection between the clouds of points describing each sphere, the calculated locations and distance among the spheres depend only on accuracy of the X-Y stage. In each sphere configuration, the measurement is carried out in reciprocal direction (forward-backward-forward) to take into account the hysteresis of the stage. The goal is to calculate the error for each length measurement. The errors were obtained by calculating the difference between the measured length by the instrument and the calibrated length (as conventional true value). Time needed to complete one direction

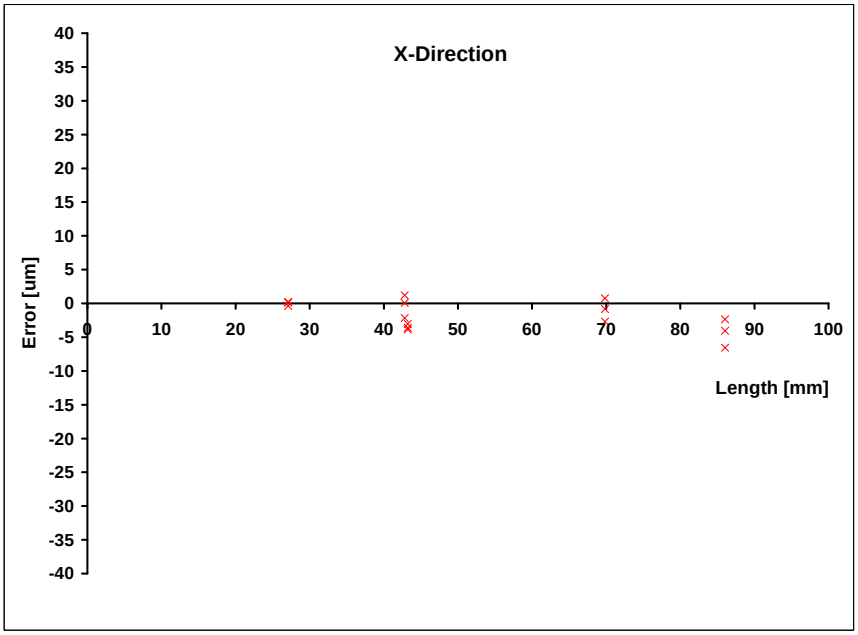

Figure 2.15: Length measurement errors in the X-direction.

in the verification procedure (forward-backward-forward measurements) is about 50 minutes. The time is obtained by considering the speed when moving from one sphere to the other such that minimizing vibration of the system. Hence, the total time needed to conduct the performance verification is about 300 minutes.

The errors in X and Y axis are depicted in fig. 2.15 and 2.16 respectively. The errors in diagonal directions, instead, are presented in fig. 2.17. As it can be observed, the maximum error of length measurement is approximately 35 μm. This error occurred in the diagonal direction. It can be caused by the combination of all the three axis imperfections (volumetric error) contributing in the diagonal length measurement. Beside, the spread of the measurement error is still considerably large to be considered as metrological instrument. Moreover, the error does not include yet probing form and probing size error [ISO10360-8 [2013]]. In fig. 2.17, an incremental pattern is apparent. An incremental pattern is typical in the case in which the axis presents a scale error; this can be concluded as systematic error and that at least the y axis requires a calibration to compensate the scale factor. Finally, all plots of error from X, Y, and the four diagonals as well as the 7-th position (auxiliary) which is selected by taking arbitrary horizontal diagonal directions are shown in fig. 2.18. In this figure, the probing errors

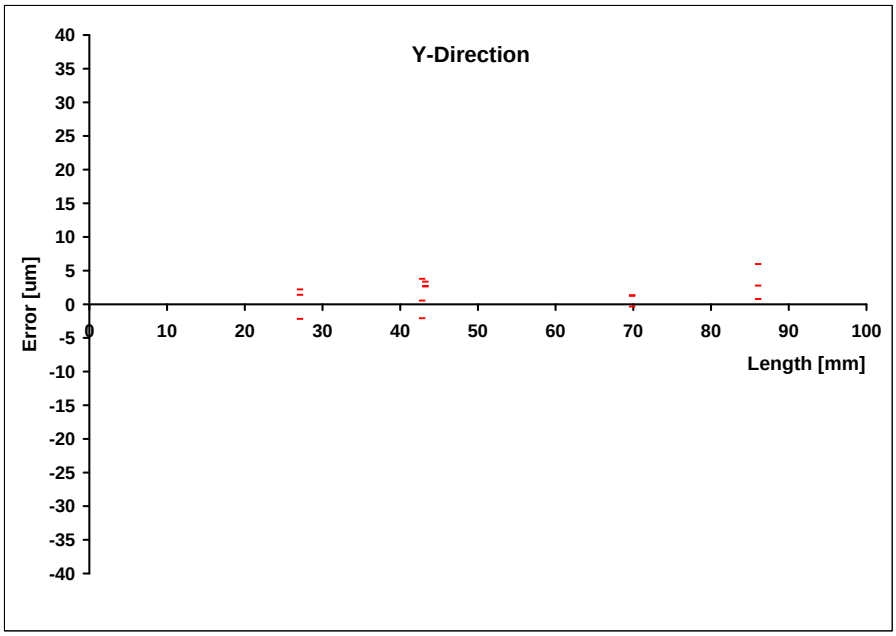

Figure 2.16: Length measurement errors in the Y-direction.

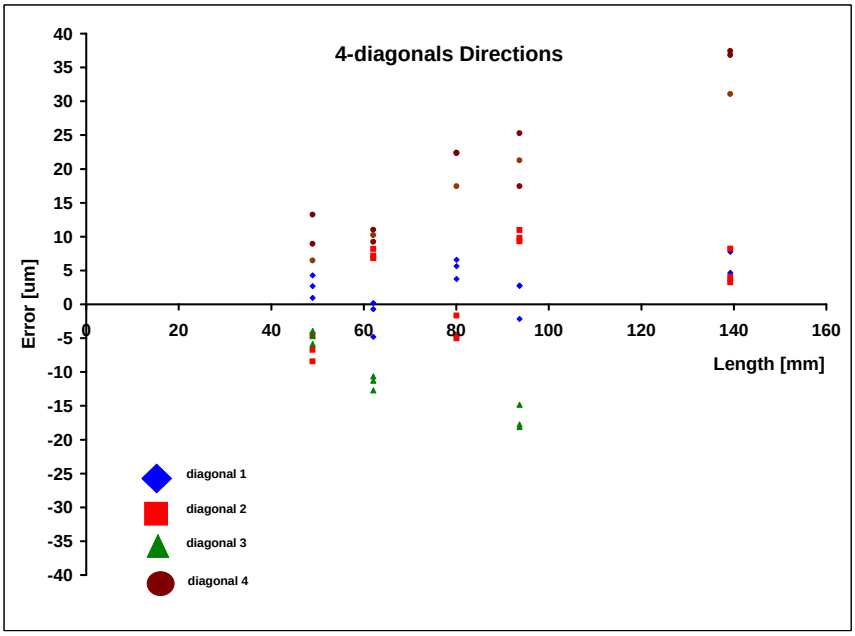

Figure 2.17: Length measurement errors in All 4 diagonals.

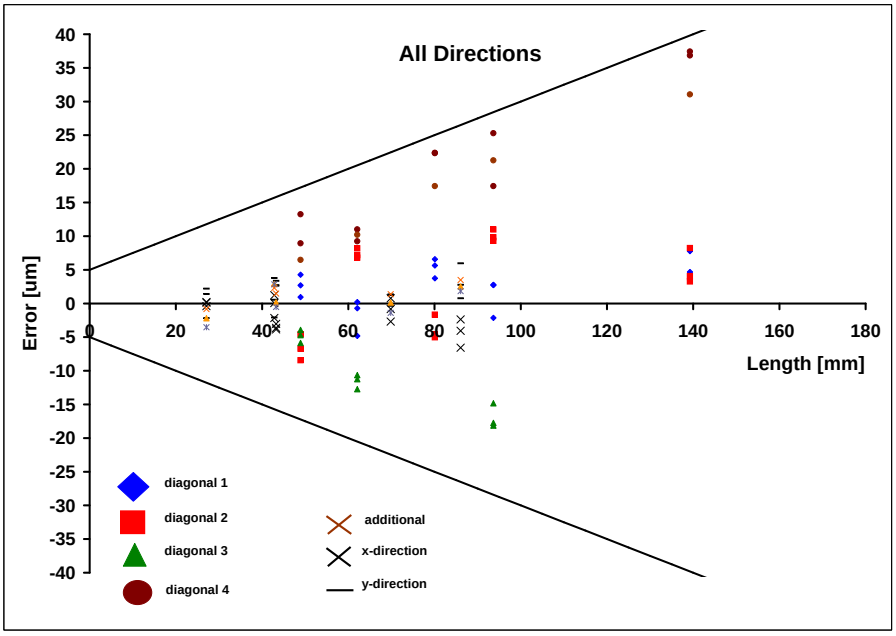

Figure 2.18: Length measurement errors for the X-axis, Y-axis, and 4 diagonals.

(size and form) are not yet included. As such, the plotted errors is still errors from unilateral measurement. From the figure, one can observed that the errors are within (the plot line):

$$\pm(5 + \frac{L}{4})$$

It is worth noting that temperature compensation was not applied. This contributes to the measurement error, but not very significantly, because the artifact is quite small, and the environment temperature was controlled $(20 \pm 0.5^0 C)$. Instead, it will include in the uncertainty of the verification process [Savio [2006]]. In addition, a possible factor which contributes to the errors is the surface fitting algorithm, which depends on a series of operator defined parameters. The uncertainty of the reference distance which is used to define the error is calculated by:

$$u(E) = \sqrt{u^2(\epsilon_{cal}) + u^2(\epsilon_\alpha) + u^2(\epsilon_{temp}) + u^2(\epsilon_{align}) + u^2(\epsilon_{fixture})} \tag{2.19}$$

where $u(\epsilon_{cal})$ is the calibration uncertainty, $u(\epsilon_\alpha)$ is error of determined coefficient thermal expansion (CTE), $u(\epsilon_{temp})$ is uncertainty due to temperature variation, $u(\epsilon_{align})$

is error caused by misalignment and $u(\epsilon_{fixture})$ is fixturing error. The last two contributors are neglected in this case since they are only considered in tactile CMM measurement. $u(\epsilon_{\alpha})$ and $u(\epsilon_{temp})$ are defined as:

$$u(\epsilon_{\alpha}) = L \times |t - 200| \times u(\alpha) \tag{2.20}$$

and:

$$u(\epsilon_{temp}) = L \times \alpha \times u(t) \tag{2.21}$$

where α is the coefficient thermal expansion of the artifact material and t is the measurement temperature. The maximum $u(E)$ calculated for the maximum length (L=140 mm) of distance between sphere is 0.30002 μm.

Following ISO10360-8, optical instrument is not a bidirectional measurement like the one of tactile CMM. The length measurement from optical instrument is defiend as unilateral measurement, $L_{Uni.meas}$ *and* $L_{Uni.cal}$, for measured and calibrated length. Hence, to state the final maximum permissible error, probing size error and probing form error should be included. The rule of determining $E_{Bi.Sph.1\times25;Tr;ODS;MPE}$, MPE for bidirectional measurement, according to ISO10360-8 is:

In the case of:

$L_{Uni.meas} - L_{Uni.cal} + P_{Size.sph.1\times25;j;ODS} > 0$, then

$E_{Bi.X;ODS;MPE} < L_{Uni.meas} - L_{Uni.cal} + P_{Size.sph.1\times25;j;ODS} + P_{Form.sph.1\times25;j;ODS}$

In the case of:

$L_{Uni.meas} - L_{Uni.cal} + P_{Size.sph.1\times25;j;ODS} = 0$, then

$E_{Bi.X;Tr;ODS;MPE} < P_{Form.sph.1\times25;j;ODS}$
and
$E_{Bi.Sph.1\times25;Tr;ODS;MPE} > -P_{Form.sph.1\times25;j;ODS}$

In the case of:

$L_{Uni.meas} - L_{Uni.cal} + P_{Size.sph.1\times25;j;ODS} < 0$, then

$$E_{Bi.X;ODS;MPE} > L_{Uni.meas} - L_{Uni.cal} + P_{Size.sph.1\times25;j;ODS} - P_{Form.sph.1\times25;j;ODS}$$

By following this rule, adding the probing size error of $P_{Size.Sph.1\times25;Tr;ODS} = 2\ \mu m$ and a probing form error of $P_{Form.Sph.1\times25;Tr;ODS} = 8\ \mu m$, the final maximum length measurement error are $E_{Uni.Sph.All;Tr;ODS;MPE} = \pm(5 + \frac{L}{4})\ \mu m$ and $E_{Bi.Sph.All;Tr;ODS;MPE} = \pm(15 + \frac{L}{4})\ \mu m$ for unidirectional and bidirectional, respectively. All parameters follow definition in ISO360-8 [ISO10360-8 [2013]].

The flatness measurement error is stated according to ISO10360-8 as:

$$E_{Form.Pla.D95\%:j:ODS} = d_{max} - d_{min} \tag{2.22}$$

where $E_{Form.Pla.D95\%:j:ODS}$ is the flatness error from associated plane in which 95% of all measured points are included. For Flatness measurement error, an approximately flat aluminum sample was used.This sample was calibrated by means of CMM, similar for size (dimensional) calibration method. Calibration results is 25.1(8) μm (see section 3.3.1.2 for calibration procedure). The errors are derived from diagonal position and skewed position as recommended position from the standard (see fig. 2.2right). Stitching operation should be included in the flatness error measurement. It is worth to note that, the two flatness error used two different types of illumination levels, which are 114 μs and 142 ms for skewed and diagonal positions respectively. It is because diagonal position needs more illumination to be able to capture the surface. The results from flatness measurement error from two type of positions are:

skewed position:
$E_{Form.Pla.D95\%:j:ODS} = 20.125\ \mu m$

diagonal position:
$E_{Form.Pla.D95\%:j:ODS} = 16.8\ \mu m$

Finally, The results of performance verification with the proposed artifact and procedure are:

Probing error from representative points=

Probing Size Error= $P_{Size.Sph.1\times25;Tr;ODS} = 2\ \mu m$

Probing Form error= $P_{Form.Sph.1\times25;Tr;ODS} = 8\ \mu m$

Probing error from point cloud ($\approx$ 2000000 points)=

Probing Size Error All= $P_{Form.Sph.All:Tr:ODS} = 6\ \mu m$

Probing Size Error All after 3-sigma-based filtering (see section 3.3.1.3)

$= P_{Form.Sph.All:Tr:ODS} = 6\ \mu m$

Probing Dispersion value= $P_{Form.Sph.D95\%:Tr:ODS} = 224\ \mu m$

Probing Dispersion value All after 3-sigma-based filtering (see section 3.3.1.3)

$= P_{Form.Sph.D95\%:Tr:ODS} = 127\ \mu m$

Length Measurement Error =

$E_{Uni.Sph.All;Tr;ODS;MPE} = \pm(5 + \frac{L}{4})\ \mu m$

$E_{Bi.Sph.All;Tr;ODS;MPE} = \pm(15 + \frac{L}{4})\ \mu m$

Flat Measurement Error=

$E_{Form.Pla.D95\%:j:ODS} = 20.125\ \mu m$ for skewed position

$E_{Form.Pla.D95\%:j:ODS} = 16.8\ \mu m$ for diagonal position

2.4 Measurement with 4-axis configuration

One of the advantages of FVM instrument is its ability to conduct measurement with 4-axis configuration. This type of measurement configuration has many potential applications, such as in micro-tool, micro-mold, or micro-device manufacturing. By this, major accessibility issue can be solved, such as measurement of undercut surface. Recently, Not only focus-variation based optical instrument but also many other optical instrument manufacturers integrate the 4-axis (rotation axis) into their system as can be seen in fig. 2.19. There are manufacturers produce instrument with additional rotational axis as the 4^{th}-axis other than the one shown in the figure. In the pure 3-axis

Figure 2.19: Many system manufacturer integrating the 4^{th}-axis (rotation axis) to improve system accessibility.

configuration, the total measuring volume is 100x100x100 mm. However, a reduction in measurement volume to 40x40x40 mm occurs if the additional rotational axis is used, as shown in fig. 2.20.

ISO10360-8 does not consider performance verification of optical CMMs with a rotational axis. Hence, the rotational axis (the 4^{th}-axis) has to be verified following ISO standard [ISO10360-3 [2007]]. This standard provides procedure to conduct performance verification for rotary table (rotational-axis) as well as the parameter which have to be derived. Artifact requirement for this type performance verification is an artifact which has two spheres placed on diametrically opposite position. The spheres should have approximately equal distance to the center (equal radius) with different height with respect to a defined reference base. Fig. 2.21a shows the artifact requirement.

For the verification procedure, a local reference system should be set on the sphere at higher position with respect to the reference base (fig. 2.21a). Total of 28 rotations have to be carried out to quantified the rotational error of the rotary (rotational) axis. From the 28 rotations, 14 rotations are clock wise and otherwise for the other 14 positions. For the clock-wise rotation, center of sphere A (at lower height position) are measured on each rotation position. Measurement of the center of sphere B are carried out for the other rotation direction (anti-clockwise) ISO10360-3 [2007]. Parameters which have to be quantified are the maximum permissible error, which are MPE_{FR}, MPE_{FA} and

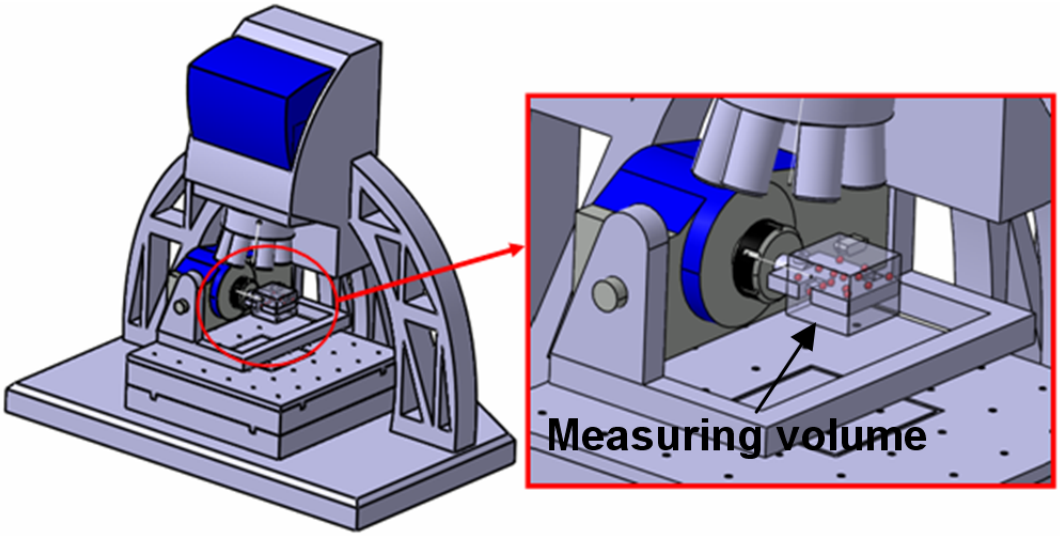

Figure 2.20: Focus variation instrument and its measuring volume in 4-axis configuration.

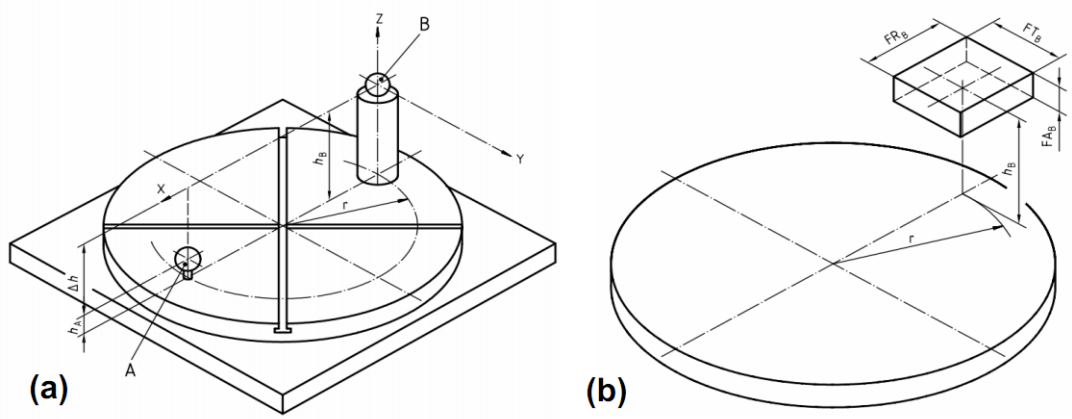

Figure 2.21: (a) Illustration of artifact requirement for rotary table (rotational axis) performance verification and (b)Illustration of the quantified error in rotation axis performance verification [ISO10360-3 [2007]]

MPE_{FT}. These parameters represent maximum permissible error in radial, axial, and tangential directions, respectively. The illustration of radial, tangential and axial errors are presented in fig. 2.21b.

2.4.1 Proposed Artifact

There are three artifacts proposed for performance verification of this configuration, which are artifact 1, artifact 2, and artifact 3. The first two artifacts (artifacts 1 and 2) are used separately to evaluate the length measurement error and the rotation axis error. Artifact 3 combines the functionality of artifacts 1 and 2 and is used both for performance verification of the length measurement error and the rotation axis error in the reduced volume. The material used in the presented artifact is not consider for a long time stability since the main purpose is to proposed the artifact configuration and the solution for the verification procedure by using the proposed artifact. Instead, the artifact is considered to be still stable for short-term period (one year).

2.4.1.1 Artifact 1: Length measurement error

Artifact 1 consists of an aluminum base plate, steel screws, and seven G5 grade steel ball bearings with a diameter of 5 mm. The specifications for G5 grade ball bearings are set according to ISO standard [ISO3290-1 [2008]]. The size of the artifact is designed to be $40 \times 40 \times 40\ mm$, corresponding to the reduced measurement volume of the instrument. Bolts were used to increase the pre-load of the screws to augment their stiffness. Metal glue was used to fix the balls to the screw heads. Fig. 2.22 depicts the 2D technical drawing of the proposed artifact 1 and fig. 2.23 presents the manufactured proposed artifact 1. steel balls with a 5 mm diameter were chosen because the image field of the lens used is smaller than the ball diameter. This is performed so that the image stitching process involved could be used to determine the center of the balls during the sphere feature association procedure. Adopting a 5X objective lens yields a field of view (FOV) equal to $2.8 \times 2.1\ mm$ and a working distance of 23.5 mm and reduces the risk of collision between the artifact and the objective nose piece.

There are two ball position configurations: in-line and diagonal (fig. 2.23, right). The in-line configuration allows the verification of performance along the X- or Y-axes, and the volumetric diagonal can be evaluated by measuring the diagonal configuration. Similar idea to the previous artifact, in each configuration, there are four balls with

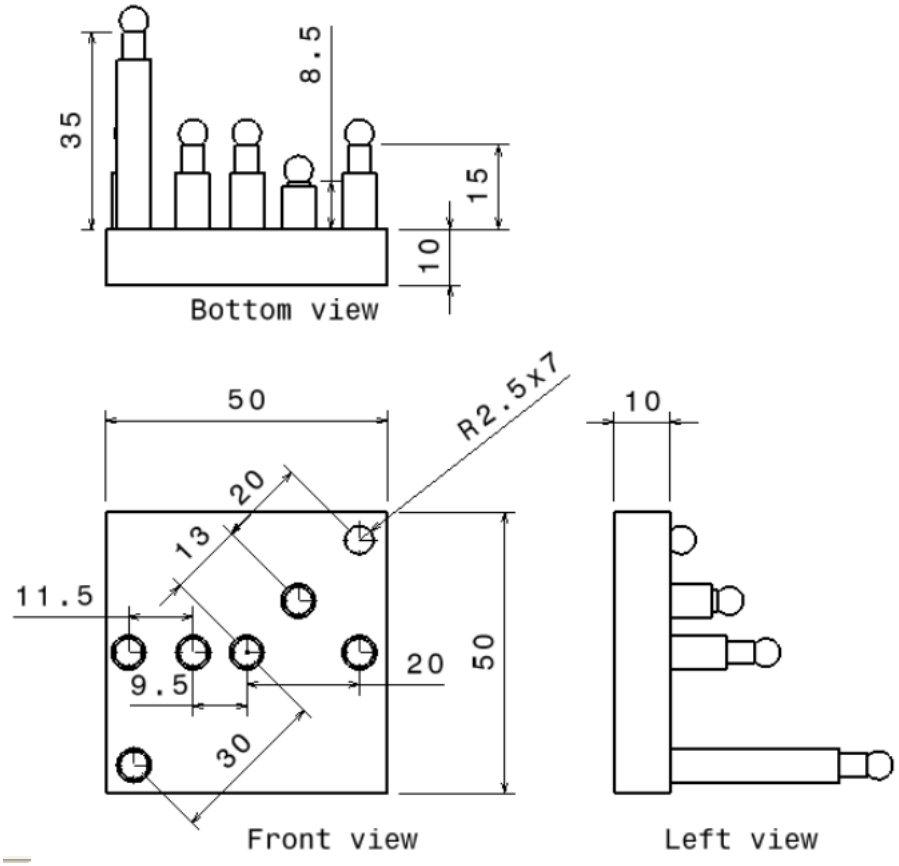

Figure 2.22: Artifact 1: 2D Technical Drawing.

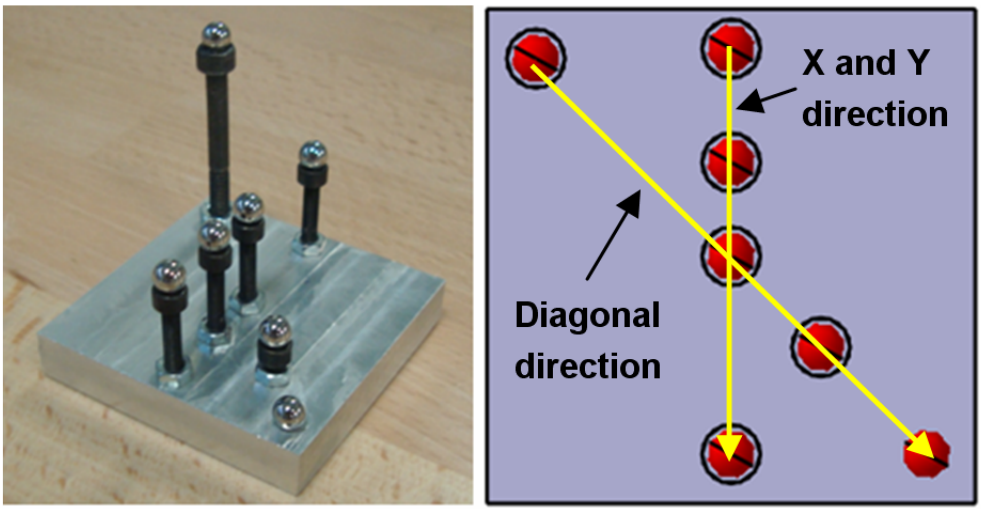

Figure 2.23: Artifact 1: length measurement error verification.

different reciprocal distances. Consequently, the minimum number of balls is used to provide five different length measurements for each configuration, as required in the ISO10360-8 [ISO10360-8 [2013]]. Each configuration has one ball in the center to use the minimum number of balls, reducing manufacturing cost and calibration time. Table 2.4 lists the reciprocal distances of the balls.

2.4.1.2 Artifact 2: Rotation axis error

Artifact 2 has a simpler design. Only two 5 mm diameter G5 grade steel ball bearings are needed to fulfill the requirements of the ISO standard [ISO10360-3 [2007]]. Spheres A and B are approximately located at an identical radius of 20 mm, are diametrically opposite of each other and are positioned at different heights with respect to the artifact base. The artifact is made of aluminum to reduce the weight (95 g) due to the 2 kg maximum payload limit of the spindle. Technical drawing of artifact 2 is shown in fig. 2.24 while fig. 2.25 presents the manufactured artifact. In this performance verification, calibration of artifact is not needed, since the procedure only measure a relative distance instead of absolute one. Also due to this reason, the test is not affected by misalignments between the artifact and axis of the rotation unit as long as the artifact is rigid during the performance verification [Savio [2006]]. The test is briefly recalled as follow. Total of 28 positions of rotation measurement are carried both for sphere A and sphere B. From the 28 positions, it covers both clock-wise and anti-clockwise rotation. The final result indicators are the radial, tangential and axial maximum error [ISO10360-3 [2007]].

2.4.1.3 Artifact 3: Combination of length measurement error and rotation axis error

Artifact 3 combines the functionality of artifacts 1 and 2 so that the verification of the length measurement and rotation axis errors can be performed with only a single artifact. The artifact has a size of 40×40 mm with weight of 118 g. Similarly with the previous two artifacts, it is composed of a rectangular aluminum plate mounted on a cylindrical gripper that is inserted into the spindle chuck. Spindle load limitations need to be considered. Fifteen G5 grade steel ball bearings with a diameter of 5 mm are used. Thirteen balls are glued to a prepared "seat" on the aluminum base. The 13 balls are used for the length measurement error evaluation. The remaining two are

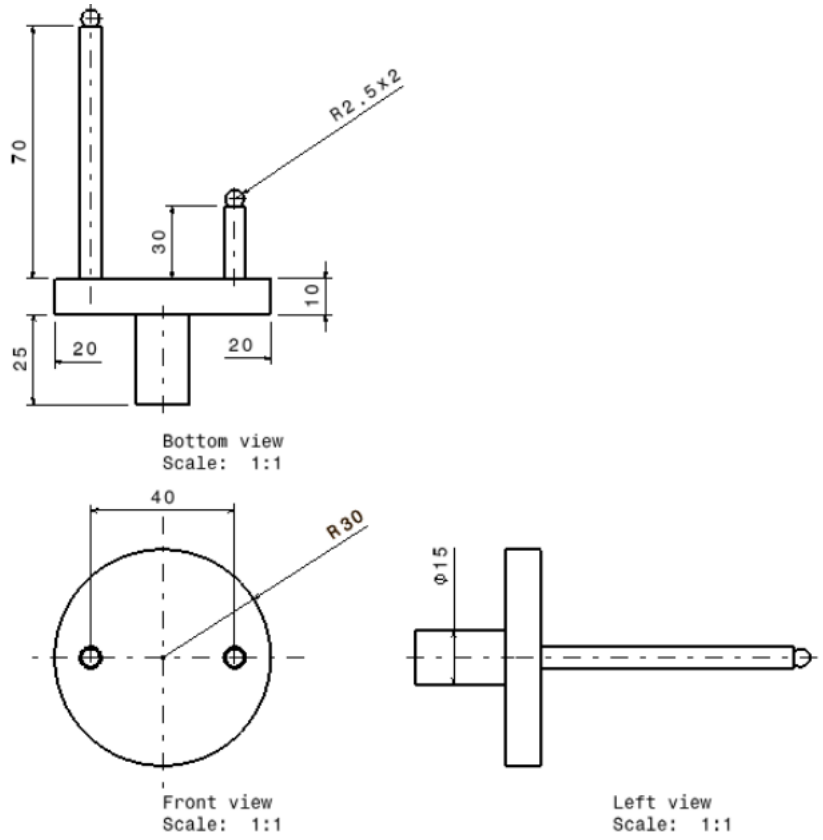

Figure 2.24: Artifact 2: 2D Technical drawing.

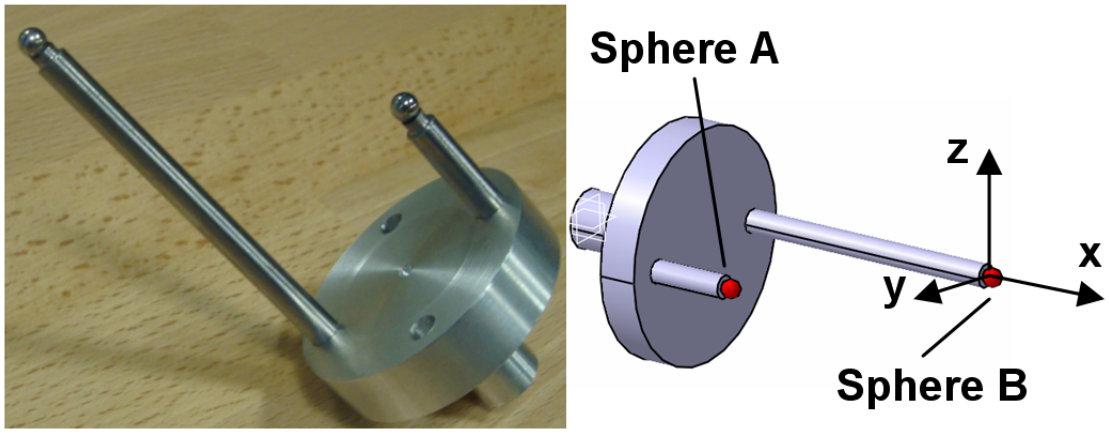

Figure 2.25: Artifact 2: rotation table (axis) error verification.

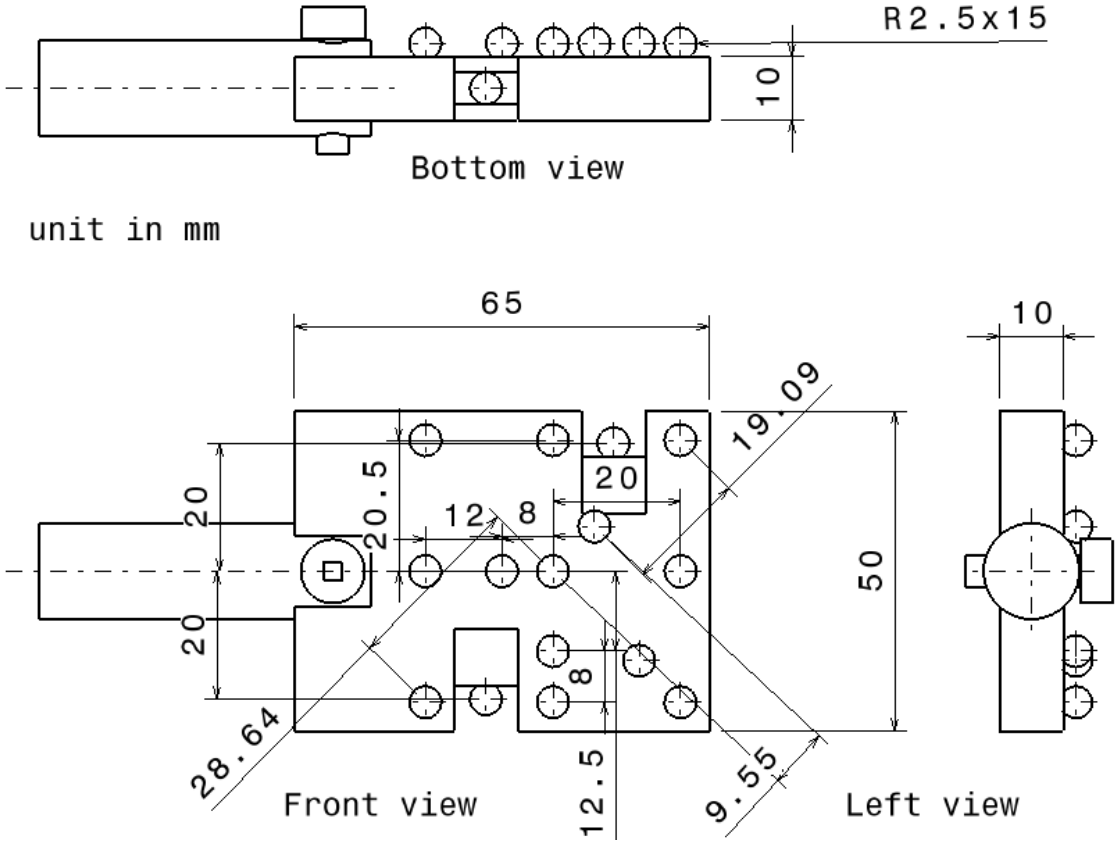

Figure 2.26: Artifact 3: 2D Technical Drawing.

glued onto screws and used for the rotation axis error evaluation. Technical drawing of the proposed artifact 3 is shown in fig. 2.26 and the manufactured one is shown in fig. 2.27.

The thirteen balls shown in 2.27 have four configurations: horizontal, vertical, diagonal 1 (from top-left to bottom-right), and diagonal 2 (from bottom-left to top-right). The horizontal and vertical configurations are used to evaluate the X- and Y-axes, respectively, whereas the other two diagonal configurations are used to evaluate the volumetric diagonal of the measurement volume by rotating the artifact $+45^0$ and -45^0. In each configuration, similarly to artifact 1, four balls are separated at different distances. Table 2.4 lists the five different lengths used in each configuration. The other two balls on the sides are used for the rotation axis error evaluation. As required by the ISO 10360-3 standard [ISO10360-3 [2007]], these balls are approximately located at a radius of 20 mm, are diametrically opposite and are at different distances from the

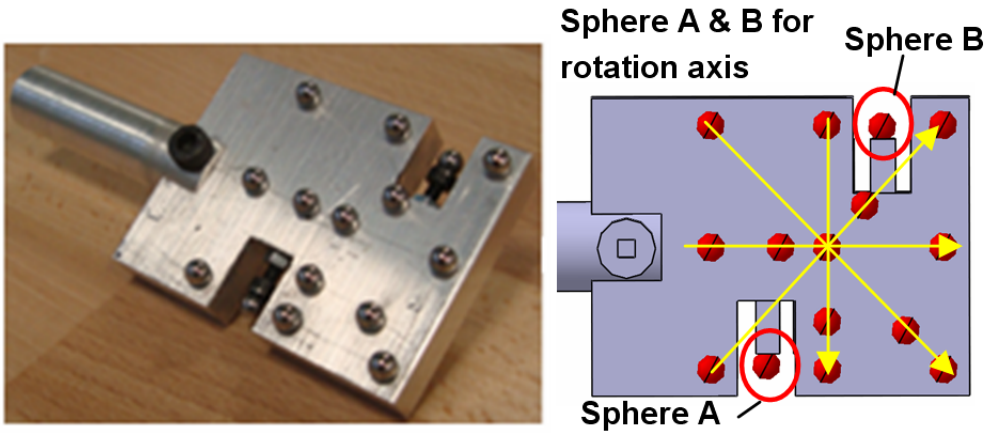

Figure 2.27: Artifact 3: innovative artifact for both performance verification of length measurement error and rotation axis error.

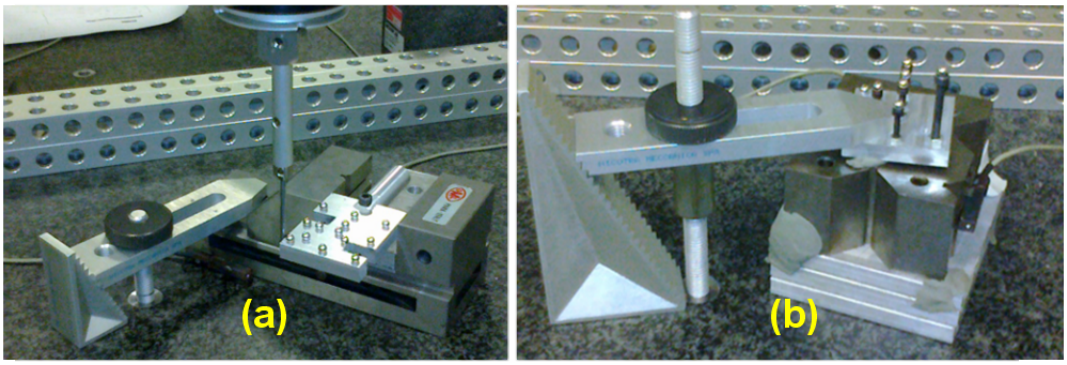

Figure 2.28: Skewed orientation in calibration (a) for artifact 3, and (b) for artifact 1.

chuck. Finally, for flat measurement error evaluation, a reference flat plane could be easily manufactured on this artifact to fulfill the requirements of the measurement test in ISO 10360-8.

2.4.2 Calibration of artifact

Calibration for the length, which is distance between two spheres, was carried by similar method with the length calibration for artifact used in 3-axis performance verification. The calibration was applied to artifact 1 and artifact 3. Figure 2.28 presents the calibration process of these artifacts. The calibration expanded uncertainty obtained for the distance between two sphere centers in artifact 1 is between 300 nm and 800 nm and is between 200 nm and 700 nm for artifact 3, depending on the length considered. From

Artifact	Configuration	Lengths [mm]
Artifact 1	In-line	9.3523(2); 11.7205(2); 20.0393(3); 29.3908(1); 41.1065(1)
Artifact 1	Diagonal	12.3996(1); 20.8125(1); 30.9691(2); 51.7087(1); 64.10263(1)
Artifact 3	Horizontal	8.5638(2); 11.9611(2); 19.9900(3); 20.5243(1); 40.5142(1)
Artifact 3	Vertical	8.0663(1); 12.5476(1); 19.8484(3); 32.3944(1); 40.4602(1)
Artifact 3	Diagonal 1	9.2722(1); 19.4042(2); 28.6665(1); 48.0651(1); 57.3362(1)
Artifact 3	Diagonal 2	9.5514(1); 18.7434(3); 28.9887(1); 38.5335(1); 57.2725(1)

Table 2.4: List of length distances for artifacts 1 and 3 with their calibration uncertainty expressed according to the GUM [100:2008 [2008]].

Table 2.4, all results of the length calibrations with their uncertainties are presented following GUM format.

2.4.3 Performance verification: proposed procedure and results

2.4.3.1 Length measurement, probing and flatness error (ISO 10360-8)

In this performance verification, artifact 1 and 3 were used. In the verification procedure, the error, similarly with the procedure for 3-axis configuration, is defined as a deviation in the distance between the two sphere centers obtained by the optical instrument from the calibrated distance values (as the conventional true values). The procedures are different for each artifact. Figure 2.29b and fig. 2.29c shows the placement of artifact 1 and artifact 3 respectively.

The procedure for artifact 1 is described as follows. Firstly, position 1 is selected such that the in-line configuration of the balls is in the horizontal position, with respect to the operator's view. In this position, the length measurement evaluations are carried out for the X-axis and for volumetric diagonal 1 (Top-Left-Corner to Bottom-Right-Corner). After that, the artifact is manually rotated 90^0 (clock-wise) such that the in-line configuration of the balls is in the vertical position with respect to the operator's

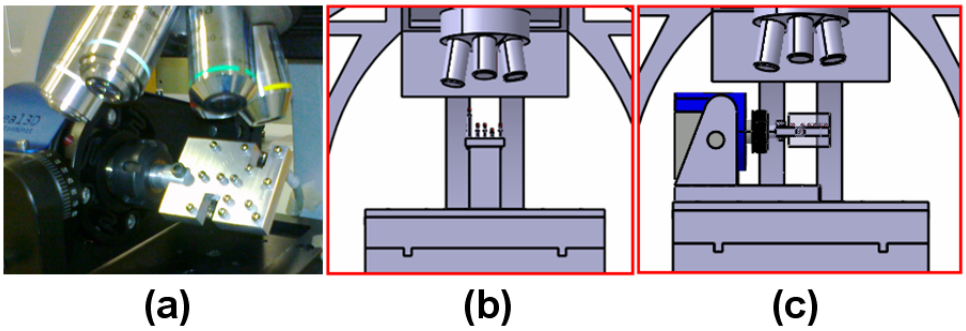

Figure 2.29: (a) Performance verification using artifact 3 rotated by -45^0, (b) placement of artifact 1, and (c) placement of artifact 3.

view. Length measurement evaluations are performed for the Y-axis and for diagonal 2 (Top-Right-Corner to Bottom-Left-Corner). Subsequently, diagonal 3 (Bottom-Right-Corner to Top-Left-Corner) and diagonal 4 (Bottom-Left-Corner to Top-Right-Corner) can be evaluated by rotating the artifact 90^0 (clock-wise). Figure 2.30 shows the detail procedure in all four positions.

The procedure for measuring artifact 3 is much simpler since it combines functionality from the two artifacts. With this artifact, operator involvement is only to mount the artifact holder to the spindle chuck and to check the inclination angle (Figure 2.29c). For the X- and Y-axis length measurement evaluation, the artifact is set to an approximately flat position before performing the verification procedure. Volumetric errors for diagonals 1 and 2 are evaluated after rotating the spindle -45^0 (2.29a) before the verification of these diagonals is carried out. Finally, for diagonals 3 and 4, the verification is performed after rotating the spindle $+45^0$, opposite to diagonal 1 and diagonal 2 measurements. The detail procedure is presented in fig. 2.31.

Similar purpose with the one applied for 3-axis performance verification artifact, the sphere diameter used is larger than the FOV of the 5X objective lens. Hence, the measurement of the center of each ball required the stitching of four image fields, such that the error in the stitching process is also taken into account. After obtaining the spheres center location, the relative distance can be calculated. In every verification direction, the measurement is carried out reciprocally (left-to-right-to-left), such that the hysteresis of the stage is taken into account. From this, three measurements for each length type are obtained. The seventh position of the verification procedure, as required by the standard, for both artifact 1 and 3 was realized by measuring arbitrary

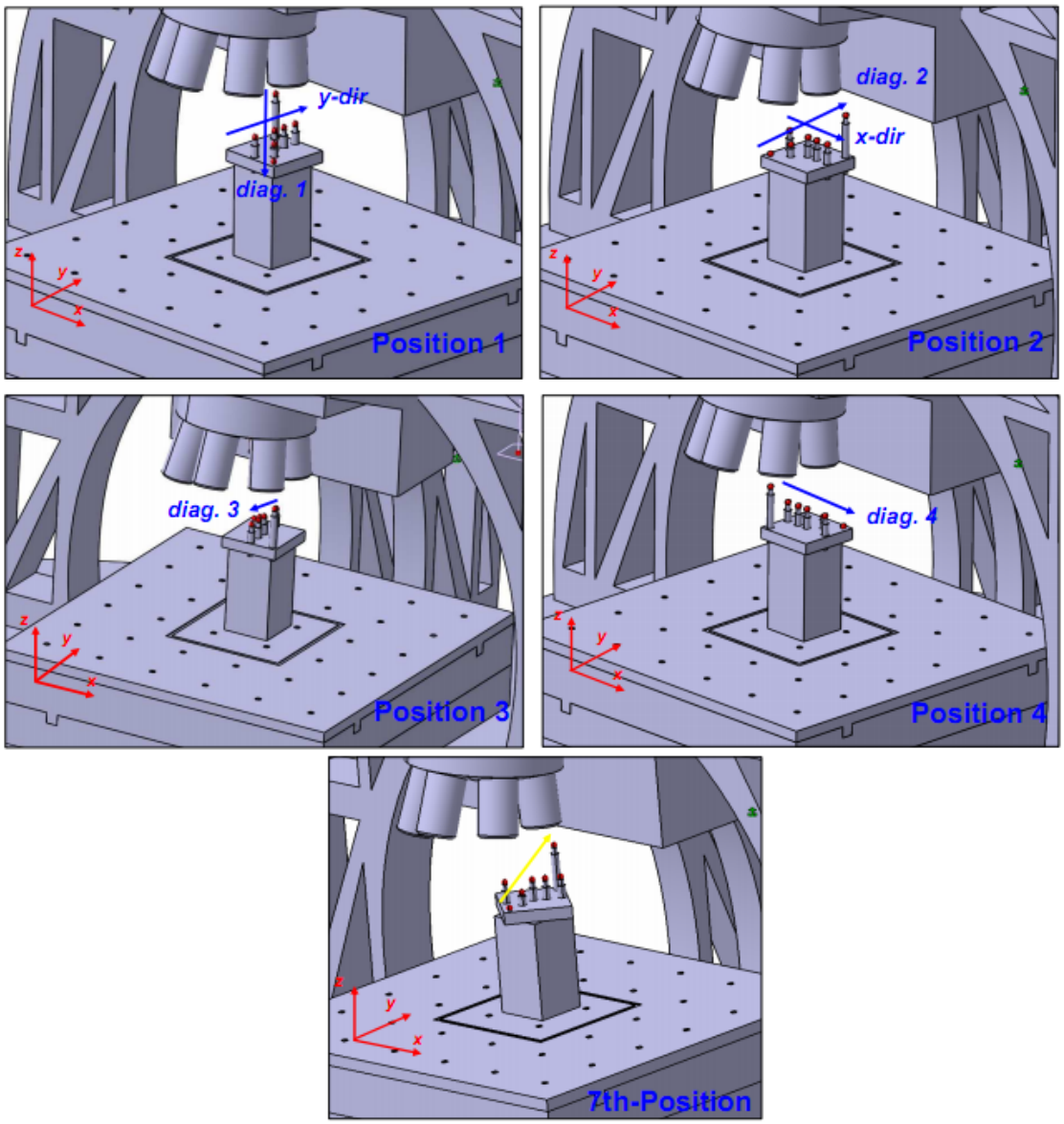

Figure 2.30: Performance verification procedure (ISO10360-8) by using artifact 1.

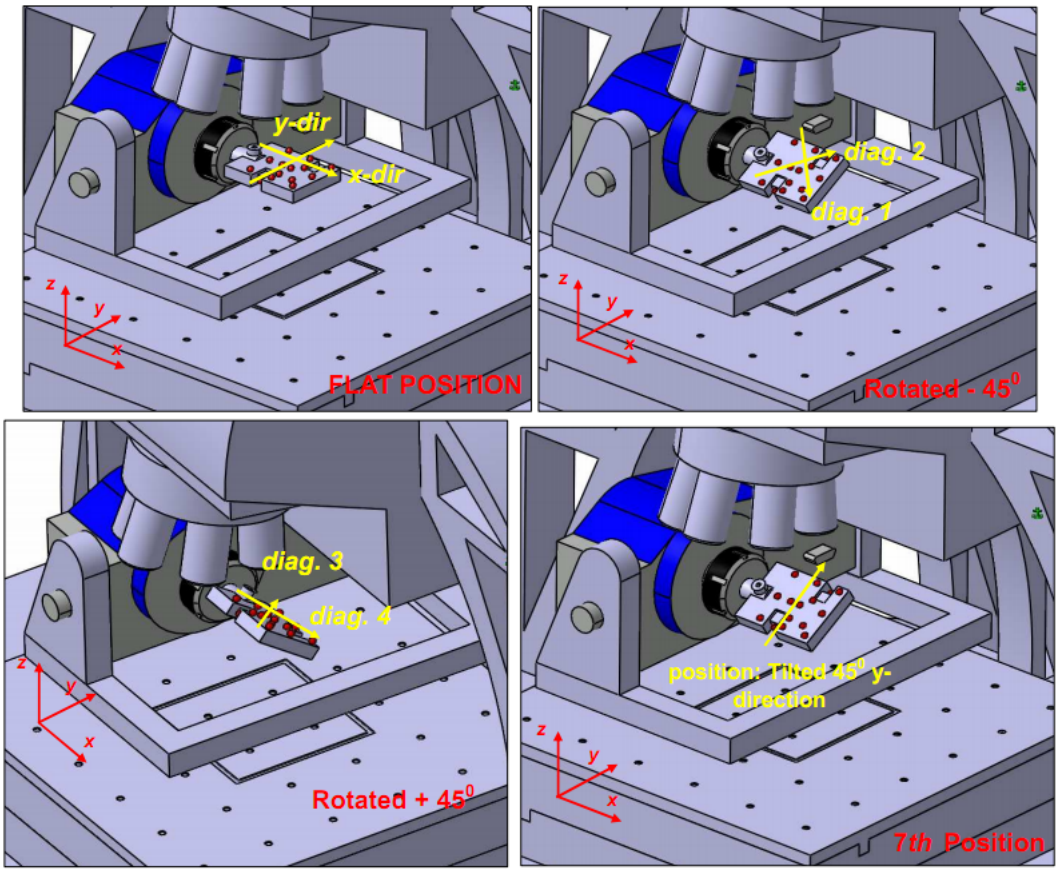

Figure 2.31: Performance verification procedure (ISO10360-8) by using artifact 3.

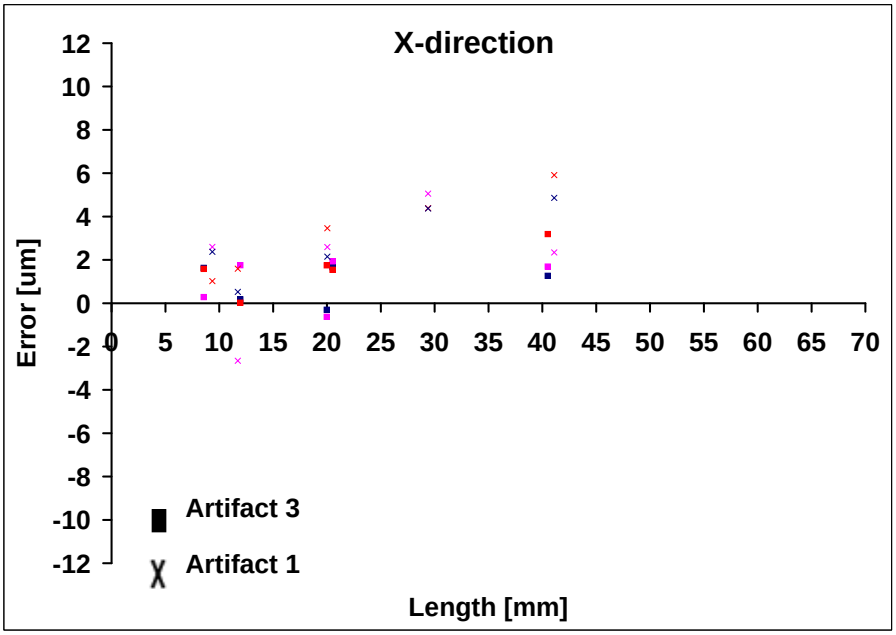

Figure 2.32: Length measurement errors in the X-direction (artifact 1 and 3).

diagonal direction due to the fact that it is impossible to have Z-axis direction for the verification procedure since the objective nose is always from the top. The results from the performance verification in the X-direction are presented in fig. 2.32. In this direction, the maximum error obtained from artifacts 1 and 3 is approximately 4.25 μm and 3.18 μm, respectively. Figure 2.33 shows the verification results in the Y-direction. Considering these measurement results, artifact 3 gives maximum error of 4.8 μm, which is approximately 1.5 μm higher than artifact 1.

Error results for the diagonals are presented in fig. 2.34. It is noted that artifact 3 contains two different diagonal configurations (table 2.4), such that two sets of errors are plotted. It is possible to note that the maximum error observed from the diagonal measurement is equal to 11.3 μm and 11.8 μm for artifacts 1 and 3, respectively. To comply with ISO 10360-8, total seven positions have to be verified. Thus, additional length verification was carried out. For artifact 1, the additional position is by measuring the diagonal spheres configuration following Y-direction (fig. 2.30 bottom). Meanwhile, for artifact 3, the seventh position measures the vertical sphere configuration after rotating the artifact around 30^0. Fig. 2.35 shows the length error for this position. Finally, from fig. 2.36 , which presents all measurements error (along the x, y

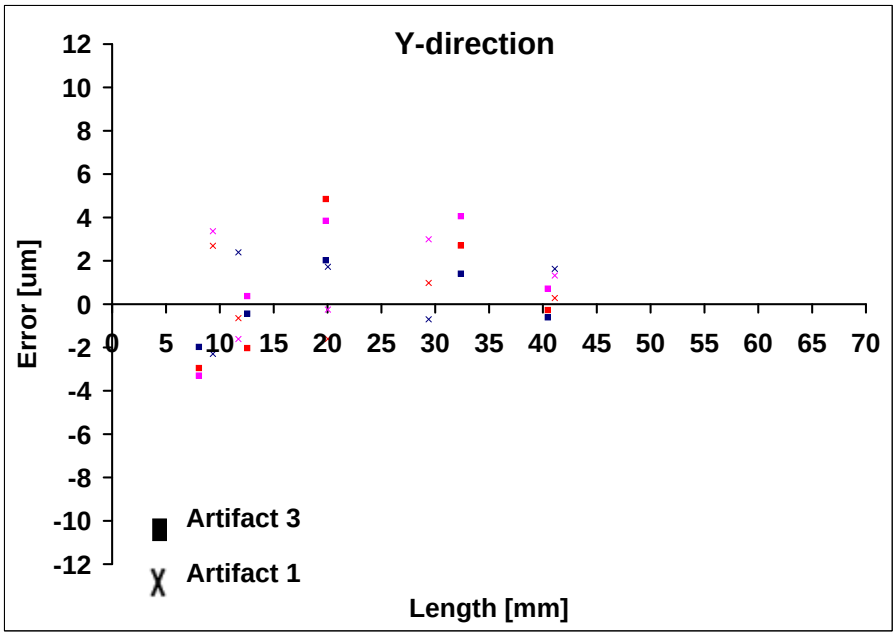

Figure 2.33: Length measurement errors in the Y-direction (artifact 1 and 3).

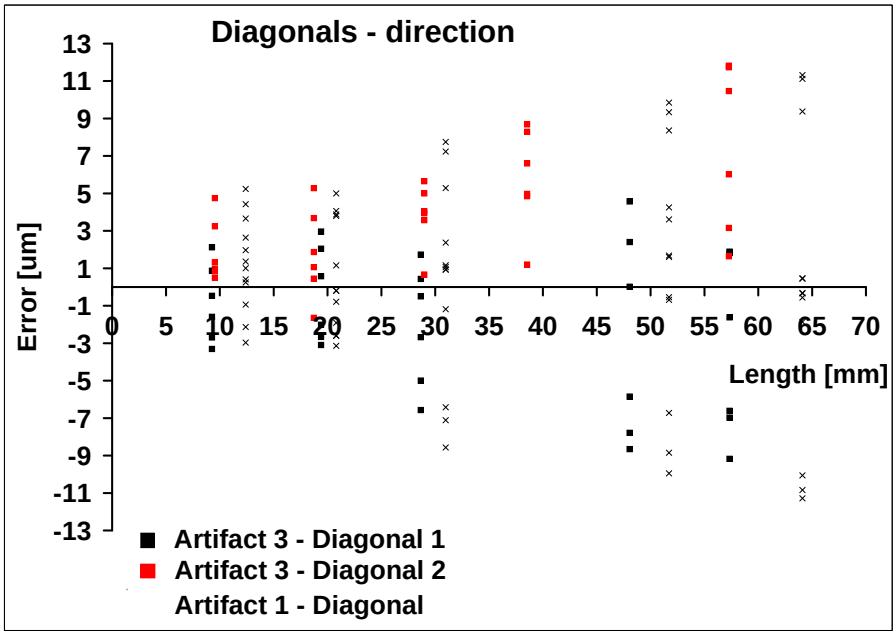

Figure 2.34: Length measurement errors in All 4 diagonals (artifact 1 and 3).

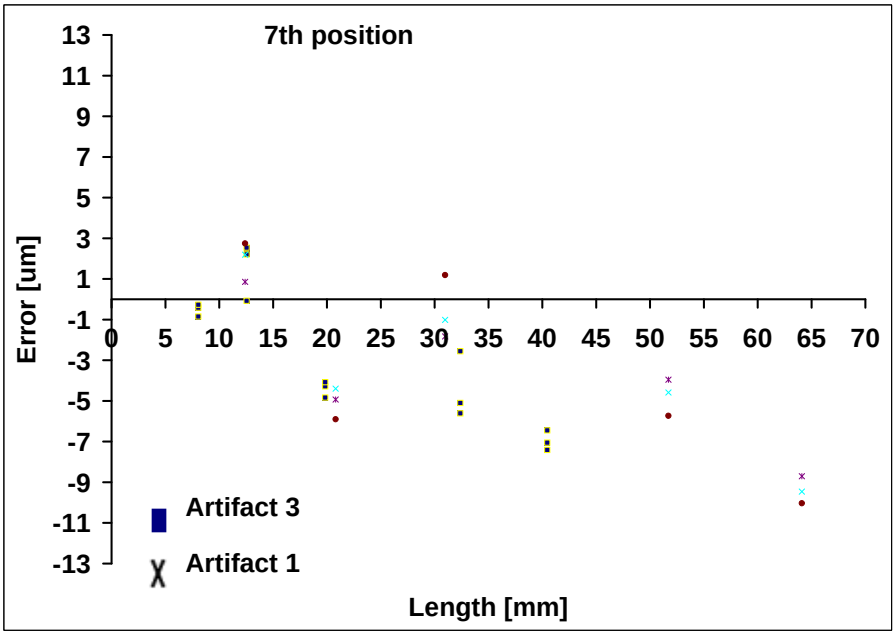

Figure 2.35: Length measurement errors for the seventh direction (artifact 1 and 3).

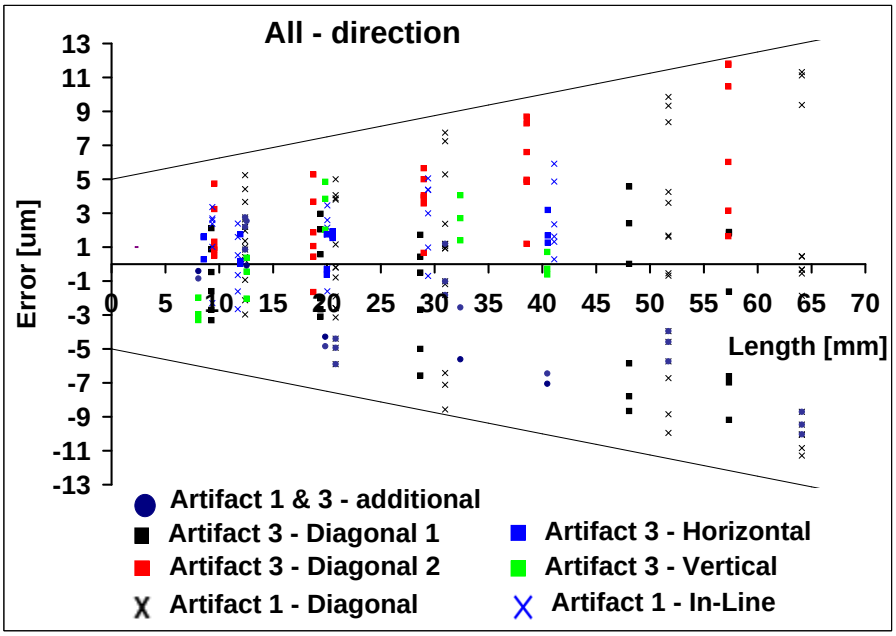

Figure 2.36: Length measurement errors for the X-axis, Y-axis, additional position and 4 diagonals (artifact 1 and 3).

and four diagonals as well as the seventh position) for both artifacts, it is worth noting that the dispersion of the errors seems to increase and that the error always seems to be less than (the plotted line):

$$\pm(5 + \frac{L}{8})$$

From this results, one can observe that with smaller working volume, there is accuracy improvement from $\pm(5 + \frac{L}{4})$ to $\pm(5 + \frac{L}{8})$. The maximum $u(E)$ calculated for the maximum length (L=58 mm) of distance between sphere is 0.3 μm.

In general, the results show good agreement between the two artifacts. One of the reasons for the difference in the errors evaluated using artifacts 1 and 3 are caused by the different types of lengths among the balls that are measured. To confirm this conclusion, a Kolmogorov-Smirnov test was conducted to compare the statistical distribution of the length measurement errors carried out on artifacts 1 and 3. The resulting p-value of 0.78 suggests there is no evidence to refuse the null hypothesis that the distributions are identical. The time needed for performance verification is similar to the one for the 3-axis configuration which is around 50 minutes for each measurement direction. Hence, total six hours is needed for the verification following ISO10360-8.

From these results, it is possible to evaluate the performance of the system as well. By considering a probing size error of $P_{Size.Sph.1\times25;Tr;ODS} = 2\ \mu m$ and a probing form error of $P_{Form.Sph.1\times25;Tr;ODS} = 8\ \mu m$, we can state that the length measurement error are $E_{Uni.Sph.All;Tr;ODS;MPE} = \pm(5+\frac{L}{8})\ \mu m$ and $E_{Bi.Sph.All;Tr;ODS;MPE} = \pm(15+\frac{L}{8})\ \mu m$ [ISO10360-8 [2013]].

Similar to the verification with 3-axis configuration, the flatness error measurement was also carried out. The flatness error was measured from the flat surface of the bottom surface of artifact 3. The measured flat surface and its verification procedure are shown in fig. 2.37. The surface was calibrated with calibration results of 7.7(6) μm (see section 3.3.1.2 for calibration procedure).

skewed position:
$E_{Form.Pla.D95\%:j:ODS} = 14.3\ \mu m$
diagonal position:

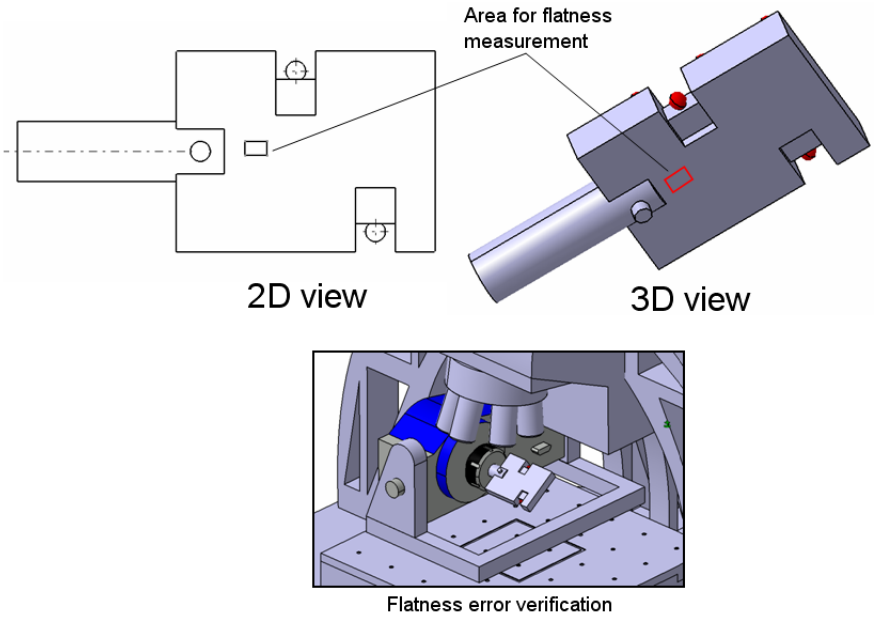

Figure 2.37: Top row: The flat surface of artifact 3 selected for flatness error verification. Bottom row: the procedure for flatness error verification.

$E_{Form.Pla.D95\%:j:ODS} = 10.5\ \mu m$

for comparison, the flatness measurement error from a calibrated flat aluminum (as being described in flatness measurement error in 3-axis configuration), the flatness error are: $E_{Form.Pla.D95\%:j:ODS} = 20.125\ \mu m$ for the skewed position and for $E_{Form.Pla.D95\%:j:ODS} = 16.8\ \mu m$ diagonal position. Maximum flatness error with respect to the calibrated value are 6.6 μm and 4.9μm for measurement with artifact 3 and flat aluminum, which is 1.7 μm difference.

Finally, the summarize of the performance verification results can be stated as:

Probing error from representative points=

Probing Size Error= $P_{Size.Sph.1\times25;Tr;ODS} = 2\ \mu m$

Probing Form error= $P_{Form.Sph.1\times25;Tr;ODS} = 8\ \mu m$

Probing error from point cloud ($\approx$ 2000000 points)=

Probing Size Error All= $P_{Form.Sph.All:Tr:ODS} = 6\ \mu m$

Probing Size Error All after 3-sigma-based filtering (see section 3.3.1.3)

$= P_{Form.Sph.All:Tr:ODS} = 6\ \mu m$

Probing Dispersion value= $P_{Form.Sph.D95\%:Tr:ODS} = 224\ \mu m$

Probing Dispersion value All after 3-sigma-based filtering (see section 3.3.1.3)

$= P_{Form.Sph.D95\%:Tr:ODS} = 127\ \mu m$

Length Measurement Error =

$E_{Uni.Sph.All;Tr;ODS;MPE} = \pm(5 + \frac{L}{8})\ \mu m$

$E_{Bi.Sph.All;Tr;ODS;MPE} = \pm(15 + \frac{L}{8})\ \mu m$

Flat Measurement Error=

$E_{Form.Pla.D95\%:j:ODS} = 14.3\ \mu m$ for skewed position

$E_{Form.Pla.D95\%:j:ODS} = 10.5\ \mu m$ for diagonal position

2.4.3.2 Rotation axis error (ISO 10360-3)

The procedure used for the rotation axis performance verification conforms to standard [ISO10360-3 [2007]]. There is a slight difference between the procedures stated in this standard regarding the determination of the reference. Due to the instrument's inherent characteristics, the reference is determined as follows (2.25right). The zero point is set at the center of sphere B. The Z-axis is parallel to the lens axis. The X-axis is along the spindle axis and the Y-axis is set perpendicular to the X-Z plane. A full 360^0 rotation was evaluated for both artifacts. An unreachable position at a rotation position between $+45^0$ to $+90^0$ from the initial flat position (0^0) was observed due to a collision between the objective nose piece and the artifact. For each predetermined rotation angle, the center of each sphere is calculated by acquiring four images of the sphere and stitching them together. The procedure for rotation axis performance verification by using artifact 2 and 3 is presented in fig. 2.38.

A comparison of the results obtained from artifacts 2 and 3 in 2.39 , 2.40 , and 2.41 shows the axis rotation error in the X-, Y-, and Z-direction, respectively. The maximum errors of each rotation angle are plotted. Errors at positive rotation angles were obtained from sphere A and errors at negative rotation angles were obtained from sphere B. From the performance verification of artifact 2, the maximum rotation axis errors for the X-, Y-, and Z-directions are approximately 5 μm, 7.5 μm, and 14.7 μm,

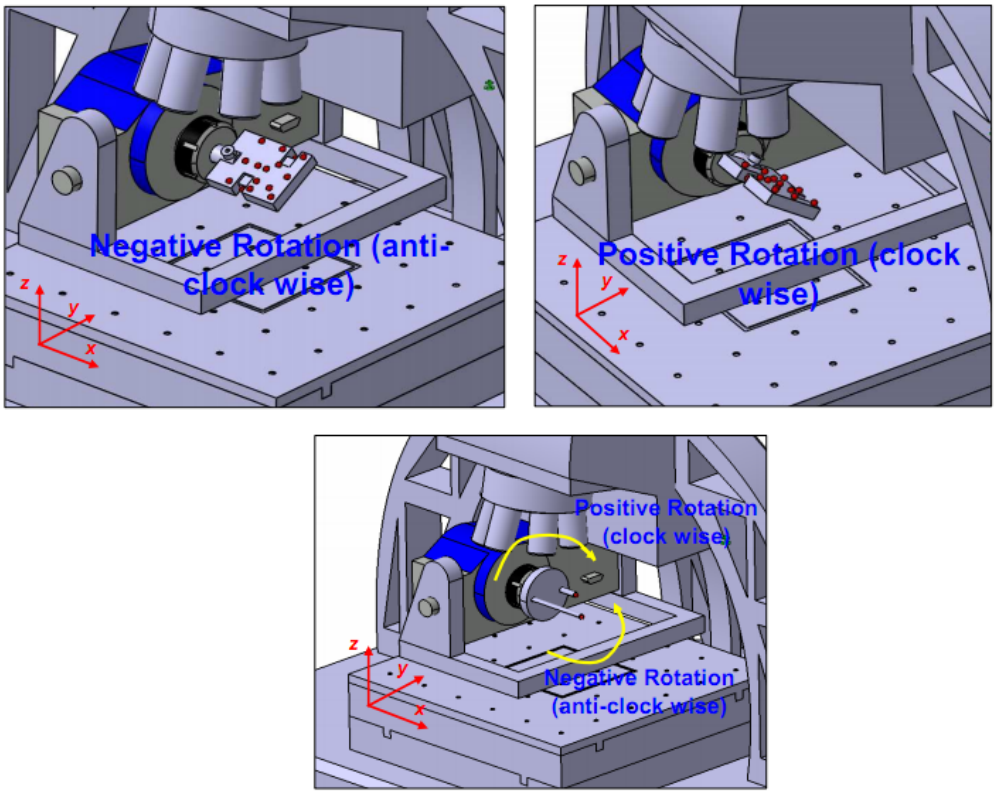

Figure 2.38: Rotation axis performance verification (ISO10360-3) by using artifact 3 (up) and artifact 2 (bottom).

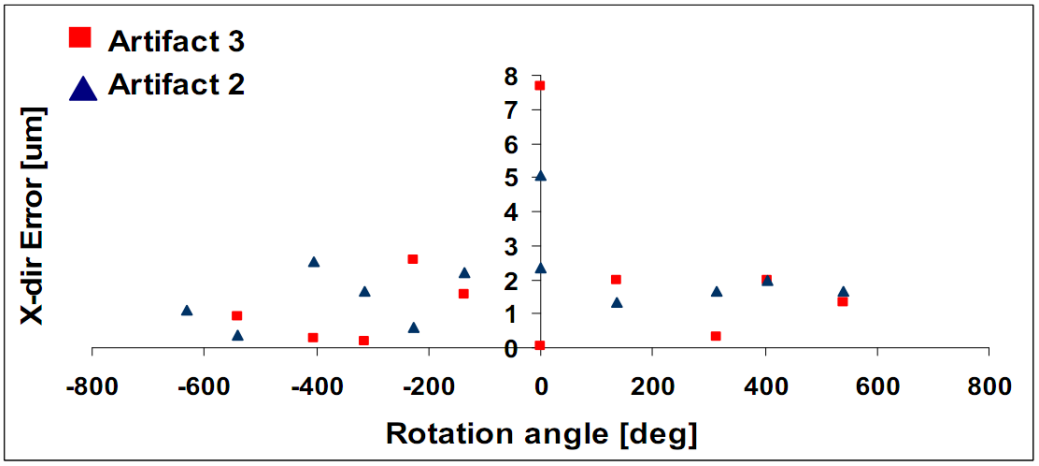

Figure 2.39: Rotation axis error in X-direction (artifact 2 and artifact 3).

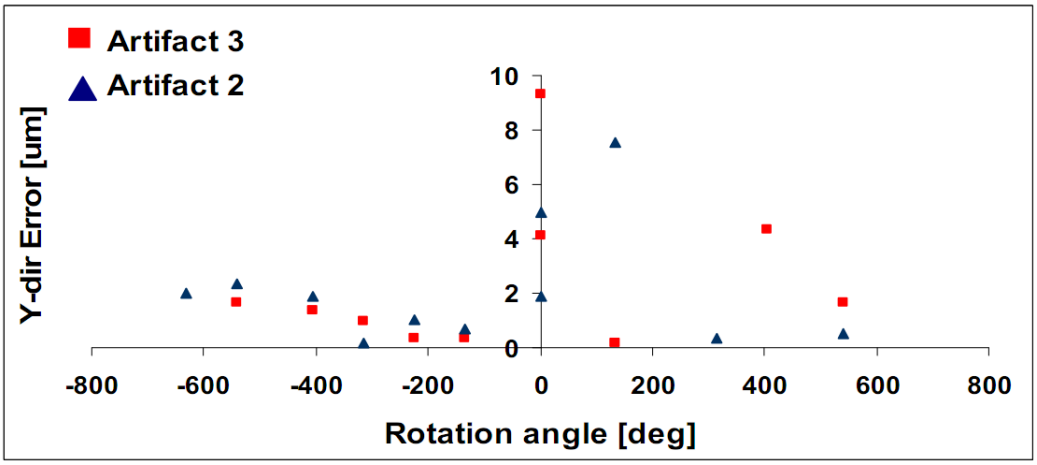

Figure 2.40: Rotation axis error in Y-direction (artifact 2 and artifact 3).

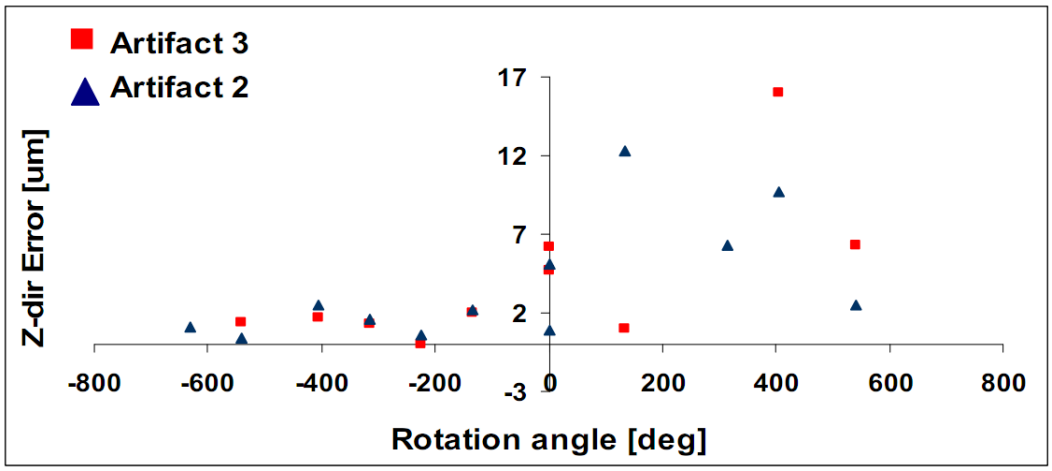

Figure 2.41: Rotation axis error in the Z-direction (artifacts 2 and 3).

respectively. Additionally, for artifact 3, the maximum errors obtained are approximately 7.6 μm, 9.3 μm, and 17.3 μm for the X-, Y-, and Z-directions, respectively. In both artifacts, the maximum errors are observed along the Z-direction. A slightly larger maximum error was observed in all directions for artifact 3, compared to the one obtained by artifact 2, ranging from 1.8 μm to 2.6 μm. This can be caused due to different distance of the spheres to the base and due to different in weight

In general, the obtained errors from both artifacts show good agreement. To strengthen this conclusion, a Kolmogorov-Smirnov test was again conducted to compare the statistical distribution of the length measurement errors for artifacts 2 and 3. The resulting p-value of 0.30 suggests that there is no evidence to refuse the null hypothesis that the distributions are identical. Finally, it is possible to evaluate the performance of the system with a rotary axis as follows: $MPE_{FR} = 18\ \mu m$, $MPE_{FT} = 10\ \mu m$, and $MPE_{FA} = 8\ \mu m$. Total time needed for the rotation axis error verification is about four hours which is two hour for each spheres.

2.5 Conclusion

In this chapter, artifacts and procedures for performance verification of a focus-variation based optical instrument are proposed. They are separated into two parts: for 3-axis configuration and for 4-axis configuration of the instrument. For 3-axis configuration, a full measuring volume is considered. The performance verification is applied only for the three translation axis, which are X, Y and Z-axis. The verification test follows ISO10360-8 for length measurement error verification. The limit of the proposed artifact for performance verification test of this configuration is that when diagonal 3 position is measured, the last sphere on the bottom can not be measured due to objective nose piece collision with the highest sphere.

While for 4-axis configuration performance verification, the verification is conducted using two approaches. First, the performance verifications were conducted separately using two artifacts for each length measurement error (ISO10360-8) and rotation axis error (ISO10360-3). Secondly, a single hybrid artifact is used for both types of performance verification. The results show good agreement between the two approaches. The use of a single artifact is an improvement (allowing the possibility of checking the rotational and volumetric performance without manually changing the system), and a

step forward in the evolution of verification procedures. The main limitation of the proposed artifacts for both 3-axis and 4-axis performance verification is that it allows only the procedure to be carried out with 5X objective lens.

The developed artifacts and procedures can be generalized for other type of optical instrument by adjusting their measuring volume considering the instrument objective nose piece and working distance to avoid collision with the artifact while performing the verification test.

Chapter 3

Task-specific uncertainty of focus variation measurement

3.1 State of the art

3.1.1 Task-specific uncertainty of measurement

In coordinate metrology, measurement uncertainty estimation is very important as it has impact on process capability estimation and tolerance verification as well as assuring the measurement traceability to the definition of meter[Leach [2009], Wilhelm et al. [2001]]. For part conformance test, it is required that uncertainty of measurement from inspection process should be quantified and stated according to [ISO14253-1 [1998]]. Traceability property is very important in the global market such that part interchangeability can be realized. In general, a complete measurement result should be presented as:

$$Y \pm U, \qquad U = ku \tag{3.1}$$

Where U is expanded measurement uncertainty of a measurement result Y which defines a range in which the true value lies and k is coverage factor. Commonly, k is estimated as $k = 2$ for 95% coverage. Hence, the measurement reliability is determined by its uncertainty (to be able to conduct measurement comparison). Not only in geometric measurement, but also in other measurement: mass, pressure, etc, uncertainty is important [Possolo [2013a], Possolo [2013b], Cox et al. [2013]]. Moreover, they are "**Task Specific**" [Wilhelm et al. [2001], ISO/TS15530-1 [2013]]. Task specific means

that every specific feature and specific measurement plan (e.g. strategy), it has its own different uncertainty. Thus, making the estimation is not an easy task. Not only in ordinary measurement, but also in calibration measurement, the uncertainty should be stated such that the calibration is traceable. For example, Acko [Acko [2003]] experimentally analyzed the uncertainty of reference squareness-artifact calibration. Meanwhile, Gusel et al [Gusel et al. [2009]] investigated the measurement uncertainty for calibration of reference surface plates flatness. ISO 15530 series provide standard to estimate the task-specific uncertainty. Currently, there are two methods which have final release of the standard [ISO/TS15530-1 [2013]]. They are uncertainty of measurement by the use of calibrated or reference artifact [ISO/TS15530-3 [2011]] and by the use of simulation [ISO/TS15530-4 [2008]]. Uncertainty determination by the use of multiple measurement strategies without calibrated artifact is still not yet published [ISO/DTS15530-2 [2003]]. In the following subsection, available methods (including one which are not published in standard) to estimate measurement uncertainty will be presented followed by previous study and discussion.

3.1.1.1 GUM method

All uncertainty contributors involved in the measurement should be quantified and then are combined using the defined error budgeting procedure based on GUM [100:2008 [2008]]. It is the main reference in metrology to evaluate measurement uncertainty. According to GUM, final measurement is the results of any uncertainty propagation in each related elements of the measurement procedure, including the parameter calculation. To follow GUM, a mathematical functional relationship between the measurand Y and its input quantities X_i which is $Y = fX_1, X_2, \cdots, X_n$ has to be established. The final uncertainty is propagated through their computational chain. Based on this document, the combined standard uncertainty of a measurement is defined as:

$$u(Y) = \sqrt{\sum_{i=1}^{n}\left(\frac{\partial f}{\partial X_i}\right)^2 u^2(X_i) + 2\sum_{i=1}^{n-1}\sum_{j=i+1}^{n}\frac{\partial f}{\partial X_i}\frac{\partial f}{\partial X_i}u(X_i, X_j)} \tag{3.2}$$

Where: $Y = f(X(1), X(2), X(3), \cdots, X(n))$ is the functional relationship between the inputs $X(1), x(2), \cdots, X(n)$ and output Y and n is number of inputs. The partial derivative of $Y = f(\cdot)$ with regards to $X(n)$ is defined as $\frac{\partial f}{\partial X(n)}$. The last term of the equation represents the correlation between inputs. If the value of this last term is 0,

then there is no correlation among data (or the correlation is negligible). There are two methods to evaluate $u(X_i)$, which are: Type A and type B methods. Type A evaluation is obtained by statistical analysis of n repeated observations. Meanwhile, type B evaluation is based on expert judgment, long term experience of the operator, calibrated certificate, historical data, manufacturer specification, and published information.

In ISO/TS standard [ISO14253-2 [2011]], implementation of GUM is described as Procedure for Uncertainty Management (PUMA). PUMA is based on iterative GUM method and is carried out until the expanded combined uncertainty is acceptable. A target uncertainty is set. A combined standard uncertainty is calculated by:

$$u_c = \sqrt{u_1^2 + u_2^2 + u_3^2 + \cdots + u_n^2} \tag{3.3}$$

Where $u_1, \cdots, u)n$ are uncertainty contributors. PUMA methods is difficult to implement due to its repetitive nature to directly follow GUM method. In fact, many measurement is a complex one and there is no close mathematical form function of the measurement. There are two alternatives of standards which are more practical to implement for the uncertainty estimation compared to GUM and PUMA method. They are ISO15530-3 and ISO15530-4.

3.1.1.2 The use of calibrated artifact Method: ISO 15530-3

The most common implementations for measurement uncertainty determination are ISO/TS 15530-3 [ISO/TS15530-3 [2011]], also known as comparison method. According to this method, the expanded uncertainty is calculated as:

$$U = k\sqrt{u_{cal}^2 + u_p^2 + u_b^2 + u_w^2} \tag{3.4}$$

u_{cal} is standard uncertainty of the calibrated artifact stated in the calibration certificate. u_p is standard uncertainty related to measurement procedure and is calculated as standard uncertainty from n measurements (usually 20). u_b is standard uncertainty related to systematic error of the measurement procedure evaluated by using calibrated artifact (20 measurements). u_w is standard uncertainty related to the contribution of manufacturing variations, such as variation of thermal expansion coefficient, form errors, roughness, elasticity and plasticity. This uncertainty is estimated by measuring around 20 pieces of manufactured parts. Finally, k is a coverage factor and selected as $k = 2$ for coverage probability of 95%.

3.1.1.3 Simulation method: ISO/TS 15530-4

This method is based on computer simulation by taking into account the most important uncertainty contributing to the measurement task [ISO/TS15530-4 [2008]]. Basically, this method was designed for tactile Coordinate Measuring Machine (CMM). By using this method, every input quantities and uncertainty contributors considered in the simulation have to be stated. The combined standard uncertainty is calculated as:

$$u_c = \sqrt{u_{sim}^2 + \sum_{i=1}^{n} u_i^2} \tag{3.5}$$

Where u_{sim} is standard uncertainty estimated by simulation. The value is derived from number of simulation runs. From these number of runs, all measurement results are stored and statistical analysis is carried out to estimate u_{sim}. u_i is standard uncertainty contributed by error sources which are not considered in the simulation.

3.1.1.4 Other methods

There are some other methods besides those found in the published standard. They are multiple measurement strategy, which is based on in different position and orientation to estimates uncertainty without using calibrated artifact, statistical estimation from long measurement historical data and direct expert judgment.

3.1.1.5 Previous studies to estimate measurement uncertainty

Many works have been reported by using the method to estimate measurement uncertainty of micro/nano scale parts by using optical/non-contact metrology instruments. Research results have been presented to verify the efficiency of the micro/nano measurement [Tosello et al. [2009], Tosello et al. [2010], Carmignato and Savio [2011], Carmignato et al. [2010]] as well as replica method for measurement of transparent surface [Gasparin et al. [2010a], Gasparin et al. [2010b]] by the knowledge of measurement uncertainty. In [Tosello et al. [2009]], they estimated uncertainty of measurement of micro-injection molding part. The measurement is a diameter and height. Both tactile and non-contact instrument were used, since the calibrated artifact used for non-contact instrument is derived from the calibration by tactile measurement. They proposed this step since there is no available representative artifact for micro injection molding part.

Hence, then they proposed their own artifact and used the tactile instrument for the calibration of the artifact (fig. 2.6g). For height (Z) measurement, a step measurement (by mounting two standard gauge block on optical glass) by tactile CMM was carried out and the estimated uncertainty is defined as (following the ISO15530-3 2004):

$$U_{TCMM,J} = k\sqrt{u_{cal}^2 + u_p^2 + u_{wl}^2 + u_{glass}^2} + |b| \tag{3.6}$$

where $T_{TCMM,J}$ is the combined standard uncertainty of the step measurement by tactile CMM. k is a coverage factor of 2. u_{cal} is standard calibration uncertainty of the gauge block. u_p is standard uncertainty of the measurement procedure which is calculated as standard deviation of 5 repeated measurements between two adjacent gauge on the optical glass. u_w is temperature related standard uncertainty which is calculated as maximum range of operating temperature of the measurement. u_{glass} is standard uncertainty of planarity of the optical glass. And finally, b is systematic error calculated as a difference between the value obtained from the gauge blocks calibration certificate and the measured values by tactile CMM. After $T_{TCMM,J}$ is calculated, they determined the calibration uncertainty as combination of $T_{TCMM,J}$ and uncertainty due to measured work piece, material, probe tip and shaft. The combined calibration uncertainty by tactile CMM is:

$$U_{cal(TCMM,J)(J)} = k\sqrt{u_{TCMM,J}^2 + u_{p,j}^2 + u_{p,j}^2} \tag{3.7}$$

Where j is the type of measurands, $u_{p,j}$ is standard deviation of repeated measurements for j-th measurand, and $u_{w,j}$ is temperature related standard uncertainty for j-th measurand which is maximum range of measurement j-th temperature condition. Finally, after $U_{cal(TCMM,J)(J)}$ were obtained, they used this as calibrated artifact uncertainty to estimate the uncertainty of optical measurement system as:

$$U_{OCMM}(j) = k\sqrt{u_{cal(TCMM)(j)}^2 + u_{p,j}^2 + u_{w,j}^2} + |b| \tag{3.8}$$

Where $U_{OCMM}(j)$ is the combined standard uncertainty of the micro-injection-molded part measured by the optical instrument.

In other study, [Tosello et al. [2010]] estimated uncertainty of measurement for SEM and AFM instrument, since these instruments are important for the measurement of

master-disk to manufacture High Definition-Digital Versatile Disk (HD-DVD). In their study, the uncertainty budget was defined as:

$$U(i) \quad = \quad k\sqrt{u_{resi}^2 + u_{ci}^2 + u_{cali}^2 + u_{repi}^2 + u_{noisei}^2} \tag{3.9}$$

Where $U(i)$ = the measurement uncertainty of the i-th measurand, $u_{res(i)}$ = instrument resolution which depends on the pixel resolution and scanning direction along horizontal or vertical directions, $u_{c(i)}$ = variability of the calibration factor calculated as standard deviation of 5 different calibration factors $c(i)$ obtained from 5 repeated independent calibrations, $u_{cal(i)}$= standard uncertainty of calibration artifacts used for scanner calibration, $u_{rep(i)}$ = measurement repeatability and defined as $u_{rep(i)} = max(u_{AFM(i)}, u_{features(i)}, u_{disc(i)})$. $u_{AFM(i)}$ = standard deviation of the same 5 measurements by AFM on the same feature on different scanning area, $u_{features(i)}$ = standard deviation of 5 different features measurements on the same scanning area, $u_{disc(i)}$= standard deviation of 5 different features on 5 different scanning areas measurements. Both from the results of these two studies by Tosello et al [Tosello et al. [2009] and Tosello et al. [2010]], they found that the measurements carried out by optical instrument still have considerably higher measurement uncertainty compared to the tactile one. As such U/T, which is the ration between uncertainty and its measurand tolerance higher. This makes the efficiency of the measurement by optical instrument is lower than the tactile CMM method.

[Carmignato and Savio [2011]] studied the traceability property of volume measurement due to its many advantages for engineering application such as volume calibration of fluid container, measurement of wear, and other cavities inspection. Volume measurement by CMM (tactile/optical) has more advantages compared to conventional gravity method such as possibility to evaluate shape and localized volume loss, and by CT system, possibility to evaluate internal cavities. In their study, there were two interesting parameters, which are relative volume uncertainty $\frac{U(V)}{V} = 3\frac{U(d)}{d}$ and volume uncertainty to surface ratio $\frac{U(V)}{S} = \frac{3}{Cs}U(d)$. Dimensional measurement uncertainty is defined as $U(d)$, where d is a one-dimensional measurement. The procedure they used to determine $U(d)$ is following ISO15360-3 [ISO/TS15530-3 [2011]]. $\frac{U(V)}{V}$ is defined as $U(d)\frac{dV}{d}$ which is a multiplication of dimensional uncertainty and the first derivation of Volume function with respect to its dimensional element. Shape factor C_S is formulated

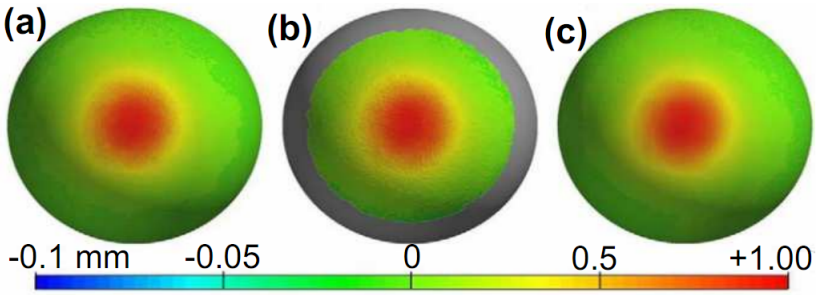

Figure 3.1: wear measurement by (a) tactile CMM, (b) optical CMM, and (c) CT system [Carmignato and Savio [2011]].

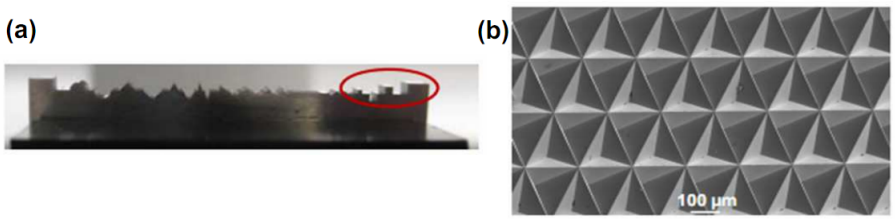

Figure 3.2: (a) calibrated surface profile, (b) micro-injection molding artifact.

as $d\frac{S}{V}$. Three types of instrument were used: tactile CMM, Optical CMM by laser scanning and CT-scan system. In their report, uncertainty of optical CMM and CT system are higher than the tactile one as expected. Fig. 3.1 shows local wear measurement results from these three types of instruments. (a) Tactile CMM, (b) optical CMM, and (c) CT system. [Gasparin et al. [2010a], Gasparin et al. [2010b]] studied the uncertainty of measurement by replication technique. This technique is a potential emerging technique to measure difficult surface, such as transparent surface or to measure an area in which putting the part on the measurement table is impossible e.g. small area of a very large part. They studied this uncertainty for two types of measurement applications: surface texture measurement [Gasparin et al. [2010a]] and micro-geometric measurement [Gasparin et al. [2010b]]. Both hard and soft polymers were used to replicate the shape or texture of the surface. Curing agent was added to harden the polymer. For surface texture measurement uncertainty study, they used a calibrated surface profile artifact. Meanwhile, for geometric one, they used triangular texture surface produce by micro-injection molding process. Fig 3.2a and fig. 3.2b depict the calibrated artifact for accessing the uncertainty of measurement of replication tech-

nique for surface-texture and micro-geometric measurement, respectively. There are reports for direct implementation of substitution/comparison method (ISO15530-3) to estimate uncertainty in CT-Scan measurement. In [Yague-Fabra et al. [2013]], they implement this method to estimate uncertainty of 3D edge detection in CT measurement. Uncertainty estimation of aluminum measurement by means of CT has been presented in Schmitt and Niggemann [2010]. Ontiveros et al [Ontiveros et al. [2012]] applied the method to estimate uncertainty from measurement of toggle for hearing aid application made of liquid crystal polymer (LCP) and miniaturized dog-bone specimen made of acetal polyoxymethylene (POM). Uncertainty estimation of dose engine part measured by CT system is reported by Muller et al []. Finally, other method of uncertainty estimation based on ISO14253-2 [ISO14253-2 [2011]] is reported by muller et al [Muller et al. [2013]]. This method is an industrial approach which does not need real part calibration. With this method, they found that the main uncertainty contributor is from the "reference" component uncertainty which is not a real calibrated artifact, instead it is calculated from uncalibrated part measured by CMM. Its uncertainty estimation takes into account the maximum permissible error of CMM, instead of uncertainty from calibration certificate.

One of the major drawbacks of the method describe in the standard [ISO/TS15530-3 [2011]] are flexibility and cost. Since measurement uncertainty is a task-specific, a different calibrated artifact will be required for uncertainty evaluation of every different part, leading to an increase of cost and time to implement the procedure. ISO 15530-4 [ISO/TS15530-4 [2008]] provides a method which are more flexible, fast, and subsequently lower cost to evaluate task-specific uncertainty. This method is based on Monte Carlo computer simulation. With this method, the task-specific uncertainty can be realized by which a measurement (part geometry, strategy, part orientation, etc) can be simulated and the uncertainty can be estimated. The basic requirement of GUM [100:2008 [2008]] method is a need of functional relationship between the input, and the output, including the filtration algorithm such as in roughness measurement [krystek [2001]]. In many case, the model of this functional relationship is difficult to build and to analytically solve [Blateyron [2006]]. Hence, the GUM method to determine measurement uncertainty is limited by the complexity of the functional relationship model of the measured parameters. Simulation method based on Monte-Carlo simulation can be a prominent choice to solve this problem as being explained in [Wilhelm et al. [2001],

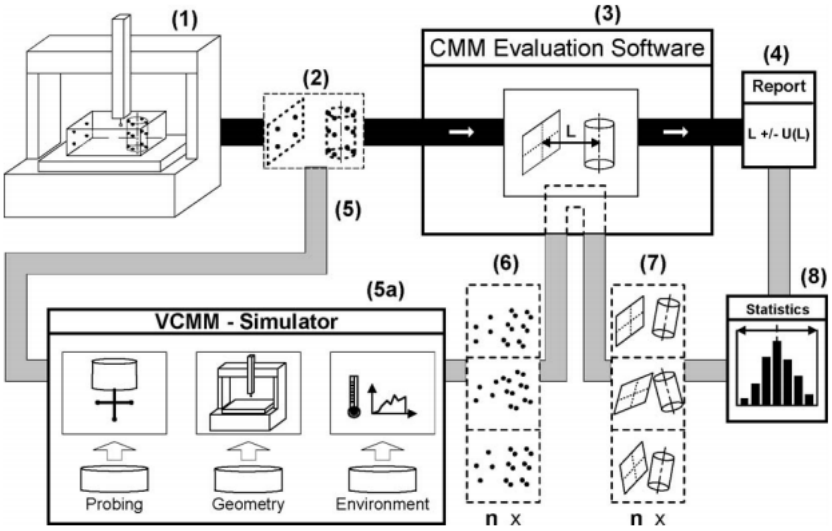

Figure 3.3: Simulation approach to evaluate measurement uncertainty by [Wilhelm et al. [2001]]

Philips et al. [2003], Haitjema et al. [2001]]. Fig. 3.3 shows the famous proposed simulation method (so-called Virtual CMM/VCMM) by Wilhelm et al. [2001]. The method was originally proposed for measurement with tactile CMM. The concept of the proposed simulation framework (VCMM) is explained as follow. Firstly, a series of points is captured by the tactile CMM (1). The captured points (2) then are evaluated to compute the substitute geometry with a certain evaluation software. From the substitute geometry, the measurand parameters are derived to estimate the conformance of the measured work piece. For the VCMM (simulation approach), the captured points from the measurement (5) are perturbed by the error simulator (5a) incorporating all the most significant error sources. The error sources for tactile CMM are part geometry, probing, machine motion (kinematic and dynamic) error, environmental influences and others contributors. The main drawback is that it is computationally intensive [Haitjema et al. [2001]], Ontiveros et al. [2012]]. Instead, due to the advance of computing power and its availability to reasonably acquire, this issue can be handled.

The fundamental requirement to be able to utilize simulation method, also commonly called as Monte-Carlo (MC) simulation, is to derive the model of the measurement process. It can be analytical-based or statistical-based model [Philips et al. [2003]]. The model should incorporates all the error contributors during the measure-

ment process to accurately simulate the measurement process and hence estimate the uncertainty. Few works have been reported to use simulation method to determine the task-specific measurement uncertainty, especially for non-contact instruments. This method has been initially applied in tactile CMM, and is called virtual CMM [Wilhelm et al. [2001]]. For CMM, a number of researches have been reported regarding the use of simulation method. These can be found in [Aggogeri et al. [2011], Balsamo et al. [1999], Schwenke et al. [1999], Baldwin et al. [2007]]. Kruth et al proposed to incorporate part form error into the Monte Carlo simulation method to have better estimate of the task-specific uncertainty [Kruth et al. [2009]]. [Moroni and Petro [2014]] utilized simulation method based on the error signal of CMM to determine optimal inspection strategy planning of geometric tolerance verification by minimizing inspection cost. The error signal method is proposed by [Drop et al. [2001]]. This method is applied by measuring a line standard to obtained the error signal of a specific bridge-type CMM.

For non-contact measurement, [Evans [2008]] implemented this method to evaluate the uncertainty of peak-to-valley surface form error measured by interferometer-based instrument. This parameter is common in inspection of lens. They convolved Monte Carlo method with the uncertainty matrix and found that this method provides a robust estimation. Giusca et al. [Giusca et al. [2011]] applied simulation method for micro scale surface area measurement. They developed the geometric model of xy-stage of their own developed surface-areal measurement instrument. From this model, they can apply Monte Carlo simulation to estimate the measurement uncertainty. Monte-Carlo simulations for CT-scan uncertainty of measurement have been reported in [Reisinger et al. [2011], Sukowski and Uhlmann [2011], Hiller and Reindl [2012]]. Based on report in [Reisinger et al. [2011] and Hiller and Reindl [2012]], they built the CT simulation model based on ray tracing to generate simulated detected object in the detector panel. Hence, they can simulate the CT measurement by means of virtual CT which is based on the Virtual CMM framework [Wilhelm et al. [2001]]. The virtual CT framework and Monte Carlo framework are depicted in 3.4. One should note that, in determining uncertainty, any systematic error (bias) in the measurement chain should be compensated and the uncertainty related to the compensation process should be taken into account or this bias should be taken into account when determining the combined measurement uncertainty [Hartig and Krystek [2009]]. Schmitt and Niggemann also implemented simulation method for CT measurement uncertainty estimation

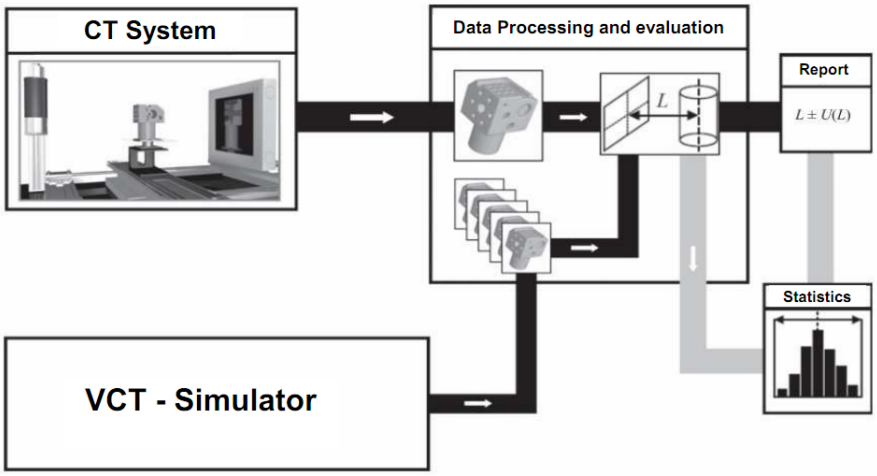

Figure 3.4: (a) Framework for the virtual CT prepared for Monte Carlo Simulation, and (b) the relation between output-input quantities in Monte Carlo Simulation [Hiller and Reindl [2012]].

[Schmitt and Niggemann [2010]]. In their simulation method, data correlation among points is not considered. Furthermore, analysis of instrument repeatability and reproducibility can be useful information in relation with the measurement uncertainty. The repeatability value describes the performance variation of the instrument within the same measurement conditions. The performance variation of the instrument in different measurement condition, such as different operator, different part or toll, different day-time, etc is represented by the value of reproducibility [Montgomery [2001]].

3.1.1.6 Discussion

GUM method is the main reference, but this method is suitable if the measurement task and device are simple since it requires measurement function. This function relates the measurand (characteristic to be measured) and the input quantities. In reality, a measurement task and devices is very complex and can not be mathematically presented in a close-form as such mathematical derivation can not be carried out to follow GUM method. The iterative PUMA method seems too complex due to its repetitive procedure. Many implementations can be found by substitute method. Since uncertainty is task specific, it has to be estimated for each different feature and measurement plan/ The GUM, PUMA, Substitute, and multiple measurement strategy are time consuming for task-specific uncertainty estimation due to many measurement experiments

should be carried out. Moreover, many measured work pieces are difficult to handle and properly placed in different orientation to follow the procedure. In addition for substitute method, a calibrated artifact similar for each measurement task is needed. This induced problems such as how the work piece can be calibrated (in the case of complex part shape) and the high cost of calibration can only be justified if it is used for mass production run. Due to these reasons, these methods are not practical to be implemented by industry. Simulation method seems to be the most promising one to estimate the task-specific uncertainty. The reason is that there is a need of general approach to estimate task-specific uncertainty such that it can be used for every specific feature. As being stated before, one consideration for simulation method is that it is computationally extensive, but with the advance of computing technology nowadays and common availability to acquire, this situation can be handled.

3.1.2 What is lacking?

Uncertainty estimation based on simulation, defined in ISO[ISO/TS15530-4 [2008]] has advantages over substitution (comparison) and the use of calibrated artifact method as stated in ISO[ISO/TS15530-3 [2011]] and others methods. Despite the advantages of simulation method for uncertainty estimation [ISO/TS15530-4 [2008]] of measurement by non-contact instrument, the use of it is still less compared to the method by using calibrated artifact [ISO/TS15530-3 [2011]] especially for optical instrument. In addition, the simulation method is less diffused even though there is already released standard. From the literature, many studies use simulation method by using the analytical model of the measurement, especially the geometric one. In fact, other statistical model can be a great advantage. In optical measurement, constructing the analytical model is more complex compared to the contact one, especially modeling the interaction between the electromagnetic wave (light) and the work piece [Leach and Haitjema [2010]]. By using statistical model, the analytical modeling of the measurement is not necessarily built. Moreover, there is still a lack for the practical procedure in estimating uncertainty by simulation. Hence, in this thesis, simulation method utilizing statistical techniques for the simulation of the perturbation point is proposed. The proposed perturbation method will take into account correlation among the measured points.

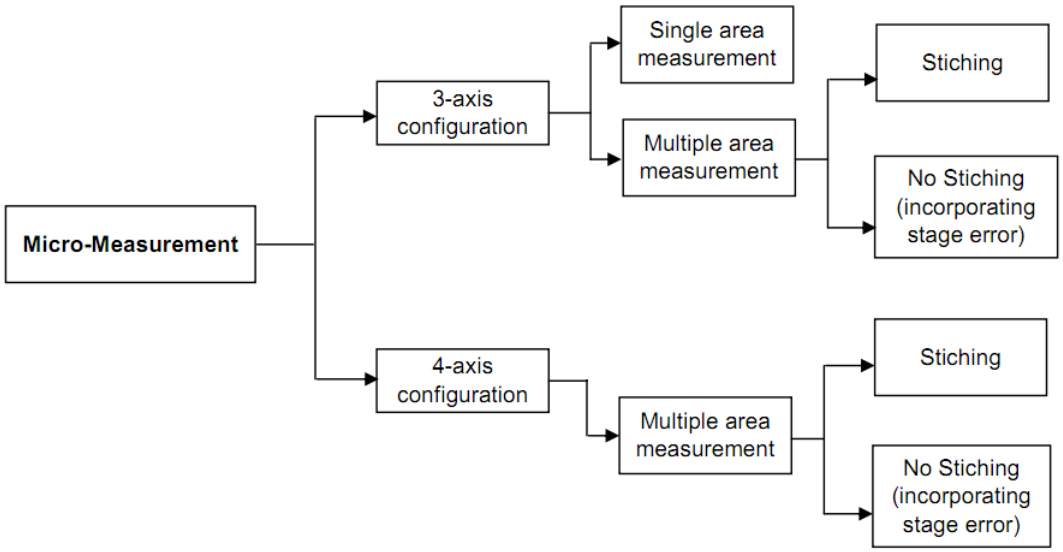

Figure 3.5: Classification of measurement by focus-variation based instrument.

3.2 Proposed method for estimation of measurement uncertainty based on simulation approach

In general, measurement by the focus-variation instrument used in this study is divided into two classes: 3-axis configuration measurement and 4-axis configuration measurement. Each of them can be split into single and multiple area measurement. In multiple area measurement, if the area measurements are adjacent, stitching procedure can be utilized to combine all the area measurements. Otherwise, stage error will be involve to the whole measurement if they are not adjacent each other. To summarize, essentially, there are three types of obtaining the measurement results: without stitching (single area measurement), without stitching (multiple area measurements incorporating stage error), and with stitching. This classification is shown in 3.5. These various type of measurement classifications increase the difficulties of measurement uncertainty estimation.

As mentioned in the state of the art section, uncertainty determination by simulation seems to be the most suitable solution for task-specific uncertainty. There are three types of task-specific uncertainty based on this method [Philips et al. [2003]], they are: simulation based on mathematical model of instrument-related error, such as

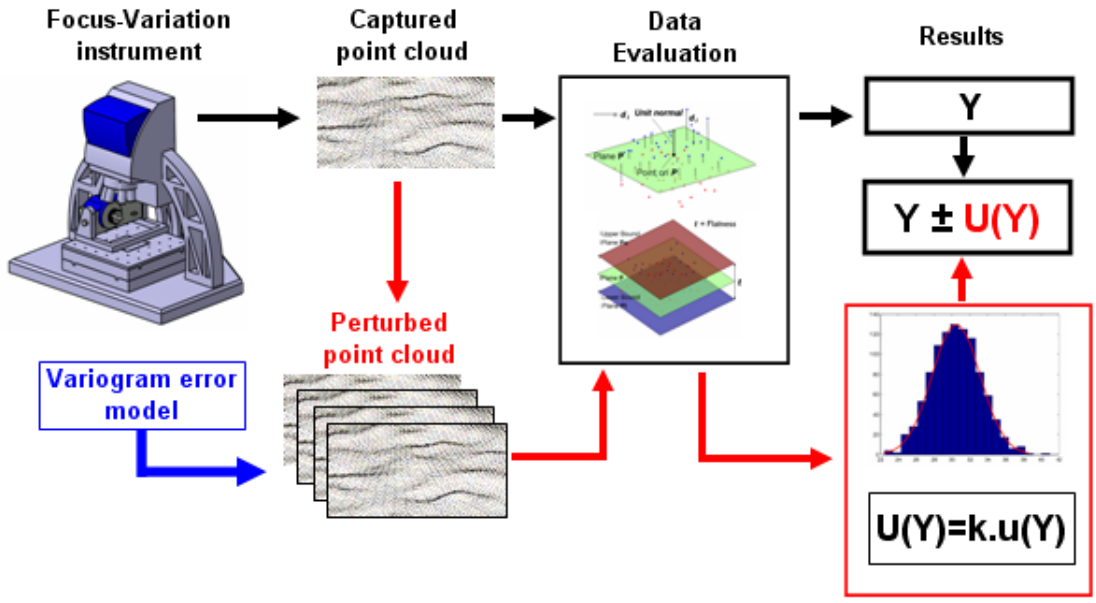

Figure 3.6: Framework of the simulation approach and the proposed error simulator (blue box).

kinematics and dynamic errors, simulation based on random point perturbation, and simulation based on empirical (statistical) model.

In this work, an error simulator based on statistical model is proposed, This simulator works inside the simulation framework based on [Wilhelm et al. [2001]] for points perturbation. The proposed error simulator model and the whole framework of the simulation approach is shown in fig. 3.6 (blue box). The framework is explained as follow. It consist of two paths, the first one (with black arrow) is to determine the measurement results in which the conformance/non-conformance test will be verified. The second path (red arrow) is to estimate the measurement result uncertainty. The flow of the first path is a set of point clouds is captured from FVM instrument. This points cloud is then processed and evaluated to associate the points with a specific substitute geometry. From this fitted substitute geometry, the dimensional and geometrical measurement results are derived. For the second path, from the captured points, a points perturbation process is carried out. This is done by the proposed error simulator. The perturbed points resulted from the error simulator are processed and evaluated with the identical evaluation software, used to evaluate the original captured points. The points perturbation process is repeated for many number of times. The measurement

result from each simulation run is stored. From all the stored measurement results, a statistical evaluation is carried out to estimate the measurement uncertainty. The estimation is derived by calculating standard deviation from the stored results (GUM Annex 3). After estimating the measurement uncertainty, the complete measurement result can be stated as: $Y \pm U$.

The proposed error simulator model utilized a spatial statistic method which emerges from a Geo-spatial study [Cressie [1993]]. Fundamental idea of spatial statistic is that points are correlated each other depends on length of their spatial distance with respect to each other. The technique is used to simulate error of points for the perturbation procedure in the simulation run. A perturbed point $\mathbf{p_i'}$ is obtained by multiplying a point $\mathbf{p_i}$, obtained from the measurement, with perturbation variance matrix $\mathbf{T_{err}}$, which can be written as:

$$\mathbf{p_i'} = \mathbf{T_{err}}\ \mathbf{p_i} \tag{3.10}$$

and matrix $\mathbf{T_{err}}$ is defined as:

$$\mathbf{T} = \begin{bmatrix} 1 & -\epsilon_{\theta z} & \epsilon_{\theta y} & \epsilon_x \\ \epsilon_{\theta z} & 1 & -\epsilon_{\theta x} & \epsilon_y \\ -\epsilon_{\theta y} & \epsilon_{\theta x} & 1 & \epsilon_z \\ 0 & 0 & 0 & 1 \end{bmatrix} \tag{3.11}$$

where $\epsilon_{\theta a}$ is rotation error around a-axis and ϵ_a is translation error along a-axis. Hence, the perturbation matrix contains six types of error of a point, which are translation error along x, y, and z-axis and rotation error around x, y, and z-axis (roll, pitch, yaw). These errors represent the volumetric error contribution in the measurement process. A function of spatial statistic technique is used to generate these errors. The function is generated from a multi-variate random distribution based on the selected variogram function. There are three main variogram functions which commonly used in this process. They are Gaussian, exponential, and spherical models. The functions are selected base on experimental data of variogram. A variogram of an observed random field Z, which is a function of spatial location, is defined as:

$$var[Z(x) - Z(y)] \tag{3.12}$$

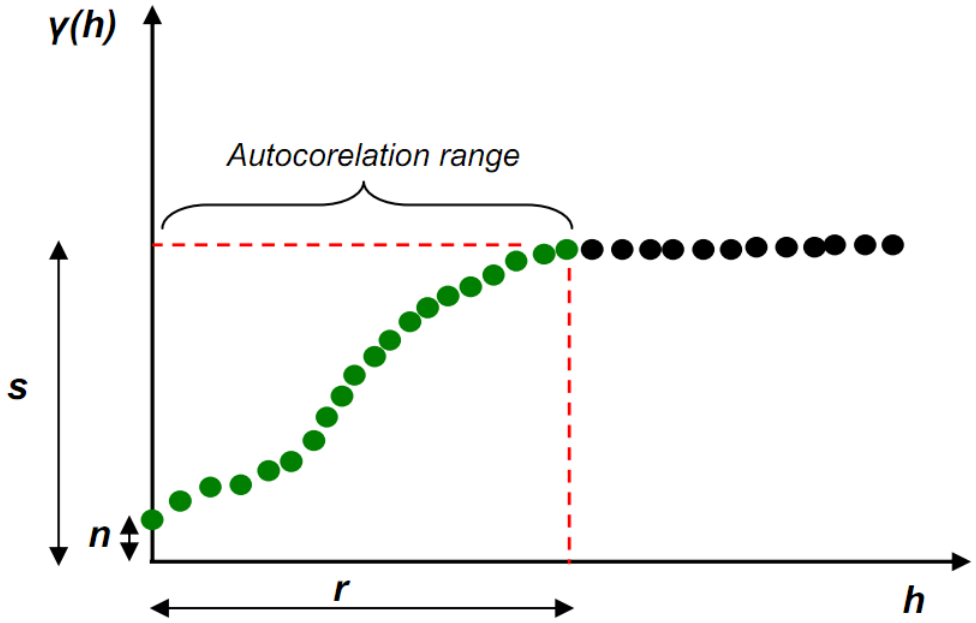

Figure 3.7: Presentation of a variogram function with its s, n ,r parameters.

Where x and y refer to a certain location (a point). Assuming the function of Z has a constant mean, the equation can be written as:

$$\begin{aligned} var[Z(x) - Z(y)] &= \mathbf{E}[(\mathbf{Z(x)} - \mathbf{Z(y)})^{\mathbf{2}}] \\ &= \frac{1}{N}\sum_{i=1}^{N}[Z(x) - Z(y_i)] \end{aligned} \tag{3.13}$$

From this point, a semi-variogram which describes the spatial autocorrelation of measurement points can be defined as:

$$\gamma(x, y) = \gamma(h) = \frac{1}{2}\mathbf{E}[(\mathbf{Z(x)} - \mathbf{Z(y)})^{\mathbf{2}}] \tag{3.14}$$

where h is distance (lagging) between point x and y. Eq. 3.14 can be presented as a graph as shown in 3.7. From this graph, there are three parameters that define a semi-variogram; they are sill (s), nugget (n), and r (range) [Cressie [1993]]. Nugget is a non-zero limit such as the variogram model is discontinuous in the origin. It represents any random error which is not included in measurement uncertainty contributors. Sill (s) resembles the variance of points which are contributed by many uncertainty sources, such as illumination, part orientation, etc. Range (r) is the limit value which determines

the limit in which the data is still correlated each other see (3.7) and it. These parameters can be used to describe isotopic variogram model. To be more comprehensive, these errors should represent the most uncertainty contributors in the measurement process. Hence, the parameter to generate this variogram should also include the uncertainty coming from sources of error in the measurement process. Hence, characterization and analysis of error sources and quantification of their influences have to be studied. The quantified error sources and their influence are used to support the model of error simulator to have a better estimate in simulating the variation during the measurement. These factors will be studied and presented in the following section. The definition of the three model of Gaussian, exponential, sphere, variograms are:

Gaussian Variogram:

$$\gamma(h) = \begin{cases} 0 & h = 0 \\ n + s\left(1 - exp\left(-3\frac{||h||^2}{r^2}\right)\right) & h \neq 0 \end{cases} \tag{3.15}$$

Exponential Variogram:

$$\gamma(h) = \begin{cases} 0 & h = 0 \\ n + s\left(1 - exp\left(-3\frac{||h||}{r}\right)\right) & h \neq 0 \end{cases} \tag{3.16}$$

Spherical Variogram:

$$\gamma(h) = \begin{cases} 0 & h = 0 \\ n + s\left(\frac{3||h||}{r} - \frac{1}{2}\left(\frac{||h||}{r}\right)^3\right) & 0 < ||h|| \leq r \\ n + s & ||h|| \geq r \end{cases} \tag{3.17}$$

3.3 Uncertainty characterization

The purpose of this section is to support the proposed error simulator such that the simulator includes the significant error sources, involved in the measurement by means of FVM instrument. This section is divided into three sub-sections. The first part, the procedures which support the study of influences factor for the measurement with FVM instrument are presented. The procedures include substitute geometry fitting, calibration of flatness (form) and filtering methods to deal with outliers. Following this part, the study of influencing factors is carried out by identifying relevant source of error in the measurement. Finally, a summary will be derived regarding the influencing factors which affect the results of measurement by means of FVM instrument.

3.3.1 Fitting procedure, flatness (form) calibration and filtering

3.3.1.1 Fitting procedure: line, plane, and sphere

There are three types of geometries used to conduct the study of uncertainty analysis; they are line, plane, and sphere. The first two are linear geometries and the last one is non linear geometry. From these basic substitute geometry, a more complex measurement can be derived as will be presented in the case studies section, such as perpendicularity measurement. The classification of linear and non-linear geometries is based on types of their defining parameters, linear or non-linear form [Shakarji [1998]]. Plane geometry was used the most in the study. Line geometry is used to study edge measurement and sphere geometry for point variability study. Two main parameters were calculated for the analysis. They are sigma of residual and form error (flatness error for the plate sample and sphere form error). The selection of sigma of residual is to understand the overall measurement noise, representing random noise, with regard to the different measurement conditions and types of material to be measured. Meanwhile, form errors are selected to represent the variation of every single point in different conditions. Since, form errors calculation is affected by every single point on the boundary as there is no averaging effect when fitting is carried out [Moroni and Petro [2008]]. Systematic error is estimated for thermal drift study of the instrument. Distance to reference plane and distance between two sphere centers from a continuous measurement sequence were calculated to estimate this error. Two types of fitting were used: least square and minimum zone fitting.

1. Least Square Fitting (LSQ)

LSQ fitting is used in verification of dimensional tolerance, such as distance, size, etc. It is a solution of non-linear optimization solution of eq. 2.13. The solution of this optimization is presented by Shakarji [Shakarji [1998]]. Thanks to line and plane which have linear defining parameters, the optimization problem can be converted from unconstrained non-linear to constrained linear optimization problem and an exact solution exist to obtain the global optimum solution. Hence, there is no uncertainty contribution from this fitting procedure. The unconstrained non-linear optimizations

are formulated as:

$$\arg\min_{\mathbf{a},\mathbf{x}} \sum_{i=1}^{n} |\mathbf{a} \times (\mathbf{x_i} - \mathbf{x})|^{\mathbf{2}} \quad \textbf{for Line} \tag{3.18}$$

$$\arg\min_{\mathbf{a},\mathbf{x}} \sum_{i=1}^{n} |\mathbf{a} \cdot (\mathbf{x_i} - \mathbf{x})|^{\mathbf{2}} \quad \textbf{for Plane}$$

where $\mathbf{a}$ is the unit normal vector, $\mathbf{x_i}$ is the i-th point, $\mathbf{x}$ is the point on line/plane, and n is number of points. Basically, these equations are minimizing the sum of square of orthogonal distance of each of the points to the fitted geometry. The procedure for fitting line and plane from points is explained as follow. One have matrix $\mathbf{M}$ which contain all the points. $\mathbf{M}$ is defined as $[x_1 \;\; y_1 \;\; z_1; \cdots ; x_n \;\; y_n \;\; z_n]$. For line and plane, the parameters to be fitted are a point on line/plane and the unit normal vector. A point on line/plane can be obtained by averaging from all the points position. Thus, it is the centroid. For the unit normal vector, Eigen vectors from the matrix M are derived. Singular value decomposition (SVD) can be used to find these vectors. Hence, unit normal vector for a line is the Eigen vector corresponds to the largest singular value. And for a plane, it is the one correspond to the smallest singular value. Meanwhile, sphere is classified as non-linear geometry. Finding solution for this fitting problem is more difficult and iterative algorithm is commonly used. Lavenberg-Marquardt (LM) algorithm is suggested by [Shakarji [1998]] to solve the fitting problem. Details of the fitting and algorithm for sphere as well as the improved version of the fitting algorithm are elaborated in Appendix A.

All the orthogonal distances of a point to the fitted geometry (line, plane and sphere) were calculated and the statistical description of the collected distance were extracted. The sigma of residual is the statistical standard deviation of all these distances, thus the standard deviation of the fitting error. The illustration of sigma of residual calculation is depicted in fig. 3.8a in the case of plane.

2. Minimum Zone Fitting (MZ)

Based on ASME Y14.5.1M [ASMEY14.5.1 [1994]], geometric tolerance verification requires MZ fitting for the procedure. This tolerance verification deals with form error evaluation. Form error is a zone (tolerance zone) in which all the obtained points from measurement lie inside the zone. The form error is illustrated in fig. 3.8b for a flatness

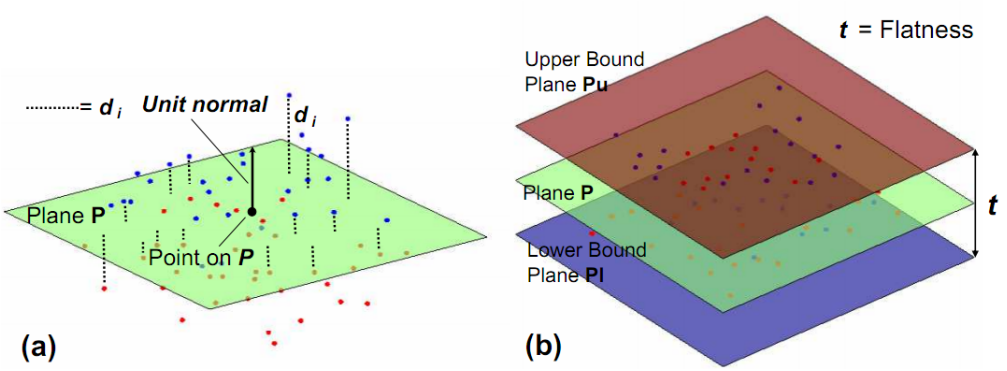

Figure 3.8: (a) distance of a point to the fitted plane, (b) flatness error.

error. The zone t is a solution of non-linear optimization as:

$$t = \underset{\mathbf{param}}{\arg\min}_{\,j}(max\ d_i - min\ d_i) \tag{3.19}$$

Where *param* is the defining parameter for the substitute geometry and d_i is the distance of points i-th to the substitute geometry. The procedures used in this study to approximate and solve this optimization problem are by first fitting substitute geometry by LSQ solution and find the different between the maximum and the minimum distance (error) of all the points to the fitted LSQ geometry.

3.3.1.2 Flatness (form) calibration

The calibration process utilized method of multi-position measurements. The calibration was carried out by a bridge-type CMM with $MPE_E = 2\mu m + \frac{L}{300}\mu m$. There are three plate samples were calibrated for their flatness values. They are aluminum, stainless steel, and titanium. These three plates are in the form of rigid thick plate, while the other samples used in this study are in the form of sheet metal such that a deflection may occurs on them. The other reason of the selection of these samples are aluminum, stainless steel, and titanium can be found in many metal-based industrial product, e. g. casting, cutting tool, mold, biomedical application, etc. Furthermore, especially for stainless steel and titanium, these metals have surface which can be considered as lambertian (see next chapter). The lambertian surface is preferable for FVM instrument since it is better in determining the focus variation of a point. By this, the identification of a surface becomes easier. The calibration for flatness is similar

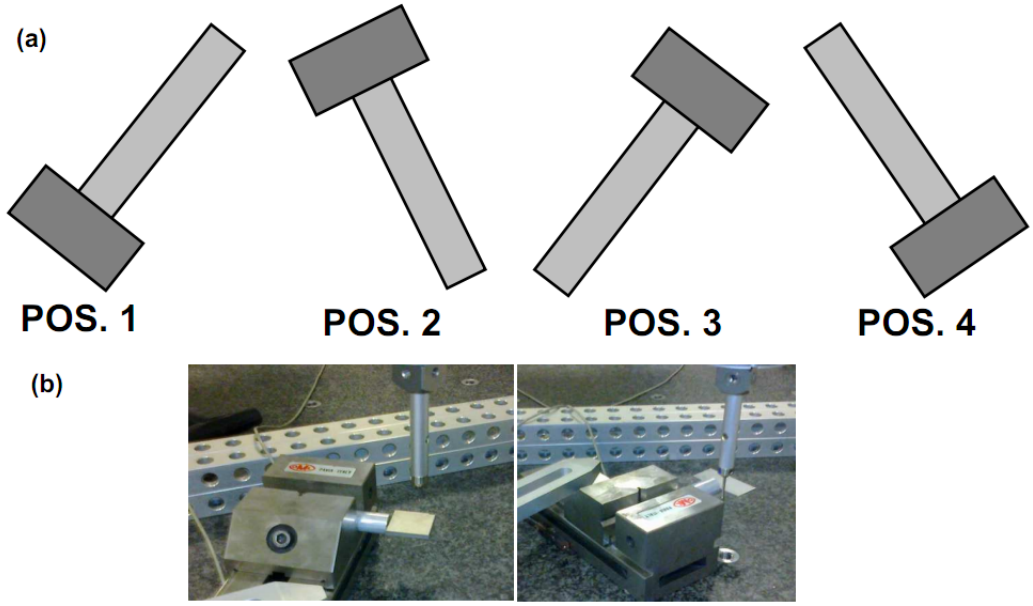

Figure 3.9: flatness calibration.

to that one for distance (length) calibration (see section 3.1.2). Instead, there is no correction to the calibrated value. Hence, there is no uncertainty contribution due to correction of measured value (u_{corr}). The calibrated value is an average result from all measurements. As such, the uncertainty contributor is simpler compared to the length calibration. The expanded uncertainty for form error calibration becomes:

$$U = k\sqrt{\frac{u_{rep}^2}{n_1} + \frac{u_{geo}^2}{n_2}} \tag{3.20}$$

where u_{rep} and u_{geo} are calculated by using (eq. 3.5) and (eq. 3.8), respectively. We can observe that the uncertainty contributors are only from the uncertainty of the repeatability of the CMM and from the form error of the measured part and CMM geometric error. The measurement data in the calibration process is arranged identical to the one presented in table 3.1. The four positioning and the calibration procedure are depicted in fig. 3.9. Meanwhile, the calibration results for the three material plates are presented in table 3.1.

	Metarial Types		
	aluminum	**Stainless Steel**	**Titanium**
Flatness [μm]	25.1(8)	4.77(5)	4.1(2)

Table 3.1: Results of the flatness calibration and their uncertainty (represented according to GUM [100:2008 [2008]]).

3.3.1.3 Data filtering for outliers removals

After acquiring the data from the instrument, filtering procedure has to carried out to remove outliers in the data points obtained by FVM instrument. They will be used for initial validation of the proposed simulation approach and for case studies. There are four types of areal filtering used for the obtained points: 3-sigma-based filter, median filter, Linear Gaussian areal filter (LG) [ISO16610-61 [2012]], and Robust Gaussian Regression (RGR) areal filter [ISO16610-71 [2014]] and media filter. The 3-sigma-based filter is the filter which will be used in the section uncertainty characterization and validation (chapter 3.3 and 3.4) which is based on removing points having distance to an ideal geometry more than three times of the standard deviation of all residuals. All the remaining points after outliers removal are the original points obtained from the acquisition. Basically, the LG and RGR types of filter are originally for the use in surface texture measurement in which the long and short-scale of surface components should be separated before characterizing the surface [ISO16610-1 [2006]]. In this case, these filters are used to deal with outliers as comparison methods to the 3-sigma-based filtering and median filtering method. The main difference of these two filters compared with the 3-sigma-based filter and median is that the resulted points after applying filtering procedure are synthetic points. Meanwhile, for 3-sigma and median filter, the remaining points are the original one. These points are resulted from a certain calculation with respect to its neighbors. General filtering can be formulated as:

$$z(x,y) \overset{filter}{\rightarrow} w(x,y) \tag{3.21}$$

Where $z(x,y)$ and $w(x,y)$ are the original and filtered-points at point (x,y). The filtered points can contain long-scale, short-scale, and certain-scale components. They depend on the type of filter applied [Leach [2013]]. High-pass filter transmits the short-scale (high-frequency) components while the low-pass filter transmits the long-scale

(low-frequency) components. Certain-scale can be transmitted with a certain band-filter (transmitting components with specific length of scale). In this case, since the goal is to remove outliers, low-pass filters are used.

Linear Gaussian areal filter is based on ISO16610-61. This filter is linear since it fulfills the requirement that if a linear filter is applied to two sets of surface data which are additively superimposed, then the resulted filtered surface is identical to the addition of the two surfaces data set which are separately filtered. Linear filter can be formulated as:

$$az_1(x,y) + bz_2(x,y) \overset{Linear filter}{\rightarrow} aw_1(x,y) + bw_2(x,y) \tag{3.22}$$

Fundamentally, linear filter is a moving average with respect to neighborhood of a point with a weighing function of certain size. The moving average of linear filtering is formulated as:

$$w(x,y) = \int_0^{l_y} \int_0^{l_x} s(x-u, y-v) z(u,v)\ du\ dv \tag{3.23}$$

where l_y and l_x are the height and width of the surface area, respectively. $s(\cdot)$ is the weighing function with filter size of u and v in $x-$ and $y-$direction, with distance between point du and dv, respectively. In order to prevent a surface with a constant topography height such that it is not affected by the filter, normalization is applied to eq. 5.3 becomes:

$$w(x,y) = \frac{\int_0^{l_y} \int_0^{l_x} s(x-u, y-v) z(u,v)\ du\ dv}{\int_0^{l_y} \int_0^{l_x} s(x-u, y-v)\ du\ dv} \tag{3.24}$$

The type of a linear filter is determined by the type of its weighing function. For Gaussian linear filter, the weighing function is:

$$s(x,y) = \frac{1}{\alpha\lambda_c} e^{-\pi\left(\frac{x}{\alpha\lambda}\right)} \frac{1}{\alpha\lambda_c} e^{-\pi\left(\frac{y}{\alpha\lambda}\right)} \tag{3.25}$$

As such, by substituting eq. 3.25 into eq. 3.24, the Gaussian linear filter is represented as:

$$w(x,y) = \frac{\int_0^{l_y} \int_0^{l_x} \frac{1}{\alpha\lambda_c} e^{-\pi\left(\frac{x}{\alpha\lambda}\right)} \frac{1}{\alpha\lambda_c} e^{-\pi\left(\frac{y}{\alpha\lambda}\right)} z(u,v)\ dudv}{\int_0^{l_y} \int_0^{l_x} \frac{1}{\alpha\lambda_c} e^{-\pi\left(\frac{x}{\alpha\lambda}\right)} \frac{1}{\alpha\lambda_c} e^{-\pi\left(\frac{y}{\alpha\lambda}\right)}\ dudv} \tag{3.26}$$

Digital implementation of eq. 3.27 can be directly applied into:

$$w(x,y) = \frac{\sum_{l=0}^{ny-1}\sum_{k=0}^{nx-1}\frac{1}{\alpha\lambda_c}e^{-\pi\left(\frac{x}{\alpha\lambda}\right)}\frac{1}{\alpha\lambda_c}e^{-\pi\left(\frac{y}{\alpha\lambda}\right)}z(u,v)\ \Delta u\Delta v}{\sum_{l=0}^{ny-1}\sum_{k=0}^{nx-1}\frac{1}{\alpha\lambda_c}e^{-\pi\left(\frac{x}{\alpha\lambda}\right)}\frac{1}{\alpha\lambda_c}e^{-\pi\left(\frac{y}{\alpha\lambda}\right)}\ \Delta u\Delta v} \tag{3.27}$$

ISO16610-71 describes Robust Gaussian Regression areal filter. This filter is a non-linear filter. The basic concept of robust regression filter can be formulated as:

$$\underset{w(x,y)}{\arg\min}\ \left(\int\int \rho(z(x,y)-w(x,y))^2 s(x-u,y-v)\ dudv\right) \tag{3.28}$$

where ρ is a lost-function. This function is selected such that the outliers will not influence the filtered points as in the case of regression method if this lost function is not applied in eq. 3.28. The residual in the regression method is estimated from the difference between the surface point to the second-degree polynomial surface applied to the points. As such, eq. 3.28 can be expanded as:

$$\underset{\beta_{h,j-h}}{\arg\min}\ \left(\rho(z(u,v)-\sum_{j=0}^{2}\sum_{h=0}^{2}\beta_{h,j-h}(x,y)(x-u)^h(j-v)^{j-h})^2 S(x-u,y-v)\ dudv\right) \tag{3.29}$$

Where $\beta(\cdot)$ is the estimated parameter for second-degree polynomial. In ISO16610-71[ISO16610-71 [2014]], the lost function is replaced with a new weighing function . This weighing function is the first derivation of the lost function according to Beaton [ISO16610-71 [2014]] and is formulated as:

$$\psi_B(u,c) = \frac{1}{2}\frac{\partial\rho_B(u)}{\partial u} = \begin{cases} u\left(1-\left(\frac{u}{c}\right)^2\right)^2 \\ 0 \end{cases} \tag{3.30}$$

Finally, according to ISO16610-71, the Robust Gaussian Regression filter is:

$$\begin{aligned}\underset{\beta_{h,j-h}}{\arg\min}\ (&\int_0^{l_y}\int_0^{l_x}(\frac{\psi_B(z(x,y)-w(x,y),c)}{z(x,y)-w(x,y)}(z(u,v)-\sum_{j=0}^{2}\sum_{h=0}^{2}\\ &\beta_{h,j-h}(x,y)(x-u)^h(j-v)^{j-h})^2 s(x-u,y-v)\ dudv))\end{aligned} \tag{3.31}$$

The standard describes in detail the digital implementation of this filter.

Median filter is also a type of filter which depends on its neighbors to determine whether a point is an outliers or a normal point. The filter procedure is as follows. For

each point $z(i,j)$, a relative distance $S(i,j)$ is a distance between $z(i,j)$ to its neighbors within a specific window of size $m \times n, \{m,n \in integers\}$. $S(i,j)$ is calculated as:

$$\begin{aligned} S(i,j)_{m,n} &= |z(i,j) - z(i \pm m, j \pm n)| \\ where\ m,n &= 0 \cdots w \end{aligned} \tag{3.32}$$

Filtered point $z_{filtered}(i,j)$ depends on a value $V(i,j)$ which is the median of $S(i,j)_{m,n}$. The filtering procedure is defined as:

$$\begin{aligned} V(i,j) &= median\left(S(i,j)_{m,n}\right) \\ z_{filtered}(i,j) &= \begin{cases} z(i,j), & V(i,j) < T \\ nearest\ z(i,j), & otherwise \end{cases} \end{aligned} \tag{3.33}$$

T is a threshold value to determine whether a point $z(i,j)$ is an outliers or ordinary point. To determine T, firstly, all the values of $V(i,j)$ $\forall z(i,j)$ are calculated. Subsequently, $V(i,j)$ is sorted in ascending order. Finally, the value T is selected as the $99\%\text{-}th$ position of the sorted $V(i,j)$. Median filter is the most computationally intensive compared to the other type of filters used in the case study since sorting procedure to determine median is needed.

3.3.2 Influencing factors

Optical instruments, especially based on image sensor, are greatly affected by the type of materials to be measured. Basically, materials are classified into three groups based on how they reflect incident light. They are lambertian, specular, and combination of them [Forsyth and Ponce [2003]]. Interaction between incident light (electromagnetic wave) and part surface is illustrated in fig. 3.10a. In the figure, the radiosity is depended on its radiance received from the illumination source. a point (x_s, y_s) is a point on the surface of the illumination source. Meanwhile, a point on surface receiving illumination is defined as (x,y). Radiance $L(x, xs \rightarrow x)$ is defined as amount of energy at a point travel per unit time per unit area perpendicular to the direction of the radiance per unit solid angle and its unit is $[Wm^{-2}sr^{-1}]$. The unit per steradian $[sr^{-1}]$ seems to be a strange definition. But, it looks reasonable since definition of illuminated point on a surface patch is modeled as a hemisphere visible from the source fig. (3.10a). Thus, the solid angle $[sr^{-1}]$ is an infinitesimal area of the incoming radiance entering

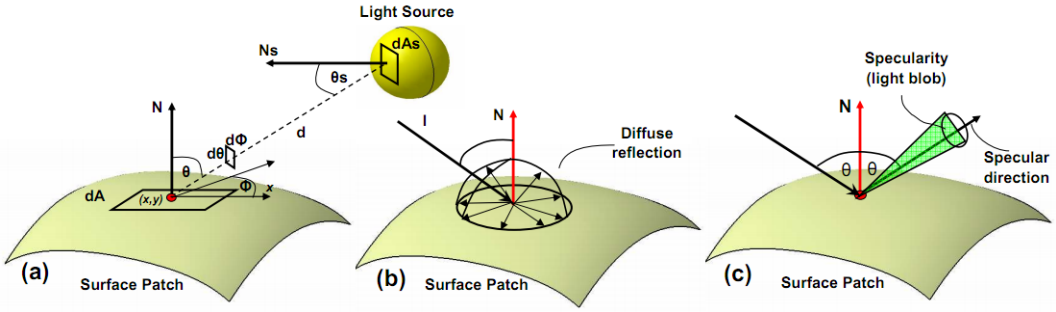

Figure 3.10: (a) Interaction between surface and incident light, (b) Lambertian surface, (c) Specular surface.

the hemisphere. The intensity of the image is linearly depended on the radiosity and formulated as:

$$B(x,y) = \rho(x,y) \int_{\Omega} L(x,y,xs,ys \rightarrow x,y) \left(\frac{cos\theta s \ cos\theta}{d^2} \right) \tag{3.34}$$

Where $L(x,y,xs,ys \rightarrow x,y)$ is its radiance and $\rho(x,y)$ is the albedo which is a ration of outgoing radiance to the input radiance and a dimensionless fraction which has value from 0 to 1. Thus, 0 means that no light is reflected and vise versa.

Lambertian surface equally reflects the intensity they receive to any direction, in other words, their response is linear. Practically, a lambertian surface will appear similar from any angle of view. The opposite is a specular surface. This surface has spurious reflection with regard to the incoming intensity; hence create a non-linear response to the image sensor. The appearance of specular surface varies based on the viewing angle, thus its directional. Fig. 3.10b and 3.10c respectively illustrate lambertian and specular surface. Based on this theoretical background, optical measurement is influenced by the variability of the incoming radiance to the image formation sensor. Fig. 3.11 show the Ishikawa diagram that influence the uncertainty of optical measurement based on the theory.

From the figure, there are four main groups of error sources related to measurement using optical FVM instrument. They are machine (instrument's parameters), material (part shape and illumination), methods (procedure) and environment (environment and drift). FVM instrument has four main parameters which have to be defined by the user and directly impact the measurement results. The parameters are exposure time

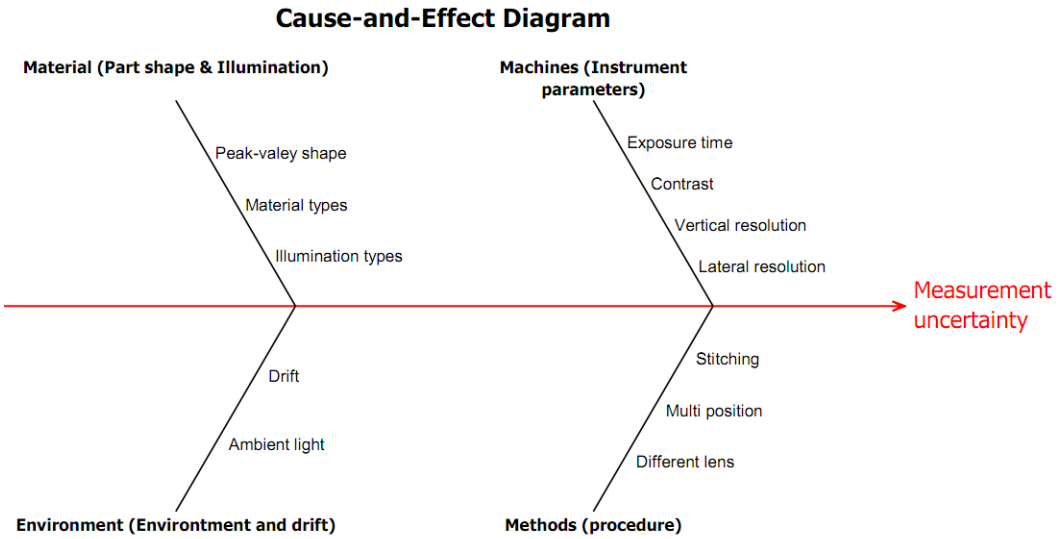

Figure 3.11: Ishikawa diagram to describe many contributors of uncertainty.

to define the power of the illumination, contrast level, and both vertical and lateral resolution. Procedure used when measurement is carried out most likely to have influence to the measurement result variation. For example, how the operator place the sample (approximately flat or tilted), what objective lens is used, and whether the measurement involves single image or stitched-multiple image measurement will contribute the the result variation. Finally, part shape (e. g. edge, peak, valley, etc) and illumination (axial, ring light and polarizer) have impact to the measurement result since they affect the incoming radiance received by the CCD sensor of the instrument. Light coming from the ambient environment, e. g. room light, and drift of the instrument due to long measurement acquisition may have the impact on the measurement result.

Various kinds of materials were used in this study. It is worth noting that all the measurement repetitions were run automatically and continuously without any intervention by developing scripting programming and run by the instrument. In this way, the repeatability results will be more guaranteed and the automatic run of the instrument will minimize other uncertainty source such as operator factor.

Measurement noise statistic, which represents the random error, is considered as a Gaussian (normal) distribution. To support this consideration, residuals from one measurement of the aluminum, stainless steel, and titanium plates are analyzed. A residual is defined as distance between a point to the least-squared (LS) fitted ideal

	Mean $[\mu m]$	**Sigma** $[\mu m]$
Aluminum	-2.28×10^{-7}	4.49
Stainless Steel	1.62×10^{-6}	1.37
Titanium	-9.15×10^{-6}	2.00

Table 3.2: Mean and sigma of the residuals for aluminum, stainless steel, and titanium plate measurement.

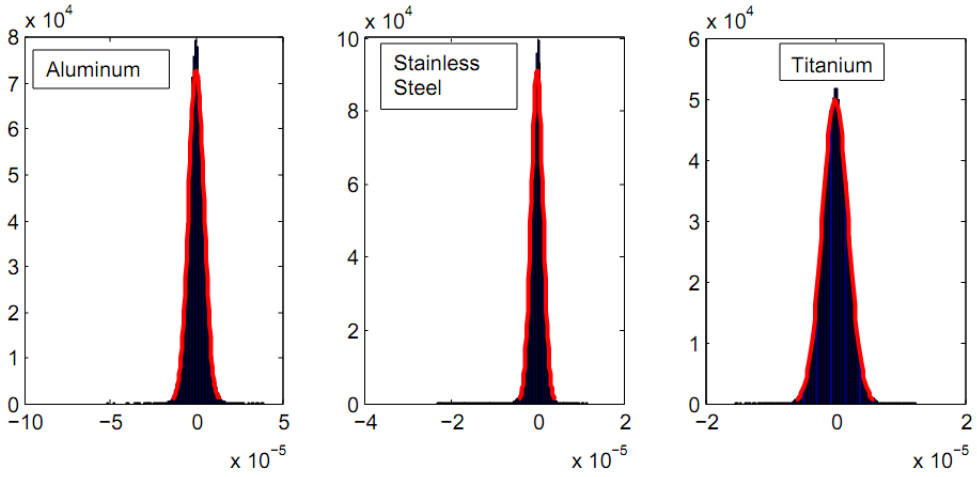

Figure 3.12: Distribution of the residual.

substitute geometry. The statistical analysis is carried by using Shapiro−Wilk method for normality test. This test is chosen due to the fact that this test is the most insensitive one with regard to data containing outliers, even though the outliers will lower the resulted test statistic [Huber-Carol et al. [2002]]. From this result, the obtained p-value are 0.02, 0.03, and 0.08 for aluminum, stainless steel, and titanium respectively. It shows that the residual statistic follow the considered distribution as being assumed with mean approximately zero and a certain value of deviation. The means and deviations of all residuals from the three material measurements are shown in table 3.2. From the table, the means of the residuals are very close to zero with a certain standard deviation (σ). In addition by visual observation shown in 3.12 , the residuals are very close to Gaussian distribution. Measurement parameters used to obtained the points to observe the error behavior are detailed in table 3.3.

Statistical analyses have been carried out to study the possible influence factors and

Material	Exposure time	Contrast	Vertical resolution	Lateral resolution
Aluminum	114.4 μs	1.33	0.4 μm	7.82 μm
Stainless Steel	116.4 μs	1	0.4 μm	7.82 μm
Titanium	224 μs	1	0.4 μm	7.82 μm

Table 3.3: The measurement parameters used to study the error behavior.

to understand how these factors affect the measurement results. Analysis of Variance (ANOVA) method is used for the statistical analyses [Montgomery [2001]]. A basic filtering by removing points having distance to the fitted geometry $> 3\sigma$ is applied before analysis is carried out. In general for this study, number of points removed (those with distance to the ideal substitute geometry $> 3\sigma$) are around $< 0.6\%$ from the total captured points. By knowing these factors, it can be used as base for uncertainty estimation. Furthermore, it contributes to the development of a good measurement procedure to reduce the uncertainty. Subsequently, the studies are consisted of:

1. Influence of ambient light and changing the magnification lens.
2. Influence of different types of illuminations.
3. Influence of different level of surface steepness from different materials.
4. Influence of edge measurement (peak-valley shape).
5. Long measurement (drift) behavior.
6. Single point uncertainty.
7. Influence of primary user-defined measurement parameters (Instrument's parameters).

3.3.2.1 Influence of ambient light and different magnification lens.

Since the FVM instruments sensor is a Charge-Couple Device (CCD) base image sensor, signal received by the CCD element is a combination of signal (light) reflected from the work piece and the signal (light) of the ambient where the measurement is conducted (fig. 3.13). Hence, the measurement result greatly dependents on illumination, both from the optical system and from the environment. Based on this, influence of ambient light variation was studied. A lambertian surface of a random structured injection-molded polymer surface was used. The material and one of the measurement results are shown in fig. 3.14. In this test, there are four different types of measurement

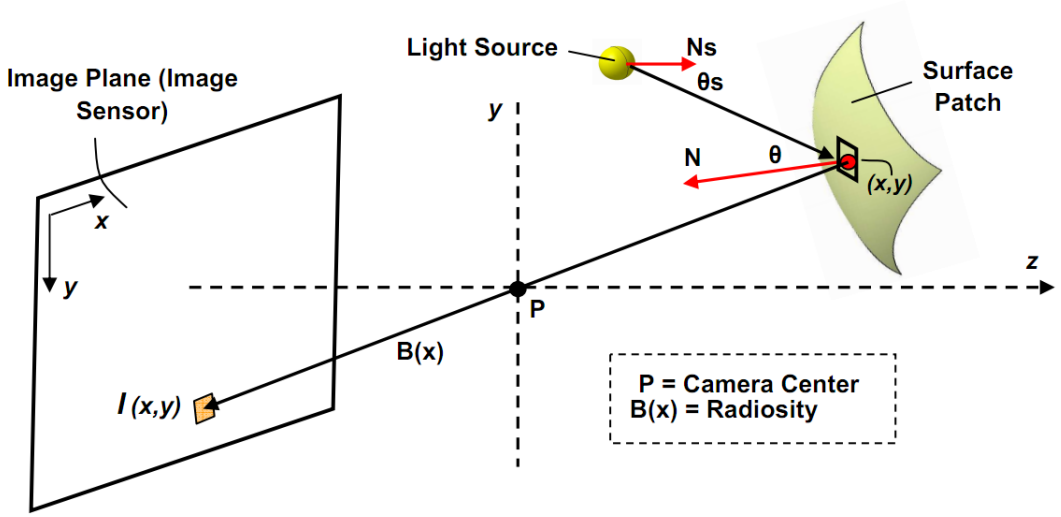

Figure 3.13: Illustration of signal acquisition on the image plane.

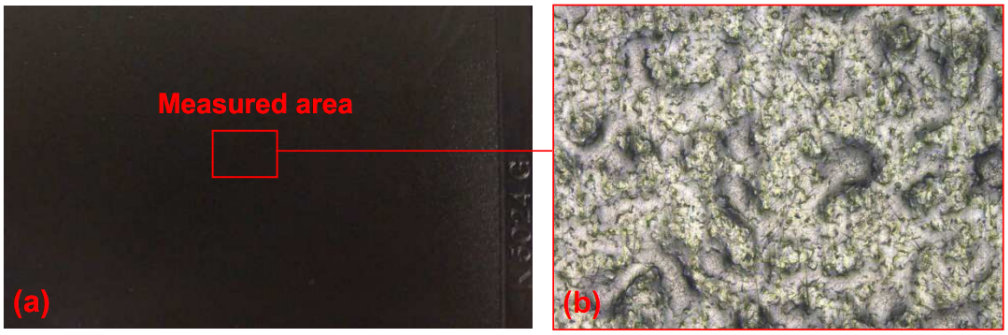

Figure 3.14: (a) Random-structure injection-molded polymer, (b) One of the measurement result by 10X objective lens utilizing axial-light.

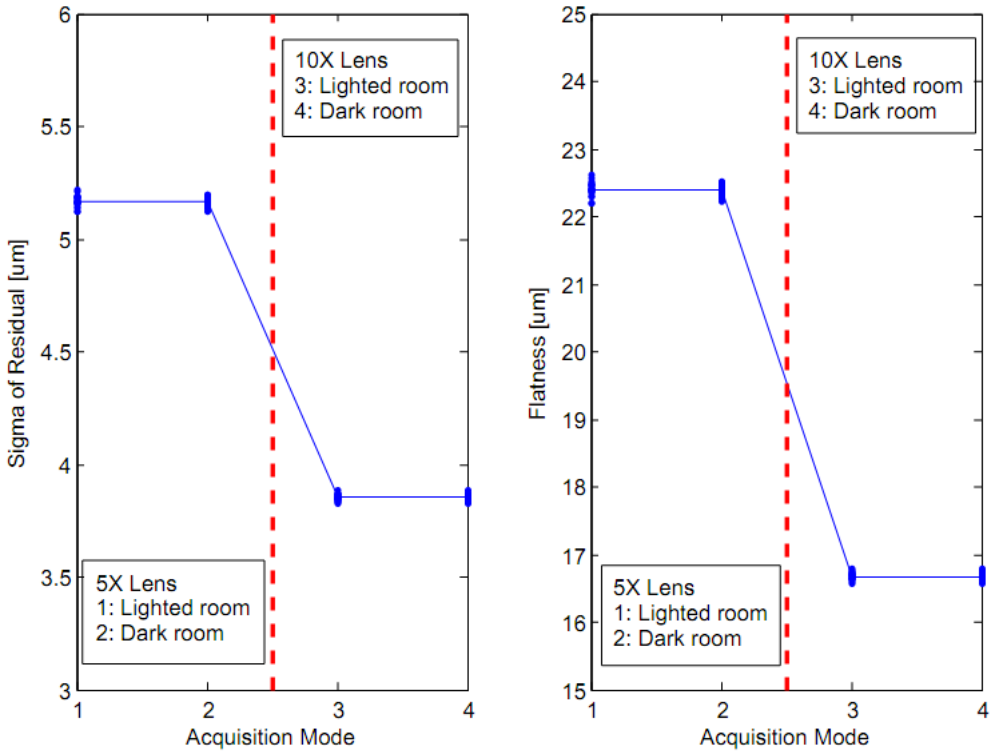

Figure 3.15: The influence ambient light.

conditions. They are measurement with 5X lens in lighted and dark room (acquisition mode type 1 and type 2 respectively) and with 10X lens in lighted and dark room (acquisition mode type 3 and type 4 respectively). In each condition, 20 measurements were repeated. For all the repeated measurement in each acquisition conditions, the measured sample area is identical except that smaller area will be obtained with 10X lens since it has smaller FOV. Polarized light was used for the measurement with 5X lens with high brightness to be able to capture the surface data. Statistical ANOVA analyses were carried out to compare and analyze the obtained results. These results are depicted in fig. 3.15. Individual plot and their means are presented. For type 1 and 2, they are shown in the left side (of the red border line) of each figure and the right side for type 3 and type 4. Mean plot and interaction plot between the two factor (Lens type and ambient light) are shown in fig. 3.16 and fig. 3.17 respectively.

From the results, different ambient illuminations do not affect the sigma of residual for both 5X and 10X objective lens. Also for flatness, there is no significant effect

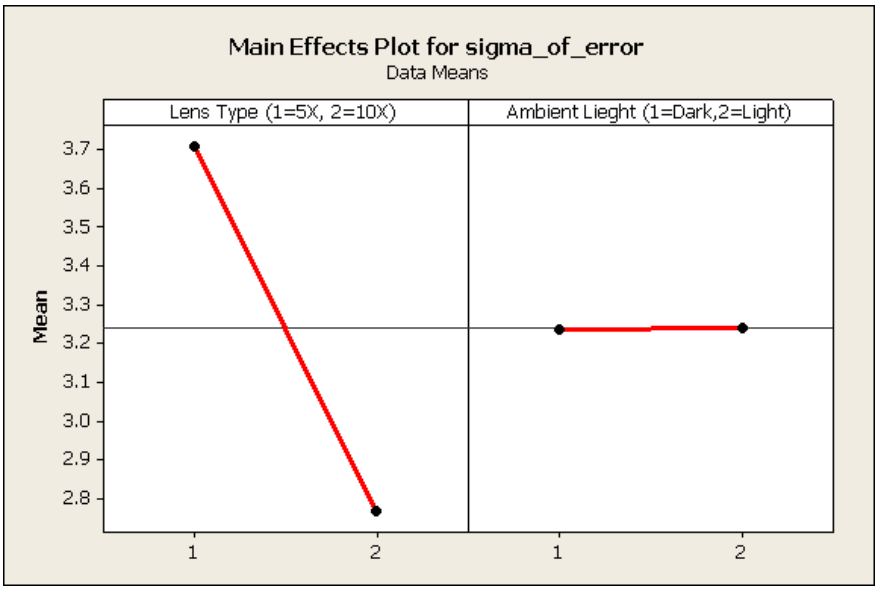

Figure 3.16: Mean plot of the two factors.

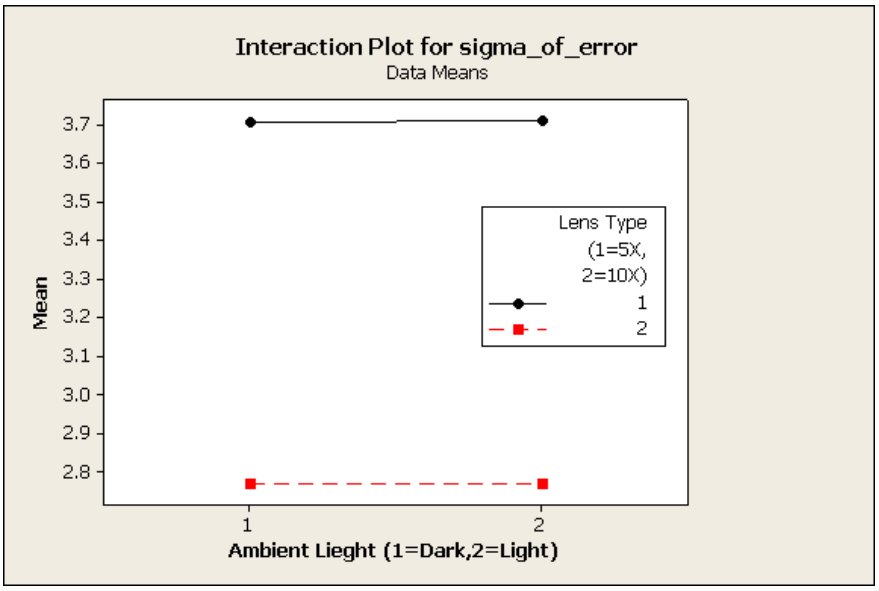

Figure 3.17: Interaction plot of the two factors.

Factors	Difference	Statistical test
from dark to lighted room	$+0.01\ \mu m$	not-significant
from 5X to 10X objective lens	$-1\ \mu m$	significant

Table 3.4: Summary of ambient light and different magnification lens.

for both 5X and 10X lens measurement results. The calculation of sigma of error and flatness involved ≈1000000 acquired points. For different magnification lens, it is clear that, there is a significant difference in the obtained results. The noise of measurement is lower for the acquisition by 10X lens (higher magnification). The reduce of noise by 10X lens is around 1.5 μm. Giusca et al [Giusca et al. [2014]] also reported similar observation in the case of measurement noise calibration for surface topography measurement. In their report, lower measurement noises were obtained with higher magnification lens. It occurs because with different magnification lens, the numerical aperture (NA) of the optical system is different. A higher magnification lens provides higher NA value. As such, higher steep surface can be measured with lens having higher NA. Moreover, the increase of magnification lens will increase the lateral resolution. The reason is by increasing the magnification lens, the FOV will be reduced with the same size of CCD image sensor. It means that the sampling distance (distance between pixel/points) will be lower and thus increase the lateral resolution. Subsequently, the surface observed by the optical system with lens having higher NA compared to the one with lower NA will be different which leads to different measurement results. From this point, it is not wise to directly compare the measurement results obtained with different magnification lens. For the interaction between the lens type and ambient light, from ANOVA test, there is no significant effect due to the interaction between them. Table 3.4 presents summary of this study.

3.3.2.2 Influence of different types of illuminations.

Since there are three different illumination sources that can be selected by the user, it is essential to study variability caused by these different illuminations. The first study used random-structures injection-molded surface (fig. 3.14) and the second one used aluminum plate (fig. 3.18a). The study using the polymer material consists of two different acquisition modes: 5x lens with ring-light and 5X lens with polarizer.

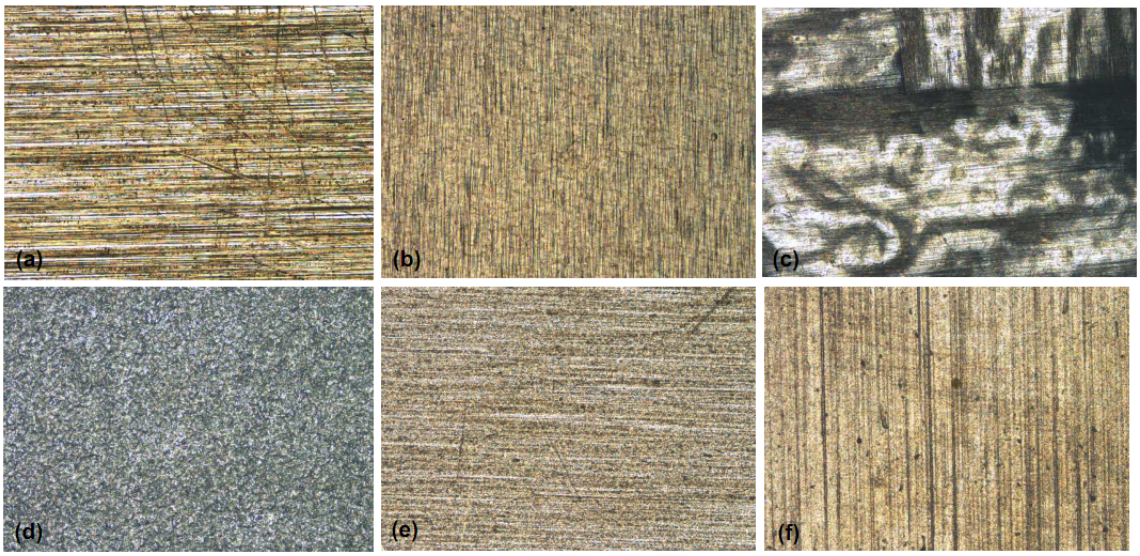

Figure 3.18: Acquisition results from six different material samples (a) aluminum, (b) steel, (c) patterned Lambert and specular, (d) black-layered coated steel, (e) stainless steel, (f) titanium.

The measurements were repeated 20 times and around 1000000 points were involved in the calculation of noise sigma and flatness. All analyses were conducted by using statistical ANOVA analysis. Fig. 3.19 shows the results. They show that the two different illuminations between ring-light and polarized light significantly affect the results. The sigma of residual calculated from points obtained by ring-light is lower around 0.6 μm compared to the one obtained by polarized light.

The second study used aluminum plate sample material which is considered as specular surface. The plate was measured in four different positions and each position was varied with a degree of $0^0, 5^0, 10^0$ and 15^0 by the use of 3D rotation unit. Position 1 and 2 are position in which the axis of the rotation unit is horizontal and position 3 and 4 for the vertical one. Each of these positions was rotated clockwise and anti-clockwise. The positioning is depicted in fig. 3.20. Five measurements were repeated for each position and each orientation. Hence, total of 80 measurements were carried out for each illumination type. The results are shown in 3.21. The first row of the figures shows the sigma of residual and the second row shows the flatness error. In this study, the three illuminations were used: axial light, ring light, and polarizer. All of them were used with 5X objective lens. Based on ANOVA statistical analysis, all the

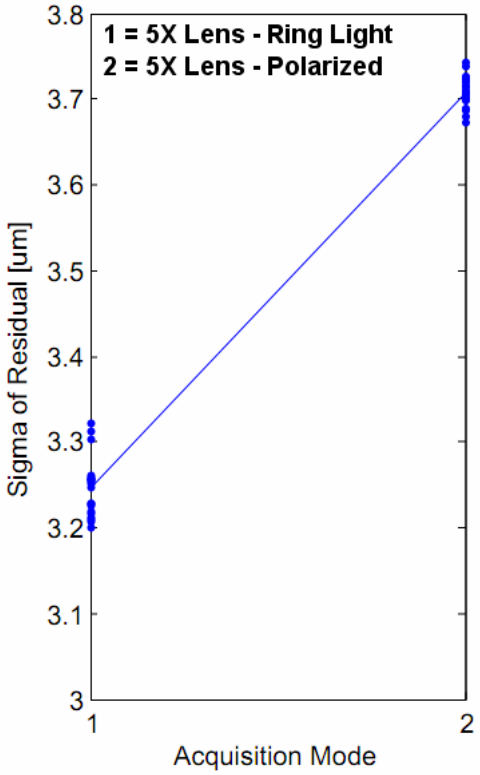

Figure 3.19: Influence of different illumination for random-structured injection-molded polymer.

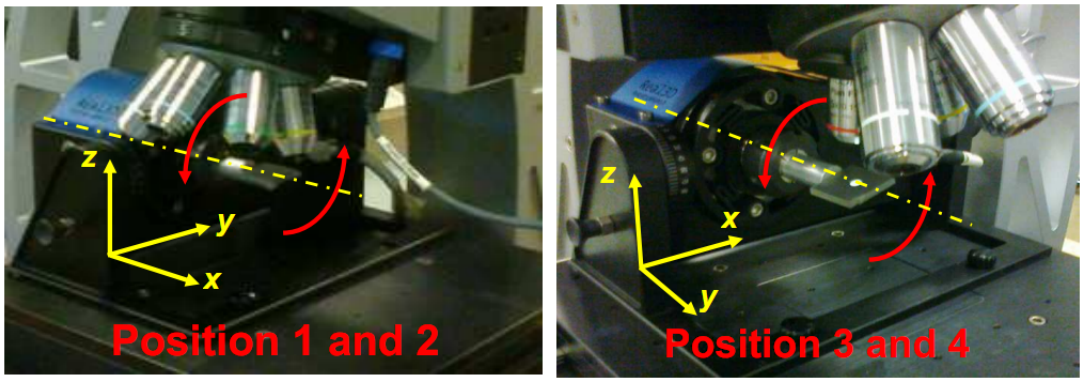

Figure 3.20: Setup for multi-position measurements.

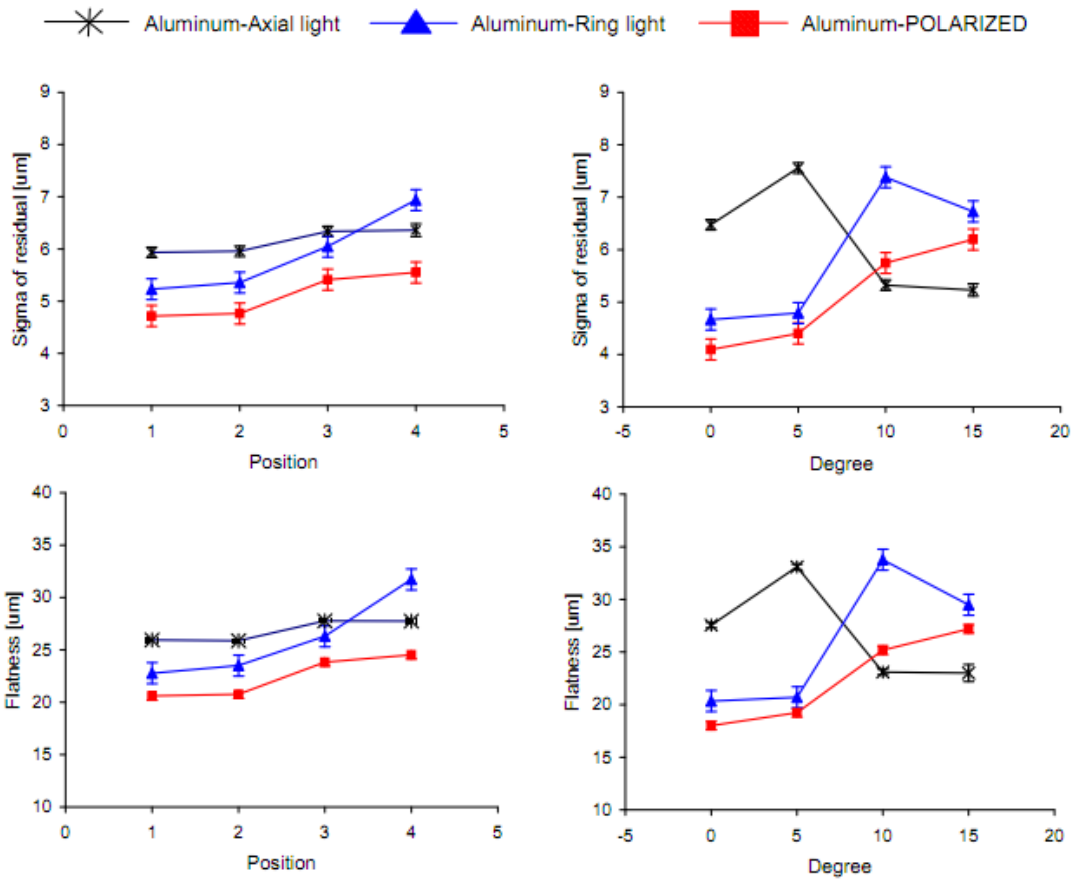

Figure 3.21: Influence of different illumination for aluminum plate in different position of measurements.

three illumination types are significantly different in their results, both for the sigma of residual and the flatness as shown in fig. 3.21 . This figure seperately presents the mean plot for each positioning and degree orientation. Moreover, they are also significantly different by variation of position and orientation angle. At 0^0 and 5^0, polarized light gives the lowest sigma of residual while ring light gives the lowest of flatness. Axial light has the highest sigma of residual and flatness. For all the four positions, polarized light gives the lowest sigma of residual. For further analysis, fig. 3.22 and fig. 3.23 shows the mean and interaction plot for all the three combined factors (illumination type, position and degree of skewness), respectively. From these two figures, the levels of illumination are 1=axial light, 2=ring light and 3=polarized light. From the combined mean plot, it shows that for aluminum sample (which is categorized as specular), by using polarized

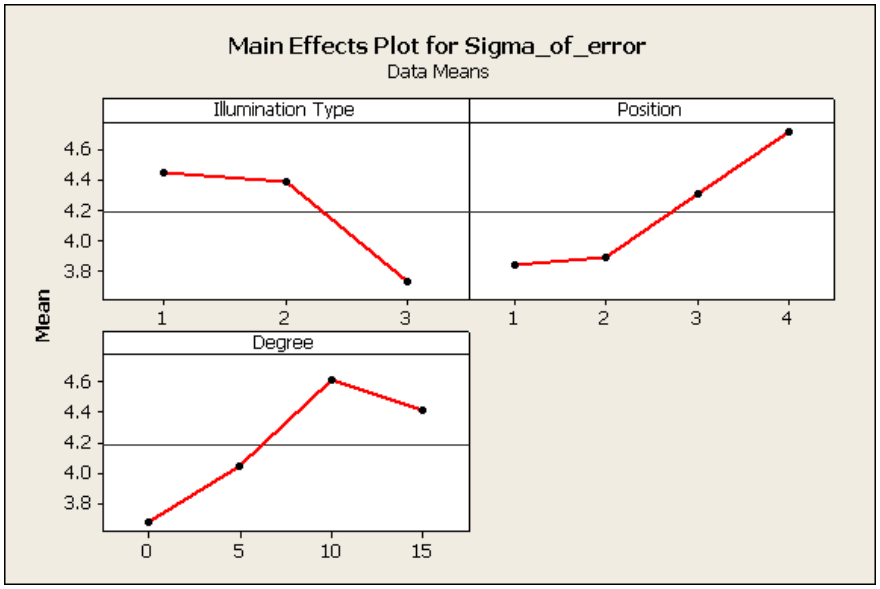

Figure 3.22: Mean plot for all the combined factors (Illumination type, position and degree of skewness).

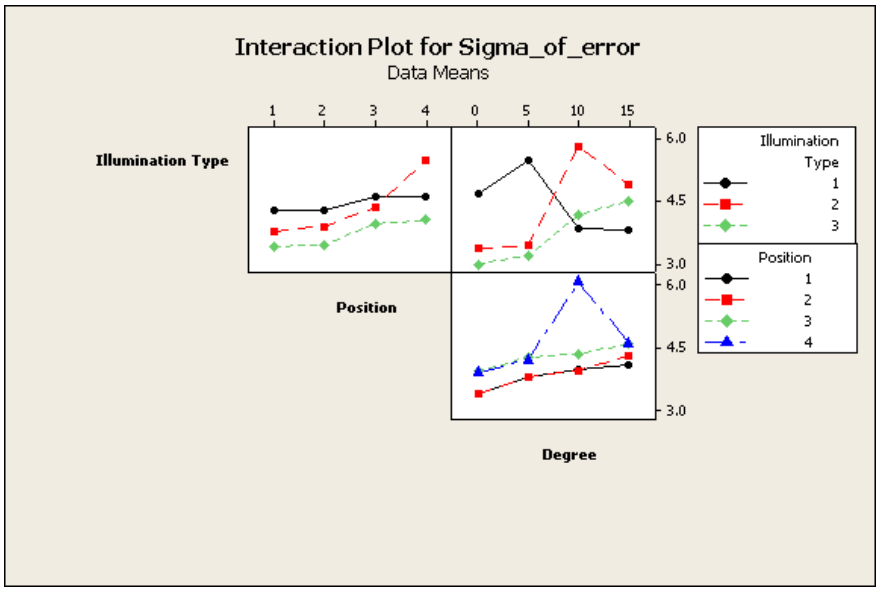

Figure 3.23: Interaction plot for all the combined factors (Illumination type, position and degree of skewness).

Factors	Difference	Statistical test
ring light to polarized (specular)	$-0.6\ \mu m$	significant
ring light to polarized (Lambert)	$+0.45\ \mu m$	significant

Table 3.5: Summary of different type of illumination.

No.	Material	Surface Type
1.	Aluminum	Specular
2.	Black-layer coated steel	Lambertian
3.	Stainless steel	Lambertian
4.	Steel	Specular
5.	Titanium	Lambertian
6.	Patterned Lambert+Specular composite	Lambertian+Specular

Table 3.6: Materials used and their classification.

light, the sigma of residual decrease around 0.8 μm and increases by around 0.7μm when the degree of skewness is increased. Moreover, There is a significant interaction between type of illumination and degree of skewness. Meanwhile, not significant interaction between illumination type-position and position-degree. In general, it seems that the increase of degree orientation, the sigma of residual and the flatness error also increase except for axial light which seems to decrease. As summary, the changes of sigma of residual from ring-light to polarized light for both Lambert (random injectioned-molded surface) and specular (aluminum) surface are depicted in table 3.5.

3.3.2.3 Influence of different level of surface steepness from different materials.

Different materials have different behavior of reflecting the incident light toward them back to the CCD sensor. Hence, it contributes to the variability of the results by different sample material. This study purposes to validate this hypothesis. There are six different materials used in this study, and they are listed in table 3.6 along with their surface type. Fig 3.18 shows the measurement results for all the six materials placed perpendicular to the axis of objective lens. The classification is based on the appearance of the surface from different angle view, either similar or depend on its directional.

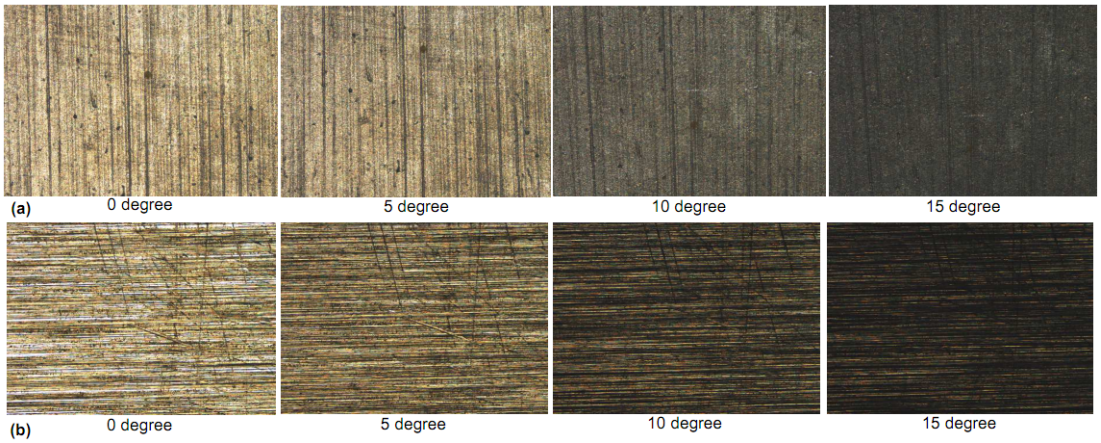

Figure 3.24: Measurement results from different orientation degree for (a) titanium (Lambertian) and (b) aluminum (Specular) with 5X lens.

These samples were placed on a cylinder rod. Then, the cylinder rod was mounted on the 3D rotation unit as shown in fig. 3.20. By this, four different positions and degree orientation can be obtained to study the effect of these variations. Each four locations were varied of $0^0, 5^0, 10^0$ and 15^0. Positions 1,2,3,4 were equal to the previous study as shown in fig. 3.20. 5X objective lens was used with default setting of lateral and vertical resolution. Acquisition results obtained from different degree orientations are depicted in fig. 3.24 for the case of aluminum and titanium. The exposure time (brightness) and contrast were adjusted accordingly to be able to capture good surface points. In one measurement cycle, 1000000 data points were obtained. There were five replications for each position and orientation so that 80 measurements for each material type have to be carried out. Results are shown in fig. 3.26 for aluminum, black-layer coated steel, stainless steel, steel, and titanium. Note that, for aluminum, it is again included for a whole view of the result comparison. In addition, this study is also carried out for a patterned Lambert and specular surface (see fig. 3.25). All results are compared by statistical ANOVA analyses.

From the results of six materials (fig. 3.26), they show that different positions and degree orientation significantly affect the measurement results. For patterned lambert and specular surface, since it has significant larger error, it is shown separately in fig. 3.27 For steel, the measurement results can be obtained only for up to 5^0 of steepness. As such, the plot only presents data up to this degree. In addition, the value of the

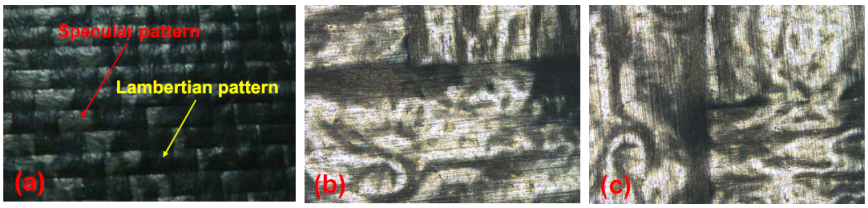

Figure 3.25: (a) Patterned Lambert+specular sample and acquisition result when rotation axis parallel to (b) x-direction and (c) y-direction.

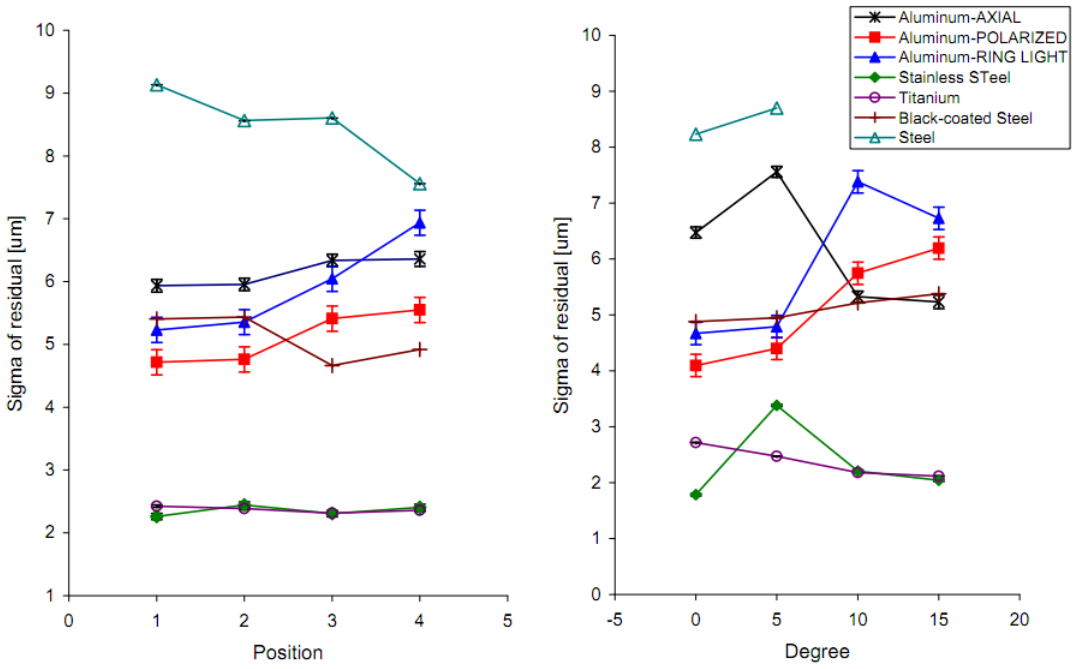

Figure 3.26: Influence of different position and orientation degree for different materials.

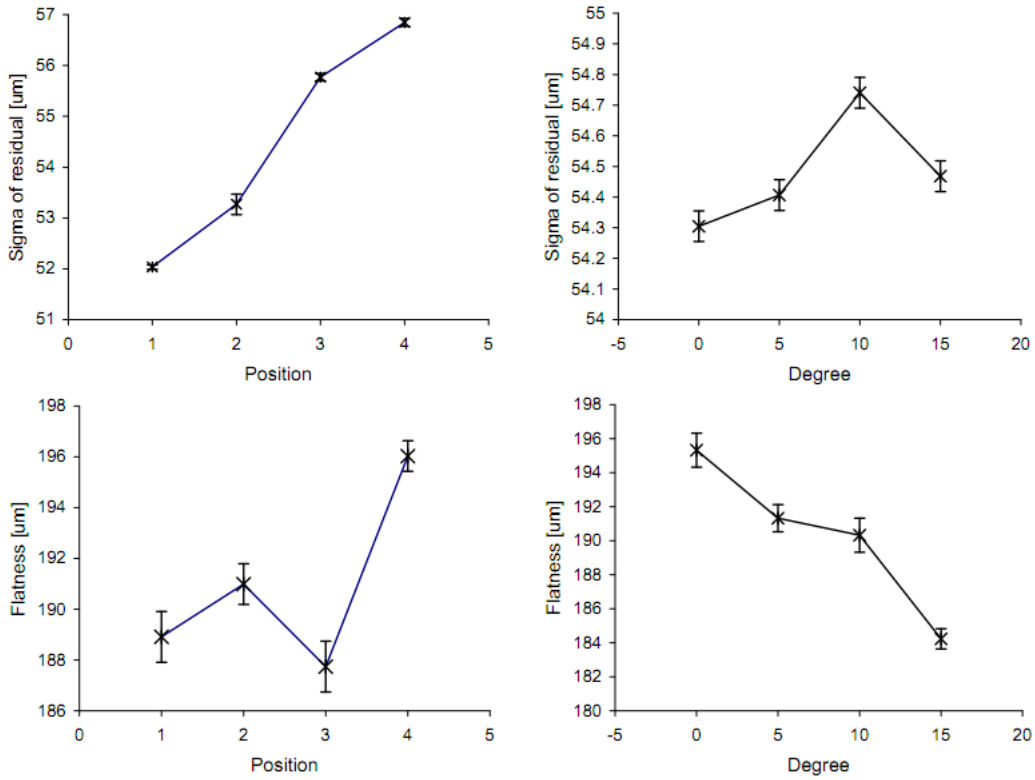

Figure 3.27: Influence of different position and orientation degree for Patterned Lambert and Specular surface.

Measurement Type	**Calibrated Flatness** $[\mu m]$	**Mean flatness at** 0^0 **orientation** $[\mu m]$	**Difference**
Aluminum (axial Light)	25.1	27.031	1.937
Stainless Steel (axial light)	4.77	8.082	3.312
Titanium (axial light)	4.1	12.034	7.934

Table 3.7: Comparison between the measured flatness and the calibrated value.

calculated sigma of residual can not be directly compared each other. The black-layer coated steel and steel are in a sheet form so that there is a possibility of deflection of these sheet during the measurement, thus increase the sigma of residual. Also for aluminum, it has higher calibrated flatness value compared to that of stainless steel and titanium. Hence, it has higher sigma of residual compared to these two materials. There are comparable results for stainless steel and titanium since both of them have similar calibrated flatness value. For this result, similar value of the sigma of residual for different positions can be observed. But, different results can be observed for these measurements with regard to different degree orientation. A linearly decreasing trend for sigma of residual is observed for titanium. A different situation occurs for the stainless steel. With this material, it seems to have similar sigma of error with respect to different orientation except for orientation at 5^0. In this orientation the value is significantly bigger compared to that one from the other degree orientation. Range of variation of the error for aluminum (axial light), stainless steel, and titanium are 5 μm, 2 μm and 2 μm, respectively. In general, it can be observed that the sigmas of residual of the three lambertian surfaces less vary compared to the specular one. It is coherent with the definition of lambertian surface in which the incident light is reflected equally to the whole direction instead of only a single direction as can be observed in the specular surface. For comparison to the calibrated flatness value, the resulted flatness error for aluminum, stainless steel, and titanium are presented in table 3.7 . From the table, there are difference for the measured flatness observed ranging from 1.9 μm to 7.9 μm, depending on the material types. In general, the range of sigma of residual for

material	range	Statistical test
Aluminum	2.5 μm	significant
Stainless steel	2 μm	significant
Titanium	1 μm	significant

Table 3.8: Summary of range of sigma of residual with respect to different placement and tilted angle.

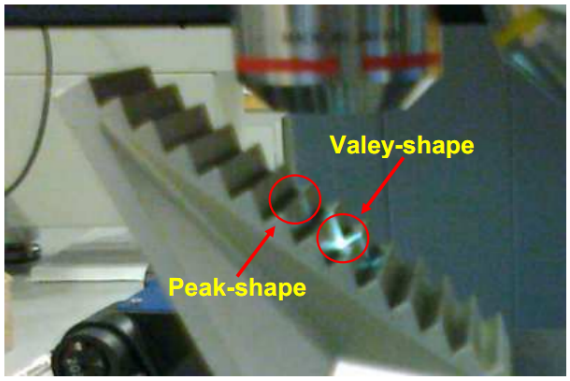

Figure 3.28: Peak and valley edge measurement.

aluminum, stainless steel and titanium surface are shown in table 3.8.

3.3.2.4 Influence of edge measurement (peak-valley shape).

[De Chiffre and Hansen [1995]] observed problem of measuring convex (peak shape) and concave (valley shape) edge since it affects the measurement results and contribute to the measurement uncertainty. Possible reason is because of inter-reflection effect from the surrounding wall in valley-shape measurement as reported by [Phong [1975]] and [Forsyth and Zisserman [1989]]. Based on this, the comparison study of the effect of measured shape (peak or valley shape) to the sigma of residual was carried out. This experiment used part of a fixture support which has saw-teeth profile. The sigma is calculated as the distance of obtained points to the fitted line, as ideal geometry. The part is made of steel and coated with grey-color layer, which makes the surface as lambertian surface. Fig. 3.28 shows the part and the measurement process. The peak and valley-shape edge measurement were obtained by measurement of the saw-teeth profile. The measurement was carried out with 5x objective lens and polarized axial-illumination to be able to capture the points. Replication was carried out 50

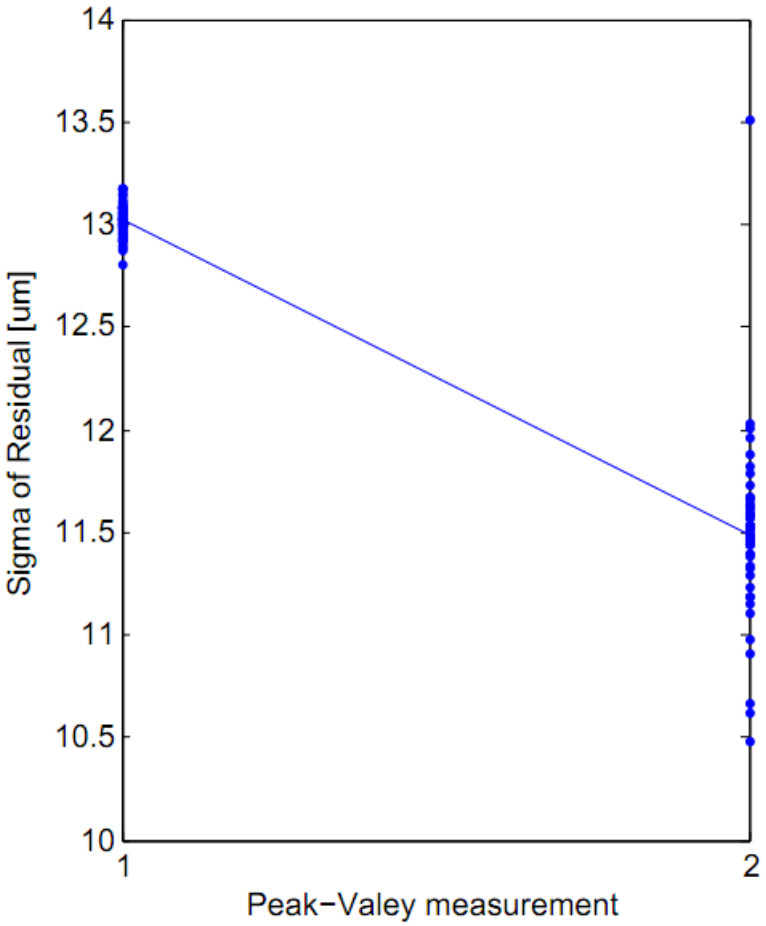

Figure 3.29: Influence of concave (valley): level 1 and convex (peak): level 2 measurement.

times for each measurement type. Around ≈30000 points and ≈45000 points were obtained for valley and peak edge measurement, respectively. Subsequently, a line is fitted from the obtained points to calculate the sigma of residual. Results of this influence study are depicted in fig. 3.29. The horizontal axis has two level, which are level 1 for valley-edge measurement and level 2 for peak-edge measurement. From the statistical comparison, it shows that the sigma of residuals is significantly different in both measurement conditions, and peak-edge measurement has lower sigma of residual. Also from the number of points obtained, peak-edge measurement can capture more points compared to the valley-edge one. Obtaining point on a valley shape can be more difficult, it can be caused due to the inter-reflection effect of the illumination light,

Factors	sigma of residual from a fitted line
Peak	13 μm
Valey	11.5 μm

Table 3.9: Summary of different type of illumination.

Measurement type	Sigma (σ)[μm]			Form error[μm]	
	x-direction	y-direction	z-direction	Mean	Sigma (σ)
Single Image	1.2	1.9	17.7	13.27	2.39
Multiple images	0.54	0.76	8.7	13.5	1.45

Table 3.10: Repeatability of a single point.

reflected to the CCD image sensor of the FVM instrument. Table 3.9 shows the mean of the sigma of the residual when measuring peak and valey surface.

3.3.2.5 Single point uncertainty (stitching/no-stitching).

This study is to observe the variability of a single point by measurement of sphere made of steel. The point is center point of a fitted sphere. There are two types of sphere measurement for this study. The first type is sphere measurement from only single image and the second one is from multiple images to involve stage movement and stitching process. Number of repetition for each type of measurement is 50 times. For sphere from single image measurement, total points obtained were ≈750000. The other measurement obtained ≈3250000 points. As mentioned in [ISO10360-8 [2013]], only 25 points were selected from all the points for the sphere fitting procedure. Table 3.10 provides detail of the results. One can observe that the repeatability of the center point obtained from stitched sphere is higher than the one from single image only. Hence, by stitching procedure there is an averaging effect to the obtained points to suppress the random noise. The result from the stitched points has around 50% higher repeatability. Table 3.11 presents the difference of sigma of residual from points with and without stitching.

Factors	Difference	Statistical test
without stitching to with stitching	$-0.9\ \mu m$	significant

Table 3.11: Summary of different type of illumination.

3.3.2.6 Long measurement (drift) behavior.

The behavior of the instrument in a long measurement is important to be investigated. It is worth to study drift behavior of the instrument due to thermal-related issue. To study this phenomenon, two types of measurement were conducted. The first one is a calibrated titanium plate measurement while steel sphere measurement was carried out for the second one. The measurement of plate did not involve stitching error as only a single image was used in the study. Meanwhile, the study by sphere measurement involved stitching operation from four images. Multiple image fields were used to obtain the sphere surface. A G10 grade ball bearing was used for the sphere measurement. ISO standard [ISO3290-1 [2008]] contains the details specification of this ball bearing. Based on the standard, this ball bearing has 0.25 μm of diameter and form deviation and roughness Ra of 0.02 μm. The measurement used 5x magnification lens with default lateral and vertical resolution for this lens.

For the plate measurement, there were 30 continuous measurements with total time span around 5 hours. Continuous measurement means that the instrument automatically measured the surface in a repetitive way without any intervention to the instrument. This can be realized by developing a measurement script and run by the FVM instrument. Around 1000000 points were involved in data processing for each measurement cycle. There are three parameters to be calculated from the measurements. They are sigma of residual, flatness, and distance to reference plane. Sigma of residual represents the measurement noise (random noise) behavior in long term measurement. Behavior of every single point can be observed from the flatness value. For systematic error, distance to reference plane was calculated to represent the measurement systematic error behavior. Detail illustration of distance to reference plane is shown in 3.30. In this figure, the reference plane P was selected as the first fitted plane from the points obtained by the first measurement cycle. Then, the distance to reference plane is defined as distance of a point on a plane, which is the centroid from all the obtained points, to the reference plane P. Result of the thermal-related measurement behavior is

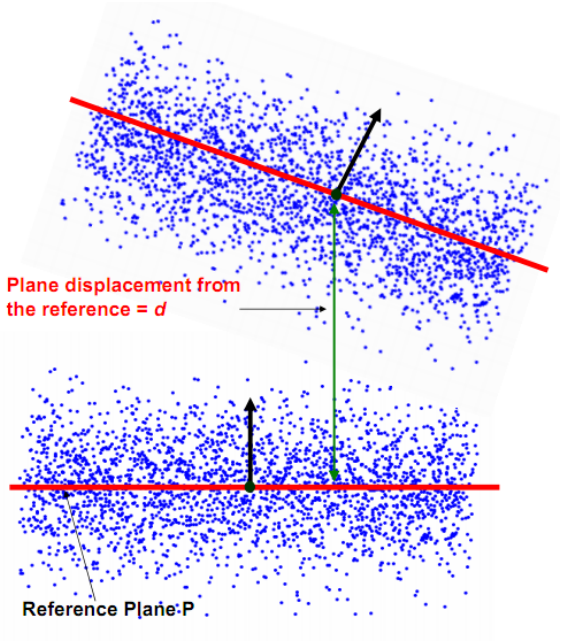

Figure 3.30: Illustration of distance to reference plane.

shown in 3.31. For single image measurement, without stitching and stage movement, we can observe that the random noise is stable in this period of time measurement. The range of the sigma of residual is 0.0067 μm within 95% confidence level (2σ). The results of the flatness calculation show a decreasing trend up to 10^{th} measurement sequence. It shows the flatness value become stable 100 minutes after the instrument run. Similar behavior is also observed for laser scanner even though in this instrument, the effect is not as significant as the laser scanner has [Gestel et al. [2009]]. The flatness interval (2σ) for the first 100 minutes measurement is 1.25 μm. Meanwhile, after the period of 100 minutes the interval becomes 0.62 μm. Systematic error, represented as distance to reference plane, is stable up to the 19th measurement which correspond to the period of around the first 190 minutes. Note that, the value is shifted one position to the left, since the 1st sequence is not included as the reference plane. Starting from 20^{th} measurement, juggling phenomenon of the results can be observed. Confidence interval (2) for the distance to reference plane value for the first 190 minutes (stable behavior) is 0.16 μm, meanwhile after this period, the interval becomes 2.72 μm.

Results of long-term sphere measurement by sphere involving stage movement and stitching are presented in 3.32. The measurement of the sphere surface involved four

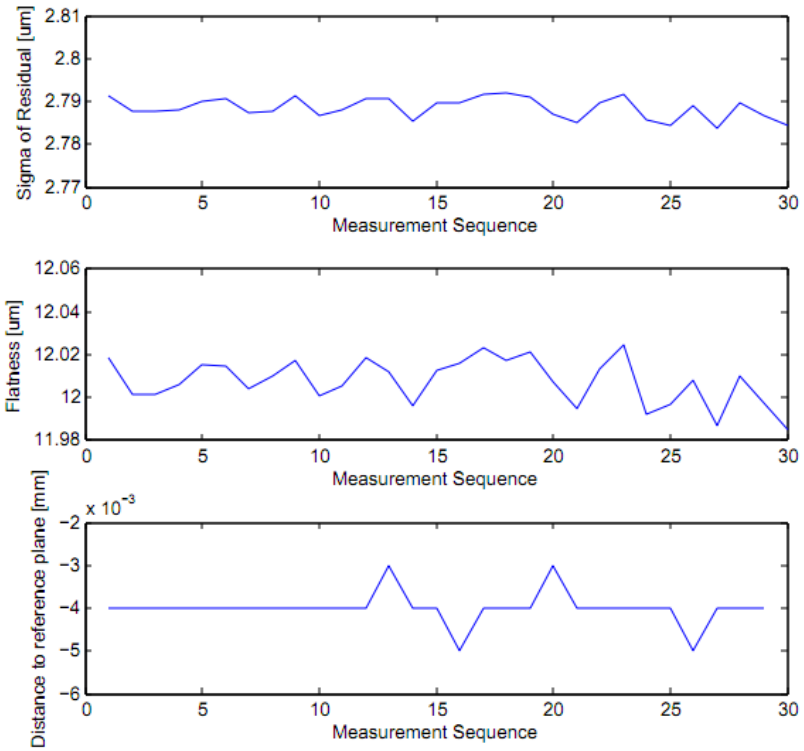

Figure 3.31: Thermal drift behavior (**without** stitching) by plane measurement.

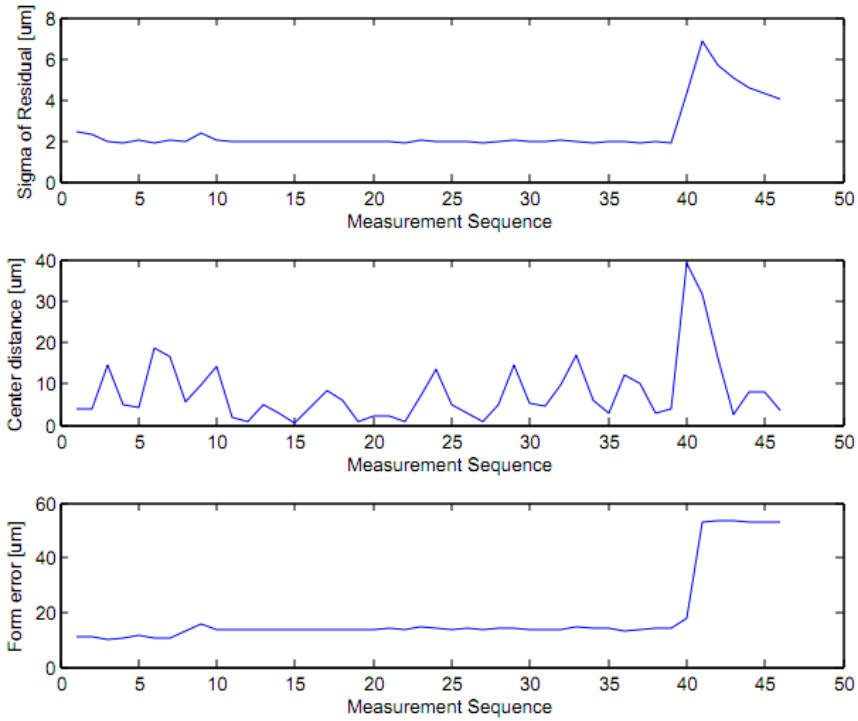

Figure 3.32: Thermal drift behavior (**with** stitching) by sphere measurement.

images and then they are stitched together into single point cloud. The measurement was run continuously for 46 measurements with total time span of around 6 hours. Total points obtained from a measurement cycle are ≈3000000 points. Instead, not all points were used for the sphere fitting. Only selected 25 points were involved in the sphere fitting. The selection of 25 points from total points obtained is based on [ISO10360-8 [2013]]. Parameters calculated from the measurement after sphere fitting are sigma of residual, distance of two consecutive centers, and sphere form error. Similar to the plate measurement, sigma of residual can present the random noise behavior. Sphere form error to describe every single point movement. The systematic error is represented by distance of the two consecutive centers. Different behavior can be observed from the result by measuring sphere. For all the three parameters, they show a similar behavior. Stable results are observed for the first 40 measurements, which correspond to the first 320 minutes of measurement. After this period, the measurement results are shifted and the variation increase. The shifting of the means for these parameters from the period before to after 320 minutes of measurement are about 3 μm for sigma of error and 40 μm for form error. While for the shifting between the mean of the center distance before 320 minutes measurement period and the center distance of the last measurement of this period and the first measurement after the period is about 25 μm.

3.3.2.7 Influence of primary user-defined measurement parameters (Instrument's parameters).

The previous sub-section studied the factors which can not be controlled by the user or operator of the instrument. Instead, this sub-section studies controllable factors which can be set by the user to get optimal captured points. This study is important to investigate the effects of the four basic parameters which should be defined by the user before they start the measurement. Moreover, these basic parameters are also relevant to other optical instrument. The four parameters are lateral resolution, vertical resolution, exposure time (brightness), and contrast. For this investigation, plate titanium was used since from the previous study, it gives a good result and is classified as a lambertian surface. Table 3.12 presents details for the study of lateral and vertical resolution and the levels correspond to the level show in fig. 3.33. The details for study of exposure time and contrast are presented in table 3.13. The levels shown in fig. 3.33

Type	**Level**	**Resolution**	**Lateral points distance** $[\mu m]$	**Number of obtained points**	**Replication**
Lateral	1	Highest	1.75	≈2000000	25
Lateral	2	Medium (default)	2.62	≈1000000	25
Lateral	3	Medium to low	4.66	≈300000	25
Lateral	4	Lowest	7.82	≈100000	25
Vertical	1	Highest	2.62	≈1000000	25
Vertical	2	Medium (default)	2.62	≈1000000	25
Vertical	3	Medium to low	2.62	≈1000000	25
Vertical	4	Lowest	2.62	≈1000000	25

Table 3.12: detail of lateral and vertical resolution influence study.

Type	**Level**	**Classification**	**Value Set**	**Lateral points distance** $[\mu m]$	**Number of obtained points**	**Replication**
Exposure time	1	Highest	339 μs	2.62	≈1000000	25
Exposure time	2	Medium (default)	240 μs	2.62	≈1000000	25
Exposure time	3	Lowest	110 μs	2.62	≈ 1000000	25
Contrast	1	Highest	1.5	2.62	1000000	25
Contrast	2	Medium (default)	1	2.62	≈1000000	25
Contrast	3	Lowest	0.5	2.62	≈1000000	25

Table 3.13: detail of brightness and contrast influence study.

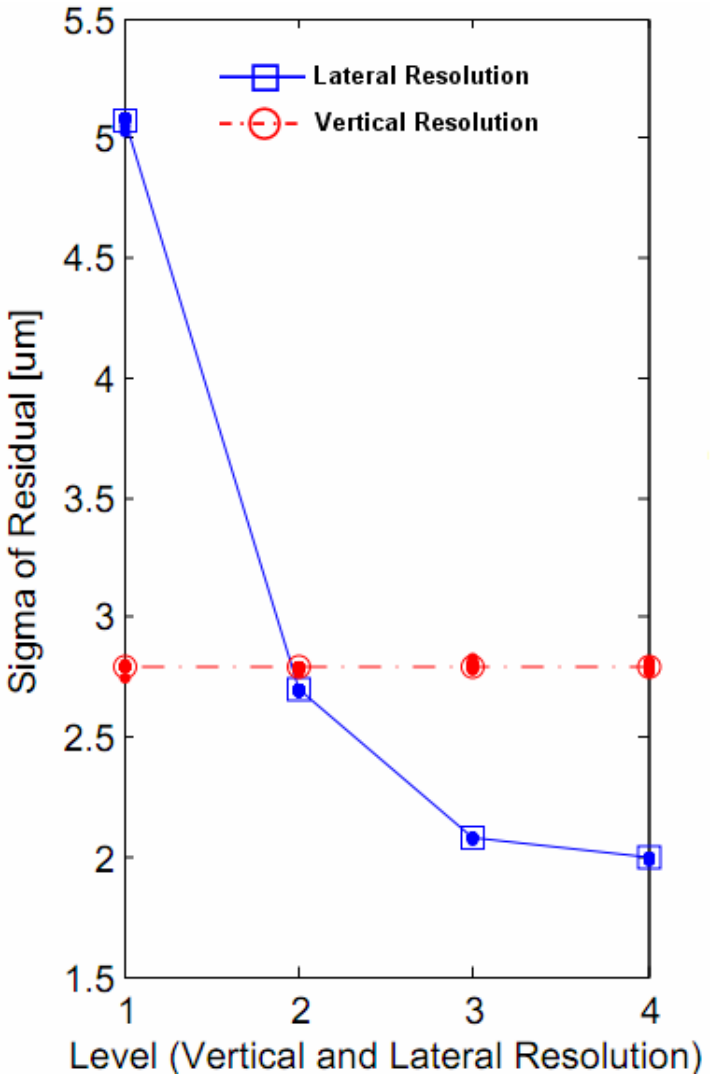

Figure 3.33: Influence of different vertical and lateral resolution.

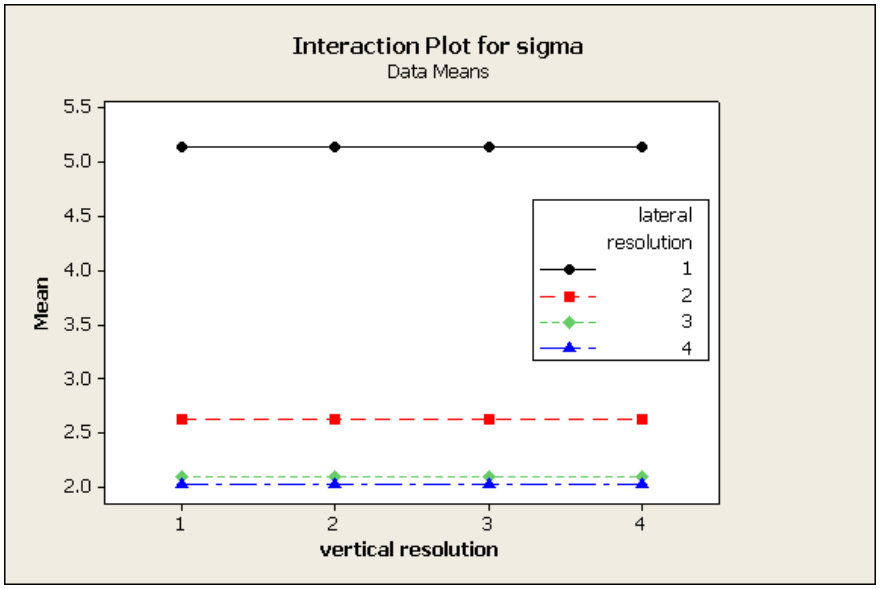

Figure 3.34: Interaction plot between vertical and lateral resolution.

are explained in this table. All measurements were repeated 25 times. 5X objective lens and axial illumination were used. Statistical analyses have been used for the influence study of these parameters to the measurement results. It is worth to note that the resolution medium (level 2) is the default parameter from the instrument software for the chosen lens. Also for the brightness and contrast, level 2 (classification medium) is the default one.

First part is the study of lateral and vertical resolution influence to the measurement results. The range of level for both lateral and vertical resolution is based on the resolution limit of 5x magnification of the objective lens. The results of this study are presented in fig. 3.33 and are statistically analyzed by ANOVA test. One can observed that there is a clear different behavior by varying the lateral and vertical resolution to the sigma of residual and flatness error results. The decrease of the sigma of residual by lowering the lateral resolution is observed. Instead, this situation does not happen to the different vertical resolution. The sigma or residuals are statistically equal after varying the vertical resolution. Interaction plot between lateral and vertical resolution is depicted in fig. 3.34. From this figure, there is no significant interaction between lateral and vertical resolution and it supports the conclusion of the reduce of sigma of error by lowering lateral resolution.

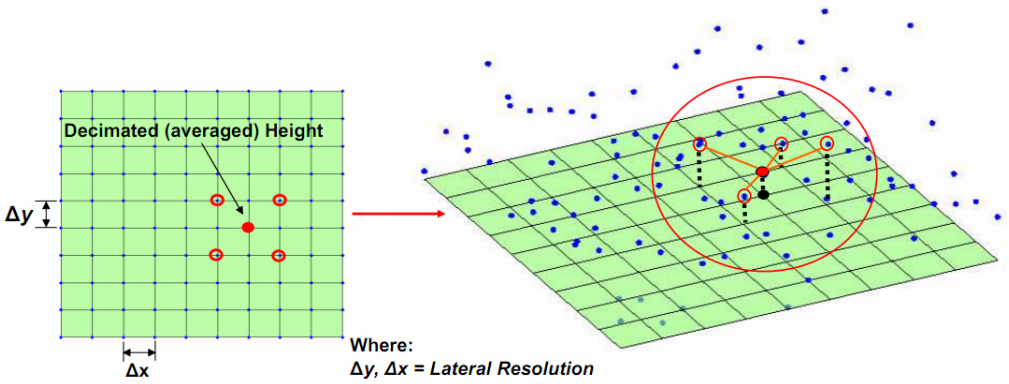

Figure 3.35: Illustration of lateral resolution.

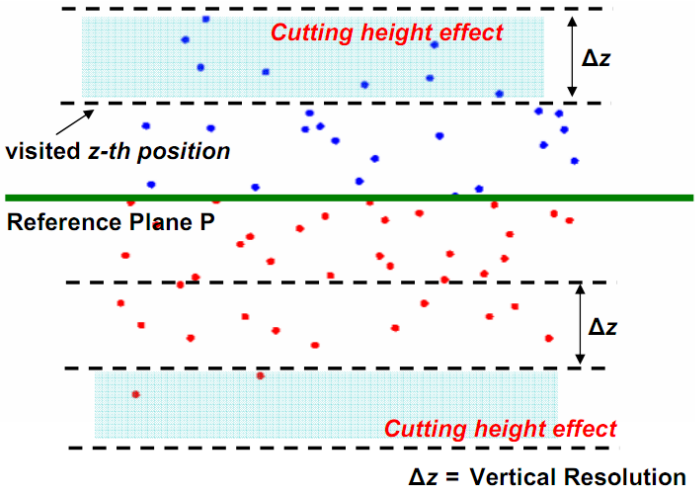

Figure 3.36: Illustration of vertical resolution.

There is a difference in the way of single point detection between the variation of lateral and vertical resolution. In lateral resolution, by lowering it (larger lateral distance), the points between the two distances of the higher resolution will be replaced by a single point which is obtained by averaging of these points. This effect is illustrated in fig. 3.35. In this figure, the new substitute point is averaged from its neighbor points depending on the lateral distance set. Hence, by averaging effect, the noise of the instrument is suppressed. As such, the sigma of residual and flatness error are reduced when the lateral resolution is decreased. Different way of point detection is observed in vertical resolution as depicted in fig. 3.36. There is no averaging effect by lowering the

vertical resolution. As shown in the figure, instead of averaging effect, a cutting effect is observed. In this effect, a surface point will be skipped, thus undetected, if it is lie between the two vertical distances. Hence, the level of the noise will be identical with varying vertical resolution as long as the lateral resolution is set equally. These results can be applied in practice for geometric measurement, especially, form measurement. As stated by Evans [Evans [2008]] and Giusca et al [Giusca et al. [2014]] that optical instrument has considerably larger noise compared to the contact one. Moreover, form measurement is very sensitive to noise. Hence, this noise should be compensated or otherwise included in the uncertainty estimation. Subsequently, for form measurement, a larger lateral resolution is preferable to suppress the measurement noise and the value depends on the material to be measured.

To analyze further regarding the effect of lateral resolution, various levels of decimations were carried out to observe the decrement of flatness error with the increase of the deviation levels. The decimations were applied to the obtained points of a measurement cycle of calibrated titanium plate. There are two types of the obtained points: type 1 which is the points obtained from a measurement with default lateral resolution of the instrument and type 2 which is obtained with the lowest lateral resolution. There are six level of decimation: 1X, 2X, 4X, 8X, 16X, and 32X. Decimation value tells that a point is calculated from average of points within a grid of $n_{dec} \times n_{dec}$. Details of the decimation levels and its corresponding flatness and lateral point distance are presented in table 3.14. Fig. 3.37 shows that, even after 32X decimation (which is the maximum value for decimation), the flatness value is still higher than the calibrated value as much as 0.7 μm. There are some possible explanations of higher result in geometric deviation values. Firstly, since the points measured by tactile CMM are much less dense compared to the result by optical instrument, some high-frequency surfaces are not captured, leading to underestimation of the flatness. Secondly, intrinsic filtering effect of the sphere of the CMM stylus reduces the magnitude of surface data so as the flatness value. Finally, bias contribution from the instrument contributes to the higher flatness value.

The next two studies for the basic user-defined parameters are exposure time (brightness) and contrast. The selected range for exposure time and contrast were based on the range in which a good surface data points can be obtain. Fig. 3.38 presents the results of these influence studies. The levels of the varied variable (hori-

Type	**Decimation**	**No. of points**	**Lateral point distance** $[\mu m]$	**flatness** $[\mu m]$
1	1X	905268	2.61	31.82798576
	2X	226044	5.21	29.22729111
	4X	56511	10.43	24.76902962
	8X	14008	20.93	20.54240418
	16X	3468	41.87	13.15038395
	32X	850	83.73	6.732644558
2	1X	100464	7.82	17.52181435
	2X	25116	15.64	13.88383389
	4X	6279	31.28	11.66873646
	8X	1530	63.26	9.627437592
	16X	374	129.41	7.262669086
	32X	88	228.81	4.821956158

Type1: Default lateral resolution with 5X lens

Type2: Lowest lateral resolution with 5X lens

Table 3.14: Flatness value with regards to level of decimation.

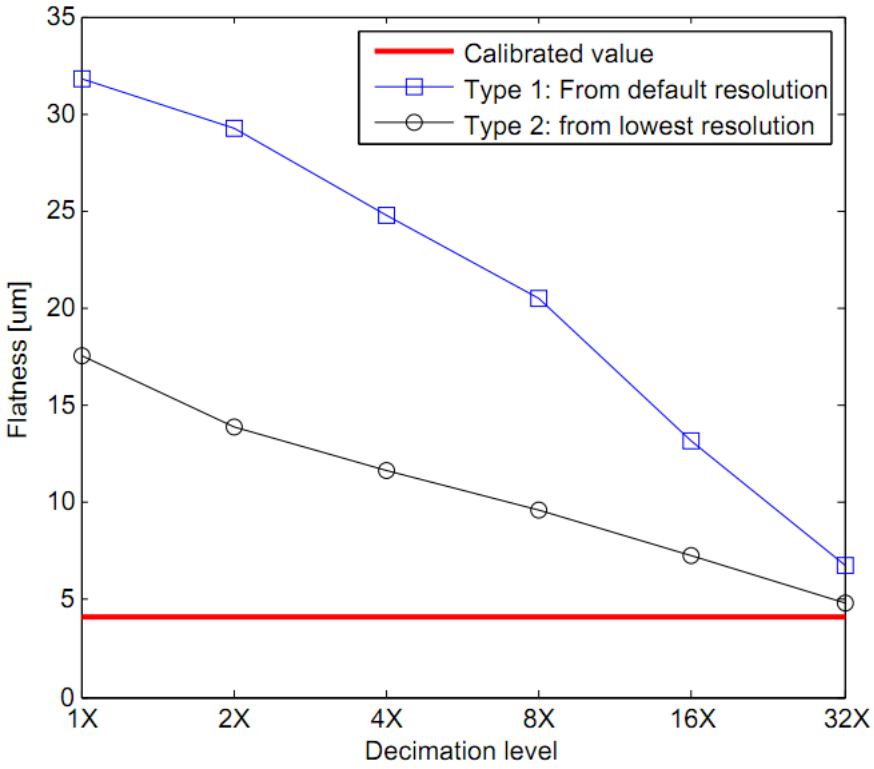

Figure 3.37: Relation between flatness value and level of decimation.

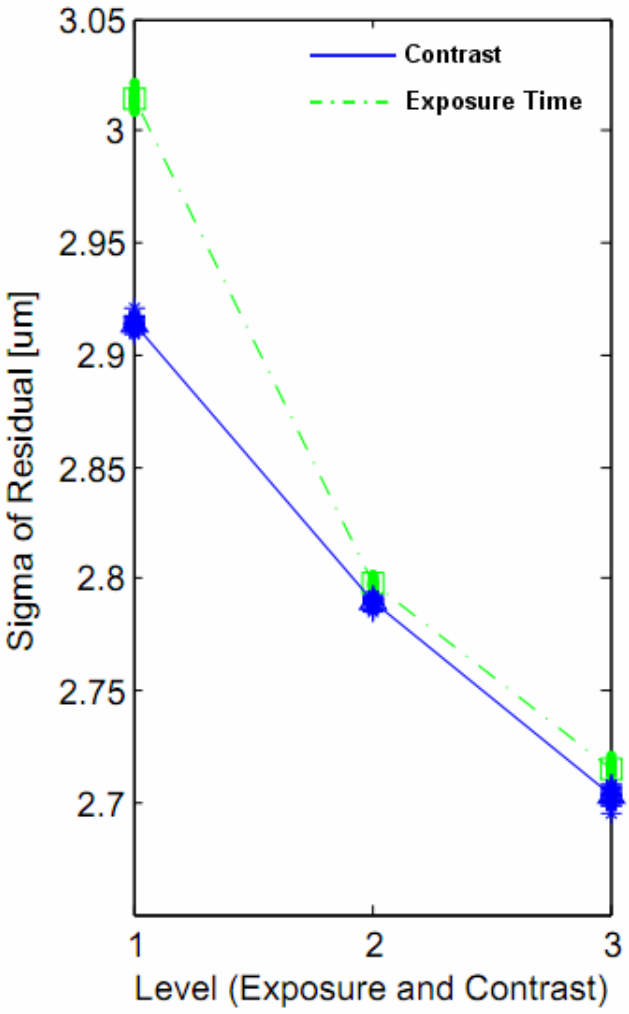

Figure 3.38: Influence of different level of exposure time and contrast.

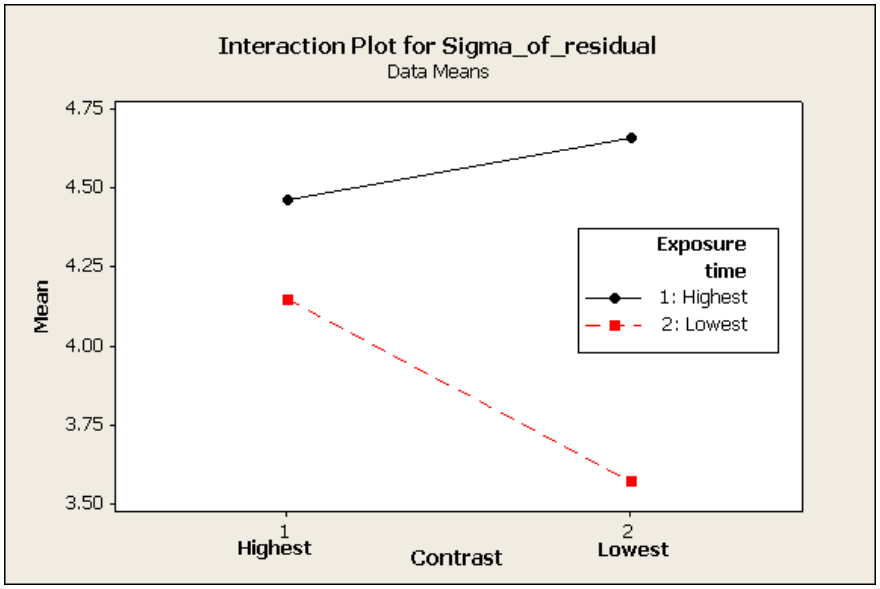

Figure 3.39: Interaction plot between vertical and lateral resolution.

zontal axes) are set from the highest to the lowest. Level 2 of the exposure time, which is medium, is a default value in the sense that this value was obtained from the software recommendation after running the automatic illumination procedure. Meanwhile, the default value of contrast is 1 (level 2). For the sigma of residual, it shows a decreasing trend when both the exposure time and contrast are set to lower value. From the statistical analyses of ANOVA, all these three different levels have significant effect to the measurement results. Moreover, interaction plot between exposure time and contrast is shown in fig. 3.39. from this figure and from ANOVA test, while there is no significant interaction between lateral and vertical resolution, a significant interaction between exposure time and contrast is observed. The lowest sigma of residual can be obtained when both exposure time and contrast are set at the lowest value. Finally, to summarize the influence of user defined parameters, table 3.15 shows the affect of these parameters.

3.3.3 Summary

From this study, summary can be derived with regard to measurement of optical instrument, especially instrument based on focus-variation method. The summary could be a useful consideration for geometric measurement using focus-variation based optical

Factors	Difference	Statistical test
High to low lateral resolution	$-3\ \mu m$	significant
High to low vertical resolution	$-0.01\ \mu m$	not-significant
High to low exposure time	$-0.3\ \mu m$	significant
High to low contrast	$-0.2\ \mu m$	significant

Table 3.15: Summary of different type of illumination.

instrument. Fig. 3.40 summarizes the main result from uncertainty characterization.

1. Measurement with optical instrument is more complex than that of the contact one, since it is more sensitive to many factors, especially illumination and material type which are not found in the contact instrument. Hence, measurement results obtained by this method should be analyzed further before making conclusions from them.

2. A priori knowledge of the sample, especially the type of the surface, will be a great advantage. Especially for focus-variation based instrument, surface roughness influences the effectiveness of measurement. To ensure measurement repeatability, not only all parameters e.g. illumination type have to be identical, but also the positioning of the sample should be hold identical for all measurement repetition. Different sample orientations result in significantly different measurement results. For a specular surface, illumination utilizing axial light is not recommended. Hence, the measurement for a certain type of measurement should be very specific for a certain condition, both for the one related to the measurement parameters and material-related aspect.

3. Using a higher magnification lens, it will reduce the random noise (error). Instead, trade-off should be made between the reduced random noise and the increase of measurement time as well as accessibility issue with regard to collision avoidance between objective nose-piece and work piece.

4. Optical measurement result is prone to outliers. To deal with these outliers, filtering of data before processing have to be applied, especially if the measurement involve a geometric characteristic verification as minimum-zone fitting to evaluate them is sensitive to outliers.

5. Lower lateral resolution and decimation procedure can be effective to suppress the random error and to remove or reduce outliers of form error measurement. Moreover, stitching procedure has an averaging effect to the data points. As a consequence, it reduces the random error.

No.	Instrument's parameters				Degree of tilted position				Lens Magnification (5X/10X)	Illumination Type			Stitching (with/without)	Shape of surface	Surface Type				Mean Sigma of residual [µm]	Section reference
	Lateral Res.	Vertical Res.	Exposure Time	Contrast	0^0 (flat)	5^0	10^0	15^0		Axial Light	Ring Light	Polarized			Specular Aluminum	Lambert Polymer	Lambert Titanium	Lambert other		
1	3.51 µm	2.51 µm	240 µs	1	●				5X	●			without	Flat			●		5.2	3.3.2.7
2	7.82 µm	2.51 µm	240 µs	1	●				5X	●			without	Flat			●		2.6	
3	14 µm	2.51 µm	240 µs	1	●				5X	●			without	Flat			●		1.9	
4	23.48 µm	2.51 µm	240 µs	1	●				5X	●			without	Flat			●		1.4	
5	7.82 µm	0.4 µm	240 µs	1	●				5X	●			without	Flat			●		2.75	
6	7.82 µm	2.51 µm	240 µs	1	●				5X	●			without	Flat			●		2.76	
7	7.82 µm	12.4 µm	240 µs	1	●				5X	●			without	Flat			●		2.75	
8	7.82 µm	23.09 µm	240 µs	1	●				5X	●			without	Flat			●		2.76	
9	7.82 µm	0.4 µm	339 µs	1	●				5X	●			without	Flat			●		3.02	
10	7.82 µm	0.4 µm	240 µs	1	●				5X	●			without	Flat			●		2.79	
11	7.82 µm	0.4 µm	110 µs	1	●				5X	●			without	Flat			●		2.73	
12	7.82 µm	0.4 µm	240 µs	1.5	●				5X	●			without	Flat			●		2.92	
13	7.82 µm	0.4 µm	240 µs	1	●				5X	●			without	Flat			●		2.78	
14	7.82 µm	0.4 µm	240 µs	0.5	●				5X	●			without	Flat			●		2.7	
15	7.82 µm	0.4 µm	11.7 ms	0.9	●				5X	●			without	Flat		●			5.2	3.3.2.1
16	3.91 µm	0.1 µm	412 µs	1	●				10X	●			without	Flat		●			3.75	
17	7.82 µm	0.4 µm	167.5 ms	0.9	●				5X		●		without	Flat				●	3.25	3.3.2.2
18	7.82 µm	0.4 µm	383 ms	1.18	●				5X			●	without	Flat				●	3.7	
19	7.82 µm	0.4 µm	114.4 µs	1.33	●				5X		●		without	Flat	●				4.4	
20	7.82 µm	0.4 µm	114.4 µs	1.33	●				5X			●	without	Flat	●				3.8	
21	7.82 µm	0.4 µm	114.4 µs	1.33	●				5X	●			without	Flat	●				6.5	3.3.2.3
22	7.82 µm	0.4 µm	114.4 µs	1.33		●			5X	●			without	Flat	●				7.5	
23	7.82 µm	0.4 µm	114.4 µs	1.33			●		5X	●			without	Flat	●				5.2	
24	7.82 µm	0.4 µm	114.4 µs	1.33				●	5X	●			without	Flat	●				5.1	
25	7.82 µm	0.4 µm	14.21ms	1.11	●				5X		●		without	Flat	●				4.5	
26	7.82 µm	0.4 µm	14.21ms	1.11		●			5X		●		without	Flat	●				4.6	
27	7.82 µm	0.4 µm	14.21ms	1.11			●		5X		●		without	Flat	●				7.3	
28	7.82 µm	0.4 µm	14.21ms	1.11				●	5X		●		without	Flat	●				6.9	
29	7.82 µm	0.4 µm	25.2 ms	0.92	●				5X			●	without	Flat	●				4	
30	7.82 µm	0.4 µm	25.2 ms	0.92		●			5X			●	without	Flat	●				4.2	
31	7.82 µm	0.4 µm	25.2 ms	0.92			●		5X			●	without	Flat	●				5.5	
32	7.82 µm	0.4 µm	25.2 ms	0.92				●	5X			●	without	Flat	●				6	
33	7.82 µm	0.4 µm	224 µs	1	●				5X	●			without	Flat			●		2.9	
34	7.82 µm	0.4 µm	224 µs	1		●			5X	●			without	Flat			●		2.8	
35	7.82 µm	0.4 µm	224 µs	1			●		5X	●			without	Flat			●		2.7	
36	7.82 µm	0.4 µm	224 µs	1				●	5X	●			without	Flat			●		2.6	
37	7.82 µm	0.4 µm	60. 3 ms	1.78	●				5X	●			without	Peak				●	13	3.3.2.4
38	7.82 µm	0.4 µm	30. 62 ms	1.78	●				5X	●			without	Valey				●	11.5	
39	7.82 µm	0.4 µm	1.45 ms	1	●				5X	●			with	Sphere				●	1.45	3.3.2.5
40	7.82 µm	0.4 µm	1.45 ms	1	●				5X	●			without	Sphere				●	2.39	

Figure 3.40: Summary of main results from uncertainty characterization study.

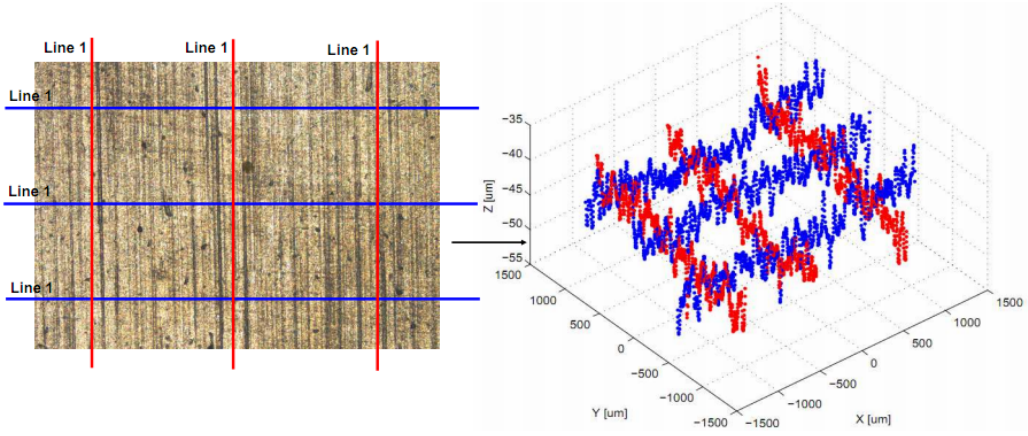

Figure 3.41: Points selection for variogram parameter determination.

3.4 Identification of variogram model

A variogram model should be selected to be used by the error simulator. From the result of uncertainty characterization study, different materials have their own error bahaviour. Hence, a variogram model has to be identified for each type of material. To select the variogram model and value of parameters sill (s), nugget (n), and range (r), experiment to obtain points from cross-section of calibrated plate of aluminum, stainless steel, and titanium measurement were carried out. Three cross-sections of the measurement data points both horizontally and vertically were taken as shown in fig. 3.41. From each cross-section, the semi-variogram was calculated based on eq. 3.14. This procedure is shown in fig 3.42. Subsequently, the parameters s, n, and r can be determined from the first section when the plot of semi-variogram starts to flatten from increasing trend as shown in fig. 3.43. By this figure, the behavior of data correlation will become clear.

Results of semi-variogram plot to determine the variogram parameters are presented in fig. 3.44 and 3.45 for horizontal and vertical direction, respectively. In each figure, there are three types of data plots. They are the semi-variogram plot for each line 1,2 and 3 as depicted in fig. 3.41(left). Hence, the variogram parameters for aluminum, stainless steel, and titanium can be estimated. The procedure to estimate the suitable variogram model and their parameters is by fitting least square curve to the experimental variogram data. The variogram fitting is carried for all the three variogram

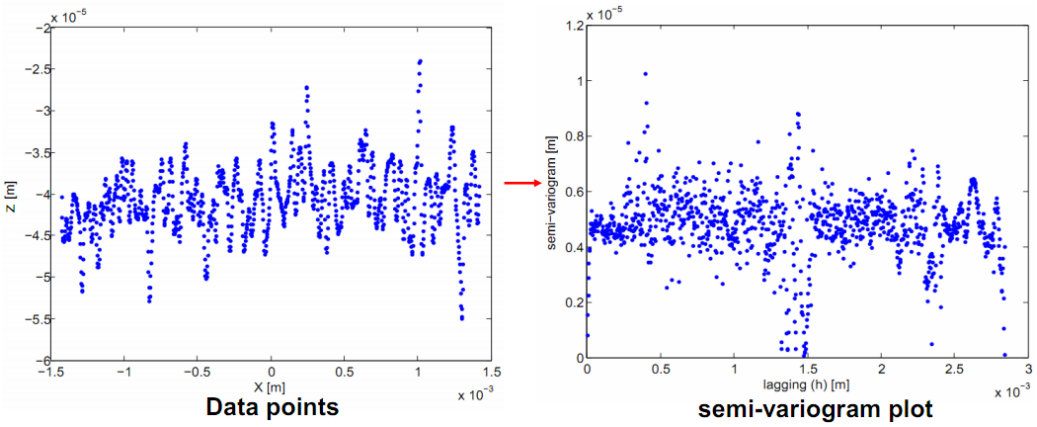

Figure 3.42: Semi-variogram determination from the measured points.

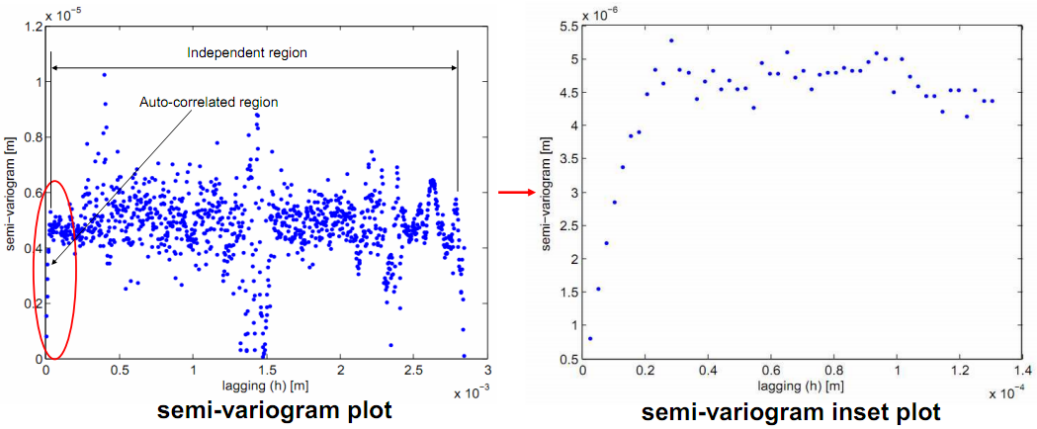

Figure 3.43: The first section of semi-variogram plot to determine the auto-correlated area (the first 50 lags).

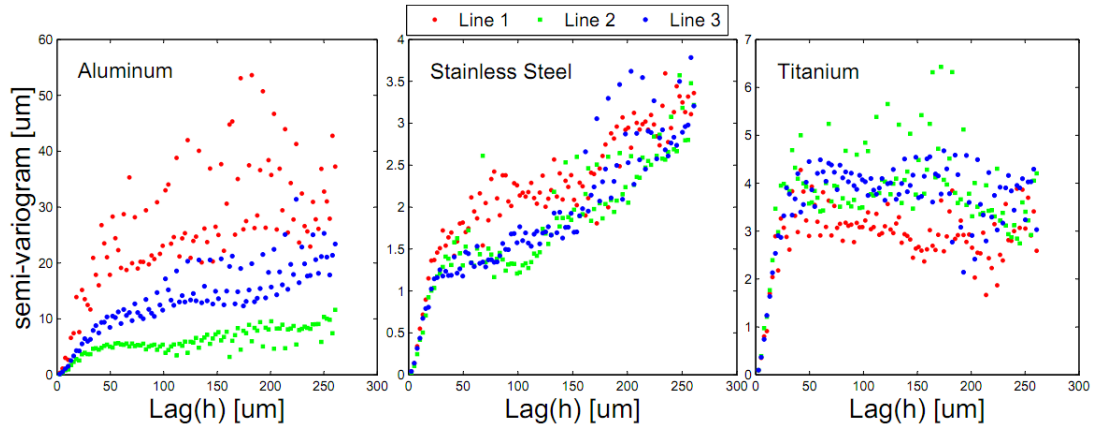

Figure 3.44: Semi-variogram from horizontally cross-sectioned points (the first 100 lags points = 250 μm).

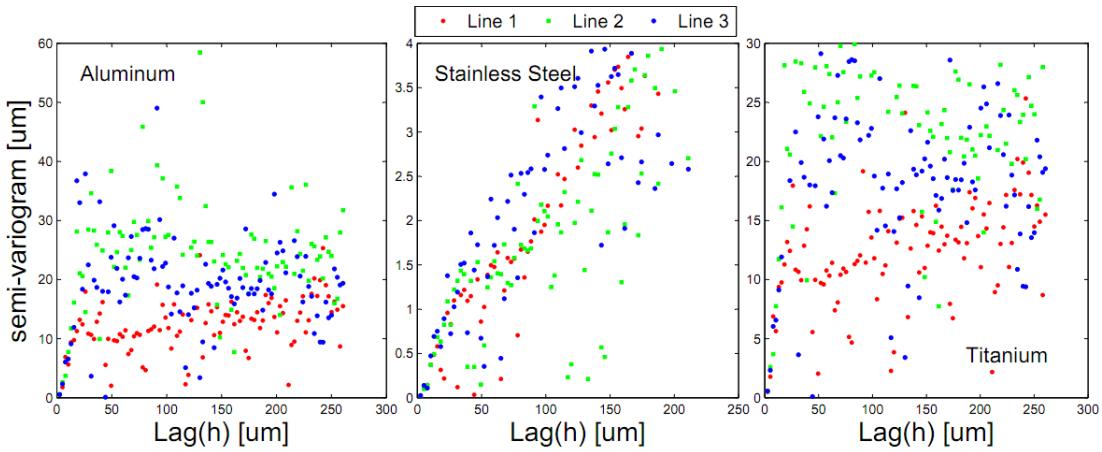

Figure 3.45: Semi-variogram from vertically cross-sectioned points (the first 100 lags points = 250 μm).

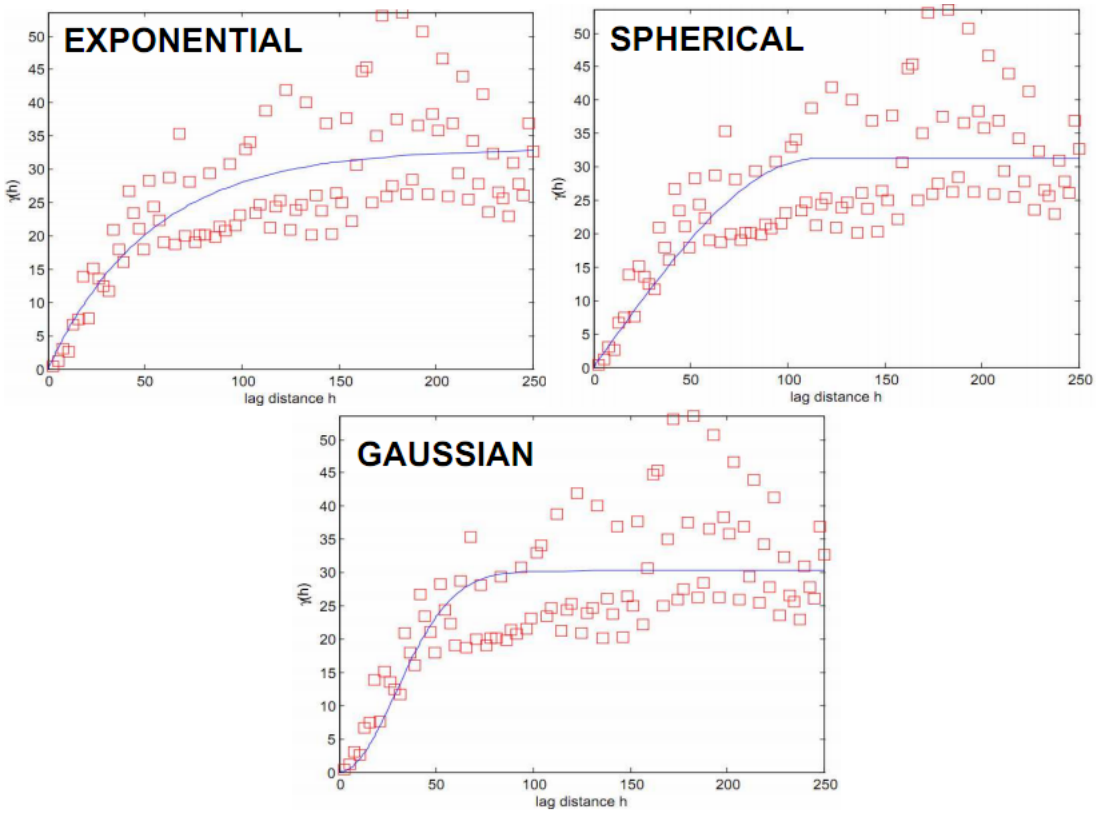

Figure 3.46: Variogram model fitting for aluminum (lag unit is in μm)

model, which are Gaussian, exponential and spherical. Selections of the model and its s, n, r parameters are by observing the statistical parameter of R^2 which represent the fitness of the fitting to the data. The experimental data of variogram which are used in the model fitting is the data from horizontal cross-section. The consideration of selecting the horizontal cross-section data is by comparing fig. 3.44 and fig. 3.45, one can observed that they are more correlated in horizontal direction compared to the vertical one. The plots of the variogram model fitting for aluminum, stainless steel and titanium are shown in fig. 3.46, fig. 3.47 and fig. 3.48 respectively. Details of the variogram model fitting are depicted in table 3.16, table 3.17 and table 3.18. Finally, the setelcted variogram model and parameters for the three materials are presented in table 3.19.

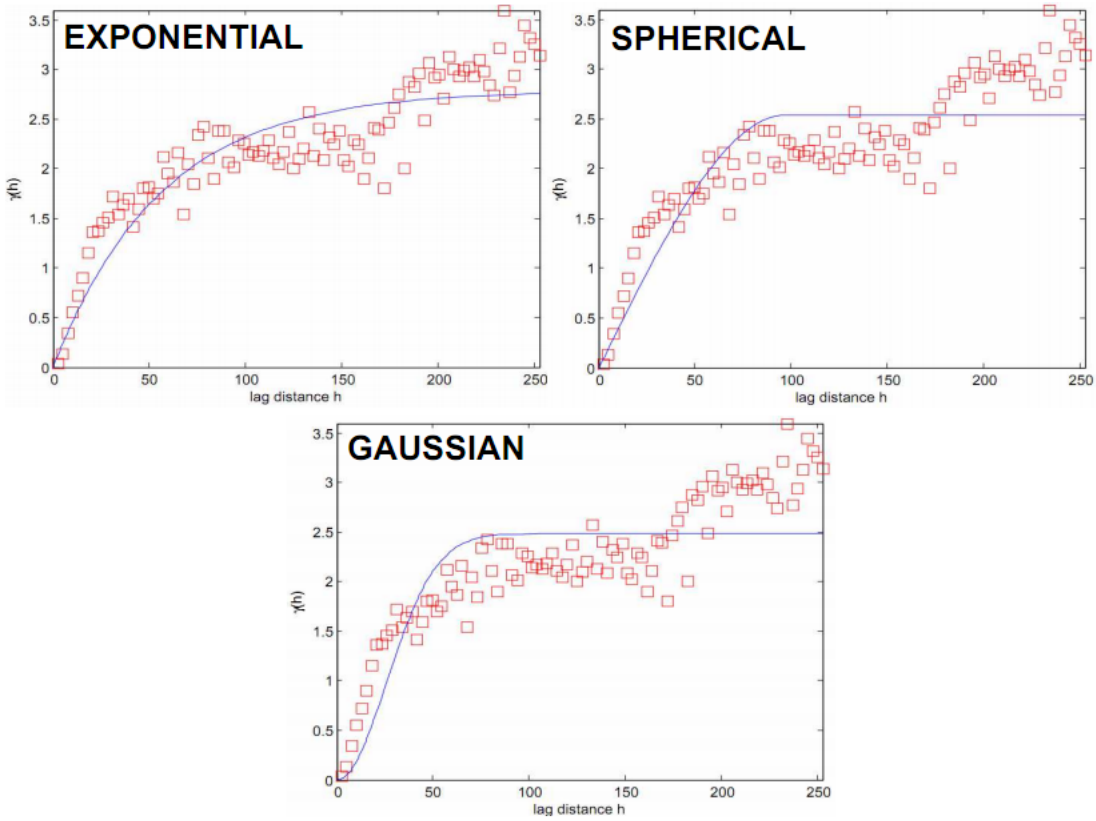

Figure 3.47: Variogram model fitting for stainless steel (lag unit is in μm)

Fitted Variogram model	**s (sill)** $[\mu m]$	**n (nugget)** $[\mu m]$	**r (range)** $[\mu m]$	R^2
Exponential	**31.232**	**0**	**114.63**	**0.5615**
Spherical	33.1	0	53.33	0.5242
Gaussian	30.26	0	41.121	0.5037

Table 3.16: Details of the fitted variogram model for aluminum material.

Fitted Variogram model	**s (sill)** $[\mu m]$	**n (nugget)** $[\mu m]$	**r (range)** $[\mu m]$	R^2
Exponential	**2.788**	**0**	**56.4**	**0.7859**
Spherical	2.537	0	97.169	06807
Gaussian	2.48	0	36.488	0.6392

Table 3.17: Details of the fitted variogram model for stainless steel material.

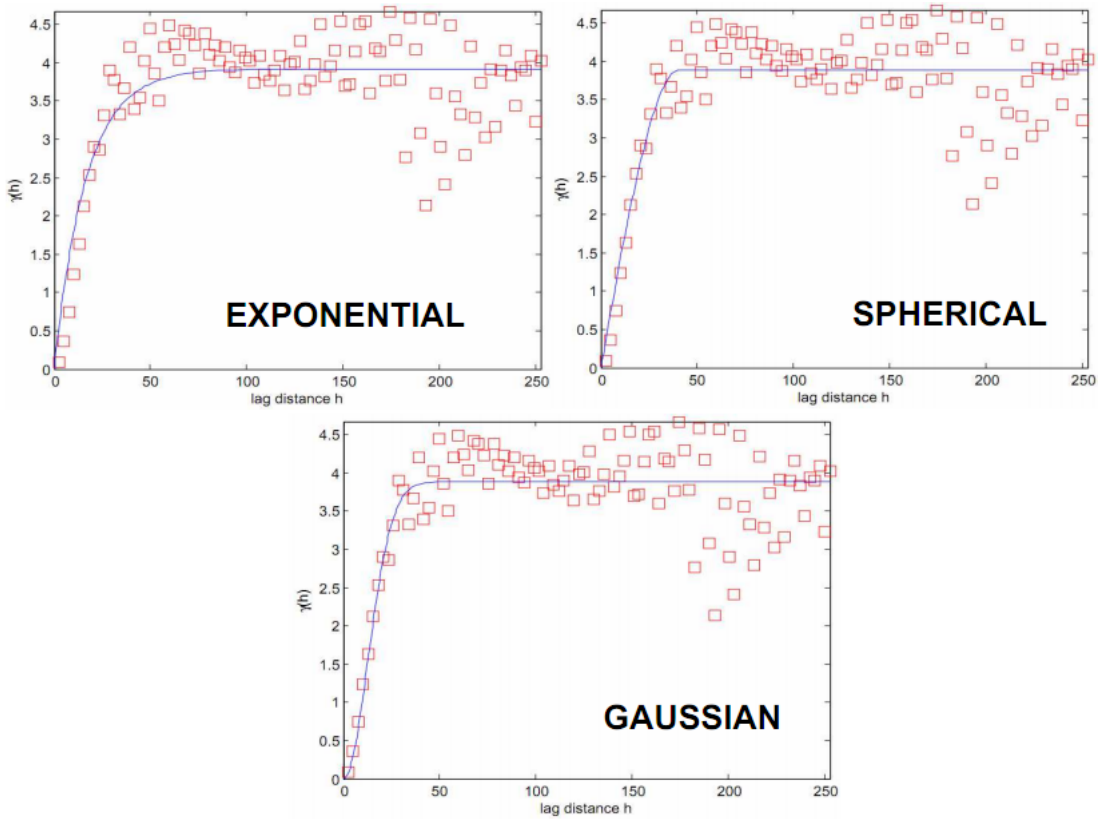

Figure 3.48: Variogram model fitting for titanium (lag unit is in μm)

Fitted Variogram model	**s (sill)** $[\mu m]$	**n (nugget)** $[\mu m]$	**r (range)** $[\mu m]$	R^2
Exponential	3.9189	0	16.5176	0.687
Spherical	3.8911	0	40.9285	0.7121
Gaussian	**3.888**	**0**	**17.986**	**0.7154**

Table 3.18: Details of the fitted variogram model for titanium material.

Material	**s (sill)** $[\mu m]$	**n (nugget)** $[\mu m]$	**r (range)** $[\mu m]$	**Selected variogram model**
Aluminum	31.232	0	114.63	Exponential
Stainless Steel	2.788	0	56.4	Exponential
Titanium	3.888	0	17.968	Gaussian

Table 3.19: Determined variogram parameters for aluminum, stainless steel, and titanium as well as the maximum sigma of random noise obtained from the experiment.

3.5 Initial validation

This section will present validation of the estimated statistic model which will be used to estimate measurement uncertainty by means of simulation procedure. In doing so, the simulation should be carried out. The simulation procedure is explained as follows. First, a set of point cloud is obtained from the instrument. Subsequently, from this set of point cloud, simulated errors are added to the points by a perturbation process. This procedure is carried out for number of repetitions. For each repetition, calculation of desired measurement is carried out and then stored. standard deviation is calculated from the stored measurement results from each simulation run as the estimation of measurement uncertainty.

There are two validations which will be carried out. Firstly, the validation of the selected semi-variogram parameters of statistical error model was conducted. Secondly, the validation was carried out for the simulated uncertainty. The validation was carried out for measurement of aluminum, stainless steel, and titanium. Estimated semi-variogram parameters used to simulate the error is based on previous section which is presented in table 3.19. The simulated error is only applied for the z-coordinate of the points since the instrument is basically generate a 3D map (2.5 D) from the acquisition process.

Fig. 3.49 and 3.50 present the results of cross-sectioned data points obtained from one of measurement execution and thus obtained from the simulation. From this observation, a good agreement can be observed between the real and perturbed data, both for horizontally and vertically cross-sectioned data points.

For the simulated uncertainty validation, It was carried according to ISO15530-4

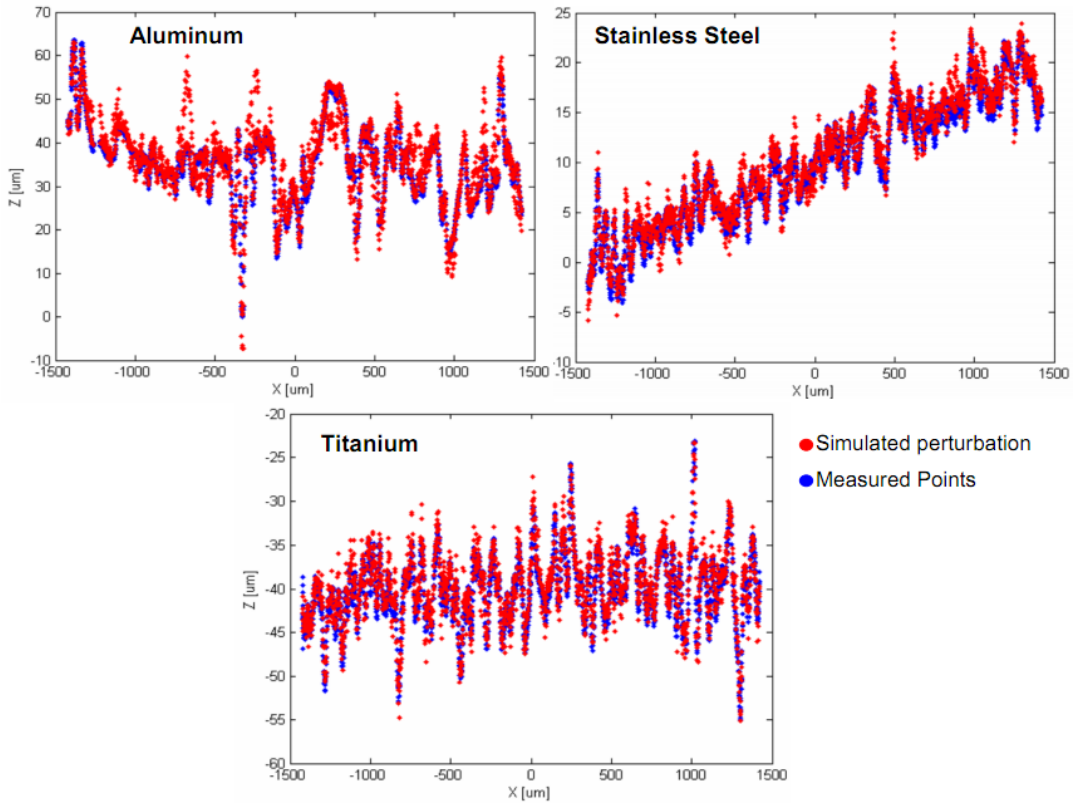

Figure 3.49: Validation of the variogram model by comparing the real and perturbed data in horizontal direction.

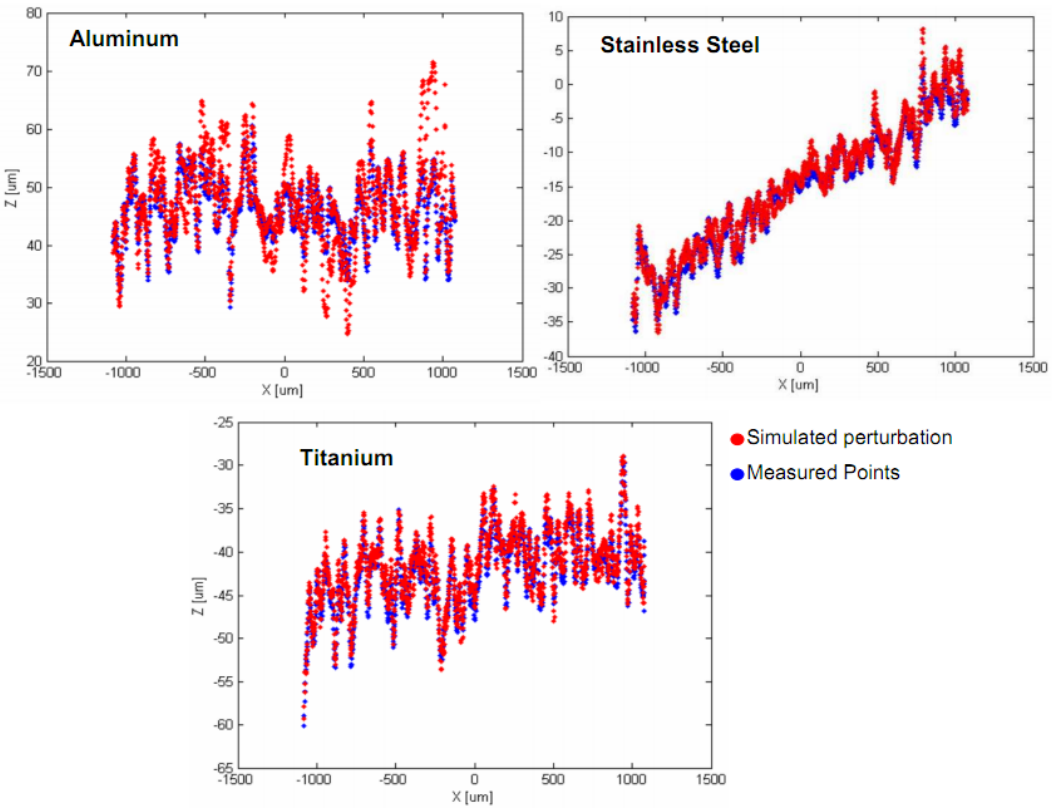

Figure 3.50: Validation of the variogram model by comparing the real and perturbed data in vertical direction.

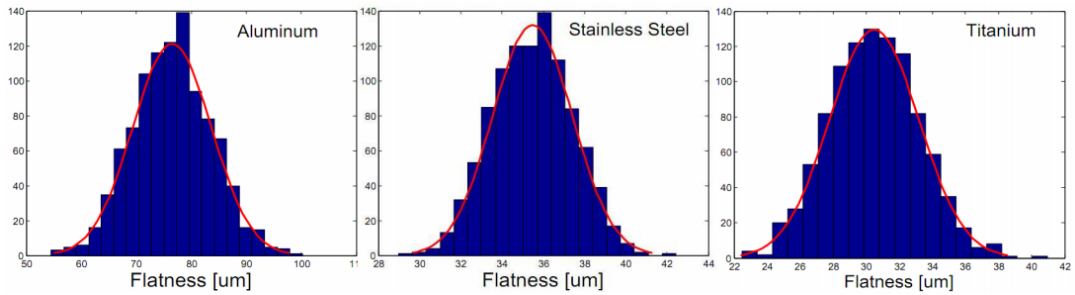

Figure 3.51: Simulated flatness for aluminum, stainless steel, and titanium.

validation procedure. According to this standard, there are four methods to validate the estimated uncertainty by means of simulation, which are: physical testing on an individual CMM, computer-aided verification and evaluation, comparison with specific reference results, and statistical long term investigation. In this study, physical testing on an individual CMM is selected for the validation process. With this procedure, the validation is carried out by calculating an index E_n. The index is given by:

$$E_n = \frac{|y_{mea} - y_{cal}|}{\sqrt{(U_{sim}^2 + U_{cal}^2)}} < 1 \tag{3.35}$$

where y_{mea} and y_{cal} are measurement value and calibrated value with their corresponding expanded uncertainties U_{sim} and U_{cal}, respectively. The calibrated value y_{cal} and its uncertainty u_{cal} are determined by multi-position strategy method as explained in section 4.2 (Flatness/form calibration). The expanded uncertainty is estimated by multiplying u_{sim} and u_{cal} by a factor of 2 ($k = 2$), by assuming normal distribution. Fig. 3.51 depicts the distribution of simulated flatness for aluminum, stainless steel, and titanium. The results were obtained from about 500 simulation runs and they follow a Gaussian distribution. The calculation of E_n is carried out for each single measurement. A good agreement can be concluded if approximately 95% of the values of E_n from all measurements are less than one. In this case around 100 or more measurements were carried out. For this initial validation, before measurement results are derived, the obtained points were filtered by means of 3-sigma-based filter to deal with the outliers. Based on ISO/TS15530-4, the uncertainty from simulation has to be combined with other uncertainty contributors which are not taken into account by the simulation process. Hence, the final estimation of combined measurement uncertainty

by simulation is formulated as:

$$u_{sim} = \sqrt{u_{est}^2 + \sum u_i^2} \tag{3.36}$$

where u_{sim} is total uncertainty estimation obtained by sum of square of u_{est} and u_i. u_{est} and u_i are uncertainty obtained from simulation and uncertainty of other i-th influences quantities which are not taken into account in simulation and are estimated by another suitable way. In our case, the proposed method combined all uncertainties inside the parameter sill (s) of the simulator model by sum squared them with the original sill parameters of the material type. Hence, the final estimated uncertainty u_{sim} is only from the results of simulation u_{est} and other uncertainty contributors u_i are not considered.

Fig. 3.52 shows the E_n values of each flatness measurement of Aluminum, Stainless steel, and Titanium. The calibrated values (along with the calibration uncertainty) for their flatness are presented in table 3.2. Expanded uncertainties U_{sim} ($k = 2$) obtained from the simulation are 13.96 μm, 7.66 μm, 10.14 μm for aluminum, stainless steel and titanium, respectively. From the validation results, the E_n values are higher than 95% which show good agreement of the estimated uncertainty. E_n values obtained for aluminum, stainless steel, and titanium are 97%, 96%, and 98% respectively. The semi-variogram parameter used is stated in table 3.19 since the flatness measurement was carried approximately on flat orientation. It is worth noting that, since the simulated points come from a real measurement, they already include the form deviation of the part. As such, the form deviation is not simulated in the process as has been pointed out by Kruth et el. [Kruth et al. [2009]].

3.6 Conclusion

In this chapter, two studies have been presented. Firstly, characterization of uncertainty of measurement by optical instrument is carried out. The purpose of this study is to understand the factors that influence the measurement results. Secondly, simulation method to estimate measurement uncertainty along with the validation method has been proposed.

From uncertainty characterization study, the results show that different material will have different response by the focused-variation based optical instrument. As

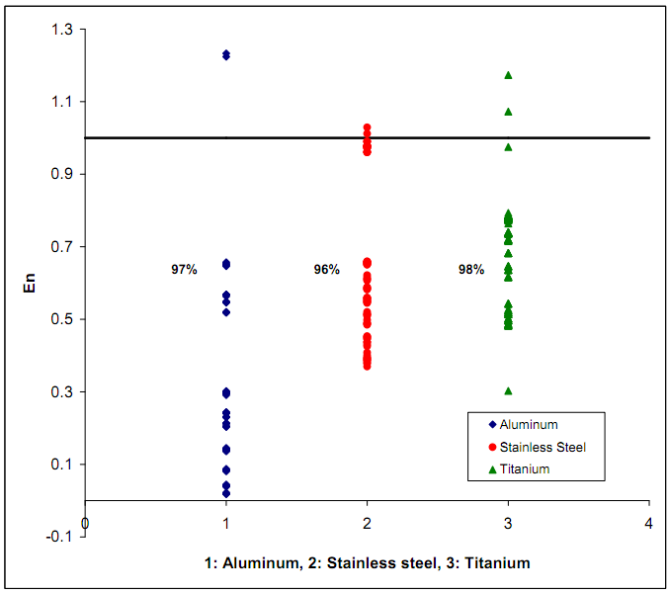

Figure 3.52: E_n value of simulated uncertainty validation by flatness measurement of Aluminum, Stainless steel, and Titanium.

can be predicted, the instrument defines a point by calculating the contrast value (variance value) from the pixel intensity value of its neighbors. This pixel intensity is strictly related to the reflectance from the measured surface. Different material will have different reflectance with respect to the incoming (incident) light receive by the work piece surface. This also explains the different results obtained by measuring equal surface with different orientation (steepness). Different orientation will affect the reflectance of the part surface. As a consequence, different materials should be treated differently, or can be grouped based on the similarity of the material having similar reflectance behavior. In addition, not only material type, but also type of illumination will directly affect the measurement results. As can be observed from the result, illumination with polarizer will give a higher measurement uncertainty. It is worth noting that measurement result obtained from different magnification lens can not be directly compared. The reason is different magnifications lens will have different NA (numerical aperture). Higher magnification lens will have higher NA resulting in capability to capture higher steep surface. Hence, the observed surface will be different with respect to the instrument. Finally, to have comparison of measurement result by means of optical instrument, all controllable parameter, mainly related to illumination

and lens, should be approximately hold constant.

The simulation method to estimate measurement uncertainty starts from the obtained points from the instrument. The obtained points are from a single real measurement result which also contains the part deviation. Subsequently, point perturbation is carried out by taking into consideration the correlation of a point with other neighbor points by means of spatial statistic method, called Gaussian process. The Gaussian process is used to simulate the error of a point. The error is then added to the original point. The simulation is repeated for certain times and the statistic of the simulation results, the standard deviation, is calculated to estimate the uncertainty. To validate the simulation approach, the method in ISO 15530-4 is used by calculating a value En for each measurement. The validation results show that more than 95% of En is less than one which means that the simulated uncertainty is in good agreement with the real measurement results. The main drawback of simulation method is that it is computationally intensive compared with comparison method with calibrated artifact, since optical instrument involve millions of data points. Instead, simulation method provides flexibility and reduces experimental cost.

Chapter 4

Case studies

To further validate the simulation approach to estimate measurement uncertainty, case studies are presented. As mentioned in the previous section 3.4 (initial validation of the simulation approach), the work piece variation is already included in the initial data points obtained from one measurement. All captured points are filtered before associating to a specific substitute geometry to remove outliers (see section 3.3.1.3). The quantification of simulation parameters (s, n and r) are based on the results in uncertainty characterization study (section 3.3). All the calibrations for the case study were carried out by means of certified tactile CMM with $E_{0,MPE} = \pm \left(2.2 + \frac{L}{300}\right)\ \mu m$. The calibration procedure can be referred in section 2.3.2 for calibration of size or dimensional quantities and section 3.3.1.2 for calibration of geometric (form) quantities. By recalling section 3.4, the validation follows one of method suggested by the ISO/TS 15530-4 standard which is physical testing on an individual CMM. This method a value E_n has to be calculated to determine the goodness of estimated measurement uncertainty by means of simulation. The value is calculated as (see section 3.4 for the detail explanation):

$$E_n = \frac{|y_{mea} - y_{cal}|}{\sqrt{\left(U_{sim}^2 + U_{cal}^2\right)}} < 1 \tag{4.1}$$

where where y_{mea} and y_{cal} are measurement value and calibrated value with their corresponding expanded uncertainties U_{sim} and U_{cal}, respectively.

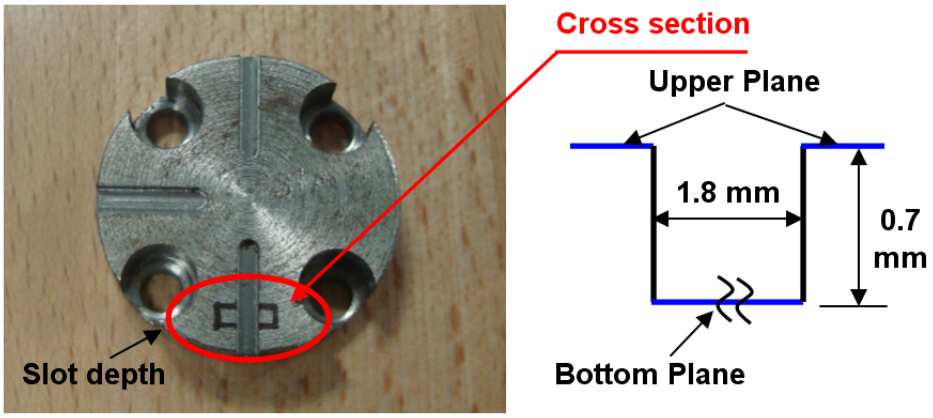

Figure 4.1: Work piece for the slot depth measurement.

Workpiece	Exposure time	Contrast	Vertical resolution	Lateral resolution
Micro milled slot	88.32 μs	0.2	0.4 μm	7.82 μm

Table 4.1: The measurement parameters used for case study 1.

4.1 Case study 1: Depth measurement of micro milled slot

Measurement of slot depth is carried out in this case study. Fig. (4.1) shows the milled workpiece as well as definition of slot depth. The work piece is made of steel and the slot was milled by a micro milling machine. Micro milling process with end mill was used to create the slot by means of KERN EVO micro-milling machine. The slot depth is defined as a height between the top surface and the bottom surface of the slot. Measurement parameters used to captured the points are shown in table 4.1. These parameters are used to acquire both bottom and upper surface. A 5X magnification lens was used. Meanwhile, fig. 4.2 shows the example of data points obtained. Measurement was taken with 5X objective lens and captured the bottom and upper surface. Since, the depth is a length measurement; the calibration is following the procedure explained in section 2.3.2. The calibrated slot depth y_{cal} (u_{cal}) obtained is 692.7(7) μm. The calibration process is presented in fig. 4.3. The material of the part (and also the material for case study 2 and 5) is made of steel. Hence, the semi-variogram for this material has to be calculated to estimate the error parameters in the simulation

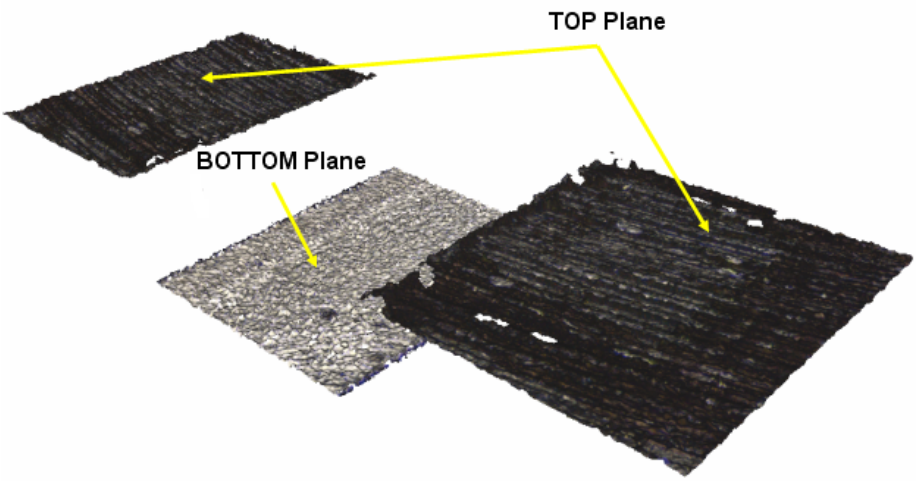

Figure 4.2: One of the obtained points for the slot measurement.

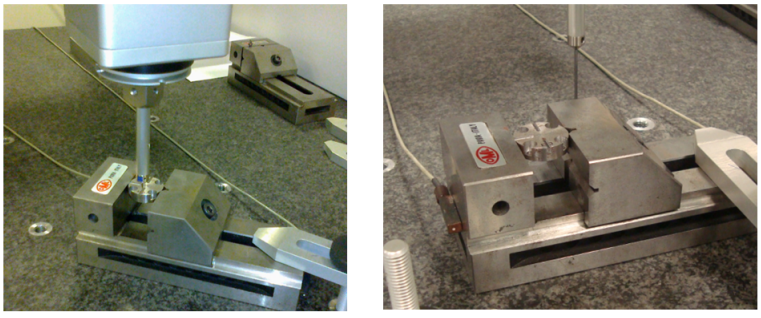

Figure 4.3: Calibration process for stopper part

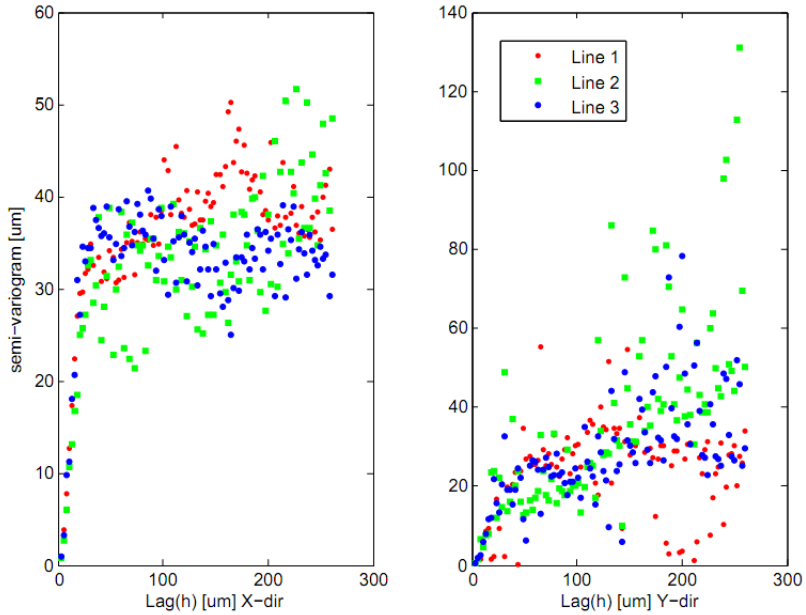

Figure 4.4: Semi-variogram of steel material to determine the error simulation parameters.

Fitted Variogram model	**s (sill)** $[\mu m]$	**n (nugget)** $[\mu m]$	**r (range)** $[\mu m]$	R^2
Exponential	13.0325	0	34.5677	0.7454
Spherical	34.4359	0	33.31	0.7946
Gaussian	**34.4334**	**0**	**14.8056**	**0.8008**

Table 4.2: Fitted model for steel variogram experimental data.

procedure. The step is similar as being presented in section 3.2. The plot of calculated semi-variogram is depicted in fig. 4.4. The experimental variogram data is fitted by least-square fitting method to find the best fit model among Gaussian, exponential and spherical variogram model. The plots of the fitted model to the variogram experimental data are shown in fig. 4.5. Table 4.2 shows the fitted variogram parameters. The selection of the model is based on the largest R^2 value. Based on this criterion, the selected variogram model is the Gaussian one since it has the largest R^2 value. Next step is by adding other uncertainty sources to the sill (s). The other uncertainty sources added are uncertainty due to placement variation and exposure time variation. From the uncertainty characterization study, the range of variation due to different positions

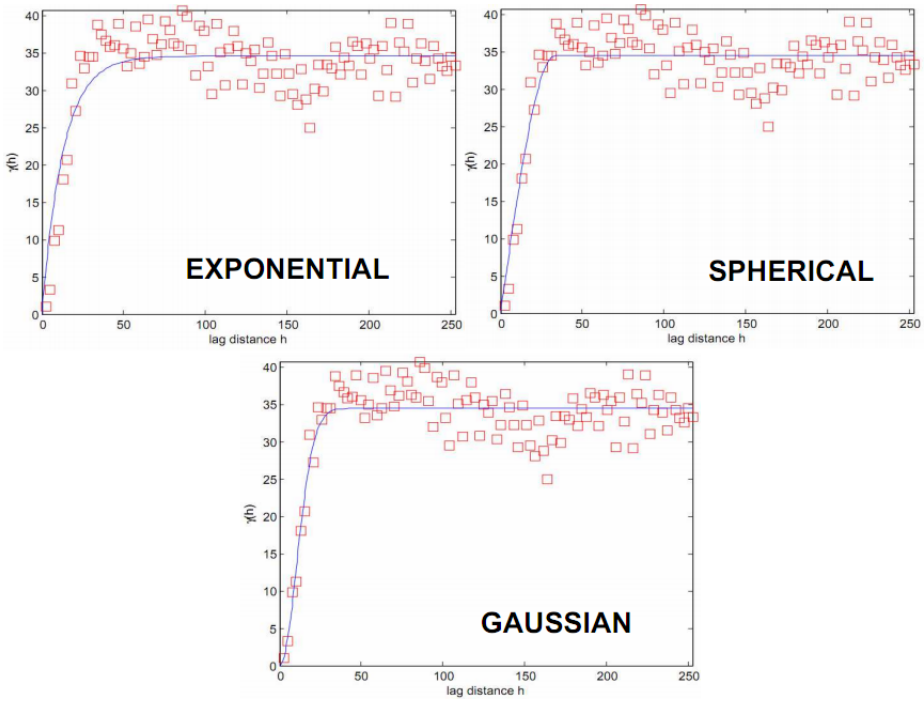

Figure 4.5: The fitted variogram to the experimental steel variogram data.

(including tilted position) and due to exposure time variation are around 1.5 μm and 0.3 μm. These other uncertainty sources are added to the sill (s) by sum of squared them with the obtained sill of steel material: $sill = \sqrt{34.4^2 + 1.5^2 + 0,3^2}$=34.434 μm. Finally, the simulation parameters for sill, nugget, and range are 34.434 μm, 0 μm, and 14.8 μm, respectively.

Number of simulation runs is about 500 runs. From the simulation, estimated expanded uncertainty U_{sim} of 0.45 μm is obtained. It is derived by calculating the standard uncertainty from the statistic of the stored 100 measurement results (after multiplying by $k = 2$). En value is calculated for each 100 measurement runs y_{mea}. The measurement calculations of slot height were obtained from the filtered points by using the four filtering methods, which are 3-sigma-based, LG, and RGR filtering and median filter. Total 93% of the calculated En has the value of < 1 for the measurement results obtained by using 3-sigma-based filter. On the other hand, E_n values of more than 95% are obtained from the other three filters. In fig. 4.6, the calculated En values are presented.

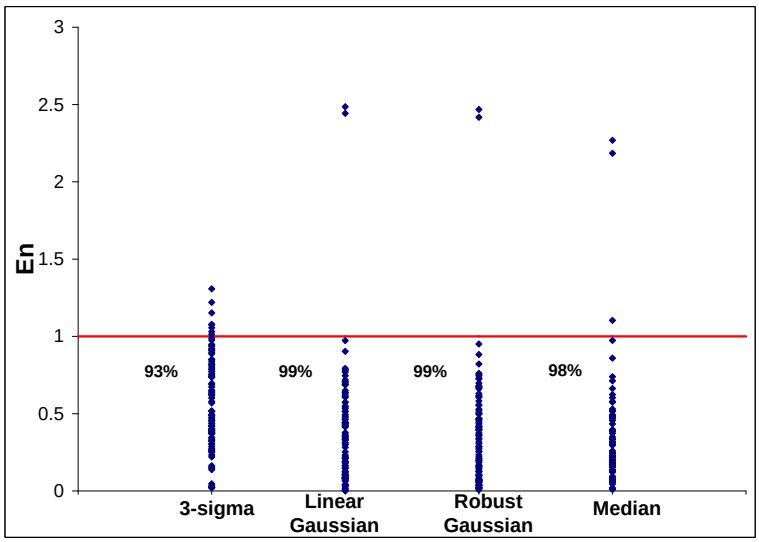

Figure 4.6: E_n values for the slot measurement.

Workpiece	Exposure time	Contrast	Vertical resolution	Lateral resolution
Micro wire	193.2 ms	0.44	0.6 μm	3.9 μm

Table 4.3: The measurement parameters used for case study 2.

4.2 Case study 2: Micro wire measurement

This case study is a size measurement. A steel-wire with diameter of 310 $\pm$ 2 μm (from the specification of the manufacturer) is used in this case study. The function of the wire is as a hole-gage to measure diameter of a small hole; in this case it is used to measure the water jet nozzle diameter. Fig. 4.7 shows the steel wire and the measured data with the optical instrument. Table 4.3 shows the parameters used to measured the micro wire. Objective lens used was 10X magnification lens. To be able to obtained a complete cylinder, the rotation unit of FVM instrument was used. By this, a complete 360^0 measurement was obtained. The final obtained points from this type of measurement comes from a stitching operation of sequence of images taken by

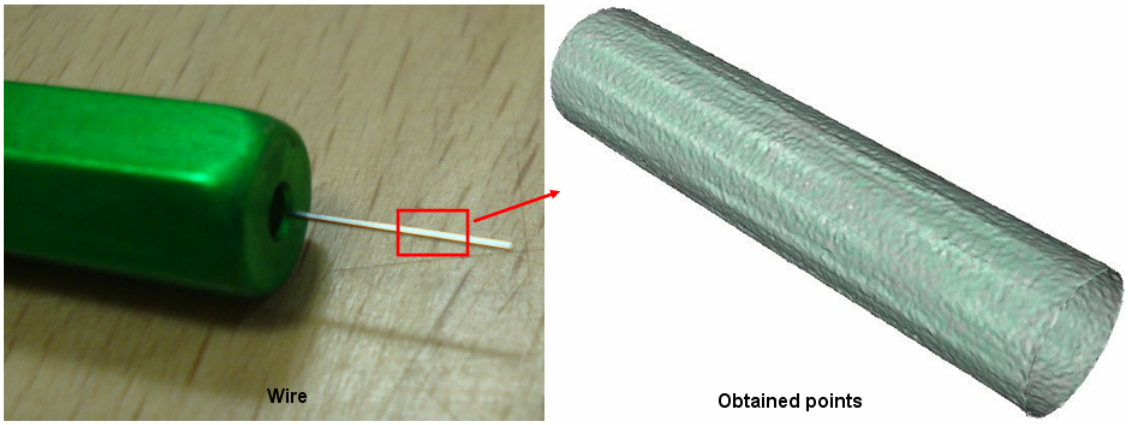

Figure 4.7: The cylinder and the obtained point cloud.

rotating the rotation axis. This operation was automatically run by the instrument. Total of 85 measurements were carried out to validate the simulated uncertainty.

Simulation parameters for sill, nugget, and range are identical with the one used in slot measurement (case study 1) which are 34.434 μm, 0 μm, and 14.8 μm, respectively. Gaussian variogram model is used. The obtained extended simulated uncertainty U_{sim} from 500 runs is 5.64 μm. The wire is not calibrated. Hence, y_{mea} and u_{cal} are estimated as the nominal value for y_{mea} and $\frac{T}{\sqrt{3}}$ for u_{cal} by considering a rectangular distribution ranging from $310-T$ to $310+T$. The k value for the extended uncertainty is equal to 2. Hence, the calibrated value and its uncertainty are $y_{mea} = 310$ μm and $U_{cal} = 2.31$ μm respectively. En value is calculated for each measurement. From 85 measurements, total of 98% have En value less than 1. Fig. 4.8 plot the En value of each measurement. Moreover, if one assumes that the wire is a perfect cylinder (with 0 deviation), the En value of around 95% is still obtained from the 85 measurements. In this case study, only 3-sigma-based filter was used. The reason is that the data points of the cylinder measurement is resulted from elaboration of data stitching process. As such, the points obtained are no longer in the 2D grid-format (3D map format) as can be obtained in planar measurement. Moreover, converting the points coordinate from Cartesian to cylindrical coordinate system is not relevant since the data format is no longer well structured.

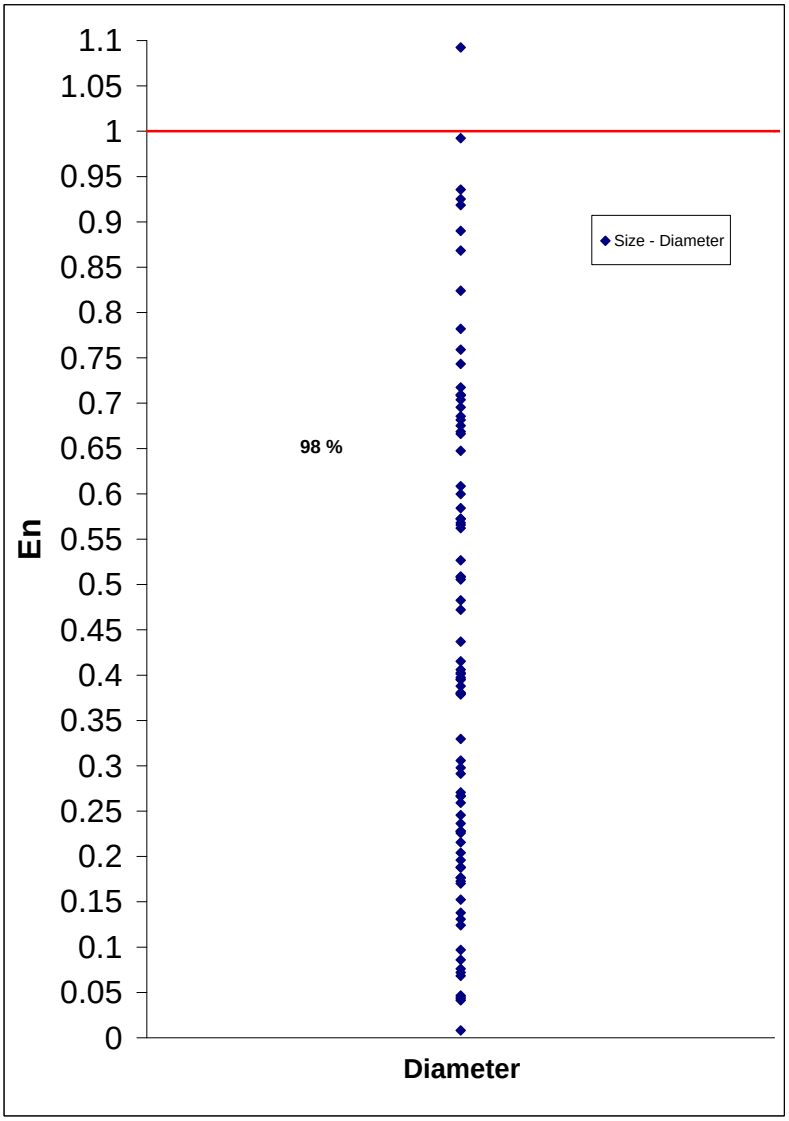

Figure 4.8: E_n values for the wire diameter measurement.

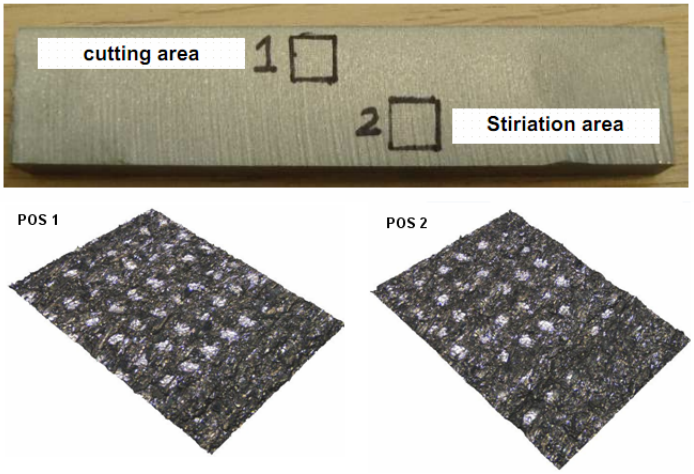

Figure 4.9: Aluminum part cut by water jet and one example of measured surface for both position.

4.3 Case study 3: Flatness of water jet cut

In this case study, a flatness measurement of an aluminum bar cut by water jet process is presented. This case study is an unrelated geometric tolerance in which there is no reference datum needed [ISO1101 [2004]][ASMEY14.5 [2009]]. The part used in this case study is not a micro, instead it is a macro part. Even though the part is a macro part, the area measured is a small portion from a large surface area. Even though it is not a micro part, the motivation of this case study is to validate a geometric measurement by optical instrument. The definition of geometric tolerance based on ASME [ASMEY14.5.1 [1994]] is a minimum separation of two identical geometry to be verified which includes all the part surface. This standard contains the mathematical definition of geometrical tolerancing. From this definition, to accurately estimate a geometric tolerance, the points obtained from the measurement should cover the entire surface of interest. As such, by using optical instrument, more comprehensive surface points can be obtained compared to that if the measurement carried out by tactile CMM. With optical instrument, many points can be obtained in considerably shorter time compared to the tactile one. Moreover, optical instrument has easier procedure in planning the measurement compared to tactile system.

Fig. 4.9 shows the part used in this case study. There are two positions where the flatness measurements were carried out: position 1 and position 2. Position 1 is the

Workpiece	Exposure time	Contrast	Vertical resolution	Lateral resolution
Position 1	195 μs	1	0.4 μm	7.82 μm
Position 2	195 μs	1	0.4 μm	7.82 μm

Table 4.4: The measurement parameters used for case study 3.

upper side position in which the water jet velocity is still high. Meanwhile, position 2 is the lower side of the exit of the jet. In this area, striations phenomenon will be observed due to reduced jet velocity. At this area, the flatness will be higher as the cutting quality reduces. Measurement parameters used to captured the points are shown in table 4.4. The objective lens used for the measurement was 5X magnification lens. Total measurement conducted for both positions are 120 measurements. For each position, the measurements were carried out in three different orientations: approximately flat, skew to the left and skew to the right. The skew direction is around 5^0 and 10^0. Since the measurement is not conducted only at approximately flat position and with different exposure time, hence the sill parameter in the error model should includes also the uncertainty due to different orientation and different exposure time, which have range about 3 μm and 0.3 μm. The uncertainty due to orientation represents fixturing or sample placement error when placing the work piece to be measured. The uncertainty is square-summed with the original sill (Aluminum material). The value of sill (s) becomes 31.345 μm compared to the original value of 31.232 μm. The nugget and range parameters are 0 μm and 114.63 μm, respectively. Variogram model used is the exponential one. The calibrated flatness values y_{cal} and their uncertainty u_{cal} are 36.7(4) μm and 81.9(5) μm for position 1 and position 2 respectively. The calibration is based on the method explained in section 3.3.1.2. All the flatness measurements calculation are obtained from the filtered points. There are four types of filtering, which are 3-sigma-based filter, LG filter, and RGR filter. From simulation, the obtained uncertainties U_{sim} ($k = 2$) are 21.004 μm and 16.457 μm for position 1 and position 2, respectively. Fig. 4.10 and fig. 4.11 depicts the E_n value for every measurement at position 1 and position 2, respectively. From the graph, it can be observed that more than 95% of the measurement results (from four different filtering methods) have $E_n < 1$.

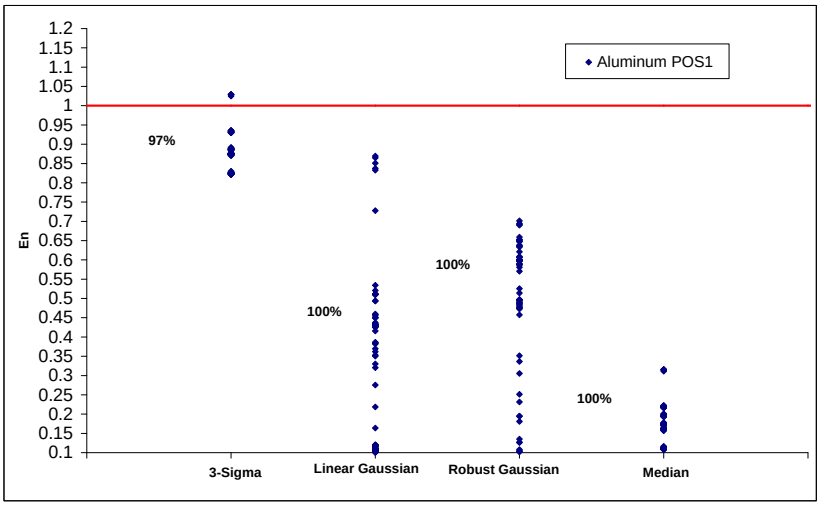

Figure 4.10: E_n value of flatness measurements at position 1.

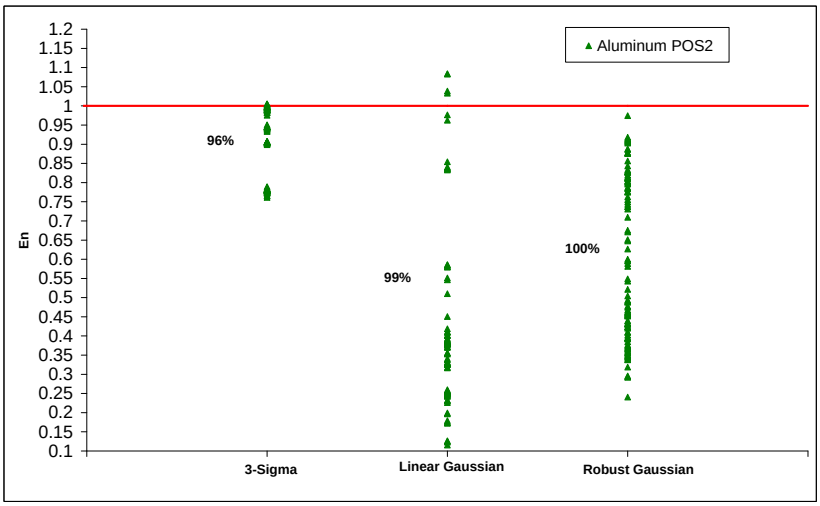

Figure 4.11: E_n value of flatness measurements at position 2.

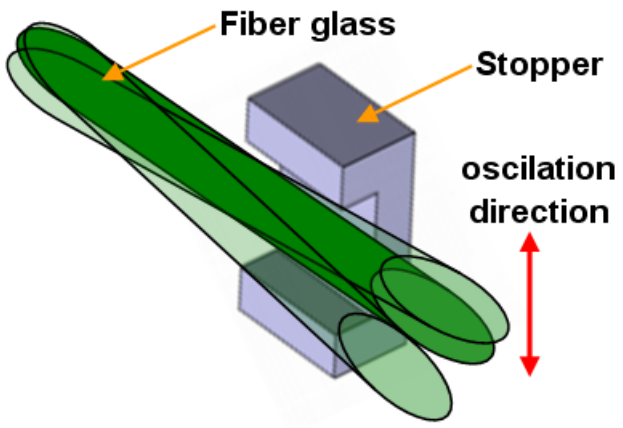

Figure 4.12: Illustration of the function of the stopper.

4.4 Case study 4: Perpendicularity of stopper from water jet cut

This case study is a related-geometric tolerance which is perpendicularity. Hence, a reference datum measurement is needed. As reported by [Petro and Moroni [2010]], in related geometric tolerance verification, the measurement uncertainty is also contributed by the uncertainty of reference datum. For this reason, the measurement should capture both reference surface and the surface of which the perpendicularity should be measured. The part used in this case study is a stopper. It is made of stainless-steel and is used to limit the movement of a glass rode inside an accelerometer. The accelerometer is used in a high speed train to measure its acceleration and deceleration. The glass rode will oscillate when the train accelerates and decelerates. A sensor will measured the magnitude of this oscillation and correlate the value to the acceleration value. Hence, by this oscillation, the acceleration and deceleration of a high speed train can be estimated. The illustration of function of the stopper is depicted in fig. 4.12. Fig. 4.13 details 2D and 3D design of the stopper and the manufactured part. The trajectory of the cut is set and optimized so as to eliminate acceleration and deceleration effect of the water jet on the inner corner of the stopper. The goal is to improve the homogeneity of the surface quality. Hence, circular-like geometries are found at both inner corner of the stopper (fig. 4.13).

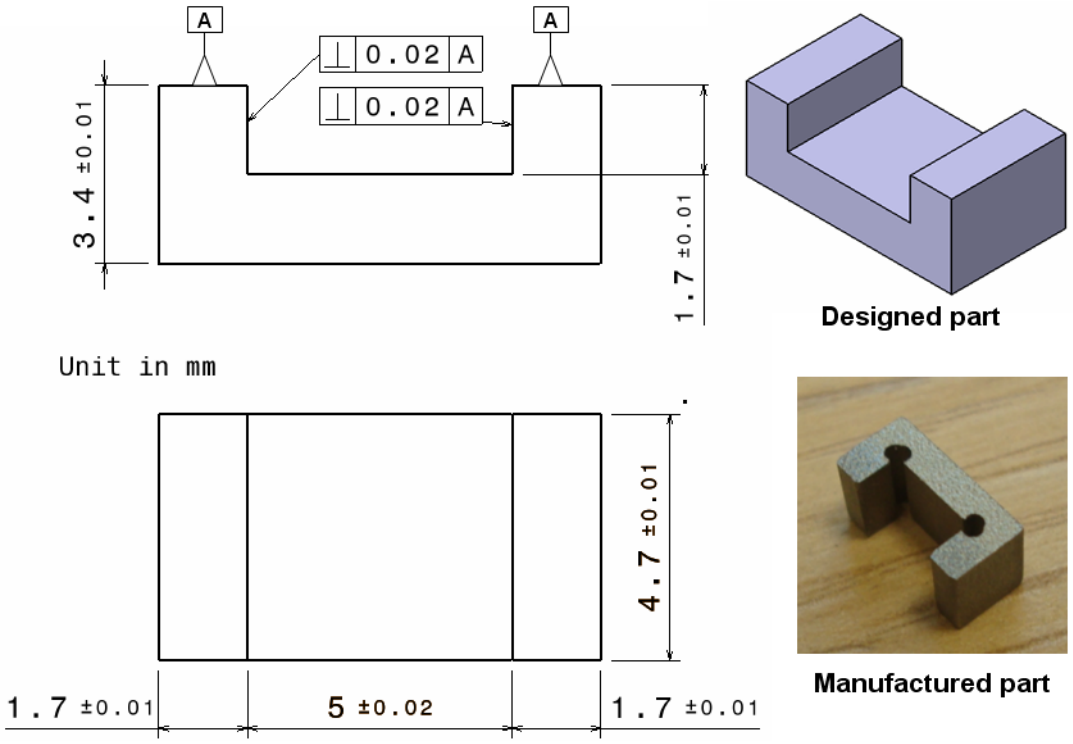

Figure 4.13: Stopper part: 2D drawing, 3D design and the manufactured part by water jet cut.

Workpiece	Exposure time	Contrast	Vertical resolution	Lateral resolution
Stopper	1.23 ms	1	0.4 μm	7.82 μm

Table 4.5: The measurement parameters used for case study 4.

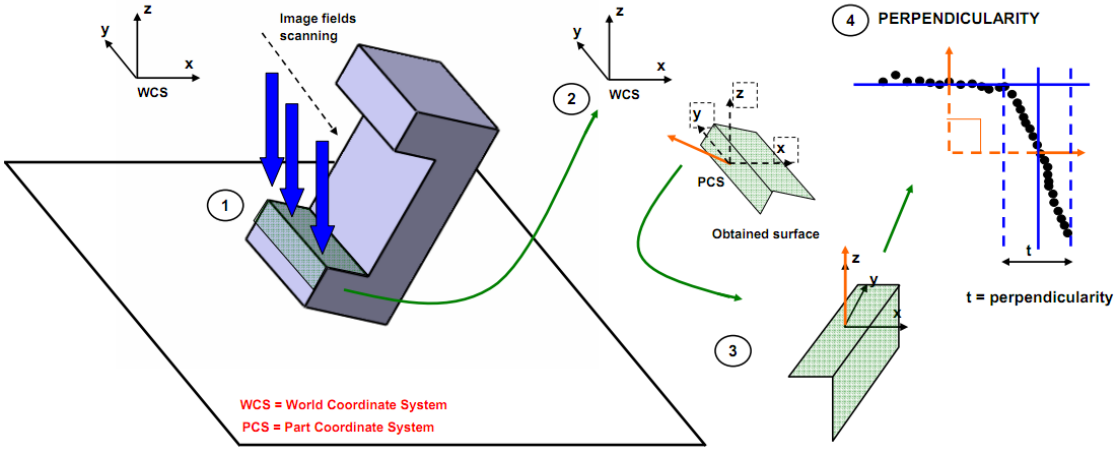

Figure 4.14: Procedure for surface acquisition and perpendicularity measurement. 1: measurement position and acquisition, 2: world coordinate system (WCS), 3: Transformation of the obtained surface points from not aligned orientation to aligned orientation with regard to WCS, 4: perpendicularity measurement value, t.

Since perpendicularity needs datum surface, the measurement of the part should capture both the reference and toleranced surface. Therefore, the measurement was carried out in skew orientation with 5X objective lens to be able to capture both surfaces (fig. 4.14 Step 1). Measurement parameters are depicted in table 4.5. The use of 5X lens is to be able to capture both surfaces since it has the highest FOV. Total 3 images fields along the scanning direction were obtained to capture all the measured surfaces. The complete procedure in processing the obtain points to calculate perpendicularity is presented in fig. 4.14.

The procedure for the calculation of perpendicularity is (fig. 4.14):

1. Capture the reference and the measured plane. Fit the reference plane and obtained the unit normal vector of the reference plane $\mathbf{a_{ref}}$.

2. Calculate the angle of $\mathbf{a_{ref}}$ with respect to world coordinate system (WCS) to obtain its spatial θ_y and planar rotation θ_z. The spatial and planar rotation can

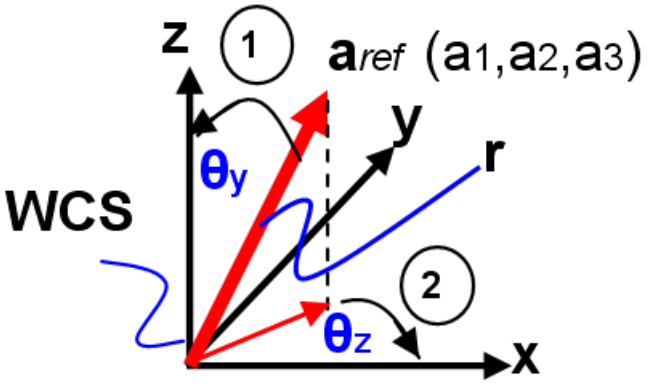

Figure 4.15: Illustration of θ_y and θ_z.

be obtained by:

$$\begin{aligned} \theta_y &= tan^{-1}\left(\frac{r}{a_3}\right) \\ r &= \sqrt{a_1^2 + a_2^2 + a_3^2} \end{aligned} \tag{4.2}$$

$$\theta_y = tan^{-1}\left(\frac{r}{a_3}\right) \tag{4.3}$$

Fig. 4.15 shows the detail of this sub-step.

3. Inverse transform (rotate) $\mathbf{a_{ref}}$ with respect to its spatial and planar rotation such that Part coordinate system (PCS) is aligned with respect to WCS (step 3). The rotation is carried out by:

$$\begin{aligned} \mathbf{a'_{ref}} &= \mathbf{T_{rotation}}\mathbf{a_{ref}} \\ \mathbf{T_{rotation}} &= \mathbf{R_y}(\theta_\mathbf{y})\mathbf{R_z}(\theta_\mathbf{z}) \end{aligned} \tag{4.4}$$

where $\mathbf{R_y}$ and $\mathbf{R_z}$ are rotation matrices along y- and z- axis, respectively.

4. Rotate $\mathbf{a'_{ref}}$ 90^0 about y-axis and consider it as unit normal vector of measured plane $\mathbf{a_{mea}}$.

$$\mathbf{a_{mea}} = \mathbf{T_{90^0 y=axis}}\mathbf{a'_{ref}} \tag{4.5}$$

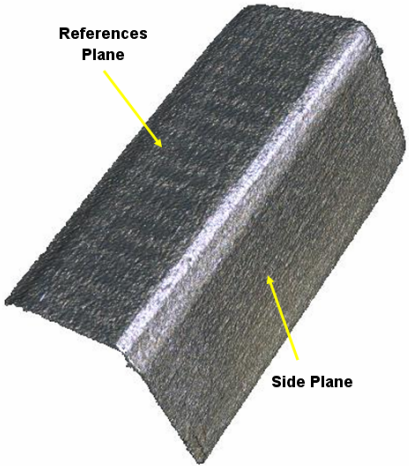

Figure 4.16: One of measured surface for the perpendicularity measurement.

5. Inverse transforms all the points (on reference and measured plane) with respect to the obtained planar θ_z and spatial θ_y rotation.

$$\mathbf{X_i'} = \mathbf{T_{rotation}} \mathbf{X_i} \tag{4.6}$$

6. Fit a plane to points on measured plane. The point on plane is the centroid of points on measured plane and its normal vector is $\mathbf{a_{mea}}$.

7. Calculate the maximum and minimum distance of the points from the fitted plane as the perpendicularity.

Example of captured surface is presented in fig. 4.16. Note that, before the procedure is applied, points at and near the edge should be removed (fig. 4.17) since these points will affect the perpendicularity measurement. Moreover, tactile CMM can not reach this area when calibration was carried out. Finally, to validate the simulation E_n value of each measurement was calculated. The measurements are obtained from filtered points by using three filtering methods: 3-sigma-based, LG, and RGR filter. Around 500 runs were carried out for the simulation. The calibrated perpendicularity value y_{cal} (u_{cal}) is 13.2(2) μm. Fig. 4.18 shows the calibration process for the stopper part. It is determined by the procedure explained in section 3.3.1.2 (form calibration). In this measurement, since the steep angle is higher than the one in characterization

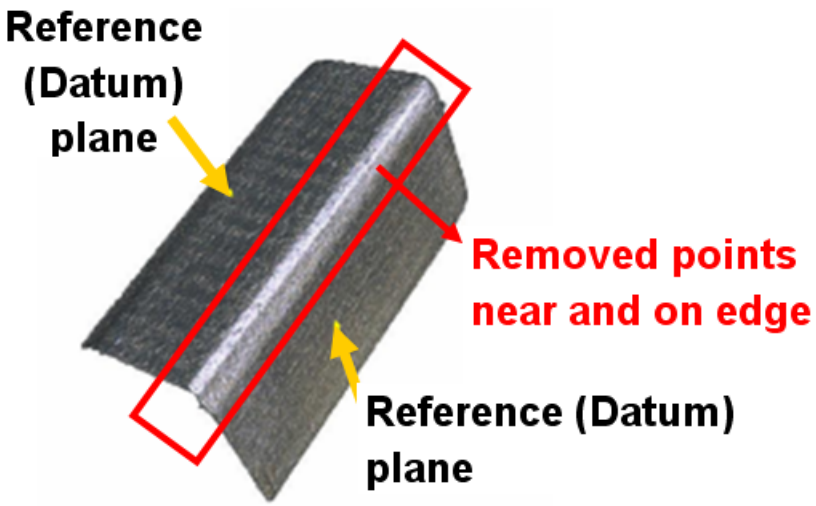

Figure 4.17: Points which have to be removed before perpendicularity measurement is carried out.

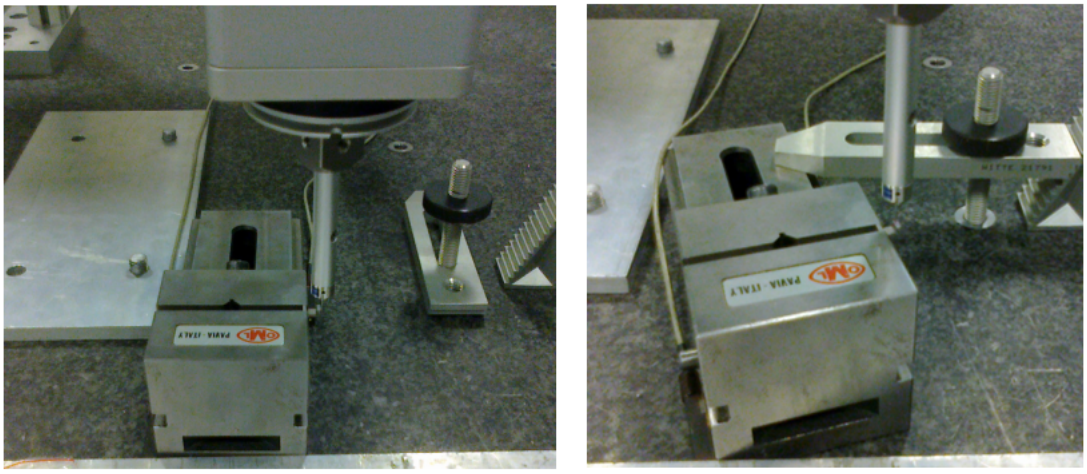

Figure 4.18: Calibration process for the stopper part.

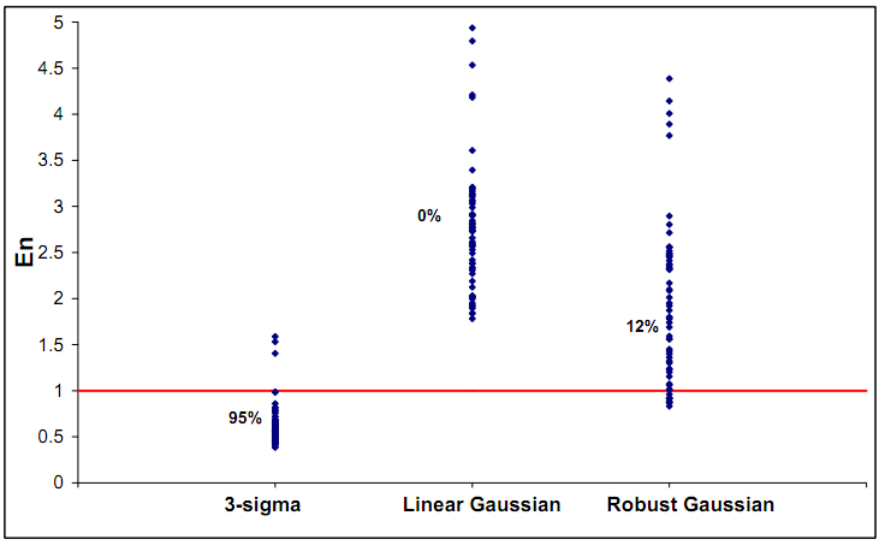

Figure 4.19: E_n value for each perpendicularity measurements.

study, different contrast and exposure time (brightness) were applied such that the surface can be captured. Hence, the sill is sum-squared with additional uncertainty due to different tilted position, contrast and exposure time. The variation range of the sigma of residual due to different contrast, exposure time, and tilted positioning are 0.2 μm, 0.3 μm and 2 μm, respectively (with reference to section 3.3. uncertainty characterization). Subsequently, the sill value becomes 3.5 μm and for the other nugget and range parameters are identical to the one used in the simulation validation section for stainless steel material. The simulation used exponential variogram model. The obtained expanded simulated uncertainty U_{sim} (k=2) is 13.295 μm. From the calculation of E_n value of 120 measurements, 95% of the measured values, obtained from 3-sigma-based filtering, are less than one. Fig. 4.19 shows the plot of En values. Meanwhile, the En values of measurements obtained from LG filtering and RGR filtering are 0% and 12%, respectively. These are caused due to the points filtered by these LG and RGR methods are synthetic points. By this, the fitted plane, both for the reference and measured one, will be different from the original one (different orientation). Hence, the perpendicularity of the measured plane will be changed. This effect is not occur in un-related geometric measurement (ex: flatness), since the plane orientation does not affect the flatness measurement.

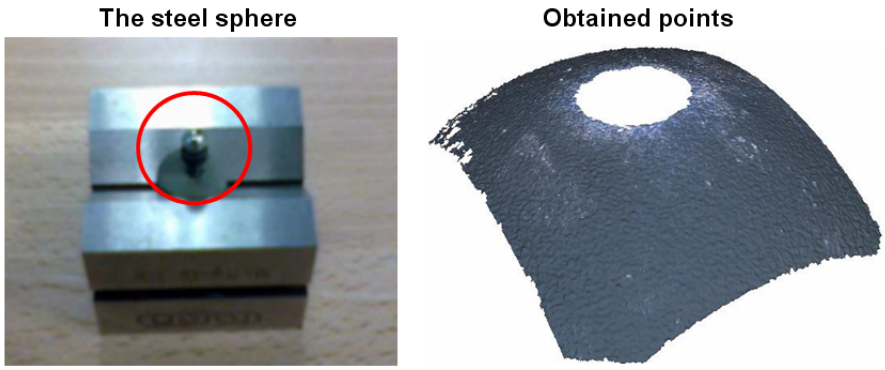

Figure 4.20: The sphere used in the case study.

Workpiece	Exposure time	Contrast	Vertical resolution	Lateral resolution
Stopper	1.45 ms	0.81	0.4 μm	7.82 μm

Table 4.6: The measurement parameters used for case study 5.

4.5 Case study 5: Sphere size and form measurement

This case study involves two types of measurement: form and size measurement. The form is an unrelated geometric-tolerance verification of spherecity. Meanwhile, radius of the sphere is a size measurement, which is dimensional-tolerance verification. Fig. 4.20 shows the sphere used in the case study. Measurement parameters used in this case study is identical to the one used for measuring spheres of the artifact used in performance verification test. Table 4.6 presents the detail of the parameters. The sphere is a ball bearing grade G10 based on ISO standard [ISO3290-1 [2008]]. The value for the steel ball based on the standard is 2.5 ± 0.00025 mm with maximum form error of 0.25 μm. Fitting of the sphere was carried out from selected 25 points from the obtained point cloud as suggested in [ISO10360-8 [2013]]. Due to this reason, filtering operation was not applied to calculate both the diameter and the form error. Meanwhile, the fitting procedure is the improved-version of standard LM algorithm (appendix A). Simulations are carried out for 500 runs. The parameter of the simulation is similar to the one used in slot height measurement case study with additional uncertainty source due to different contrast measurement, which is 0.2 μm. Hence, the s,n and r parameter of the simulation are 34.44 μm, 0 $\mu m$and 14.8 μm respectively. Gaussian variogram

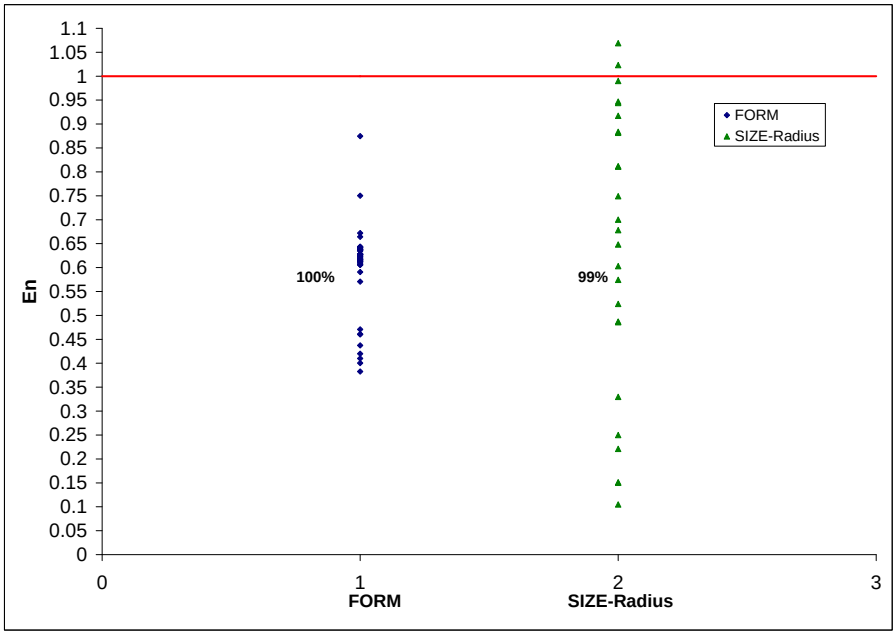

Figure 4.21: E_n value for both form error and radius measurement.

model was used. The sphere was calibrated by the similar multi-position strategy (section 3.3.1.2 for form error calibration and section 2.3.2 for radius calibration). The calibration results for form error and radius of the sphere are 4.27(1) μm and 2493(1.2) μm, respectively. Meanwhile, simulated expanded uncertainty U_{sim}, $k = 2$ for form error is 15.369 μm and for size error is 7.48 μm. En value was calculated for each 50 measurements. The results show that more than 95% of the $E_n < 1$ are obtained. For form error, the 100% of En values are less than one. Meanwhile for radius measurement, around 99% of En values are less than one. The resulted En values are shown in fig. 4.21.

4.6 Case study 6: Micro turning insert automatic rake angle measurement algorithm

A rake angle measurement is presented in this case study. This measurement is classified as dimensional tolerance verification. Motivation of this case study is that micro manufacturing becomes more diffused due to its important for new application product. Hence, micro machining plays an important role for such process [Dornfeld et al.

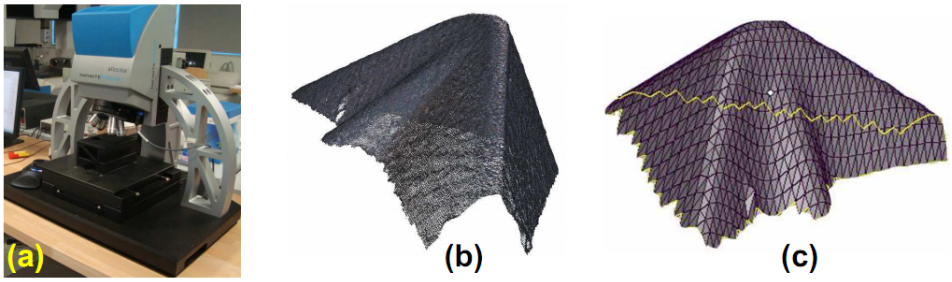

Figure 4.22: (a) The instrument, (b) Points cloud, (c) Triangle-mesh of the points cloud.

[2006]]. As a consequence, metrology of micro cutting tool is demanding. From machining process point of view, rake angle is a very important quantity. This case study develops algorithm for automatic rake angle measurement of micro-turning tool from their acquired points. The algorithm is useful to ensure repeatability of the measurement, which is not provided by most instruments software. Moreover, it is useful for the estimation of task-specific uncertainty (ISO15530-4) and automatic in-line inspection systems. Fig. 4.22 shows the micro-insert turning tool measurement.

Unlike micro-milling, the tool size of micro-turning is not necessarily in micro-scale. As such, small insert tool is still used for micro-turning in millimeter scale [Dornfeld et al. [2006]]. The developed algorithm steps are:

1. Point normal vector and curvature estimation. It is worth to note that Triangle-mesh of the points cloud is utilized as input for the algorithm which can be exported directly from the instrument software. In addition, triangle-mesh format is a common representation of a 3D model due to its flexibility to present complex free-form surfaces with a neutral and simple format.

2. Reference plane and cutting plane construction.

3. Point segmentation and line fitting.

4. Rake angle calculation.

4.6.1 Algorithm steps

STEP 1: Point normal vector and curvature estimation.
The algorithm for curvature calculation is adapted from [Hamann [1993]]. For each

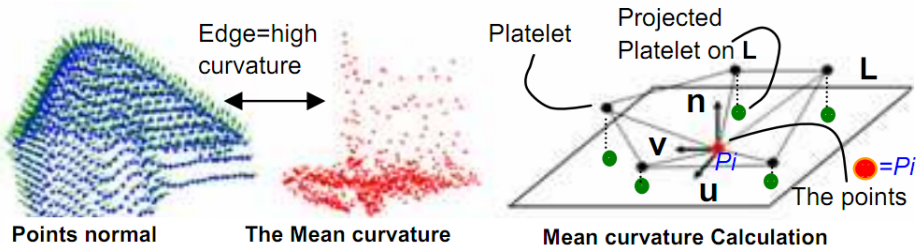

Figure 4.23: Normal and mean curvature of the points.

point $\mathbf{P_i}$, its normal vector $\mathbf{n}$ is estimated by $\sum_{i=1}^{n} \frac{\mathbf{n_i}}{N}$ where $\mathbf{n_i}$ is normal of all adjacent faces and N is number of adjacent faces at the point (4.23 left). Subsequently, the mean curvature $H = (k_1 + k_2)$ is calculated $\forall$ point P_i . k_1 and k_2 are two principal curvatures of P_i. As such, all points lie on edge will have considerably significant value of compared to others points which are not lie on the edge (4.23center). $k_1 and k_2$ are determined from the platelets, which are all the points adjacent to point $\mathbf{P_i}$ (4.23 right).

Procedure to calculate k_1 and k_2 is as follows. For each point $\mathbf{P_i}$, plane PL is defined by implisit function of:

$$(\mathbf{n} \cdot (\mathbf{x} - \mathbf{P_i})) = \mathbf{nx}(\mathbf{x} - \mathbf{P_x}) + \mathbf{ny}(\mathbf{y} - \mathbf{P_y}) + \mathbf{nz}(\mathbf{z} - \mathbf{P_z}) \tag{4.7}$$

Subsequently, $\mathbf{Platelet_j}$ which are all platelet of $\mathbf{P_i}$ are projected to the defined plane PL. The projected $\mathbf{Platelet_j}$ on PL is called as $\mathbf{Platelet_j^p}$ and calculated as:

$$\mathbf{Platelet_j^p} = \mathbf{Platelet_j} - \mathbf{d_j n} \tag{4.8}$$

where d_j is the orthogonal distance of $\mathbf{Platelet_j}$ to plane PL. Each point of $\mathbf{Platelet_j^p}$ is, then, translated into a coordinate system centered on $\mathbf{P_i}$ with basis unit vector defined by $< \mathbf{u}, \mathbf{v} >$. In order to do this, a difference vector $\mathbf{d_j}$ between $\mathbf{Platelet_j^p}$ and $\mathbf{P_i}$ is calculated as $\mathbf{d_j} = \mathbf{Platelet_j^p} - \mathbf{P_i}$. This difference vector $\mathbf{d_j}$ can be represented in the form of linear combination of $< \mathbf{u}, \mathbf{v} >$ as:

$$\mathbf{d_j} = (\mathbf{d_j} \cdot \mathbf{u})\mathbf{u} + (\mathbf{d_j} \cdot \mathbf{v})\mathbf{v} \tag{4.9}$$

Hence, the component local coordinate based on $< \mathbf{u}, \mathbf{v} >$ of $\mathbf{Platelet_j^p}$ is:

$$(p_j, q_j)^T = (\mathbf{d_j} \cdot \mathbf{u}, \mathbf{d_j} \cdot \mathbf{v})^\mathbf{T} \tag{4.10}$$

$< \mathbf{u}, \mathbf{v} >$ is calculated as:

$$\mathbf{u} = \frac{\mathbf{a}}{||\mathbf{a}||} \quad \textbf{and} \quad \mathbf{v} = \mathbf{n} \times \mathbf{u} \tag{4.11}$$

where $\mathbf{a}$ is a vector perpendicular to $\mathbf{n}(\mathbf{a} \cdot \mathbf{n} = \mathbf{0})$, which is:

$$\mathbf{a} = \begin{cases} \frac{1}{nx}(-(ny+nz), nx, nx)^T \\ \frac{1}{ny}(ny, -(nx+nz), ny)^T \\ \frac{1}{nz}(nz, nz, -(nx+ny))^T \end{cases} \tag{4.12}$$

A second degree of polynomial f having absisca of and ordinate is defined as:

$$f(p,q) = \frac{1}{2}\left((c_1 p_j^2 + 2c_2 p_j q_j + c_3 q_j^2)\right) \tag{4.13}$$

and in matrix form:

$$\begin{bmatrix} p_1^2 & 2p_1q_1 & q_1^2 \\ \vdots & \vdots & \vdots \\ p_n^2 & 2p_nq_n & q_n^2 \end{bmatrix} \begin{bmatrix} c_1 \\ c_2 \\ c_3 \end{bmatrix} = \begin{bmatrix} d_1 \\ \vdots \\ d_n \end{bmatrix} \tag{4.14}$$

to solve c by least square estimation, eq. 4.14 becomes:

$$\begin{bmatrix} p_1^2 & 2p_1q_1 & q_1^2 \\ \vdots & \vdots & \vdots \\ p_n^2 & 2p_nq_n & q_n^2 \end{bmatrix} \begin{bmatrix} p_1^2 & 2p_1q_1 & q_1^2 \\ \vdots & \vdots & \vdots \\ p_n^2 & 2p_nq_n & q_n^2 \end{bmatrix} \begin{bmatrix} c_1 \\ c_2 \\ c_3 \end{bmatrix} = \begin{bmatrix} p_1^2 & 2p_1q_1 & q_1^2 \\ \vdots & \vdots & \vdots \\ p_n^2 & 2p_nq_n & q_n^2 \end{bmatrix} \begin{bmatrix} d_1 \\ \vdots \\ d_n \end{bmatrix} \tag{4.15}$$

Finally, after solving $c_1,\ c_2,\ c_3$, the two priciple curvatures k_1 and k_2 are the root of $k^2 - (c_1 + c_3)k + c_1c_3 - c_2^2$.

STEP 2: Reference plane Pr and cutting plane P construction.

The Pr is determined from the points on edge. It can be done by selecting the points having significant value (above determined threshold=10) of H. The plane is constructed by a point on plane and its normal direction. Orthogonal fitting is used by finding the eigen vector correspond to the minimum Eigen values of M , which is a $n \times 3$ matrix containing the edge points P_i coordinates. While, point on plane is the centroid (mean) of all considered points. The plane equation used, from $\mathbf{n} \cdot (\mathbf{P_i} - \hat{\mathbf{P}}_\mathbf{i}) = \mathbf{0}$, is defined similar to 4.7.

The plane Pr (plane lie on the cutting edge) is used to determined plane P which is perpendicular to plane Pr. The unit normal of Plane P is obtained by rotating unit normal of plane Pr 90^0 around an axis, which is orthogonal to the cutting edge line,

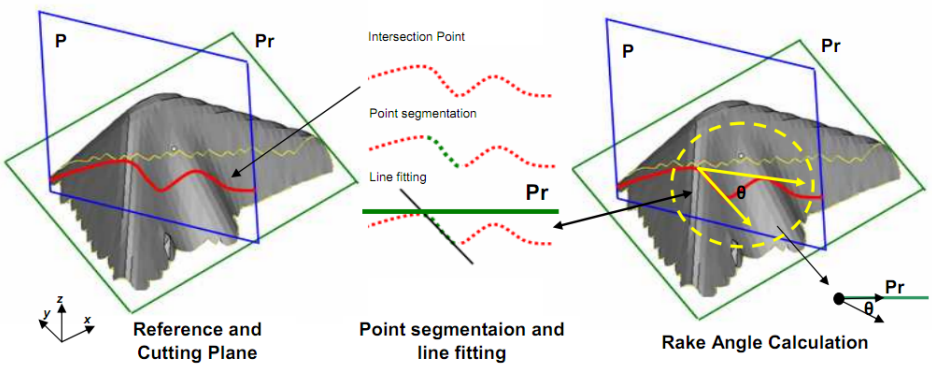

Figure 4.24: Constructed planes, point segmentation and fitting, rake angle calculation.

and the point on P is identical with the point on Pr (4.24left).

STEP 3: Point segmentation and line fitting.

Segmentation is applied to the intersection points between the cutting plane P and the triangle-mesh model of the tool (4.24center). In this algorithm, parametric equation of line is used. A line from two points $\mathbf{Pt_1}, \mathbf{Pt_2}$ is defined as $\mathbf{Pt} = \mathbf{Pt_1} + \mathbf{t}(\mathbf{Pt_2} - \mathbf{Pt_1})$ where t is a scalar quantity (scale) used to define the point on the line. By substituting this parametric equation to plane equation, then, t can be calculated as:

$$t = \frac{-[APt_{1x} + BPt_{1y} + CPt_{1z} + D]}{A(Pt_{2x} - Pt_{1x}) + B(Pt_{2y} - Pt_{1y}) + C(Pt_{2z} - Pt_{1z})} \tag{4.16}$$

After obtaining t, intersection points between cutting plane P and the triangles can be obtained. Subsequently, point segmentation can be carried out. First, the points far from Pr are deleted. Subsequently, the intersection points are sorted (ascending) with regard to $x-$ and then $y-$coordinate position by using *selection sort algorithm*. Finally, the points are scanned starting from the left-edge point (4.24center). This point is identified by checking the point which has the minimum $y-$coordinate. The first 15 points are scanned and a line is orthogonally fitted. Then, the scanning is continued for the next point and the sigma of the error σ of the fitting is calculated, if $\sigma_{new} < \sigma$,then the point is stored. This step is carried out until there are three consecutive points contribute to have $\sigma_{new} > \sigma$, when the line is re-fitted.

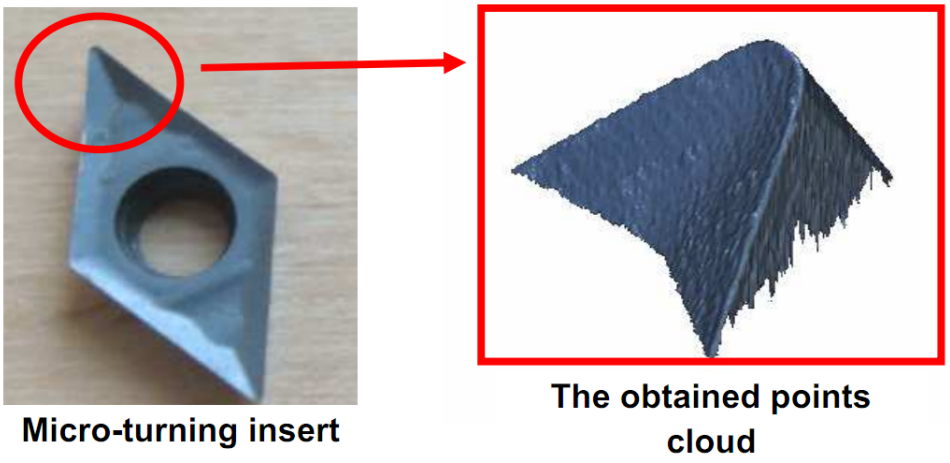

Figure 4.25: Micro-turning insert, points cloud obtained, results statistic.

Workpiece	Exposure time	Contrast	Vertical resolution	Lateral resolution
Stopper	1.226 ms	1	0.4 μm	7.82 μm

Table 4.7: The measurement parameters used for case study 6.

STEP 4: Rake angle calculation.

Rake angle θ is angle between line of segmented point and line projected to Pr (4.24center). To calculate this angle, the unit normal of the fitted-line $\mathbf{n_{line}}$ from STEP 3 is projected into Pr (4.24right). The projected normal is calculated as:

$$\mathbf{n_{line_{proj}}} = \mathbf{n_{line}} - \mathbf{n_{plane\ Pr}}||\mathbf{n_{plane\ Pr}}[\mathbf{n_{line}} \cdot \mathbf{n_{plane\ Pr}}]|| \tag{4.17}$$

Finally, the rake angle $\theta$is calculated as the angle between $\mathbf{n_{line}}$ and $\mathbf{n_{line_{proj}}}$.

4.6.2 Algorithm Implementation

In this implementation, insert tool for micro-turning was used and measured by the focus variation instrument (4.25). The material of the tool is tungsten carbide. The measurement parameters used are shown in table 4.7. Firstly, the s, n, r parameters of the variogram model are quantified with similar method in the other material presented in the previous section. Fig. 4.26 shows the semi-variogram plot in horizontal direction with consideration that the data is horizontally more correlated. The obtained

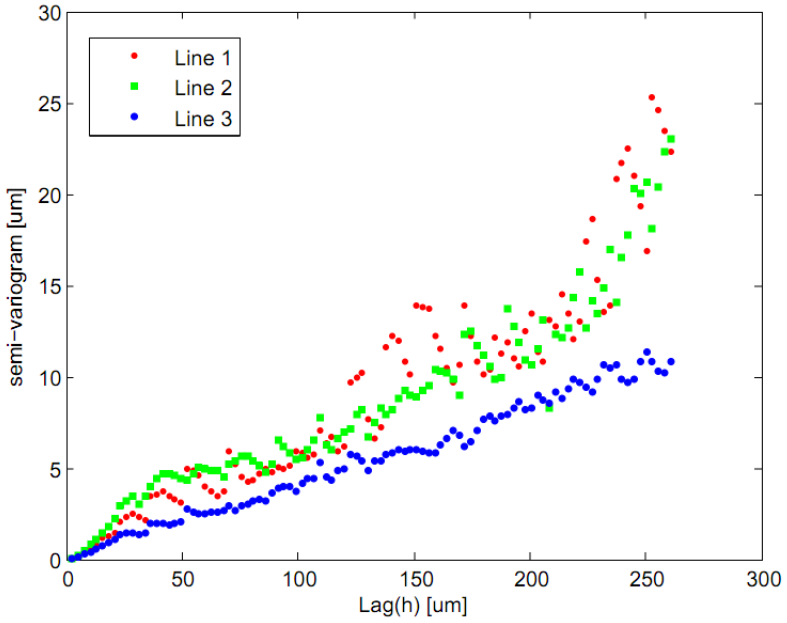

Figure 4.26: Semi-variogram plot of the cutting tool surface measurement data.

parameters for s, n, and r are 2 μm, 0.05 μm, and 25 μm respectively. About 100 simulation runs were carried by perturbing the points with errors model of a Gaussian process using the obtained parameters. In each simulation, rake angle is automatically calculated and stored. The results statistic of the rake angle are mean = 11.2893^0 and sigma = 1.4^0. In this case, the comparison is only carried out with result from manual measurement. From the manual procedure, the obtained rake angle is about 10.761^0. As a matter of fact, for comparison, the manual measurement significantly depends on operator as can be seen in 4.27.

4.7 Conclusion

The case studies consist of two main measurement tasks: dimensional (including size) measurement and geometric measurement. From case studies presented, the results of uncertainty estimation by the proposed simulation approach show a good agreement with the real measurement. A good agreement is obtained by calculating E_n value which are around 95% are less than (some case studies have E_n value near to 95%). The validation method is based on ISO 15530-4 standard. In addition, there are important aspects which can be derived:

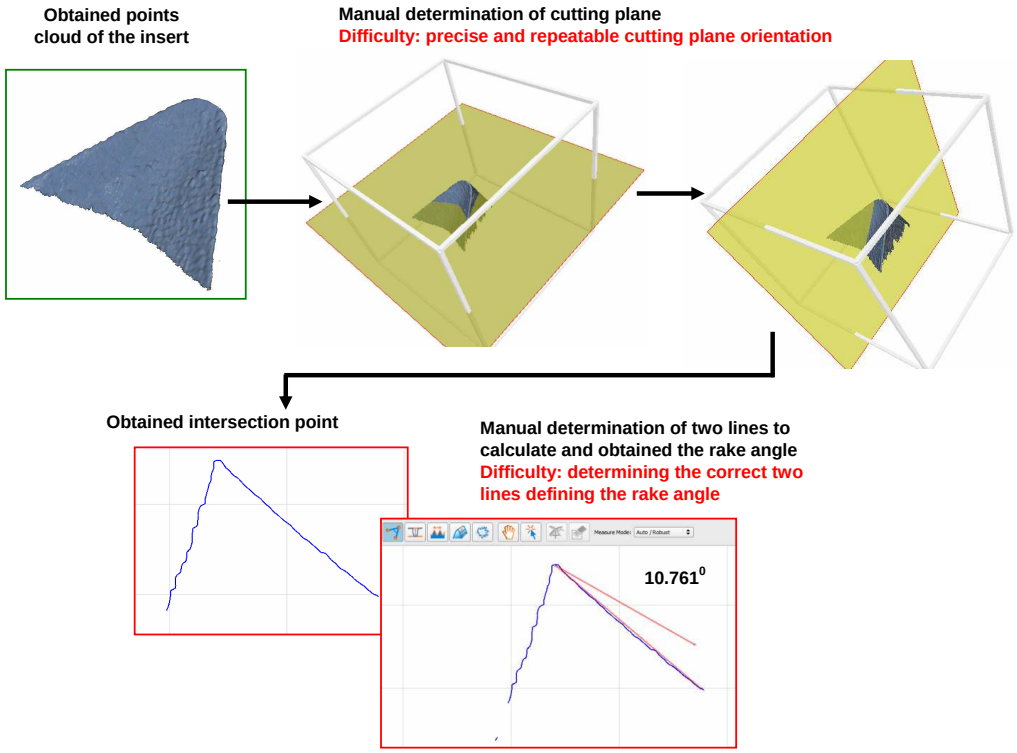

Figure 4.27: Semi-variogram plot of the cutting tool surface measurement data.

1. A database of Gaussian process parameters (s,n, and r) can be created for many type of materials. The procedure is simple. For each material, a flat measurement is carried out. From the obtained data, semi-variogram plot can be derived for each horizontal and vertical profile to estimate the Gaussian process parameters. These parameters will be used for the simulation to estimate the uncertainty according to the proposed framework.

2. Outliers removal has always to be carried out. The reason is that data points obtained by means of optical instrument is prone to outlier. This outlier will affect the measurement results, especially measurement for geometric characteristic. From the results of case studies, the basic 3-sigma based filter can be used in many types of measurement situations to deal with outliers.

3. Selection of fitting method to derive a measurement results from data points has to be correctly chosen. For dimensional and size measurement, LSQ fitting (best fitting/Gaussian fitting) should be used. Meanwhile for geometric measurement, Based on ISO 1101 and ASME Y14.5, MZ fitting (MinMax fitting or Chebyschev fitting) should be selected.

Chapter 5

General conclusion and future works

In this study, there are two main results which have been presented. The first is procedure and calibrated artifact for performance verification of focus-variation based instrument, both for 3-axis and 4-axis configurations. Secondly, uncertainty characterization to study the influence factors which affect the results of focus-variation based and a simulation approach, as well as its validation, to estimate measurement uncertainty have been presented. In addition, improvement in LSQ fitting for non linear geometries, automatic measurement algorithms for certain measurement, and case studies are also discussed.

The proposed procedure and artifacts for performance verification comply with ISO 10360-8 and ISO 10360-3. The verification is separated into different procedure and artifacts for each 3-axis and 4-axis configuration. In 3-axis configuration, total measuring volume of the instrument is 100 x 100 x 100 mm. A reduce in volume is observed if the instrument is set into 4-axis configuration since the rotational-axis occupied part of the total measuring volume. In this configuration, the measuring volume becomes 40 x 40 x 40 mm to avoid the collision among the objective nose-piece, work piece and the rotational-axis unit. A hybrid artifact which can be used to verified both the performance for length measurement (ISO 10360-8) and rotational axis (ISO 10360-3) has also been reported. The procedures and artifacts are useful for both instrument manufacturers and users.

The results from uncertainty characterization show that measurement by means of

FVM instrument is affected by many factors. The influence factors are grouped into four: Environment and drift (ambient light, drift), procedure (different objective lens, multi-position, stitching), instrument parameters (vertical and lateral resolution, exposure, contrast), and part shape and illumination (peak-valley shape, material types, illumination types). All of them are statistically significant in affecting the measurement results except the ambient light.

The proposed simulation-based approach to estimate measurement uncertainty comply to ISO 15530-4 is a suitable method to estimate task-specific measurement uncertainty, especially in non-contact measurement. The proposed method considers the correlation among points obtained by the optical instrument. Thanks to the spatial statistic method of Gaussian process, the error of a point can be modeled and simulated by taking into account the correlation among points. Parameters for the error simulation have to be estimated separately for each material type, since each material have different response to the incident light. As such, different material will have different response by the instrument. The validation is carried out and the results show that the simulated uncertainty have a good agreement with a real measurement with the optical instrument.

In addition, an improvement to the LSQ fitting of non-linear geometry is presented. The idea is to refine the initial guest of the solution such that it is near to the optimal solution since standard LSQ method is prone to be trapped in local optima in the searching process for the optimum value. Automatic perpendicularity measurement and rake-angle measurement of micro turning tool from the obtained point cloud are also presented. Finally, case studies are presented to apply the proposed simulation approach in estimating measurement uncertainty and measuring algorithm. From the case study, the simulated uncertainty is verified by calculating the E_n value (based on ISO 15530-4) which is more than 95% is less than one.

There are aspects which have to be further investigated and studied for future works. Procedure and artifact for performance verification involving simultaneous movement of translational and rotational axis is needed to quantify the instrument error while measuring this kind of measurement, for example cylindrical tool measurement. From the result comparison obtained by optical and contact instrument, it is observed that the measurement results of geometric tolerance verification by optical instrument are always higher than the calibrated value obtained by contact CMM. Subsequently, a

bias can be observed. Hence, this bias has to be studied such that a compensation technique can be applied. Finally, regarding the uncertainty estimation by means of simulation method (ISO 15530-4), it is highly computational intensive. A method to run the simulation more efficient should be developed such as utilizing parallel processing technique.

References

JCGM 100:2008. Evaluation of measurement data guide to the expression of uncertainty in measurement (gum). Technical report, JCGM, 2008. xvii, 42, 59, 74, 80, 94

B. Acko. Experimental analysis of uncertainty of squareness calibration on a co-ordinate measuring machine. In *Proceeding of IMEKO World Congress, June 22-27, Dubrivnik, Croatia, pp. 1306-1309..*, 2003. 74

B. Acko, M. McCarthy, F. haertig, and B. Buchmeister. Standard for testing freeform measurement capability of optical and tactile coordinate measuring machines. *Measurement Science and Technology*, 23:1–13, 2012. 32

F. Aggogeri, G. Barbato, E. M. Bariani, G. Genta, and R. Levi. Measurement uncertainty assesment of coordinate measuring machines by simulation and planned experimentation. *CIRP Journal of Manufacturing Science and Technology*, 4:51–56, 2011. 82

L. Alting, F. Kimura, H. N. Hansen, and G. Bissacco. Micro engineering. *CIRP Annals Manufacturing Technology*, 52, No. 2:635–657, 2003. 5

G. T. Anthony, H. M. Anthony, B. Bittner, B. P. Butler, M. G. Cox, R. Drieschner, R. Ellingsen, A. B. Forbes, H. Gross, S. A. Hannaby, P. M. Harris, and J. Kok. Reference software for finding chebyschev best-fit geometrc elements. *Precision Engineering*, 19:28–36, 1996. 196, 201

A. Armillotta and Q. Semeraro. *Geometric Tolerances Specification, in Colosimo, B. M., Senin, N. (Eds), Geometric Tolerances-Impact on Product Design, Quality Inspection and Statistical Process Monitoring-Chapter 1.* Springer-Verlag, London, UK, 2011. 193

ASMEY14.5. Dimensioning and tolerancing. Technical report, ASME, 2009. 157, 193, 194, 196

ASMEY14.5.1. Mathematical definition of dimensioning and tolerancing principles. Technical report, ASME, 1994. 91, 157, 194, 196

J. M. Baldwin, K. D. Summerhays, D. A. Campbell, and R. P. Henke. Application of simulation software to coordinate measurement uncertainty evaluatons. *Measure*, 2, No. 4:40–52, 2007. 82

REFERENCES

A. Balsamo, M. Di Ciommo, R. Mugno, B. I. Rebaglia, E. Ricci, and R. Grella. Evaluation of cmm uncertainy through monte carlo simulation. *CIRP Annals Manufacturing Technology*, 48, No. 1:425–428, 1999. 82

BIPM, ISO, IEC, IFCC, IUPAC, IUPAP, and OIML. *International Vocbulary of Metrology Basic and General Concepts and Associated Terms VIM 3rd ed.* JCGM, 2008. 1, 2, 23

F. Blateyron. New 3d parameters and filtration techniques for surface metrology. Technical report, Digital Surf, 2006. 80

P. Blenko, G. Kos, F. Varady, L. Andor, and R. Martin. Constrained fitting in reverse engineering. *Comouter Aided Geometric Design*, 19:173–205, 2002. 196

R. K. Burdick, C. M. Borror, and D. C. Montgomery. *Design and Analysis of Gauge R&R Studies.* SIAM: USA, 2005. 29

S. Carmignato and E. Savio. Traceable volume measurements using coordinate measuring system. *CIRP Annals Manufacturing Technology*, 60, No. 1:519–522, 2011. xi, 9, 76, 78, 79

S. Carmignato, A. Voltan, and E. Savio. Metrological performance of optical coordinate measuring machine under industrial conditions. *CIRP Annals-Manufacturing Technology*, 59, No. 1:497–500, 2010. ix, 28, 76

K. Carr and P. Ferreira. Verification of form tolerances part 1: Basic issues, flatness, and straightness. *Precision Engineering*, 17:131–143, 1995a. 196

K. Carr and P. Ferreira. Verification of form tolerances part 2: cylindricity and straightness of a median line. *Precision Engineering*, 17:144–156, 1995b. 196

M. G. Cox, A. B. Forbes, and P. M. Harris. Discussion of five examples of assessment and expression of measurement uncertainty by antonio possolo. *Applied Stochastic Models in Business and Industry*, 2013. 73

N. A. C. Cressie. *Statistics for spatial data.* John Wiley and Sons: New York, 1993. 87, 88

R. Danzl, F. Helmli, and S. Scherer. Focus variation a robust technology for high resolution optical 3d surface metrology. *Strojniski Vestnik Journal of Mechanical Engineering*, 57, No. 3:245–256, 2010. 18

L. De Chiffre and H. N. Hansen. Metrological limitations of optical probing techniques for dimensional measurements. *CIRP Annals Manufacturing Technology*, 44, No. 1:501–504, 1995. 115

D. Dornfeld, S. Min, and Y. Takeuchi. Recent advances in mechanical micromachining. *CIRP Annals - Manufacturing Technology*, 55, No. 2:745–768, 2006. 168, 169

B. Van Drop, H. Haitjema, F. Delbressine, R. Bergmans, and P. Schellekens. Virtual cmm using monte carlo methods based on frequency content of the error signal. In *Proceeding of SPIE 4401, Recent Development in Traceable Dimensional Measurement.*, 2001. 82

N. Einecke, S. Rebhan, and J. Eggert. Direct surface fitting. In *Proceeding of International Conference on Computer Vision Theory and Applications.*, 2010. 195

C. J. Evans. Uncertainty evaluation for measurements of peak-to-valley surface form errors. *CIRP Annals - Manufacturing Technology*, 57, No. 1:509–512, 2008. 82, 127

D. Forsyth and A. Zisserman. Mutual illumination. In *Proceeding of IEEE conference on CVPR, 4-8 June 1989, Sandiego, California, pp. 466-473.*, 1989. 115

D. A. Forsyth and J. Ponce. *Computer Vision: A Modern Approach.* Pearson Prentice-Hall: New Jersey, USA, 2003. 97

S. Gasparin, H. N. Hansen, and G. Tosello. Traceable surface characterization using replica molding technology. Technical report, Department of Mechanical Engineering, Denmark Technical University, 2010a. 76, 79

S. Gasparin, G. Tosello, H. N. Hansen, I. Di Vora, S. Priante, and S. Sinesi. Replication quality control of metal and polymer micro sturctred optical surfaces. Technical report, Department of Mechanical Engineering, Denmark Technical University, 2010b. 76, 79

N. V. Gestel, S. Cuypers, P. Bleys, and J. P. Kruth. A performance evaluation test for laser line scanners on cmms. *Optics and Laser in Engineering*, 47:336–342, 2009. x, 28, 29, 119

C. L. Giusca, R. K. Leach, and A. B. Forbes. A virtual machine-based uncertainty evaluation for a traceable areal surface texture measuring instrument. *Measurement*, 44:988–993, 2011. 82

C. L. Giusca, J. D. Claverley, W. Sun, R. K. Leach, F. Helmli, and M. P. J. Chavigner. Practical estimation of measurement noise and flatness deviation on focus variation microscope. *CIRP Annals Manufacturing Technology*, 64, No. 1:545–548, 2014. 105, 127

G. Guennebaud and M. Gross. Algebraic point set surfaces. *ACM Transaction on Graphics*, 26, No. 3:1–9, 2007. 200

A. Gusel, B. Acko, and V. Mudronja. Measurement uncertainty in calibration of measurement surface plates flatness. *Strojniski vestnik Journal of Mechanical Engineering*, 2009. 74

H. Haitjema, B. Van Drop, M. Morel, and P. H. J. Schellekens. Uncertainty estimation by the concept of virtual instruments. In *Proceeding SPIE 4401, Recent Developments in Traceable Dimensional Measurements.*, 2001. 81

B. Hamann. Curvature approximation for triangulated surface. *Computing*, 8:139–153, 1993. 169

REFERENCES

H. N. Hansen, K. Carneiro, H. haitjema, and L De Chiffre. Dimensional micro and nano metrology. *CIRP Annals Manufacturing Technology*, 55, No. 2:721–743, 2006. 1, 9

F. Hartig and M. Krystek. Correct treatment if systematic errors in the evaluation of measurement uncertainty. In *Proceeding of ISMTII Russia, pp. 16-19.*, 2009. 82

C. J. Hellier and M. Shakinozsky. *Handbook of Nondestructive Evaluation, 2nd Ed.* McGraw-Hill Education: USA, 2012. ix, 7, 8

F. Hiersemenzel, J. D. Claverley, J. Singh, J. N. Petzing, F. Helmli, and R. K. Leach. Iso compliant reference artifacts for the verification of focus variation-based optical micro-coordinate measuring machines. In *Proceeding of the 13th euspen International Conference, Berlin, May 2013.*, 2013. 31

J. Hiller and L. M. Reindl. A computer simulation platform for the estimation of measurement uncertainties in dimensional x-ray computed tomography. *Measurement*, 45:2166–2182, 2012. xi, 82, 83

R. J. Hocken, N. Chakraborty, and C. Brown. Optical metrology of surfaces. *CIRP Annals Manufacturing Technology*, 54, No. 2:169–183, 2005. 9

T. H. Hopp. Computational metrology. *ASME Manufacturing Review*, 1:1–11, 1993. 193

G. Q. Huang, A. Zhang, and X. Liu. A supply chain configuration model for reassessing global manufacturing in china. *Journal of Manufacturing Technology Management*, 24, No. 5, 2013. 5

C. Huber-Carol, N. Balakrishnan, M. S. Nikulin, and M. Mesbah. *Goodness-of-Fit Tests and Model Validity.* Springer: USA, 2002. 100

S. Ibaraki and W. Knapp. Indirect measurement of volumetric accuracy for three-axis and five-axis machine tools: A review. *International Journal of Automation Technology*, 6, No. 2:110–124, 2012. 2

ISO10360-11. Geometrical product specifications (gps) -acceptance and reverification tests for coordinate measuring machines (cmm) -part 11: Computed tomography. Technical report, ISO/WD, 2011. 21, 24

ISO10360-2. Geometrical product specifications (gps) -acceptance and reverification tests for coordinate measuring systems (cms) -part 2: Cmms used for measuring linear dimension. Technical report, ISO, 2009. 38

ISO10360-3. Geometrical product specifications (gps) -acceptance and reverification tests for coordinate measuring systems (cms) -3: Cmms with rotation table. Technical report, ISO, 2007. x, 51, 52, 55, 57, 68

ISO10360-4. Acceptance and re-verication test for coordinate measuring machines - part 4: Cmm used in scanning measuring mode. Technical report, ISO, 2010. 203

ISO10360-5. Acceptance and re-verication test for coordinate measuring machines - part 5: Cmm using single and multiple styluses contacting probing system. Technical report, ISO, 2010. 203

ISO10360-7. Geometrical product specifications (gps) - acceptance and reverification tests for coordinate measuring machines (cmm) -part 7: Cmms equipped with imaging probing systems. Technical report, ISO, 2011. 21, 24

ISO10360-8. Geometrical product specifications (gps) -acceptance and reverification tests for coordinate measuring systems (cms) -part 8: Cmms with optical distance sensors. Technical report, ISO, 2013. ix, 21, 23, 24, 25, 27, 34, 37, 45, 49, 55, 66, 117, 122, 167

ISO10360-9. Geometrical product specifications (gps) -acceptance and reverification tests for coordinate measuring systems (cms) - part 9: Cmms with multiple probing systems. Technical report, ISO, 2011. 21

ISO1101. Geometrical product specifications (gps) geometrical tolerancing tolerances of form, orientation, location, and run out. geneva, switzerland: International organization for standardization. Technical report, ISO, 2004. 157, 193, 194, 196

ISO14253-1. Geometrical product specification (gps)- inspection by measurement of workpieces and measuring equipment-part 1: Decision rules for proving conformance or non-conformance with specifications. Technical report, ISO, 1998. 4, 73

ISO14253-2. Geometrical product specifications (gps) inspection by measurement of workpieces and measuring equipment part 2: Guidance for the estimation of uncertainty in gps measurement, in calibration of measuring equipment and in product verification - first edition. Technical report, ISO, 2011. 75, 80

ISO16610-1. Geometrical product specifications (gps) filtration part 1: Overview and basic concepts. Technical report, ISO, 2006. 94

ISO16610-61. Geometrical product specifications (gps) filtration part 61: Linear areal filters-gaussian filters. Technical report, ISO, 2012. 94

ISO16610-71. Geometrical product specifications (gps) filtration part 71: Robust areal filters: Gaussian regression filters. Technical report, ISO, 2014. 94, 96

ISO25178-6. Geometrical product specifications (gps) - surface texture: Areal - part 6: Classification of methods for measuring surface texture. Technical report, ISO, 2010. 11, 23

ISO25178-602. Geometrical product specifications (gps) - surface texture: Areal - part 602: Nominal characteristics of non-contact (confocal chromatic probe) instruments. Technical report, ISO, 2010. ix, 12

REFERENCES

ISO25178-603. Geometrical product specifications (gps) - surface texture: Areal - part 603: Nominal characteristics of non-contact (phase shifting interferometric microscopy) instruments. Technical report, ISO, 2011. ix, 13, 14

ISO25178-604. Geometrical product specifications (gps) - surface texture: Areal - part 604: Nominal characteristics of non-contact (coherence scanning interferometry interferometry) instruments. Technical report, ISO, 2011. ix, 14

ISO25178-605. Geometrical product specifications (gps) - surface texture: Areal - part 605: Nominal characteristics of non-contact (point autofocus probe) instruments. Technical report, ISO, 2011. ix, 15, 16

ISO3290-1. Rolling bearings-balls. part 1: Steel balls. geneva, switzerland: International organization for standardization. Technical report, ISO, 2008. 36, 53, 118, 167

ISO/DIS25178-606. Geometrical product specifications (gps) surface texture: Areal part 61: Nominal characteristics of non-contact (focus variation) instruments. Technical report, ISO, 2013. 17

ISO/DTS15530-2. Geometrical product specifications (gps) - coordinate measuring machines (cmm): Technique for determining the uncertainty of measurement - part 2: Use of multiple measurement strategies. Technical report, ISO, 2003. 74

ISO/TS15530-1. Geometrical product specifications (gps) - coordinate measuring machines (cmm): Technique for determining the uncertainty of measurement - part 1: Overview and metrological characteristic. Technical report, ISO, 2013. 3, 73, 74

ISO/TS15530-3. Geometrical product specifications (gps) - coordinate measuring machines (cmm): Technique for determining the uncertainty of measurement - part 3: Use of calibrated workpieces or measurement standards. Technical report, ISO, 2011. 74, 75, 78, 80, 84

ISO/TS15530-4. Geometrical product specifications (gps) - coordinate measuring machines (cmm): Technique for determining the uncertainty of measurement - part 4: Evaluating task-specific measurement uncertainty using simulation. Technical report, ISO, 2008. 74, 76, 80, 84

B. L. W. Jiang. Optimizing complex functions by chaos search. *Cybernetic System*, 29, No. 4: 1366–13751, 1998. 214, 224

X. Jiang. A decomposition approach to geometric fitting. In *IAPR Workshop on Machine Vision Applications, November 28-30, 2000, Tokyo, Japan. pp. 467-470.*, 2000. 195

X. J. Jiang and D. J. Whitehouse. Technological shift in surface metrology. *CIRP Annals Manufacturing Technology*, 61, No. 2:815–836, 2012. 6

A. Kawalec and M. Magdziak. Usability assessment of selected method of optimization for some measurement task in coordinate measurement technique. *Measurement*, 45:2330–2338, 2012. 228

J. P. Kruth, N. Van Gestel, P. Bleys, and F. Welkenhuyzen. Uncertainty determination for cmms by monte carlo simulation integrating feature form deviations. *CIRP Annals Manufacturing Technology*, 58, No. 1:463–466, 2009. 82, 145, 213

J. P. Kruth, M. Bartscher, S. Carmignato, L De Chiffre, and A. Weckenmann. Computed tomography for dimensional metrology. *CIRP Annals Manufacturing Technology*, 60, No. 2: 821–842, 2011. ix, 8, 9

M. krystek. Measurement uncertainty propagation in the case of filtering in roughness measurement. *Measurement Science and Technology*, 12:63–67, 2001. 80

H. Kunzmann, T. Pfeifer, R. Schmitt, H. Schwenke, and A. Weckenmann. Productive metrology - adding value to manufacture. *CIRP Annals Manufacturing Technology*, 54, No. 2:155–168, 2005. 3

R. Leach and H. Haitjema. Bandwith characteristics and comparisons of surface texture measuring instruments. *Measurement Science and technology*, 21:9pp, 2010. 10, 11, 84

R. K. Leach. *Fundamental Principles of Engineering Nanometrology.* Elsevier: New York, 2009. 2, 73

R. K. Leach. *Optical Measurement of Surface Topography.* Springer Verlag: Berlin, 2011. ix, 2, 11, 13, 15, 16, 17, 18, 19, 20, 21, 36

R. K. Leach. *Characterization of areal surface texture.* Springer Verlag: Berlin., 2013. 94

C. H. Loch, L. Van der Heyden, L. N. Huchzermeier, and C. Escalle. *Industrial excellence: Management quality in manufacturing.* Springer: London, 2003. 1

Y. Z. Luo, G. J. Tang, and N. L. Shou. Hybrid approach for solving systems of nonlinear equations using chaos optimization and quasi-newton method. *Applied Soft Computing*, 8, No. 2:1068–1073, 2008. 209

F. Marinello, E. Savio, S. Carmignato, and L De Chiffre. Calibration artifact for the microscale with high aspect ratio: The fiber gauge. *CIRP Annals Manufacturing Technology*, 57, No. 1:497–500, 2008. 28

D. W. Marquardt. An algorithm for least-squares estimation of nonlinear parameters. *Journal of Society of Industrial Applied Mathematic*, 11, No. 2:431–441, 1963. 195, 205

T. Masuzawa. State of the art of micromachining. *CIRP Annals Manufacturing Technology*, 49, No. 2:473–488, 2000. 5

REFERENCES

A. Mea, L. Profumo, and A. Rossi. Optimum dataset size and search space for minimum zone roundness evaluation by genetic algorithm. *Measurement Science Review*, 13, No. 3:100–107, 2013. 198

D. C. Montgomery. *Design and Analysis of experiment.* John Wiley and Sons: New York, 2001. 83, 101

G. Moroni and S. Petro. Geometric tolerance evaluation: A discussion on minimum zone fitting algorithms. *Precision Engineering*, 32:232–237, 2008. 90, 197

G. Moroni and S. Petro. *Coordinate Measuring Machine Measurement Planning, in Colosimo, B. M., Senin, N. (Eds), Geometric Tolerances-Impact on Product Design, Quality Inspection and Statistical Process Monitoring-Chapter 4.* Springer-Verlag, London, UK, 2011. 194

G. Moroni and S. Petro. Automatic cutting edge detection for a cylindrical mill. In *Proceeding of VRAP 2013, Leira, Portugal, pp. 457-461.*, 2013. xv, 202

G. Moroni and S. Petro. Optimal inspection strategy planning for geometric tolerance verification. *Precision Engineering*, 38, No. 1:71–81, 2014. 82

G. Moroni, S. Petro, and T. Tolio. Early cost estimation for tolerance verification. *CIRP Annals Manufacturing Technology*, 60, No. 1:195–198, 2011. 3

E. Morse. *Specification of Design Intent: Introduction to Dimensioning and Tolerancing, in Hocken R. J., Pereira, P. H (Eds), Coordinate Measuring Machines and Systems (2nd Edition)-Chapter 2.* CRC Press, Boca raton, Florida, USA, 2012. 193

P. Muller, Angela Cantatore, Jan L. Andreasen, Jochen Hiller, and L De Chiffre. Computed tomography as a tool for tolerance verification of industrial parts. *Procedia CIRP*, 10:125–132, 2013. 80

J. C. Nash. *Compact Numerical Methods for Computers Linear Algebra and Function Minimization.* Adam Higler Ltd: Bristol., 1979. 205, 208

S. K. Nayar and Y. Nakagawa. Shape from focus. *IEEE Transactions on Pattern Analysis and Machine Intelligence*, 16, No. 8:824–831, 2011. 18

U. Neuschaefer-Rube, M. Neugebauer, W. Ehrig, M. Bartscher, and U. Hilpert. Tactile and optical microsensors: test procedures and standards. *Measurement Science and Technology*, 19:5pp, 2008. 30, 31, 32

U. Neuschaefer-Rube, M. Neugebauer, T. Dziomba, H. U. Danzebrink, L. Koenders, and H. Bosse. New developments of measurement standards and procedures for micro and nanometrology at the ptb. In *11th International Symposium on Measurement and Quality Control 2013, September 11-13, Cracow-Kielce, Poland*, 2013. 29, 32

A. Ontiveros, J. A. Yague-Fabra, S. Jimenez, G. Tosello, S. Gasparin, A. Pierobon, S. Carmignato, and H. N. Hansen. Dimensional measurement of micro-molded parts by computed tomography. *Measurement Science and Technology*, 23:1–9, 2012. 80, 81

E. Pairel. Three-dimensional metrology with the virtual fitting gauges. In *Proceeding of 11th CIRP International Conference on Computer Aided Tolerancing, Annecy, France.*, 2009. 197

S. Petro and G. Moroni. Modeling of surfaces subject to orientation tolerances. In *Proceeding of the ASME 2010 10th Biennial Conference on Engineering Systems Design and Analysis, ESDA 2010, 12-14 July, Istanbul, Turkey.*, 2010. 160

S. D. Philips, B. Bordchart, A. J. Abackerli, C. Shakarji, D. Sawyer, P. Muray, B. Rasnick, K. D. Summerhays, J. M. Baldwin, R. P. Henke, and M. P. Henke. The validation of cmm task specific measurmeent uncertainty software. In *Proceeding of ASPE Summer Topical Meeting CMM, USA.*, 2003. 81, 85

B. T. Phong. Illumination for computer generated pictures. *Communication of the ACM: Graphics and Image Processing*, 18, No. 6:311–317, 1975. 115

A. Possolo. Five examples of assessment and expression of measurement uncertainty. *Applied Stochastic Models in Business and Industry*, 2013a. 73

A. Possolo. Five examples of assessment and expression of measurement uncertainty - rejoinder. *Applied Stochastic Models in Business and Industry*, 2013b. 73

R. L. Rardin. *Optimization in Operation Research.* Addison-Wesley: Addison Wesley, 2006. 208, 209

S. Reisinger, S. Kasperls, M. Franz, J. Hiller, and U. Schmid. Simulation-based planning of optimal condition for industrial computed tomography. In *International Symposium on Digital Industrial Radiology and Computed Tomography, pp. 1-8.*, 2011. 82

A. Rossi and M. Lanzetta. Optimal blind sampling strategy for minimum zone roundness evaluation by metaheuristics. *Precision Engineering*, 37, No. 2:241–247, 2013. 198

A. Rossi, M. Antonetti, M. Barloscio, and M. Lanzetta. Fast genetic algorithm for roundness evaluation by the minimum zone tolerance (mzt) method. *Measurement*, 44:1243–1252, 2011. 198

C. Rusu, M. Tico, P. Kuosmanen, and E. J. Delp. Classical geometrical approach to circle fitting review and new developments. *Journal of Electronic Imaging*, 12, No. 1:179–193, 2003. 201

G. L. Samuel and M. S. Shunmugam. Evaluation of straightness and flatness error using computational geometry techniques. *Computer-Aided Design*, 31:829–843, 1999. xv, 198, 199

REFERENCES

G. L. Samuel and M. S. Shunmugam. Evaluation of circularity from coordinate and form data using computational geometry techniques. *Precision Engineering*, 24:251–263, 2000. xv, 198, 199

G. L. Samuel and M. S. Shunmugam. Evaluation of sphericity error from coordinate measuring data using computational geometry techniques. *Computer Methods in Applied Mechanics and Engineering*, 190:6765–6781, 2001. 198

G. L. Samuel and M. S. Shunmugam. Evaluation of sphericity error from form data using computational geometry techniques. *International Journal of Machine Tools and Manufacture*, 42:405–416, 2002. 198

G. L. Samuel and M. S. Shunmugam. Evaluation of circularity and sphericity from coordinate measuring data. *Journal of Materials Processing Technology*, 139:90–95, 2003. 198

E. Savio. Uncertainty in testing the metrological performances of coordinate measuring machines. *CIRP Annals Manufacturing Technology*, 55, No. 1:535–538, 2006. 47, 55

E. Savio and L De Chiffre. An artefact for traceable freeform measurements on coordinate measuring machines. *Precision Engineering*, 26:58–68, 2002. 31

E. Savio, H. N. Hansen, and L De Chiffre. Approaches to the calibration of freeform artifacts on coordinate measuring machines. *CIRP Annals Manufacturing Technology*, 51, No. 1:433–436, 2002. 31

R. Schmitt and C. Niggemann. Uncertainty in measurement for x-ray-computed tomography using calibrated work pieces. *Measurement Science and Technology*, 21:1–9, 2010. 80, 83

H. Schwencke, W. Knapp, H. Haitjema, A. Weckenman, R. Schmitt, and F. Delbressine. Geometric error measurement and compensation of machines an update. *CIRP Annals Manufacturing Technology*, 57, No. 2:660–675, 2008. 2

H. Schwenke, B. R. L. Siebert, F. Waldede, and H. Kunzman. Assesment of uncertainties in dimensional metrology by monte carlo simulation: Proposal of a modular and visual software. *CIRP Annals Manufacturing Technology*, 49, No. 1:395–398, 1999. 82

H. Schwenke, U. Neuschaefer-Rube, T. Pfeifer, and H. Kunzman. Optical methods for dimensional metrology in production engineering. *CIRP Annals Manufacturing Technology*, 51, No. 2:685–699, 2002. 9

C. M. Shakarji. Least-squares fitting algorithms of the nist algorithm testing system. *Journal of Research NIST*, 103:633–641, 1998. 90, 91, 194, 195, 206, 213

C. M. Shakarji. Reference algorithms for chebyschev and one-sided data fitting for coordinate metrology. *CIRP Annals - Manufacturing Technology*, 53, No. 1:439–442, 2004. 197

C. M. Shakarji. *Coordinate Measuring System Algorithms and Filter, in Hocken R. J., Pereira, P. H (Eds), Coordinate Measuring Machines and Systems (2nd Edition)*. Boca raton, Florida, USA, 2012. xiv, 196, 197, 199

F. Sukowski and N. Uhlmann. Monte carlo simulations in ndt. In *Applications of Monte Carlo Method in Science and Engineering, Prof. Shaul Mordechai (Ed.), ISBN: 978-953-307-681-1, InTech, pp. 1-19.*, 2011. 82

W. P. Syam and I. M. Al-Harkan. Comparison of three meta heuristics to optimize hybrid flow shop scheduling problem with parallel machines. *World Academy of Science, Engineering and Technology*, 62:271–278, 2010. 197, 209

M. S. Tavazoei and M. Haeri. An optimization algorithm based on chaotic behavior and fractal nature. *Computational Applied Mathematic*, 206, No. 2:1070–1081, 2008. 210

G. Tosello, H. N. Hansen, and S. Gasparin. Applications of dimensional micro metrology to the product and process quality control in manufacturing of precision polymer micro components. *CIRP Annals Manufacturing Technology*, 58, No. 1:467–472, 2009. 9, 31, 76, 78

G. Tosello, H. N. Hansen, F. Marinello, and S. Gasparin. Replication and dimensional quality control of industrial nanoscale surfaces using calibrated afm measurements and sem image processing. *CIRP Annals Manufacturing Technology*, 59, No. 1:563–568, 2010. 9, 76, 77, 78

T. B. Trafalis and S. Kasap. A novel metaheuritics approach for continuos global optimization. *Journal of Global Optimization*, 23:171–190, 2002. 198, 228

D. J. Whitehouse. *Handbook of surface and nanometrology.* CRC Press: UK, 2011. 6

D. E. Whitney. *Mechanical Assemblies: Their Design, Manufacture, and Role in Product Development.* Oxford University Press:USA., 2004. 204

R. G. Wilhelm, R. Hocken, and H. Schwenke. Task specific uncertainty in coordinate measurement. *CIRP Annals Manufacturing Technology*, 50, No. 2:553–563, 2001. xi, 3, 73, 80, 81, 82, 86

J. A. Yague-Fabra, S. Ontiveros, R. Jimenez, S. Chitchian, G. Tosello, and S. Carmignato. A 3d edge detection technique for surface extraction in computed tomography for dimensional metrology application. *CIRP Annals - Manufacturing Technology*, 62:531–534, 2013. 80

D. Yang, G. Li, and G. Cheng. On the efficiency of chaos optimization algorithms for global optimization. *Chaos, Solitons and Fractals*, 34, No. 4:1366–13751, 2009. 210

Appendix A

Performance improvement in non-linear geometric fitting

A.1 State of the art

Optical instrument is able to obtain many points. Hence, further process has to be carried out to obtain the final measurement result. The basic process is to associate (fitting) these points with specific feature. Data association is the basic function of data analysis software [Hopp [1993]]. Hence, algorithm has a fundamental role in the whole measurement cycle.

A.1.1 Fitting and automatic-measurement algorithm

There are two main functions of measurement algorithm: association (fitting) of points to a specific geometry and specific measurement algorithm. Firstly, fitting of points to geometry has to be carried out to verify both dimensional and geometric tolerance. In mechanical tolerancing, geometric tolerance is important in offering a better way in communicating the design intent of the designer [ISO1101 [2004], ASMEY14.5 [2009], Armillotta and Semeraro [2011], Morse [2012]]. Secondly, specific measurement algorithm is used to be able to automatically calculate a certain measurement task.

Dimensional tolerance is defined by "+/-" symmetric-tolerance (two-sided tolerance), for example: length tolerance, diameter/radius tolerance, angle tolerance, etc. Verification of dimensional tolerance is straight forward. The ideal geometry is fitted or associated from the obtained point cloud and the derived dimension from this fitted

geometry is compared to its nominal design whether it is inside the tolerance zone or outside the tolerance zone. Only dimensional tolerance is not sufficient to represent the design intent of the designer and can wrongly convey the design message from the designer to the shop floor (manufacturing process). A new paradigm of tolerancing is geometric tolerance. Geometric tolerancing is a language of the designer to talk to the manufacturing engineer. Different with dimensional tolerance, geometric tolerance is a one-sided tolerance system in which only the maximum allowable value is stated and the minimum value is always zero. Geometric tolerances are divided into five main classes: form, profile, orientation, location, and run-out [ISO1101 [2004] and ASMEY14.5 [2009]]. The first two classes are un-related feature tolerance in which there is no datum needed. These types of tolerance are used to tolerance the datum surface. The later three are related-feature tolerance since datum reference is needed in the verification procedure.

The role of geometry association for tolerance verification is illustrated in A.1. Geometry association algorithm can be divided into three classes: Least Square (LSQ)/ Gaussian/ Best) fitting, MinMax (Chebyschev/ Minimum Zone) fitting, and other fitting such as minimum circumscribe, maximum inscribe, etc. This classification is based on the type of objective function. LSQ fitting is used for dimensional tolerance verification. Shakarji [Shakarji [1998]] divides basic geometry into linear (line and plane) and non-linear (circle, sphere, cone, and torus) geometry based on their defining parameter. Other than these basic geometries, they are grouped into free form surface. Meanwhile, MinMax fitting is used for geometric tolerance verification and conform to the description of ASME Y14.5.1-M [ASMEY14.5.1 [1994]].

1. Least Square Fitting (LSQ)/Gaussian)

LSQ fitting is the standard fitting method since it is considered more robust with regard to noise [Moroni and Petro [2011]]. The fundamental idea of LSQ is to minimize the sum of square of the distance function from a point to its fitted geometry. It is formulated as unconstrained non-linear optimization problem:

$$\underset{param}{\arg\min} \quad F \;=\; \sum_{i=1}^{n} d_i^2(param) \tag{A.1}$$

where *param* is the defining parameters of the geometry to be fitted. For line and plane, an optimum solution exists by solving Eigen value problem to fit these geometries

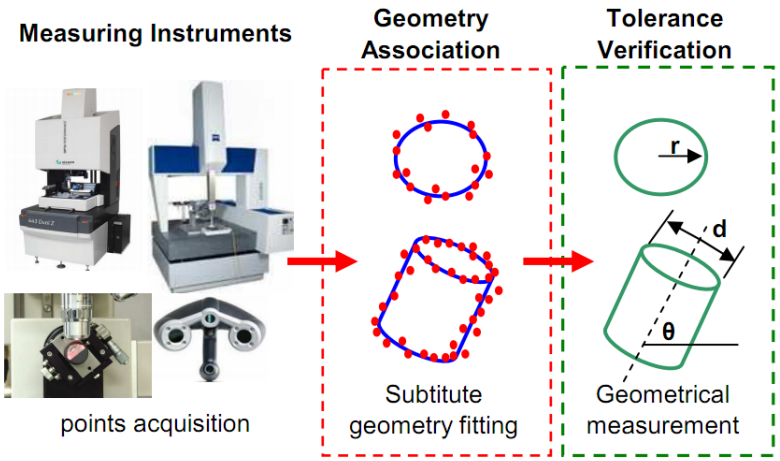

Figure A.1: Geometric fitting is a critical step in metrology.

[Shakarji [1998]]. Meanwhile, other basic geometries are solved by means of iterative algorithm as explained in [Shakarji [1998]] and is as standard LSQ fitting algorithm used in National Institute of Standard and Technology (NIST). This iterative algorithm is based on Levenberg-Marquardt (LM) [Marquardt [1963]].

Beside NIST standard algorithm for solving LSQ fitting, there are also other type of solutions. Jiang [Jiang [2000]] proposed a decomposition approach. The idea is to reduce the number of parameters which should be optimized by decomposed them into smaller optimization problem. By rewriting eq. A.1 as:

$$\vec{a_{opt}} = \arg\min_{a} \sum_{i=1}^{n} d(p_i, f(\vec{a})) \tag{A.2}$$

Optimal parameter vector is defined as $\vec{a_{opt}}$ with size of k number of parameters. $d(p_i, f(\vec{a})$ is the distance cost which should be minimized. p_i is the i-th point and $f(\vec{a})$ is a function defining the geometry. The idea is to decomposed $\vec{a_{opt}}$ having k number of parameter into $\vec{a_1}$ with k_1 number of parameters and $\vec{a_1}$ with $k_1(\cong k - k_1)$ number of parameters. There are $2^n - 2$ total possible decomposition. Hence, it becomes $\vec{a} = \vec{a_1}\vec{a_2}$:

$$\vec{a_{opt}} = \arg\min_{a_1} \left(\sum_{i=1}^{n} d(p_i, f(\vec{a_1}, \vec{a_2})) \right) \tag{A.3}$$

Einecke et al [Einecke et al. [2010]] used Hookes-Jeeves optimization method applied to direct surface fitting from 3D data, instead of common Gauss-Newton step or Steepest-

Decent step. This method is a direct method which does not need derivatives of the objective function. Blenko et al [Blenko et al. [2002]] studied Lagrangian multiplier and sequential constraint satisfaction method for fitting geometry with a constraint. This situation is commonly found in the Computer Aided Design (CAD) system. Their study also noticed the problem of initial value determination to start the iterative processes.

2. MinMax (Chebyschev) fitting

MinMax/Chebyschev fitting is inherently a non-linear optimization problem [Shakarji [2012], Carr and Ferreira [1995a], Carr and Ferreira [1995b]]. This method is best to interpret the tolerance zone based on ASME standard [ASMEY14.5 [2009], ASMEY14.5.1 [1994]] and ISO standard [ISO1101 [2004]]. The implementation of MinMax fitting is called Minimum Zone fitting (MZ). The geometry of MZ fitting is a geometry which lies in the middle of minimum separation of two identical and parallel geometries containing all the data points [Shakarji [2012]]. MZ fitting is defined as a solution of the following non-linear optimization problem:

$$\arg\min_{param} \left(\max_{i} |d_i(param)| \right) \tag{A.4}$$

Eq. A.4 is computationally more expensive to solve compared to LSQ fitting (Eq. A.1). In addition, MZ fitting is less robust to noise compared to the LSQ one. MS fitting is only affected by points on the boundary meanwhile LSQ fitting considers all the points, thus it has an averaging effect. Since MZ fitting is not robust and very sensitive, a careful measurement should be carried out since only a single noise point will greatly affects the fitting results. Fig. A.2 illustrates the different between LSQ fitting and MZ fitting. As can be observed from this figure, MZ fitting is only considering the points on the boundary meanwhile LSQ considers all the points and has an averaging effect. Hence, LSQ suppresses random error in the points. Finally, effective algorithm plays an important role to solve this optimization problem.

Carr and Ferreira [Carr and Ferreira [1995a], Carr and Ferreira [1995b]] elaborated in detail for minimum tolerance zone fitting as stated in ASME Y.14.5 [ASMEY14.5 [2009]]. Anthony et al [Anthony et al. [1996]] proposed a reference algorithm for MZ.

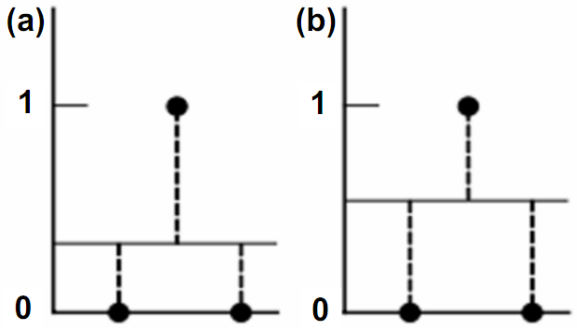

Figure A.2: (a) LSQ fitting (averaging effect) and (b) MZ fitting [Shakarji [2012]].

They convert MZ objective function into constrained linear optimization as:

$$\begin{aligned} &\arg\min_{param} MinS \\ s.t.\ \ &S - d_i(param) \geq 0 \end{aligned} \tag{A.5}$$

Shakarji [Shakarji [2004]] also proposed solution method to solve MZ fitting problem. In this method, he used a heuristic search of simulated annealing (SA) by considering its computational efficiency since SA algorithm is considered as one of efficient meta-heuristic technique [Syam and Al-Harkan [2010]]. His proposed procedure is summarized as follows:

1. Fit the associate geometry to the data by LSQ fitting.
2. Rotate and translate the data based on the computed LSQ fitting.
3. Search for the optimum solution with simulated annealing technique.

Moroni and Petro [Moroni and Petro [2008]] proposed a very efficient algorithm for solving the MZ fitting problem. They call their proposed method as Loop Control Algorithm (LCA) which is a modification of Speeded-up Brute Force Attack algorithm. Their method only considers the points on the border of the tolerance zone. These points are defined as essential points. Their innovative idea directly discards the non-contacting points and chooses the next point to be included in the essential subset as the most external point from the tolerance zone. Pairel [Pairel [2009]] proposed algorithm of virtual gage for checking geometric tolerance.

APPENDIX A. PERFORMANCE IMPROVEMENT IN NON-LINEAR GEOMETRIC FITTING

A computational geometry techniques have been exploited by Samuel and Shunmugam [Samuel and Shunmugam [1999], Samuel and Shunmugam [2000], Samuel and Shunmugam [2001], Samuel and Shunmugam [2002], Samuel and Shunmugam [2003]] for form error evaluation (geometric tolerance verification). Evaluation of straightness and flatness are studied in [Samuel and Shunmugam [1999]]. They used convex-hull method. To compute convex-gull, divide-and-conquer algorithm was implemented. Finally, the minimum zone is calculated as antipodal pairs of the convex hull. Antipodal pair of a convex hull is a pair of points which are supporting parallel line or plane of the convex hull (A.3a). In other words, it can be interpreted as clipper holding the convex hull. Circularity/roundness form error, MI circle and MC circle evaluation are reported in Samuel and Shunmugam [1999], Samuel and Shunmugam [2000]]. The method is based on convex-hull. Equi-distant (Voronoi) diagram (ED) and equi-angular diagram (EA) are used to asses the circularity form error. Illustration of equi-distant and equi-angular line and diagram is presented in A.3b. MC and MI circle are evaluated from the farthest ED and the nearest ED diagram, respectively in A.3c. EA diagram is used for the alternative of evaluating MC and MI circle by the method of limacon. The extension of these ED and EA diagram into sphere form error evaluation are presented in [Samuel and Shunmugam [2001], Samuel and Shunmugam [2002], Samuel and Shunmugam [2003]].

Heuristic search [Trafalis and Kasap [2002]], as a general optimization solver, can also be utilized for MZ evaluation. Genetic Algorithms (GA) is highly utilized to evaluate roundness error are reported in [Rossi et al. [2011], Rossi and Lanzetta [2013], citemea2013]. The GA is modified to improve its effectiveness and efficiency, especially minimizing the computation time for large cloud of sample points. In [[Rossi and Lanzetta [2013]] and Mea et al. [2013]], studies related to optimal blind sampling for roundness to relate and to find the optimum sample size are presented. The fitness function for their GA is defined as:

$$\begin{aligned} MZE &= minR(x,y) \\ &= \begin{cases} min[maxr(x,y,\theta_i) - minr(x,y,\theta_i)] \\ s.t.\ \ (x,y) \in E_{r(x,y,\theta)} \end{cases} \end{aligned} \tag{A.6}$$

3. Other fitting

Besides LSQ fitting and MinMax fitting, there are exist other types of geometric.

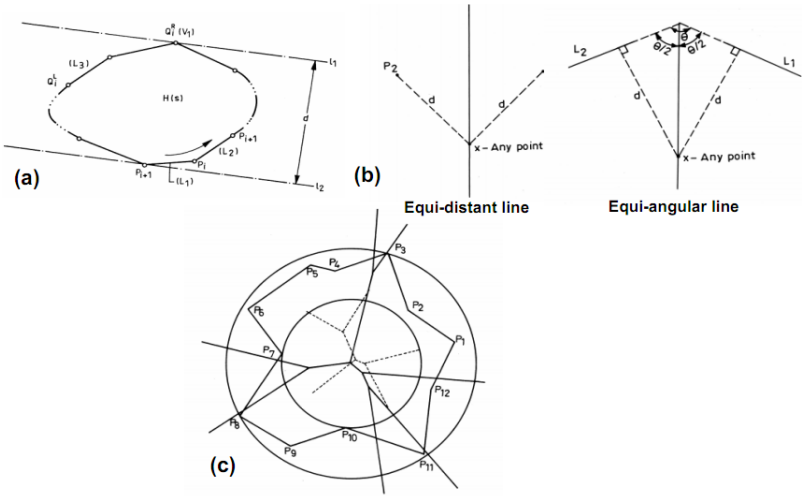

Figure A.3: (a) 2D convex hull which shows the parallel support line from antipodal pairs [Samuel and Shunmugam [1999]] and (b) Illustration of ED and EA diagram [Samuel and Shunmugam [2000]], and (c) MZ fitting from superimposed MC and MI circle fitted by farthest ED and nearest Ed diagram respectively [Samuel and Shunmugam [2000]].

Minimum-total-distance (MTD) fitting [Shakarji [2012]] is a fitting method which solves the following optimization problem:

$$\arg\min_{param} \sum_{i=1}^{n} |d_i(param)| \tag{A.7}$$

MTD fitting is the unsigned version of LSQ fitting. The fundamental idea of this fitting is it is constrained to follow the majority of points. Thus, MTD fitting is considering the median of the data points. This fitting method may useful in the case of associating a datum plane which can simulate the contact between the planar feature of a work piece and a surface plate [Shakarji [2012]]. MTD fitting is depicted in A.4a. From this figure, one can observe that the "false" points (in red) can be neglected by the fitting algorithm.

There are a special fitting method only for certain geometry of circle, sphere and cylinder. These special fittings are Maximum-Inscribed (MI) fitting and Minimum-Circumscribed (MC) fitting (A.4b). They are constrained optimization. MI fitting is

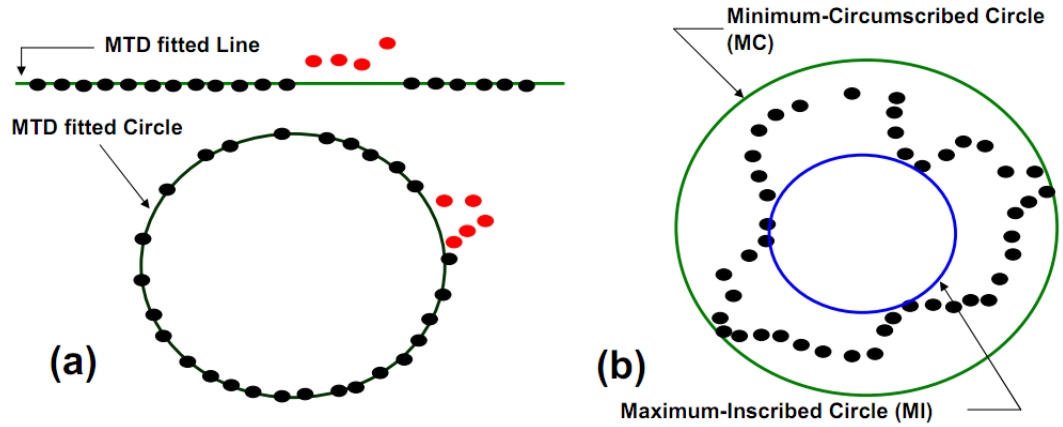

Figure A.4: (a) MTD fitting and (b) MI and MC fitting.

defined as:

$$\begin{aligned} &\underset{param}{arg\ Max}\ r \\ s.t.\ \ &\forall d_i(paramP) \geq 0 \end{aligned} \tag{A.8}$$

While MC fitting is defined as:

$$\begin{aligned} &\underset{param}{\arg\min}\ r \\ s.t.\ \ &\forall d_i(paramP) \leq 0 \end{aligned} \tag{A.9}$$

Gannebaud and Gross [Guennebaud and Gross [2007]] proposed a method to fit a sphere taking advantage of the normal vector of the points. In addition, they use algebraic distance instead of geometric (Euclidean) distance. Algebraic sphere is defined as the 0-isosurface $S_u(x) = [1, x^T, x^T X]u$ where $u = [u_0, u_1, u_2, u_3]$ is the sphere defining parameters. The algebraic sphere function is:

$$u(x) \quad = \quad \underset{u, u\neq 0}{\arg\min} \, ||W^{\frac{1}{2}}(x)Du|| \tag{A.10}$$

where $W(x) = \begin{bmatrix} w_0(x) & 0 & 0 \\ 0 & \ddots & 0 \\ 0 & 0 & w_{n-1}(x) \end{bmatrix}$ is $n \times n$ diagonal weight matrix,

$D = \begin{bmatrix} 1 & p_0^T & p_0^T p_0 \\ \vdots & \vdots & \vdots \\ 1 & p_{n-1}^T & p_{n-1}^T p_{n-1} \end{bmatrix}$ is $n \times (d+2)$ design matrix.

n is the number of points and $w_i(x)$ is weight of the point p_i . Their main goal is to fit a complex surface with algebraic point set surfaces, constructed from algebraic sphere fitting.

Rusu et al [Rusu et al. [2003]] studied and improved weighted total least squares (WTLS) circle fitting by using inversion transformation and providing different weight for each point observation. The WTLS circle fitting is a solution of optimization:

$$\arg\min_{a,b} \sum_{i=1}^{N} w_i[(u_i - \hat{u}_i)^2 + ((v_i - \hat{v}_i)^2] \tag{A.11}$$

where w_i is a certain weight . $(\hat{u}_i, \hat{v}_i)$ is a closest point on a line $v = a + bu$ for a certain point . The coordinate of $(\hat{u}_i, \hat{v}_i)$ is defined as:

$$\hat{u}_i = \frac{bv_i + u_i - ab}{1 + b^2} \quad and \quad \hat{v}_i = a + b\frac{bv_i + u_i - ab}{1 + b^2} \tag{A.12}$$

Beside proposing solution for MZ fitting, Anthony et al [Anthony et al. [1996]] also proposed solution for MI and MC fitting by converting them into constrained linear optimization problem. For MC fitting, the constrained linear optimization becomes:

$$\begin{aligned} &\arg\min_{param} S \\ s.t.\ \ &S - r_i(param) \geq 0 \end{aligned} \tag{A.13}$$

And for MI fitting, it is converted into:

$$\begin{aligned} &\arg\min_{param} S \\ s.t.\ \ &S + r_i(param) \geq 0 \end{aligned} \tag{A.14}$$

The solution by Anthony et al [Anthony et al. [1996]] after converting unconstrained non-linear optimization into constrained linear optimization for MZ, MI, and MC fitting is by applying Kuhn-Tucker first order condition form:

$$\begin{aligned} Feasibility: \\ c_i(u*) \geq 0 \\ Firstorder: \\ \lambda_i* \geq 0 \end{aligned} \tag{A.15}$$

where $u*$ is the parameter to be optimized. The second order condition form is defined as Hessian matrix $H(u*, \lambda*)$. Hence, their solution approach to their algorithm is:

APPENDIX A. PERFORMANCE IMPROVEMENT IN NON-LINEAR GEOMETRIC FITTING

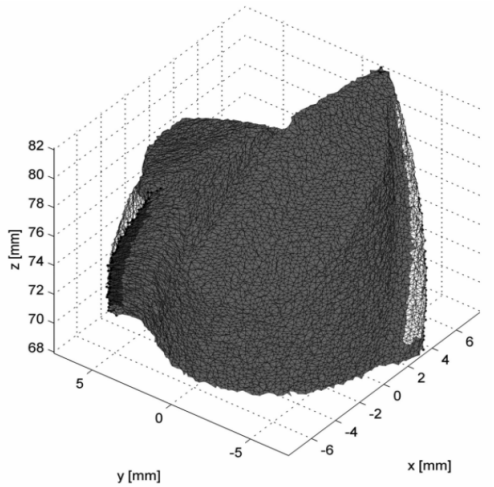

Figure A.5: Automatic cutting edge detection of cylindrical mill [Moroni and Petro [2013]].

1. Form and solve Kuhn-Tucker equations $K(u, \lambda) = 0$ for $u*$ and Lagrange multipliers $\lambda*$.

2. Check the optimality conditions: first order and second order.

3. If $\lambda_i* < 0$ drop a constraint from i^a (for example drop a constraint in which λ_i* is the most negative); If $c_i(u*)$ then drop a constraint to i^a. Return to step 1.

Beside algorithm development for geometry fitting from points, algorithm for automatic measurement of specific measurement-task is also important. This situation involve many 3D noised points which make the procedure is not an easy task. Furthermore, efficient algorithm is needed such that the computation cost is reasonable for industrial application. Only with this procedure, measurement repeatability can be assured. Moroni and Petro [Moroni and Petro [2013]] developed algorithm to automatically segment the edge area of a cylindrical mill. The algorithm starts from triangular-mesh file. It has fundamental contribution for further automatic calculation of tool geometry, such as rake angle as well as tool wear measurement. Fig. A.5 shows the functionality of the developed algorithm.

A.1.2 What is lacking?

Regardless many studies in formulating geometric fitting as well as finding their solution, there are some aspects which needs further investigation. In many situations, the obtained points from the instrument do not cover all or majority of the part surface which will be fitted. Hence, these situations make the fitting procedure more difficult, such as fitting a cylinder from points which only cover half or quarter of the whole cylinder surface. Computation performance of the fitting process is becoming more relevant aspect. The reason is that, non-contact instruments are able to obtained many points, even millions, in one measurement cycle. The algorithm used to compute the fitting process should be efficient so that the measurement result can be obtained in reasonable time, depending on the situation. Finally, from the literature review, more studies are devoted for geometry fitting (association) studies. In fact, since measurands are varying and some of them complex, automatic measurement algorithm is urgently required. Only by this algorithm, measurement repeatability can be guaranteed. Furthermore, for instruments to be used for in-line quality inspection, automatic measurement is required. Automatic measurement from 2D image for in-line inspection of basic geometries, such as diameter, gap width, etc can be found, but for inspection dealing with 3D points is still very rare.

A.2 Non-linear Fitting

There are two types of substitute geometries: linear and non-linear geometry. The grouping criterion is based on their defined parameters. Line (both 2D and 3D) and plane fall into linear geometry, as their defining parameters are linear. On the other hand, other basic geometry such as circle, sphere, cylinder, cone and torus have non-linear parameters defining their shapes. Hence, they are categorized as non-linear geometries. Direct solutions which result in exact method are available for linear geometry fitting. Meanwhile, iterative method should be applied to fit a non-linear geometry. In this section, LS tting of circle, sphere and cylinder will be addressed. Circle and sphere geometries have many applications, for example sphere is a common artifact geometry for calibration of dimensional metrology instruments [ISO10360-4 [2010]],[ISO10360-5 [2010]]. In addition, many mechanical products have rotational functionality which is

constituted in the form of shafts and holes. Cylinder is a geometry representation of these shaft-hole systems [Whitney [2004]].

The basis of LS tting is the minimization of an objective function constituted by a sum of square of errors. Error is defined as the difference between estimated and measured value. In dimensional metrology, error is usually assimilated to the local geometrical deviation, i.e. the orthogonal distance between measured points and the ideal substitute geometry (A.6). LS tting objective function is defined as:

$$\arg\min_{\mathbf{P}} F(\mathbf{P}, \mathbf{x_i}) = \sum_{\mathbf{i=1}}^{\mathbf{N}} \mathbf{d_i^2}(\mathbf{P}) \tag{A.16}$$

where F is the distance function of points $\mathbf{x}$ to the fitted geometry. $\mathbf{x_i}$ is a cloud of n points sampled on a surface and $\mathbf{P}$ is set of parameters on which a distance function $d_i(\mathbf{P})$ depends on, so that $d_i(\mathbf{P})$ is the distance of the i-th point from the substitute geometry defined by $\mathbf{P}$. For the circle, the distance function is ((A.6a left):

$$d_i(\mathbf{x_0}, \mathbf{r}) = ||\mathbf{x_i} - \mathbf{x_0}|| - \mathbf{r} = \sqrt{(\mathbf{x_i} - \mathbf{x_0})^2 + (\mathbf{y_i} - \mathbf{y_0})^2} - \mathbf{r} \tag{A.17}$$

Where $\mathbf{x_0} = [\mathbf{x_0}, \mathbf{y_0}]^\mathbf{T}$ is the circle center, r is the circle radius, and $\mathbf{x_i} = [\mathbf{x_i}, \mathbf{y_i}]^\mathbf{T}$ is the i-th point, and $||\mathbf{x}||$ is -norm of a vector $\mathbf{x}$, e.g. $||\mathbf{v}|| = \sqrt{\mathbf{v_1^2} + \mathbf{v_2^2} + \mathbf{v_3^2}}$. Similarly, for the sphere, the function can be formulated as:

$$d_i(\mathbf{x_0}, \mathbf{r}) = ||\mathbf{x_i} - \mathbf{x_0}|| - \mathbf{r} = \sqrt{(\mathbf{x_i} - \mathbf{x_0})^2 + (\mathbf{y_i} - \mathbf{y_0})^2 + (\mathbf{z_i} - \mathbf{z_0})^2} - \mathbf{r} \tag{A.18}$$

Where $\mathbf{x_0} = [\mathbf{x_0}, \mathbf{y_0}, \mathbf{z_0}]^\mathbf{T}$ is the sphere center, r is the sphere radius, and $\mathbf{x_i} = [\mathbf{x_i}, \mathbf{y_i}, \mathbf{z_i}]^\mathbf{T}$ is the i-th point. The distance function of a point to a cylinder is more complex (see A.6a right):

$$d_i(\mathbf{x_0}, \mathbf{n}, \mathbf{r}) = \mathbf{d_{3dp2Axis}} - \mathbf{r} = \frac{||\mathbf{x_i} - \mathbf{x_0} \times \mathbf{n}||}{||\mathbf{n}||} \tag{A.19}$$

where r is the radius of the cylinder and $d_{3dp2Axis}$ is defined as distance between 3D point $\mathbf{x_i}$ to the axis of cylinder (a straight line). The axis is defined by a point x_0 belonging to it and a direction vector $\mathbf{n}$ (A.6b). It can be observed that the objective function F which has to be minimized is a non-linear multi-modal function which has many local minima and/or maxima.

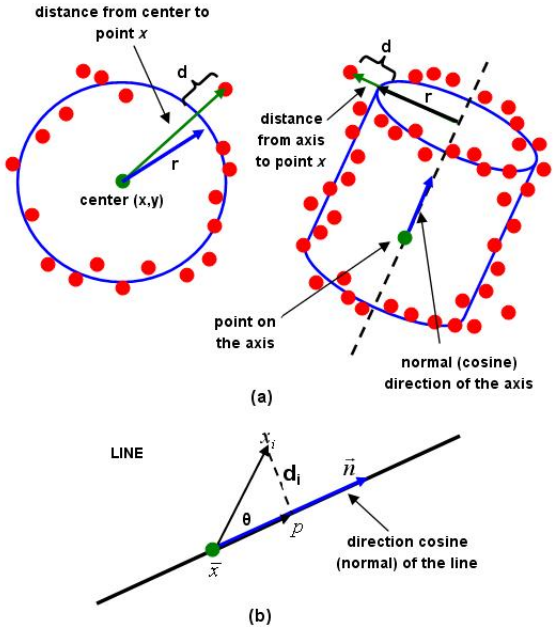

Figure A.6: (a) Definition of point distance for circle (sphere) and cylinder, (b) definition of point distance for 3D-line.

A.3 Levenberg-Marquardt Algorithm

Levenberg-Marquardt (LM) algorithm is a well-known approximation method for solving non-linear least square problems that has applications in many elds [Marquardt [1963],Nash [1979]]. The main principle of LM algorithm is the blending between steepest-decent (gradient search) step method and Gauss-Newton step method. When the current solution is far from the optimal, the LM method acts like a steepest-decent method. Subsequently, LM method will become a Gauss-Newton when the solution is near optimal. The basis of steepest-decent method is searching with regard to the direction of the gradient. Let F be the function to optimize, and x_k be the candidate solution at step k. Since in this case minimization is the problem to solve, the next step in the searching procedure is:

$$x_{k+1} = x_k - \lambda_s \nabla F \tag{A.20}$$

where $\nabla F = (\partial F/\partial x, \partial F/\partial y, \partial F/\partial z)$ is the gradient of the objective function as well as the search direction, and λ_s is the step size which determines how far the next candidate solution will be from the current one. Hence, if the value of λ_s is set very small, then it

will take longer to reach convergence. Otherwise, if the value of λ_s is very large, there is a high probability that the searching process will over-step the optimum value. In Gauss-Newton method, linearization by using Taylor expansion series is deployed. The series are:

$$\nabla f(\mathbf{p}) = \nabla \mathbf{f}(\mathbf{p_0} + (\mathbf{p} - \mathbf{p_0})^{\mathbf{T}} \nabla^{\mathbf{2}} \mathbf{f}(\mathbf{p_0}) + \underbrace{\cdots + \left[(\mathbf{p} - \mathbf{p_0})^{\mathbf{T}}\right]^n \nabla^n f(\mathbf{p_0})}_{\textbf{Higher order form}} \tag{A.21}$$

Commonly, higher order expansions are not considered. Not only the algorithm is more efficient to reach the convergence, but also the form is mathematically tractable to solve $\mathbf{p}$. By setting $\nabla f(\mathbf{p}) = \mathbf{0}$, the next step of the Gauss-Newton can be calculated as:

$$\mathbf{p_{j+1}} = \mathbf{p_j} - (\mathbf{J_d^T J_d})^{-\mathbf{1}} \mathbf{J_d^T d}(\mathbf{p_j}) \tag{A.22}$$

Where $\mathbf{d}(\mathbf{p_j})$ is the vector of the residual (distances) at step j, and $\mathbf{J_d}$ is the Jacobian matrix of this vector of distance functions. Note that Taylor expansion series is accurate only for a small range of region, the so-called trust region. This small region is a region where the non-linear estimation of a function by using Taylor expansion is still reasonably valid. It implies that Gauss-Newton method is valid for searching through a small area of the neighborhood. Subsequently, the method is effective when the initial guess is near the optimum solution.

The LM method combines the advantages of steepest-decent and Gauss-Newton methods. A vector of input parameters $\mathbf{p_0}$, which includes the parameters that will be optimized, is supplied to the LM algorithm, along with matrix $\mathbf{M}$ which is a $n \times 3$ matrix of all the data points, defined as: $[x_1 \quad y_1 \quad z_1; \cdots \quad \cdots \quad \cdots; x_n \quad y_n \quad z_n]$, so that an optimized vector of parameters $\mathbf{p}$ is obtained. The LM method used here is based on the LM used by NIST [Shakarji [1998]] for their algorithm testing system. The LM algorithm is shown in Table A.1.

λ is LM variable, which is increased and decreased by 10 and 0.04, respectively, according to NIST suggestion [Shakarji [1998]]. $\mathbf{J_0}$ is a Jacobian matrix which elements on its i-th row are $\nabla d_i(\mathbf{p_0})$, which are the first-order partial derivatives of d_i respect to each parameter which has to be estimated for each i-th point. For circle, the parameters $\mathbf{p_0}$ are x_0, y_0 of its center and radius r. For sphere, only one additional element z_0 for its 3D position of the center is added to the parameters. Finally, the parameters for cylinder are x_0, y_0, z_0 which is a point on the axis, having vector of cosine direction

Algorithm 1: Levenberg-Marquardt Algorithm	
Input:	Vector $\mathbf{p_0}$ which is the initial guess for the parameter and matrix M which is the point cloud to be fitted.
Output:	Vector $\mathbf{p}$ which is the fitted parameter
1:	Set $\lambda = 0.0001$
2:	DO { decrease λ
3:	set $\mathbf{U} = \mathbf{J_0^T J_0}$
4:	set $\mathbf{v} = \mathbf{J_0^T d(p_0)}$
5:	set $F_0 = \mathbf{d^T(p_0)d(p_0)}$
6:	DO { increase λ
7:	set $\mathbf{H} = \mathbf{U} + \lambda\,(\mathbf{I} + \mathbf{diag(U)})$
8:	solve $\mathbf{Hx} = -\mathbf{v}$
9:	set $\mathbf{p_{new}} = \mathbf{p_0}$; set $F = \mathbf{d^T(p_{new})d(p_{new})}$
10:	IF converge THEN return $\mathbf{p_0} = \mathbf{p_{new}}$
11:	UNTIL $F_{new} < F_0$ or stop criterion is *true*
12:	IF $F_{new} < F_0$ THEN $\mathbf{p_0} = \mathbf{p_{new}}$
13:	UNTIL stop criterion is *true*

Table A.1: LM Algorithm.

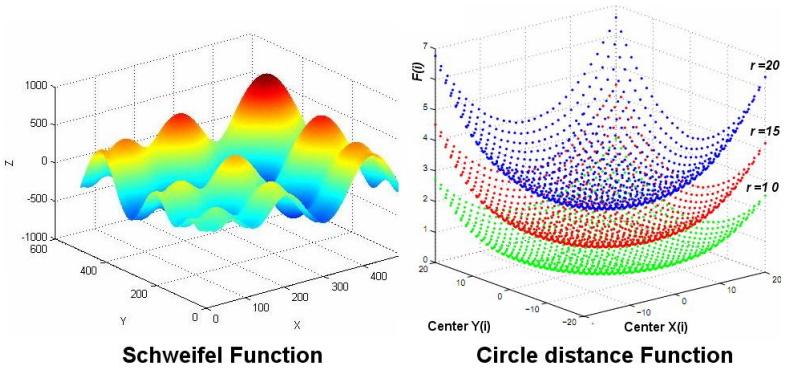

Figure A.7: Illustration of Schweifel and Square of circle distance multimodal function.

(normal) $\mathbf{n(n_1, n_2, n_3)}$, and finally its radius r. The number of column of matrix $\mathbf{J_0}$ corresponds to the number of parameters to be estimated, and the number of rows corresponds to number of points the substitute geometry will be fitted to.

The central idea of this LM method lies on the equation $\mathbf{Hx} = -\mathbf{v}$. If this equation is enlarged into $\mathbf{J_0^T J_0} + \lambda \left(\mathbf{I} + \mathbf{diag}\left(\mathbf{J_0^T J_0 x}\right)\right) = -\mathbf{J_0^T d(p_0)}$, one can observe that if λ is zero or small, LM behavior become Gauss-Newton method. In the opposite, if λ is large, then the off-diagonal elements of $\mathbf{J_0^T J_0}$ will have less effect such that LM behaves like steepest-decent method. The term $\mathbf{I}+\mathbf{diag}(\mathbf{J_0^T J_0})$ is used instead of $\mathbf{D^T D}$.This is a weighted distance matrix (depending on the geometry which will be estimated), based on Nash [Nash [1979]] suggestion, such that $\mathbf{Hx} = \mathbf{J_0^T J_0} + \lambda \left(\mathbf{I} + \mathbf{diag}\left(\mathbf{J_0^T J_0 x}\right)\right) = -\mathbf{J_0^T d(p_0)}$ becomes positive definite.

A.4 Initial Point Problem

LM iterative method mentioned in the previous section depends significantly on the initial guess of a set of solutions, $\mathbf{p_0}$ [Rardin [2006]]. This situation is similar to any other iterative algorithm. The function to be optimized is a multi-modal function with a complex contour and many local optimums. Subsequently, the risk exists that the search is trapped in a local optimum region. The illustration of multi-model function is shown in A.7 (left) by using Schweifel function and square of the summation of a circle distance function, which is $F = \sum_{i=1}^{N} d_i^2$, where d_i is declared in eq. A.17.

As mentioned before, the LS nonlinear function which to be minimized to fit geometries is multi modal. Hence, it has many local minima, only one being the global

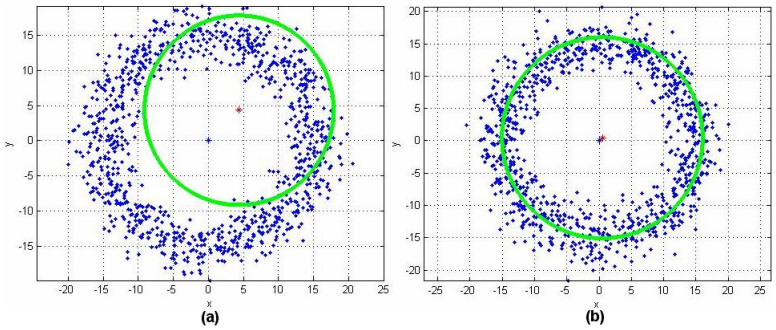

Figure A.8: Different initial solutions affect the nal solution. (a) Initial guess is far from optimal, (b) initial guess is near optimal.

optimum. If the optimization process gives a local minimum solution, then the solution is sub-optimal. The searching procedure can be trapped in local minima depending on where the initial guess is put. Subsequently, as it can be presumed, the result is significantly affected by the initial guess [Rardin [2006]]. For example, the objective function to fit a circle is shown in A.7(right). The surface is constructed by varying the (x, y) center position of the circle. The different colors show how the surface changes as the candidate radius r changes. Even though in this case the optimization zone is convex, different levels of radius r create different separated optimization zones. This can trap the searching process in one of the optimization zones. Therefore, it is possible the final solution is not a global optimum, depending on the initial solution. Fig. A.8 illustrates how initial guess as starting solution affects the final results. If the initial guess is far from optimum, an unexpected final result can be obtained (A.8a). On the other hand, a good initial guess significantly improves the final solution reducing the objective function value (A.8b).

A.5 Chaos Optimization

Chaos is defined as a semi-randomness property. This property is generated by a nonlinear deterministic equation. It creates a chaotic dynamic step which can easily escape from local optima. The concept is different with using rejection-accepting probability test in random-based algorithms, such as improvement heuristic search [Syam and Al-Harkan [2010]]. Searching through regularity of chaotic motion, represented by one-dimensional logistic map, is its fundamental recipe [Luo et al. [2008]]. Chaos op-

APPENDIX A. PERFORMANCE IMPROVEMENT IN NON-LINEAR GEOMETRIC FITTING

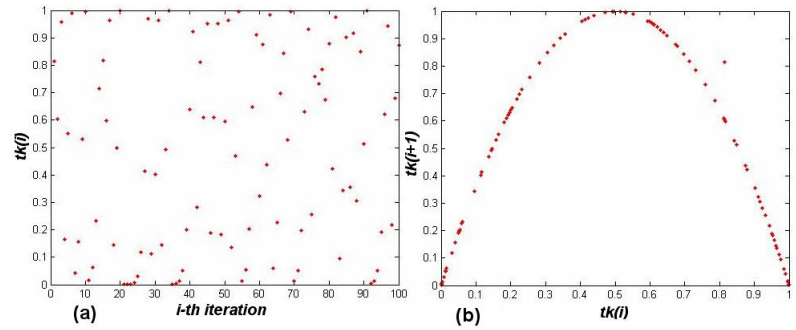

Figure A.9: Logistic map. (a) time-series plot of logistic map, (b) paired-plot between two consecutive chaos variables.

timization (CO) uses these chaos properties, which are ergodicity, stochastic property, and regularity [Tavazoei and Haeri [2008]]. The one-dimensional logistic map used is:

$$\mathbf{t_{k+1}} = \lambda_{\mathbf{c}}(\mathbf{1} - \mathbf{t_k}) \tag{A.23}$$

Where $\lambda_c \in \{3.56, 4\}$ is a control argument and k is iteration number. Yang [Yang et al. [2009]] recommended $0 \leq \mathbf{t_0} \leq \mathbf{1}$ where $\mathbf{t_0} \notin \{\mathbf{0}, \mathbf{0.25}, \mathbf{0.5}, \mathbf{0.75}, \mathbf{1.0}\}$. The behavior of eq. A.23 becomes chaotic in the sense that its value is drastically changed within the limit of λ_c and $\mathbf{t_k}$ presenting the regularity of chaotic motion. Fig. A.9 shows the plot of time series of this function and paired-plot between two consecutive chaos variables.

This CO is used to improve the initial guess of LM non-linear fitting iterative method, so that the initial guess is near the optimal solution, thus preserving the computation time, which is very important when the sample size is large (millions of points). The combination of CO algorithm with LM algorithm to improve the initial guess can be found in table A.2.

To adjust small ergodic range around p_i*, the parameters are set as $\lambda = 0.45$ [Tavazoei and Haeri [2008]], $\lambda = 4$ [Yang et al. [2009]], $r_{max} = 50$, and $K_{max} = 50$. The value $\lambda = 4$ is set such that a signicant difference in the long term will be obtained from a small change of t. As it can be seen from A.9right, with a small change in two consecutive $\mathbf{t}$, a chaotic behavior will be observed in the time series manner (A.9left). The value of K_{max} and r_{max} were chosen to minimize the overhead computational cost in determining the initial point. The statements IF $a_i^{r+1} > a_i^r$ THEN $a_i^{r+1} = a_i^r, \lambda \in \{0, 0.5\}$ and IF $b_i^{r+1} < b_i^r$ THEN $b_i^{r+1} = b_i^r, \lambda \in \{0, 0.5\}$ are to encourage movement farther from the initial bounding area, set in the beginning of the search. With reference

Algorithm 2: Chaos search to improve the initial guess in LM method	
Input:	Vector $\mathbf{p_0}$ is the initial guess for the parameter $(1 : n - param)$
Goal:	New vector $\mathbf{p_0}$ is the improved initial guess by Min $F(\mathbf{p_i})$, $\mathbf{p_i} \in \{\mathbf{a_i}, \mathbf{b_i}\}$, let $\mathbf{p^k} = (\mathbf{p^1} : \mathbf{p^k})$ where: $\mathbf{p}$=$(p_1, \cdots, p_n)$ and $\mathbf{t}$=$(t_1, \cdots, t_n)$
1:	Set $k = 0,\ r = 0$, Set $k_{max} = 10,\ r_{max} = 30$
2:	Produce randomly. $\mathbf{t_0} \in \{\mathbf{0}, \mathbf{1}\}$ and $\notin \{0, 0.25, 0.5, 0.75, 1.0\}$
3:	Set $\mathbf{t^k} = \mathbf{t^0}$, $\mathbf{t}* = \mathbf{t^0}$, $\mathbf{a^0} = \mathbf{p} - \mathbf{MPE}$, $\mathbf{b^0} = \mathbf{p} + \mathbf{MPE}$ Where: $\mathbf{a} = (\mathbf{a_i}, \cdots, \mathbf{a_n})$, $\mathbf{b} = (\mathbf{b_i}, \cdots, \mathbf{b_n})$
4:	Set $\mathbf{p}* = \mathbf{p_0}$ $\rightarrow$ **initial guess parameter**
5:	DO WHILE $\{\ r < r_{max}$; DO WHILE $\{\ k < k_{max}$;
6:	Set $p_i = a_i^r + t_i^r(b_i^r - a_i^r)$ Calculate $F^k = sum_{i=0}^{N} d_i^2(p_i)$
7:	IF $F^k < F*$ THEN $F* = F(p^k)$, $p* = p^k$, $t* = t^k$
8:	$k = k + 1;\ t_i^k = \lambda t_i^{k-1}(1 - t_i^{k-1}),\ \lambda \in \{3.54, 4\}$
9:	}END k-th iteration; $r = r + 1$
10:	$a_i^{r+1} = p_i * -\lambda(b_i^r - a_i^r)$ and $b_i^{r+1} = p_i * +\lambda(b_i^r - a_i^r)$
11:	IF $a_i^{r+1} > a_i^r$ THEN $a_i^{r+1} = a_i^r$, $\lambda \in \{0, 0.5\}$
12:	IF $b_i^{r+1} < b_i^r$ THEN $b_i^{r+1} = b_i^r$, $\lambda \in \{0, 0.5\}$
13:	IF r, r_{max} THEN produce $t_0 \in \{0, 1\}$ by random, $k = 0,\ \mathbf{t^k} = \mathbf{t^0}$ GO TO (7) ELSE Chaos Optimization (CO) is terminated.
14:	return $\mathbf{p_0} = \mathbf{p}*;\}$ END r-th iteration
15:	Insert the new $\mathbf{p_0}$ into **Algorithm 1: LM Algorithm**

Table A.2: Chaos Algorithm.

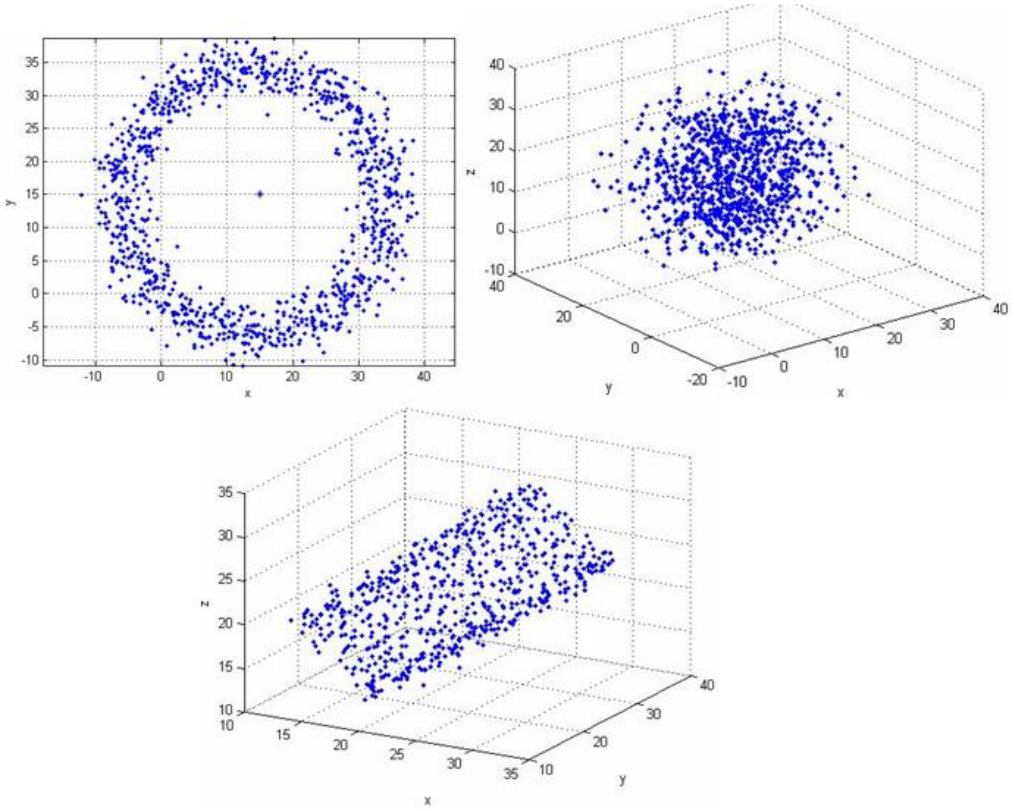

Figure A.10: Illustration of data generated for circle, sphere, and cylinder.

to Fig. A.8(right), the initial guess is expected to be placed on the correct optimization zone to find the global optimum.

A.6 Implementation and Discussion

A.6.1 Performance Improvement

Points with random error according to uniform distribution and normal distribution were generated as presented in table A.3. For Chaos-LM method, initial point guess of the initial solution of LM optimization iteration was improved by sending it to CO method. In LM algorithm, the stopping rule is set as maximum iteration = 1000 and 100 for the Chaos-LM method. Fig. A.10 visualizes the generated data by plotting the points cloud. The algorithm is implemented in MATLAB and run on an Intel Centrino Core 2 Duo 2.2 GHz.

Type of Data		**Number of points and Nominal Parameter**		
		Circle	Sphere	Cylinder
Uniform	Range (μm)	(x,y,r) = (15,15,20) mm	(x,y,z,r) = (15,15,15,20) mm	(x,y,z,r) = (15,15,15,5) and **n** (1,1,1) mm
Type 1	[-2.2,2,2]	1000 pts	grid [30x30]	grid [25x25]
Type 2	[-5,5]	1000 pts	grid [30x30]	grid [25x25]
Normal	sigma σ			
Type 1	1.1	1000 pts	grid [30x30]	grid [25x25]
Type 2	2.5	1000 pts	grid [30x30]	grid [25x25]

Table A.3: Details of data generation.

The initial guess of the center of circle and sphere is the centroid. The centroid location for each x, y, z is the average of the points $\sum_{i=1}^{n} \frac{\mathbf{x_i}}{n}$. The centroid is also the initial guess of point on the axis of a cylinder. For the radius, its initial estimation is:

$$r_0 = \frac{1}{2}\left(\frac{(max\ x_i - min\ x_i) + ((max\ y_i - min\ y_i)}{2}\right) \tag{A.24}$$

for the circle, and:

$$r_0 = \frac{1}{2}\left(\frac{(max\ x_i - min\ x_i) + ((max\ y_i - min\ y_i) + ((max\ z_i - min\ z_i)}{3}\right) \tag{A.25}$$

For the sphere and cylinder. For the special case of a cylinder, its initial guess for cosine direction of the axis is derived by fitting a 3D line to the point clouds. The fitting method is implemented with a method according to NIST [Shakarji [1998]]. Two levels of sigma for the data deviation were considered. Type 1 represents only the uncertainty of the instrument (Maximum Permissible Error/MPE), while type 2 simulates the uncertainty due to the part and the instrument. Type 2 data represents a more realistic situation since an inspected part always contains feature deviation from its nominal [Kruth et al. [2009]].

Results from 100 runs show that the combination of these methods, Chaos and LM, increases the accuracy of the fitting process. The indication is that the fitted geometry has less residual error, in term of the magnitude of their norm of sum of square residuals, while preserving the computation cost. Table A.4 provides the complete

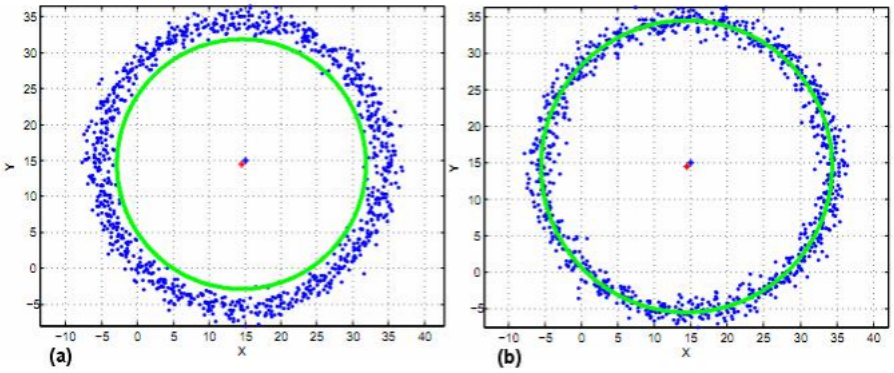

Figure A.11: Substitute full circle tting results of (a) LM method and (b) Chaos-LM.

results of the fitting of full geometry point clouds both with only LM method and with Chaos-LM method. Chaos-LM encourages the initial guess of the solution to move to a better starting point, thanks to the property of the chaotic motion which non-repeatedly searches through a set of states in a certain bounded domain [Jiang [1998]]. Sensitiveness of the final solution of LM method to where the initial guess starts is related to the Taylor approximation in the Gauss-Newton method, which depends highly on the non-linearity degree of the neighborhood. The quality of this Taylor approximation, which is usually until first term approximation, decreases for higher non-linear function. Because of this, a trapped condition during searching process can occur. Fig. A.11, A.12 and A.13 propose some visualizations of the fitting result for circle, sphere and cylinder respectively. From this, one can observe that the Chaos-LM fitting (fig. A.11, A.12, and A.13 right) finally lie on the middle of the point cloud. This is coherent with the fundamental behavior of least-square fitting which is an average over the considered data (in this case the point cloud). Plot of the norm of residual and Central Processing Unit (CPU) time for circle, sphere, and cylinder are respectively presented in fig. A.14 and A.15. In the special case of a cylinder fitting result, the computation time slightly increases compared to the LM method. Indeed, the improvement in the sum of squared residuals is significant. Furthermore, from the graph one can observe that the variation interval of the CPU time for this cylinder fitting is intersecting each other, so they are not significantly different.

A very important condition, difficult to address with standard approaches to fitting, arises when the cloud of points does not cover the whole feature, e.g. only a hemisphere has been sampled. This may be due to access limitation of the sensor to capture part

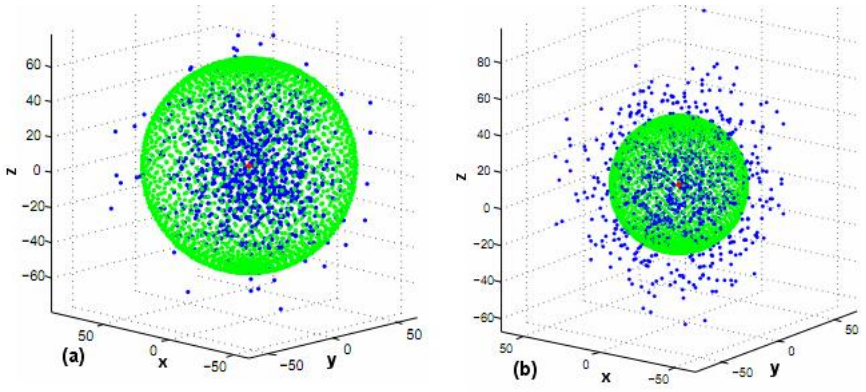

Figure A.12: Substitute full sphere tting results of (a) LM method and (b) Chaos-LM.

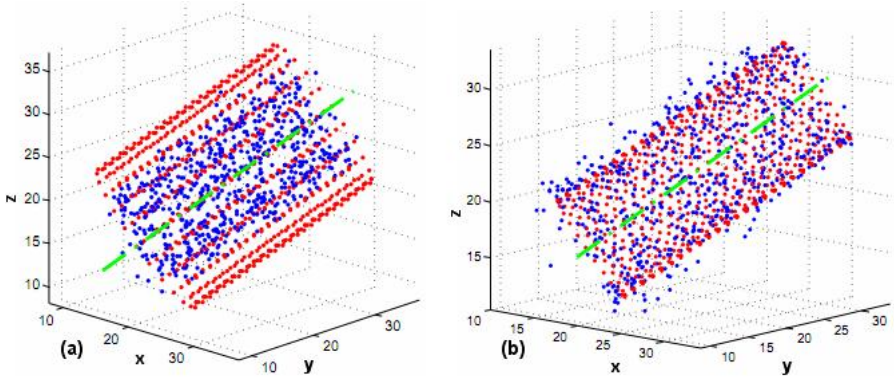

Figure A.13: Substitute full cylinder tting results of (a) LM method and (b) Chaos-LM.

APPENDIX A. PERFORMANCE IMPROVEMENT IN NON-LINEAR GEOMETRIC FITTING

Random Error Type [μm]	**Levenberg-Marquardt Algorithm**					
	Circle		Sphere		Cylinder	
	$\|\|r\\|\|$ ($\mu \pm 3\sigma$) [mm]	CPU ($\mu\pm 3\sigma$) [s]	$\|\|r\\|\|$ ($\mu \pm 3\sigma$) [mm]	CPU ($\mu\pm 3\sigma$) [s]	$\|\|r\\|\|$ ($\mu \pm 3\sigma$) [mm]	CPU ($\mu\pm 3\sigma$) [s]
U [-2.2,2.2]	75.2584 ± 0.0627	0.8334 ± 0.0502	4.1007 ± 0.2632	1.0459 ± 0.1059	71.427 ± 0.0646	0.5114 ± 0.0512
U [-5,5]	75.26 ± 0.0548	0.8081 ± 0.0244	7.6507 ± 1.2160	0.5935 ± 0.0442	71.4316 ± 0.1288	0.6317 ± 0.0825
N (σ=1.1)	75.2265 ± 0.0166	0.825 ± 0.0376	1.5108 ± 0.0202	1.0353 ± 0.1272	71.4232 ± 0.0150	0.6368 ± 0.0766
N (σ=2.5)	75.225 ± 0.0375	0.8754 ± 0.1270	1.6651 ± 0.0453	1.0694 ± 0.1653	71.4252 ± 0.0363	0.6276 ± 0.0804
Random Error Type [μm]	**Chaos and Levenberg-Marquardt Algorithm**					
	Circle		Sphere		Cylinder	
	$\|\|r\\|\|$ ($\mu \pm 3\sigma$) [mm]	CPU ($\mu\pm 3\sigma$) [s]	$\|\|r\\|\|$ ($\mu \pm 3\sigma$) [mm]	CPU ($\mu\pm 3\sigma$) [s]	$\|\|r\\|\|$ ($\mu \pm 3\sigma$) [mm]	CPU ($\mu\pm 3\sigma$) [s]
U [-2.2,2.2]	5.6646 ± 1.6784	0.5578 ± 0.0539	2.79 ± 0.2570	0.5634 ± 0.05555	5.7257 ± 2.0102	0.6225 ± 0.0277
U [-5,5]	4.3562 ± 1.3061	0.5551 ± 0.0338	6.2199 ± 0.4602	0.5628 ± 0.1088	5.7994 ± 2.9641	0.6706 ± 0.0515
N (=1.1)	5.1907 ± 1.2732	0.5677 ± 0.1053	0.4279 ± 0.1524	0.5458 ± 0.0569	6.9329 ± 2.9690	0.6788 ± 0.0907
N (=2.5)	5.469 ± 1.4621	0.5442 ± 0.0836	0.8185 ± 0.0991	0.4663 ± 0.0512	6.9169 ± 1.6543	0.6987 ± 0.1103

Table A.4: Simulation results of the full-geometric point cloud fitting.

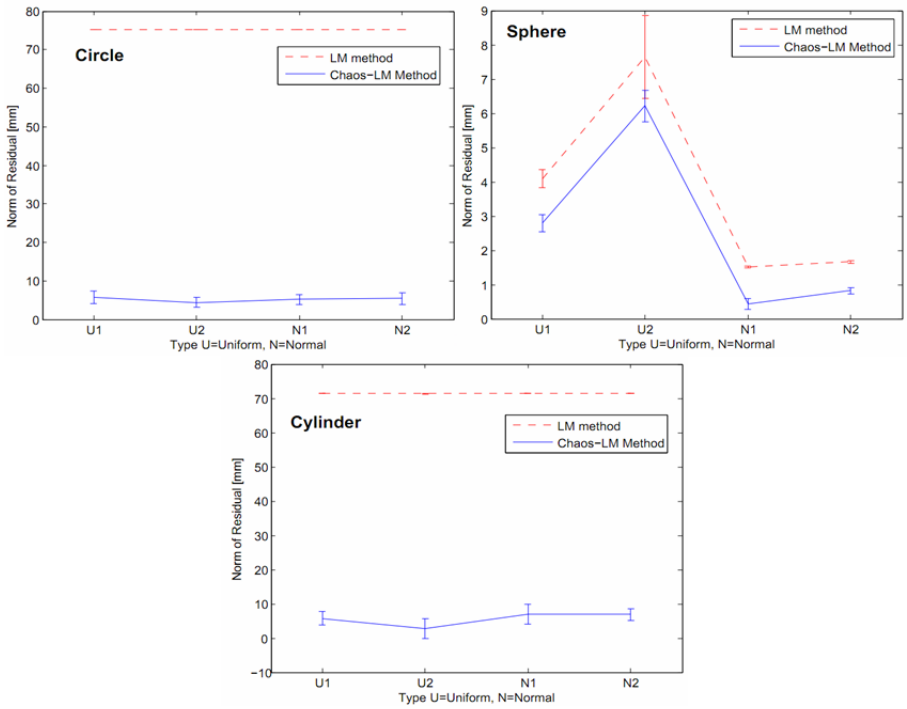

Figure A.14: Norm of residual of LM method and Chaos-LM method for full point cloud geometry fitting.

APPENDIX A. PERFORMANCE IMPROVEMENT IN NON-LINEAR GEOMETRIC FITTING

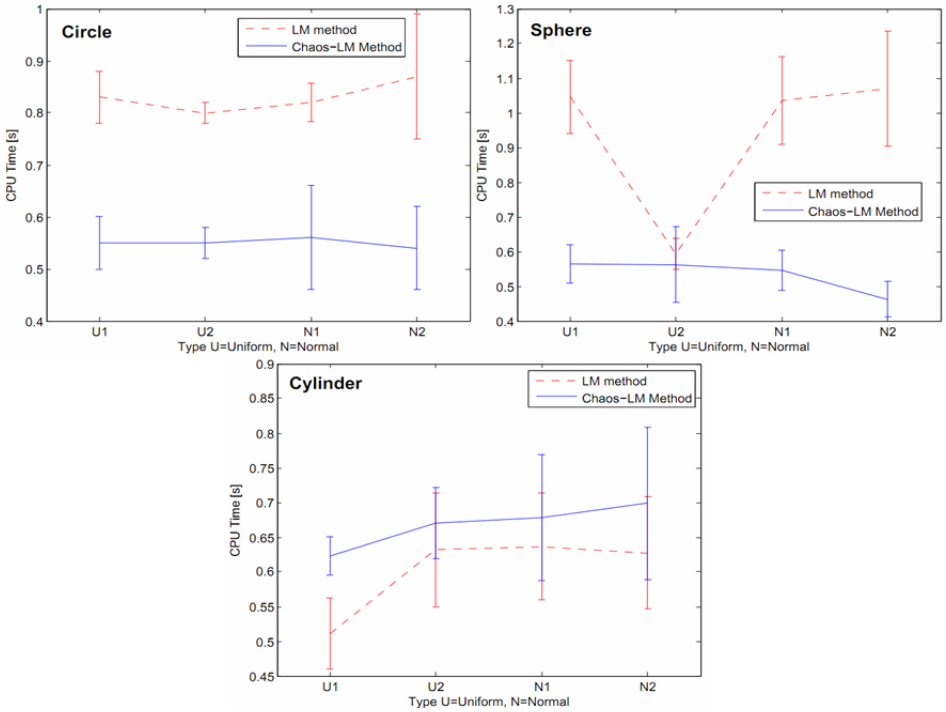

Figure A.15: CPU time of LM method and Chaos-LM method for full point cloud geometry fitting.

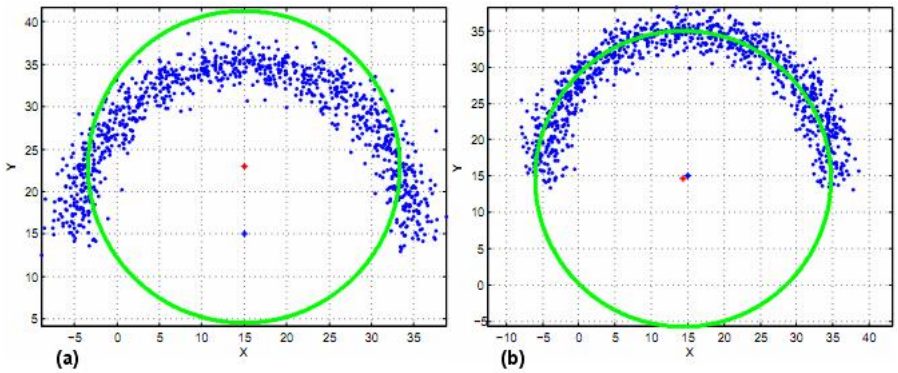

Figure A.16: Substitute Half circle point cloud tting results of (a) LM method and (b) Chaos-LM.

surface, like e.g. in the case of laser scanning instruments, or to the real incompleteness of the sphere, like in the case of a circular groove. Both LM and Chaos-LM methods are applied to half-circle, half-sphere, and half-cylinder point clouds. This is a significantly more difficult situation compared to fitting a complete cloud of points. One of the reasons is that the estimation of initial solution tends to be less accurate since, in general, the initial estimation is based on the symmetrical properties of the geometry to be fitted. The data generation is identical to the one considered for the full-geometry case as presented in table A.3. From this data generation, half of the cloud of points is then discarded to get the half-geometry. The number of runs in the simulation and the performance measures of both fitting methods are identical to the previous "normal case". Details of all results of the simulation runs are presented in table A.5. One can observe that the accuracy of fitting half-geometry point clouds is significantly improved by Chaos-LM method compared to only LM method. Instead, the CPU time needed for Chaos-LM to have better result is higher than the one of the LM method. Since there are increments in CPU time to get a better result of Chaos-LM method, the comparison of the two algorithms in this case has to be further investigated. Graphical presentation of the fitting results for half-circle, half-sphere and half-cylinder are provided in fig. A.16, A.17, and A.18 respectively to intuitively understand the significant result of accuracy improvement by Chaos-LM in the case of half-geometries fitting. Finally, to graphically explain the results in table A.5, fig. A.19 andA.20 respectively plot the norm of residual and CPU time of the half-geometries fitting.

APPENDIX A. PERFORMANCE IMPROVEMENT IN NON-LINEAR GEOMETRIC FITTING

Random Error Type [μm]	**Levenberg-Marquardt Algorithm**					
	Circle		Sphere		Cylinder	
	$\|\|r\\|\|$ ($\mu \pm 3\sigma$) [mm]	CPU ($\mu\pm 3\sigma$) [s]	$\|\|r\\|\|$ ($\mu \pm 3\sigma$) [mm]	CPU ($\mu\pm 3\sigma$) [s]	$\|\|r\\|\|$ ($\mu \pm 3\sigma$) [mm]	CPU ($\mu\pm 3\sigma$) [s]
U [-2.2,2.2]	88.0124 ± 0.0087	0.8263 ± 0.0610	41.9479 ± 0.4454	0.2918 ± 0.0128	41.2638 ± 0.0271	0.6307 ± 0.0412
U [-5,5]	88.0106 ± 0.0209	0.8364 ± 0.0869	41.1334 ± 0.9747	0.2931 ± 0.0153	41.2651 ± 0.0510	0.6273 ± 0.0557
N (=1.1)	88.0143 ± 0.0021	0.4542 ± 0.0535	21.2072 ± 0.0603	0.2916 ± 0.0155	41.2643 ± 0.0067	0.4978 ± 0.0159
N (=2.5)	88.0149 ± 0.0053	0.4634 ± 0.0551	21.1117 ± 0.1741	0.2957 ± 0.0285	41.2636 ± 0.0140	0.6243 ± 0.0895
Random Error Type [μm]	**Chaos and Levenberg-Marquardt Algorithm**					
	Circle		Sphere		Cylinder	
	$\|\|r\\|\|$ ($\mu \pm 3\sigma$) [mm]	CPU ($\mu\pm 3\sigma$) [s]	$\|\|r\\|\|$ ($\mu \pm 3\sigma$) [mm]	CPU ($\mu\pm 3\sigma$) [s]	$\|\|r\\|\|$ ($\mu \pm 3\sigma$) [mm]	CPU ($\mu\pm 3\sigma$) [s]
U [-2.2,2.2]	14.8104 ± 7.5609	1.2904 ± 0.0361	8.5878 ± 4.8903	0.5509 ± 0.0450	18.9191 ± 3.1847	1.2009 ± 0.0611
U [-5,5]	15.9923 ± 12.0558	1.2212 ± 0.1456	9.2163 ± 6.3610	0.413 ± 0.0247	18.7634 ± 3.0584	1.2185 ± 0.1001
N (=1.1)	15.0230 ± 13.5643	1.2944 ± 0.0831	4.9317 ± 4.002	0.4170 ± 0.0269	18.7751 ± 3.5261	1.0946 ± 0.1623
N (=2.5)	16.7502 ± 12.1930	1.3000 ± 0.08	4.9572 ± 2.3395	0.55 ± 0.0335	19.1193 ± 4.0786	1.2163 ± 0.0627

Table A.5: Simulation results of the half-geometric point cloud fitting.

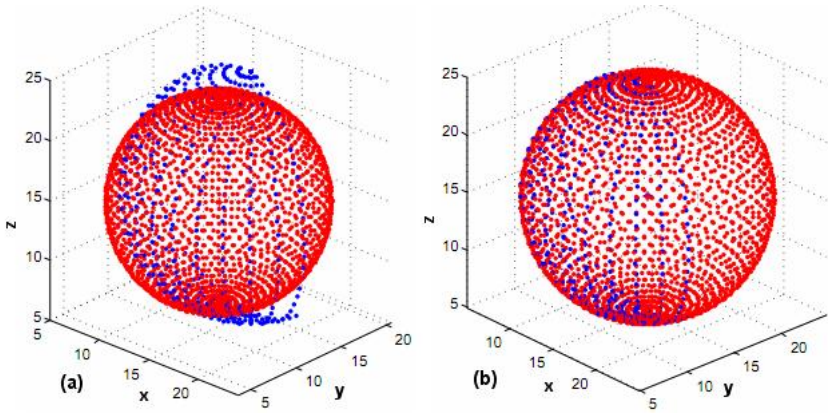

Figure A.17: Substitute Half sphere point cloud tting results of (a) LM method and (b) Chaos-LM.

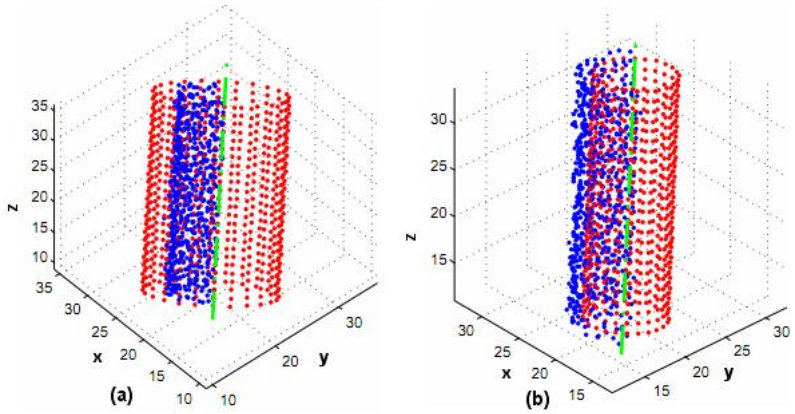

Figure A.18: Substitute Half cylinder point cloud tting results of (a) LM method and (b) Chaos-LM.

APPENDIX A. PERFORMANCE IMPROVEMENT IN NON-LINEAR GEOMETRIC FITTING

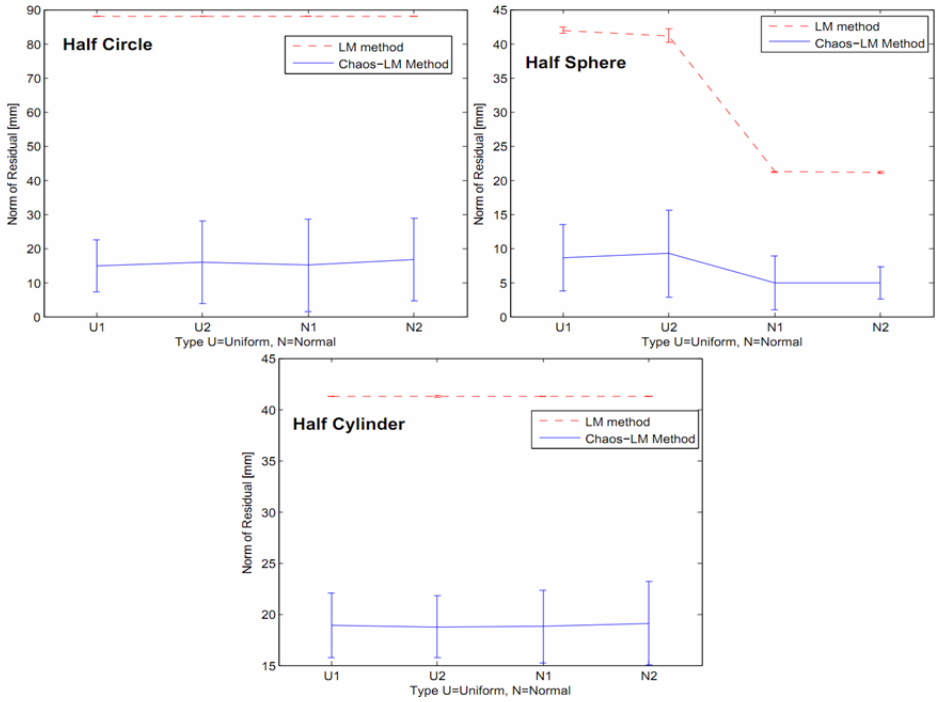

Figure A.19: Norm of residual of LM method and Chaos-LM method for Half point cloud geometry fitting.

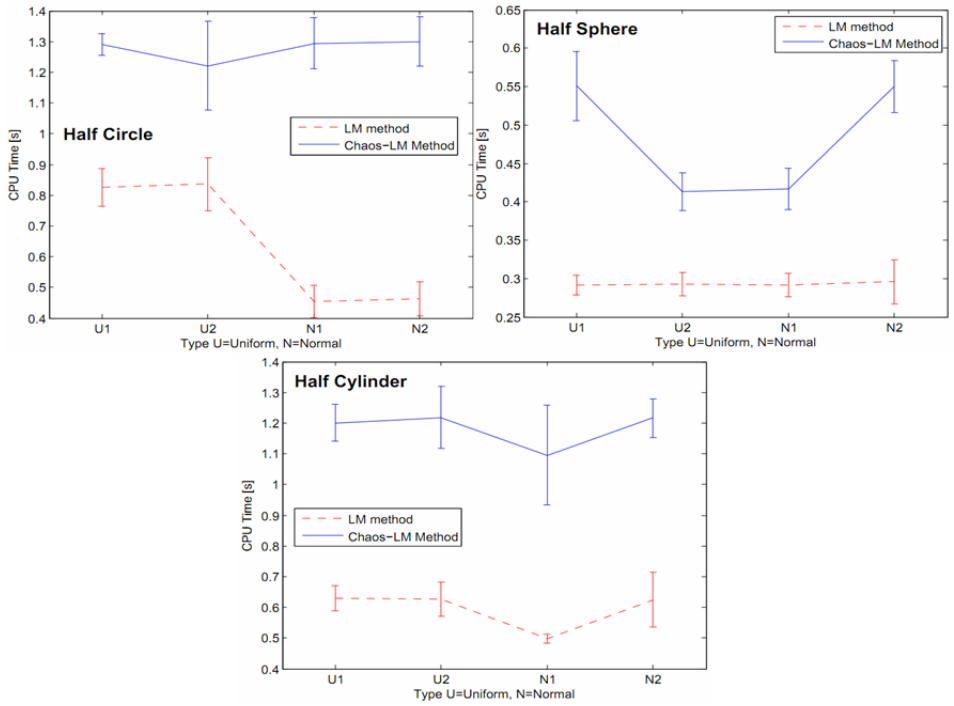

Figure A.20: CPU time of LM method and Chaos-LM method for half point cloud geometry fitting.

APPENDIX A. PERFORMANCE IMPROVEMENT IN NON-LINEAR GEOMETRIC FITTING

Convergence curve analyses are presented in two parts which are for full- and half-geometries fitting. One should note that in both cases, the value of convergence curve can not reach zero since error exist on the points to be fit due to the simulated perturbation. The selected type of simulation is uniform distribution in the range of -5m and 5 m U [-5,5]. For each group, three convergence curves are shown corresponding to circle, sphere and cylinder. On the x-axe of the graph, there are two types of iteration. For LM method, it corresponds to LM number of iterations which ranges from 100 to 1000 iterations. For Chaos-LM, this axis corresponds to the number of chaos iteration in the range from 10 to 100 iterations. In the case of full-geometric fitting, the convergence rate is much faster in the case of circle and cylinder. Fig. A.21, fig. A.22, and fig. A.23 depict the convergence curves for the full-geometries case. The convergences rate of LM method for circle and cylinder fitting are much slower, as the small gradient of the curve compared to the Chaos-LM one denotes. In the case of the sphere, both LM and Chaos-LM method have a similar convergence rate though Chaos-LM method is faster with respect to the LM one. Clearer trapped phenomena of LM method in fitting can be observed in the case of half-geometries fitting problem. The convergence curves for the half-geometries are shown in fig. A.24, A.25, A.26 respectively. From all these three figures, the LM method does not show improvement as the number of LM iterations is increased. This situation clearly shows that LM has been trapped in some local optimum region. It means that, although the number of iteration is increased, the result of LM can not give a better result so one can say it is early converged. On the other hand, a different situation can be seen for the Chaos-LM method. This method can escape from a local optimum with an increase of the chaos iterations. The reason is that, by using chaotic movement and increasing the number of iterations, more regions are visited to explore new better feasible solution that can give a better result. Chaos-LM can show a significant improvement and convergence result without a large number of iteration increments. From the investigation of the convergence, one can observe that the best number of chaos iterations for Chaos-LM is around 30.

The chaos optimization to improve the initial guess is effective in LS fitting problem. The chaos search encourages the initial guess of the solution to move to a better starting point that is nearer to the true solution thanks to the property of the chaotic motion that non-repeatedly searches through a set of states in a certain bounded domain [Jiang [1998]]. With this property, the searching process can cover a wider search

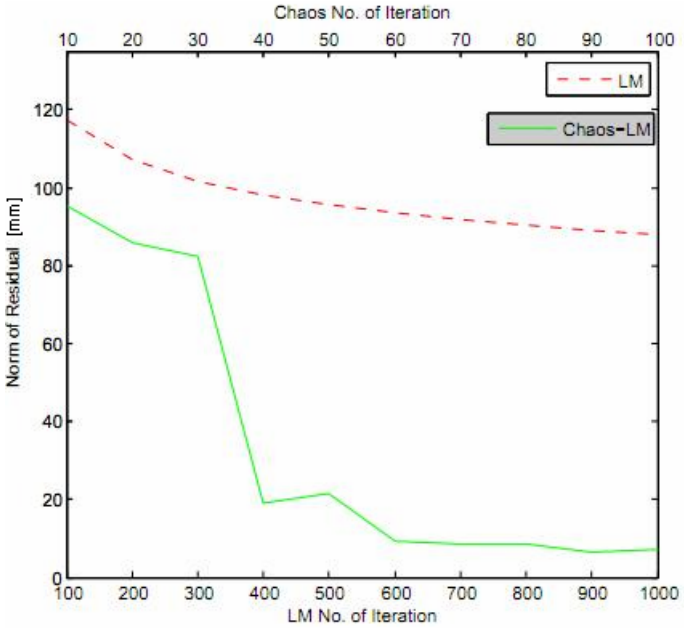

Figure A.21: Convergent rate for fitting full circle point cloud.

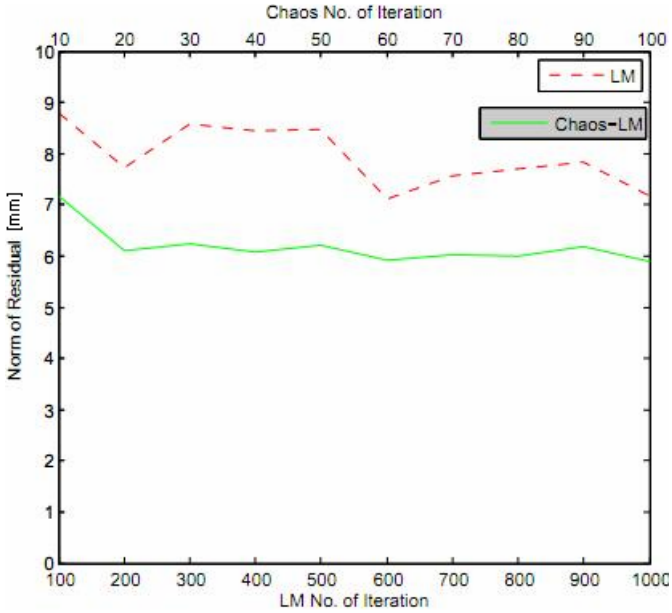

Figure A.22: Convergent rate for fitting full sphere point cloud.

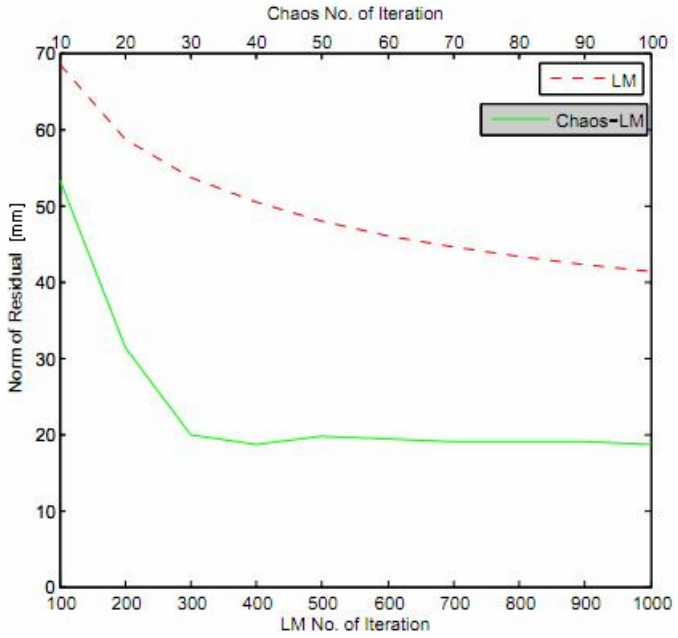

Figure A.23: Convergent rate for fitting full cylinder point cloud.

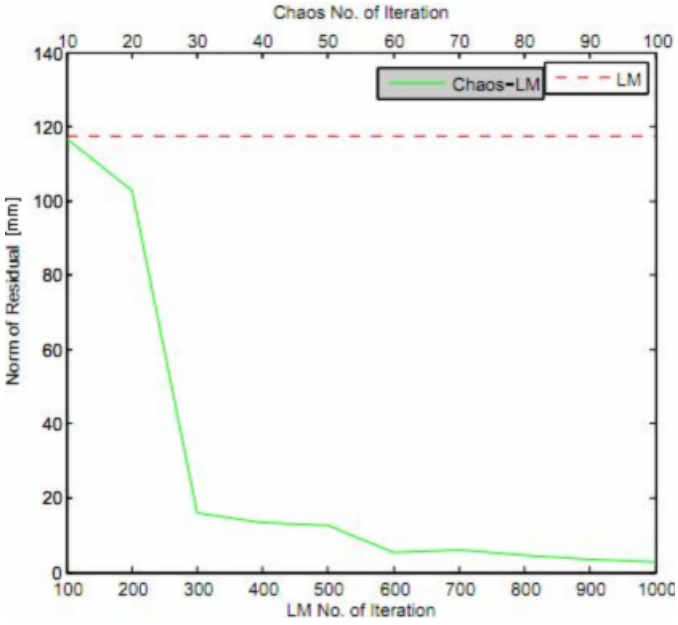

Figure A.24: Convergent rate for fitting half circle point cloud.

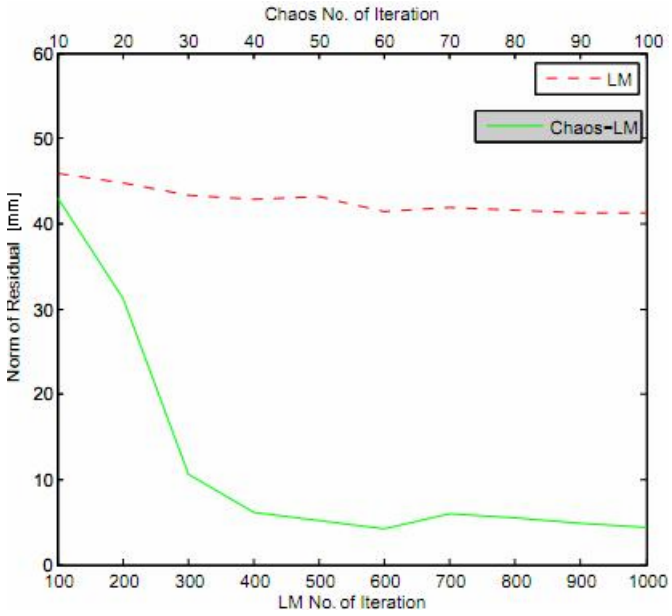

Figure A.25: Convergent rate for fitting half sphere point cloud.

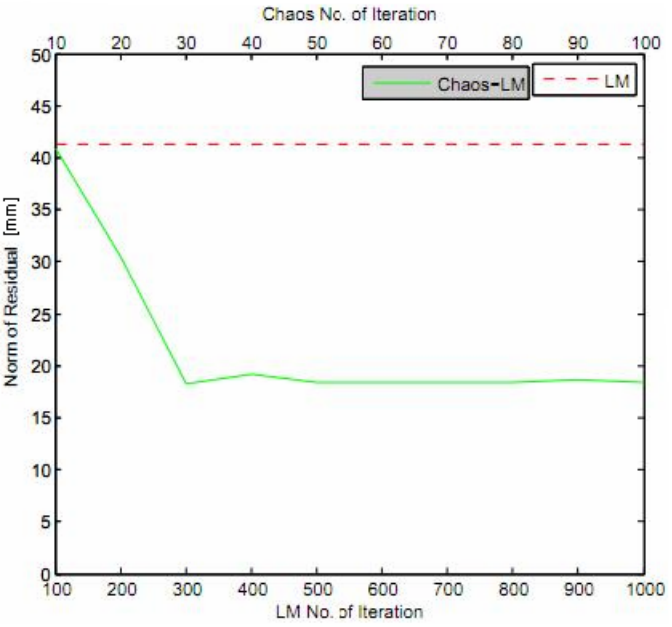

Figure A.26: Convergent rate for fitting half cylinder point cloud.

space within a small number of iteration. This is a different property compared to improvement heuristic search such as genetic algorithm, tabu search, etc [Trafalis and Kasap [2002]]. Generally, improvement heuristic searches algorithm need larger number of iterations to increase the visited feasible solution around the search space in which the computational cost becomes problematic.

Combinations of Chaos and LM algorithms have a linear complexity in term of the relation between number of points processed and the increase in computation time. One can see that they are constructed from two algorithms, which are the Chaos and the LM algorithm. Each of them contains two nested loops inside their algorithm. Since the two loops of the algorithm are not related to the number of the points n, which are the points to be fitted, the relation of the algorithm steps to their inputs is only in the calculation to evaluate the objective function through all number of points. Let the total order of the algorithms be $f(n) = n_1 + n_2 = n + n = 2n$ where subscript 1 and 2 correspond to algorithm 1 (chaos) and 2 (LM), respectively. Hence, the algorithm efficiency is $O(n)$ since $\exists n_0 > 0$ and $k > 0 \Rightarrow \forall n > n_0,\ f(n) \leq k\ g(n)$ such that $f(n) = n_1 + n_2 = O(n)$.

A.6.2 Case Studies

To test the Chaos-LM method in a real fitting situation, a case study was carried out. It is derived from Kawalec and Magdziag [Kawalec and Magdziak [2012]]. In their case, a calibrated ring gauge was used since they focused on comparison of methods to solve the circle fitting problem. Instead, in the proposed case study, measurement of a calibrated ceramic sphere of a "ZEISS" CMM for stylus qualification was used as shown in A.27. The sphere has a calibrated radius of 14.991 mm. The CMM machine used was "ZEISS PRISMO HTG" with $MPE_E = 2\mu m + \frac{L}{300}\mu m$. The choice of sphere is due to the fact that a 3D geometry fitting can be applied and a sphere is a good example of a common artifact for CMMs. The strategy used to obtain the points was by means of scanning strategy. The point cloud to be fit is a half-geometry. There are two types of point clouds. The first type is low density cloud and the second type is high density (A.28). The low density point cloud contains 312 points. A total of 3435 points were collected for high density point cloud. The initial parameter of the sphere, for both LM and Chaos-LM method, has been chosen near the optimal. The initial x and y are from the average of respectively $x-$ and $y-$position of the points, and z is selected from

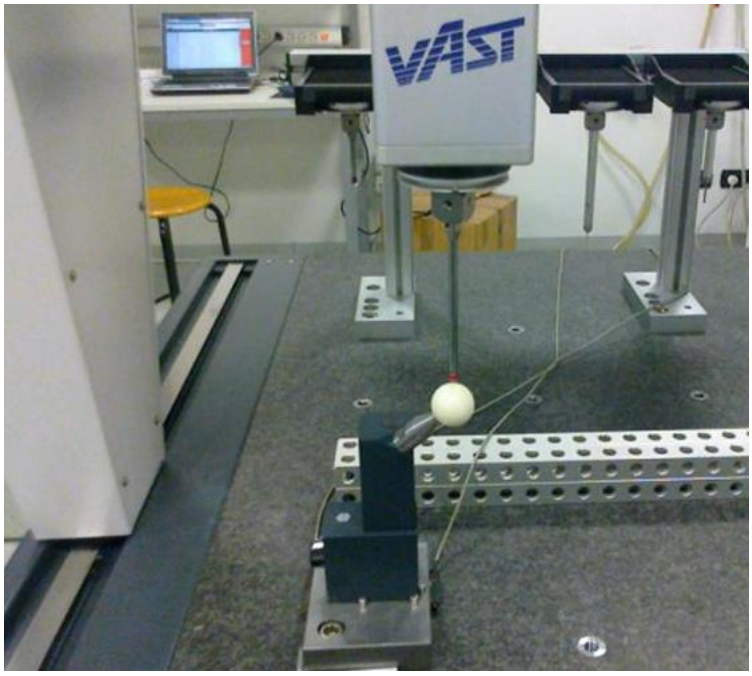

Figure A.27: Measurement of calibrated ceramic sphere with Bridge-type CMM.

maximum z-position of the points minus the known nominal radius of 15 mm. Table A.6 summarizes both the fitting results and the deviation from the calibrated radius of the sphere. From the results, the fitted radius of the sphere from Chaos-LM method is much better than the LM one. Note that the results of LM method are already from 50000 iterations. Both in the low and high density cases, the procedures are run with the same number of iteration. In the case of low density, the accuracy is even better than in the high density one since for high density, more solution space is obtained such that an increase of iterations can produce similar results with regard to the lower density result. Visualization of the fitting results is provided in A.29 both for low and high density points respectively.

Another case study was carried out by measuring and fitting an industrial-made cylinder work piece made of hardened steel having nominal diameter of 6 mm. The measurement procedure is shown in A.30a. Total points obtained were 190 points by circular path scanning strategy of three segments. Fig. A.30b presents the fitting result. The blue points are the obtained points. Meanwhile, the red points are the fitted cylinder with its axis line in green. Since the geometry is symmetry, the selection

APPENDIX A. PERFORMANCE IMPROVEMENT IN NON-LINEAR GEOMETRIC FITTING

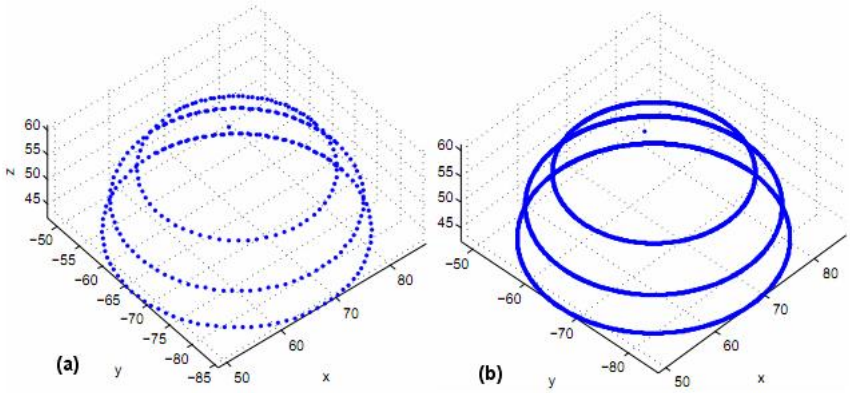

Figure A.28: Obtained point cloud. (a) Low density, (b) High density.

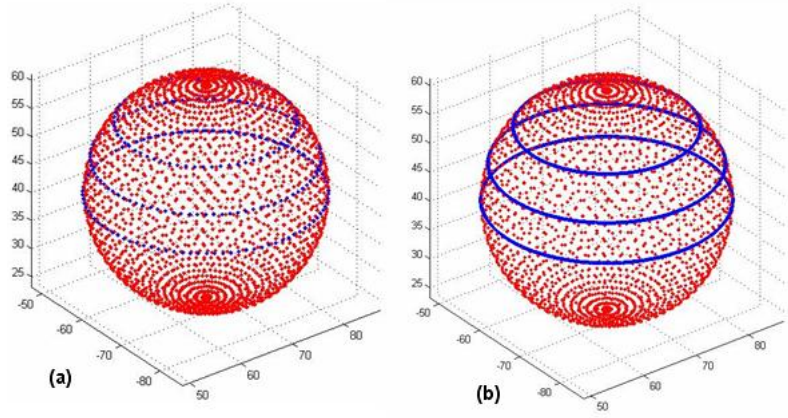

Figure A.29: Sphere fitting of (a) low density, (b) high density.

	x (mm)	y (mm)	z (mm)	radius (mm)	deviation from calibrated radius (mm)
Calibrated Value	-	-	-	14.9911	-
High Density					
LM Method	68.2182	-66.1638	41.9932	14.9111	0.08001
Chaos-LM Method	67.5716	-66.7949	42.2488	14.9919	0.00080
Low Density					
LM Method	68.261	-66.1605	41.9712	14.9009	0.09020
Chaos-LM Method	67.5458	-66.7681	42.2524	14.9904	0.00070

Table A.6: Results of fitting half-calibrated sphere for high and low density point cloud.

for initial parameters is identical to the one set in the simulation run of section 6.1 for cylinder case. The results show the improvement of Chaos-LM fitting. Details of the results are depicted in table A.7. The cylinder is not calibrated. Subsequently, the norm of residual $||r||$ is presented to compare the fitting quality. In this case, Chaos-LM gives better result. Moreover, from the table, it can be observed that the fitting result by LM is outside the tolerance limit, meanwhile the Chaos-LM result is inside.

A.7 Concluding Remarks

The problem of fitting non-liner geometries has been addressed. This problem is critical in dimensional metrology to assure the quality of manufacturing products. The geometries considered are circle, sphere and cylinder due to their various and common use in applications such as metrological calibration and mechanical assembly. The increasing capability of modern metrology instruments in sampling high density clouds of points in short time demands accurate and fast fitting procedures. Both cases of fitting full- and half-geometries are presented. From the fitting of full-geometries, results show that the use of chaos optimization to improve the initial guess for LM non-linear

APPENDIX A. PERFORMANCE IMPROVEMENT IN NON-LINEAR GEOMETRIC FITTING

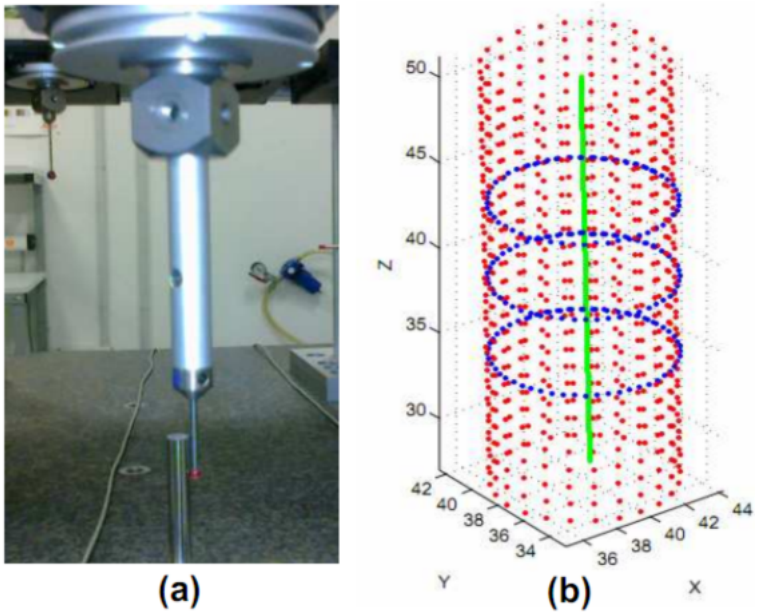

Figure A.30: (a) Measurement of industrial cylinder, (b) The fitting results.

	x [mm]	**y [mm]**	**z [mm]**	**nx**	**ny**	**nz**	**Diameter [mm]**	$\|\|r\|\|$ **[mm]**
Nominal Value	-	-	-				6 ± 0.01	-
LM Method	39.7946	37.5621	39.6751	-0.007	-0.0181	-0.9191	5.928	3.489
Chaos-LM Method	39.6788	37.2259	38.9024	-0.0531	-0.0571	-1.8548	6.0018	1.8278

Table A.7: Results of fitting industrial cylinder.

least square fitting has significantly improved the accuracy of the fitting and kept the computational time small. A slower fitting is observed in the case of half-geometries. Even though slower, Chaos-LM method can give the expected results by escaping from local optima. LM method is trapped and early converged in the case of half-geometries fitting, so that no improvement of the result can be obtained by increasing the number of iterations. Convergent rate efficiency of the proposed method is significantly higher in the case of incomplete points cloud. It seems that the LM method could have higher probability to be trapped in the local optima in this case. Two real case studies are presented. The case studies are to fit a calibrated sphere from point clouds representing half of the sphere geometry and to fit an industrial-made cylinder. The Chaos-LM method gives expected results. Finally, a note should be highlighted that a filtering procedure of the point cloud may be needed before the fitting process is carried out, since least-square fitting procedure is not completely robust to the outliers points. The future direction of this work is to identify the link between the non-linear problem and chaos property such that an adaptive region bounding and chaotic motion generation can be determined precisely.